Probing Structural Reorganization and Hydration inside Triblock Copolymer-Surfactant, Polyelectrolyte-Surfactant Assemblies using Excited-State Proton Transfer of Pyranine

A dissertation

as partial fulfillment of the requirement

for the degree of Doctor of Philosophy in Chemistry

By

Tapas Pal

176122025

Department of Chemistry
Indian Institute of Technology Guwahati,
Guwahati-781039,
Assam, India

Dedicated to My Family

Declaration

I do hereby declare that the work contained in this thesis entitled **"Probing Structural Reorganization and Hydration inside Triblock Copolymer-Surfactant, Polyelectrolyte-Surfactant Assemblies using Excited-State Proton Transfer of Pyranine"** is the outcome of the research work carried out by me under the supervision of Prof. Kalyanasis Sahu, Professor, Department of Chemistry, Indian Institute of Technology Guwahati, India.

In keeping with the general practice of reporting scientific observations, due acknowledgments have been made whenever the work described here has been based on the findings of other investigators. This work has not been submitted elsewhere for the award of any degree.

Dated: 29/05/2023

Tapas Pal

(Tapas Pal)

Department of Chemistry

Indian Institute of Technology Guwahati,

Guwahti-781039, India

INDIAN INSTITUTE OF TECHNOLOGY GUWAHATI

Department of Chemistry

CERTIFICATE

This is to certify that **Tapas Pal** (Roll No. 176122025) has been working under my supervision since July 2017 as a regular registered Ph.D. student. His thesis entitled **"Probing Structural Reorganization and Hydration inside Triblock Copolymer-Surfactant, Polyelectrolyte-Surfactant Assemblies using Excited-State Proton Transfer of Pyranine"** is an authentic record of the results obtained from the research work carried out under my supervision in the Department of Chemistry, Indian Institute of Technology Guwahati, Assam, India. I am forwarding his thesis to submit for the award of Doctor of Philosophy degree from this institute. I hereby certify that he has fulfilled all the requirements, according to the rules of this institute, regarding the investigations embodied in his thesis and this work has not been submitted elsewhere for a degree.

Prof. Kalyanasis Sahu

(Thesis Supervisor)
Professor
Department of Chemistry
IIT Guwahati, Assam - 781039,
India

Acknowledgment

First of all, I want to take this opportunity to extend my extreme gratitude to my thesis supervisor Prof. Kalyanasis Sahu for his constant guidance and support throughout this journey. From fruitful discussion to his supreme mentoring made this thesis a reality.

I want to acknowledge my doctoral committee members, Prof. Anumita Paul (Chairperson), Prof. Bhubaneswar Mandal, and Prof. Debasis Manna, for their periodic evaluation of my progress with suggestions and encouragement. I want to thank Prof. T Punniyamurthy, Prof. Gopal Das (former HODs), Prof. Aditya Narayan Panda (HOD) and all staff members of the Department of Chemistry, Central Instrumental Facilities (CIF), IIT Guwahati for providing me with the instrumental facilities and necessary helps.

Thanks to all my seniors and labmates, Aparajita Phukon, Debabrata Singha, Dillip Kumar Sahu, Tousif Hossen, Subhashree Sahu and project student Kamin Saroh for their help and cooperation during this Ph.D. journey. During the initial phase, I gain practical knowledge regarding nanomaterials from Dillip da. Tousif da helped me during the ITC experiment and with technical things. I will cherish the moments we have spent together, sometimes in seriousness, sometimes in laughter and humor.

I am taking this moment to thank all my teachers who have shaped my educational roadmap to reach here. I would also like to thank my Ph.D. batchmates and friends, all research scholars in the department. Many times, they have extended their needful help to me. I want to thank my hostel floormates-cum-brothers Dharmendra Adak and Raju Mondal from the core of my heart for their help in many aspects. The natural beauty and the greenery of my institute campus give me freshness every time during this journey.

I will remain thankful to my Lohit hostel warden Prof. Chandan Karfa who legally helped me to reach my home during a family emergency in January 2022 when I was in my hostel's Covid containment zone. Ultimately my family is my strength. I want to express my love to my parents and sister. Without their support, it would not be possible to be here to complete this journey.

Sincerely
Tapas Pal

Table of Contents

Synopsis of the Thesis

Abstract

The thesis represents the application of excited-state proton transfer (ESPT) of a photoacid 8-hydroxypyrene-1,3,6-trisulfonate (HPTS) to explore structural reorganization and hydration changes that occurs during the interaction of a triblock copolymer or a polyelectrolyte with different surfactants. The emission property of the fluorophore is susceptible to minute changes in the local hydration, enabling the detection of delicate changes in the polymer-surfactant or polyelectrolyte-surfactant assembly due to variations of chain length or headgroup charges of the surfactants. The investigations can also predict the most compact assembly, which can be important for various applications such as drug delivery systems and nanostructure templates. The content of the thesis is divided into seven chapters.

Chapter 1 briefly reviews the recent experimental investigations and molecular dynamics in mixed aggregate formulations of the triblock copolymer, polyelectrolyte molecules, and various short-chain ionic, zwitterionic surfactants. ***Chapter 2*** describes the chemicals used in the experiments, measurement techniques, data analysis and interpretation methods. ***Chapter 3*** deals with the interaction pattern of cationic surfactant dodecyl trimethylammonium bromide (DTAB) with pluronic triblock copolymer F127 (poly-(ethylene oxide)$_{101}$ (EO$_{101}$)−poly(propylene oxide)$_{56}$ (PPO$_{56}$)−PEO$_{101}$). Anomalous ESPT dynamics variation was observed with the composition of the assembly. ***Chapter 4*** describes the effect of chain length variation of cationic surfactants and initial concentrations (premicellar or post micellar) of F127 on interaction pattern, subsequently, application of these micelles to anisotropic gold nanostructure synthesis. ***Chapter 5*** describes how surfactant headgroup charge impacts the interaction between homolog surfactants and pluronic F127. ***Chapter 6*** includes the effect of salt on the variation of the ESPT dynamics pattern of zwitterionic surfactant-pluronic F127. In ***Chapter 7,*** we explored the ESPT dynamics at the interface of polyelectrolyte-surfactant assembly. By observing the TRANES isoemissive point shift, transfer of the probe between micelle and polyelectrolyte was proposed.

Chapter 1: Introduction:

Molecular fluorescent probes play a vital role as an experimental tool for exploring biological, chemical, and material science in various aspects.[1-5] Photoacids are molecular probes with widely different pKa values in the ground and excited states.[6] 8-Hydroxypyrene-1,3,6-trisulfonate (HPTS or pyranine) is a very popular photoacid with a pK_a of 7.2-7.7 and a quite low pK_a^* of 0.5-1.5.[7] Pyranine shows distinct emission maxima at 440 nm and 510 nm for the protonated (ROH) and deprotonated (RO) forms, respectively. The emission intensity ratio (ROH/RO) is very sensitive to local hydration and structural reorganization.[8-11] Broadly, ESPT may occur in three steps: initial proton transfer, recombination of the geminate ion pair and followed by dissociation of the geminate ion pair into solvated ions. Another model is possible where geminate recombination is absent and direct proton transfer occurs.[12] For the last few decades, different kinetic models emerged to explain the ESPT.[7-8, 13-19] The ESPT of the molecular probe HPTS has been extensively investigated in various micelles, reverse micelles, membranes, binary solvent mixtures, biomolecular interface and correlation was drawn between dynamics and structure.[20-23] More importantly, very few reports exist where ESPT of HPTS has been employed to investigate Pluronic triblock copolymers - surfactant mixed micelles or polyelectrolyte assembly.[24]

In brief, Pluronic triblock copolymers are composed of hydrophilic poly(ethylene oxide) (EO) and hydrophobic poly(propylene oxide) (PO) blocks, having the general formula (EO)n-(PO)m-(EO)n.[25] Pluronic micelles have a core-shell structure; the hydrophobic PO blocks at the core are surrounded by the hydrophilic EO blocks forming the corona region.[26] Polyelectrolyte molecules are composed of ionic molecular units in polymeric form. These polymeric copolymers and polyelectrolytes received intense research interest over the last few decades for unique solution behavior, ability to form mixed assemblies with short-chain surfactants and extensive applications.[27-29] Self-assemblies of triblock copolymers are useful in drug delivery systems,[30-31] for sequestration of drugs,[32] and in synthesizing shape-controlled nanomaterials.[33] Still, the self-assembly of the solely pluronic molecule or polyelectrolyte cannot fulfill the purpose well; instead, the presence of a minute amount of ionic, zwitterionic surfactants in those assemblies can increase their efficacy a lot.[34]

So, to gain molecular level insight, compactness, and hydration properties of mixed micellar, polyelectrolyte aggregates, ESPT dynamics of HPTS is the most suitable pathway. Hence, we have explored the interaction pattern of pluronic triblock copolymer F127 and cationic polyelectrolyte PDADMAC with different cationic (DTAB, TTAB, CTAB), anionic (SDS) and zwitterionic (SB12) surfactants at various compositions employing mainly steady-state and time-resolved fluorescence of HPTS as a tool. Further, we explored how ionic strength modulates the ESPT dynamics in a mixed micellar interface. Finally, the correlation between dynamics and structure leads us to consider these mixed assemblies for application purposes.

Chapter 2: Experimental and Analytical Methods:

This chapter includes the purity, sources of all the chemicals used and sample preparation procedures. Further, we have added the specifications of the instruments used like all spectrophotometers, including UV Visible spectrophotometer, Steady-state fluorimeter, time-correlated single photon counting (TCSPC) setup, dynamic light scattering (DLS), Isothermal titration calorimetry (ITC), FETEM setup etc. The data analysis methods, models and software are also discussed. To interpret the time-resolved area normalized spectra (TRANES), we have incorporated a recently developed TRANES intensity ratio fitting equation to gain the exact deprotonation time value.[19, 35] The fluorescence anisotropy decay data were analyzed applying the "Wobbling in cone model" .[36]

Chapter 3: Anomalous Variation of Excited-State Proton Transfer Dynamics inside a Triblock Copolymer−Cationic Surfactant Mixed Micelle.[37]

In this chapter, we investigated the excited state proton transfer (ESPT) dynamics of photoacid probe 8-hydroxypyrene-1,3,6-trisulfonate (HPTS) in mixed micelle of a triblock copolymer F127 (EO_{101}–PO_{56}–EO_{101}) and a cationic surfactant dodecyl trimethylammonium bromide (DTAB) at various compositions and elucidated the micellar structure. The emission spectrum and intensity ratio (ROH/RO) of HPTS modulate anomalously with the variation of DTAB concentration, i.e., the ratio should be increased regularly with DTAB concentration, but here first it increased, then again decreased and finally got a steady value.

Time-resolved measurements also support that ESPT dynamics varies unusually with the concentration of DTAB in the mixed micelle; substantial ESPT retardation is observed up to ~12 mM of DTAB, but after that, the dynamics become somewhat faster upon further addition. Moreover, dynamic light scattering (DLS) measurements exhibited that the size of the mixed micelle decreases sharply in the low concentration region (<20 mM DTAB) but decreases moderately at high concentration. Thus, the nature of the mixed micelle is very different at low and high concentrations of DTAB. At low concentrations, incorporating DTAB results in a more compact, less hydrated mixed micelle, whereas a more hydrated, less organized assembly is formed at a high concentration of DTAB.

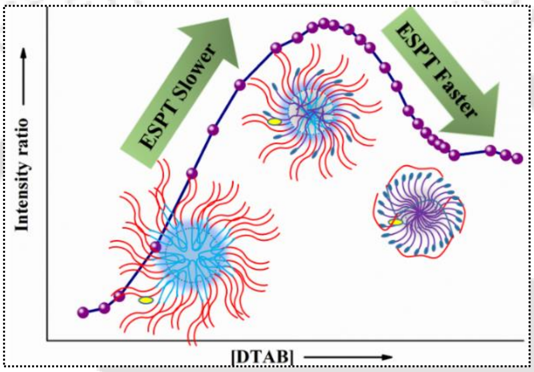

Figure 3.1. Schematic representation of ESPT dynamics in mixed micellar assemblies.

Chapter 4: Sub-Micellar Triblock Copolymer-Cationic Surfactant Aggregate Assisted Gold Nanostructure Synthesis: A Photophysical Investigation.[38]

This chapter describes the optimization of the size and interfacial packing of a sub-micellar aggregate of a triblock copolymer F127 (poly-(ethylene oxide)$_{101}$ (EO$_{101}$)−poly(propylene oxide)$_{56}$ (PPO$_{56}$)−PEO$_{101}$), and cationic alkyl trimethylammonium surfactants of various chain lengths at minute concentrations using an ultrasensitive photoacid 8-hydroxypyrene-1,3,6-trisulfonate (HPTS or Pyranine) and demonstrated its feasibility in synthesizing gold nano-triangles. The emission intensity (protonated/deprotonated) ratio of HPTS follows an intricate pattern against the surfactant concentration displaying transition points of initial, maximum and end portions.

Fluorescence anisotropy measurements revealed that the most organized state is near the critical point at the maximum intensity ratio. Isothermal titration calorimetry (ITC) showed maximum enthalpy change at the same composition confirming optimum interaction. Finally, we show that the assemblies containing ultralow concentrations of F127 and cationic surfactant can be a potent medium for synthesizing gold nano-triangles.

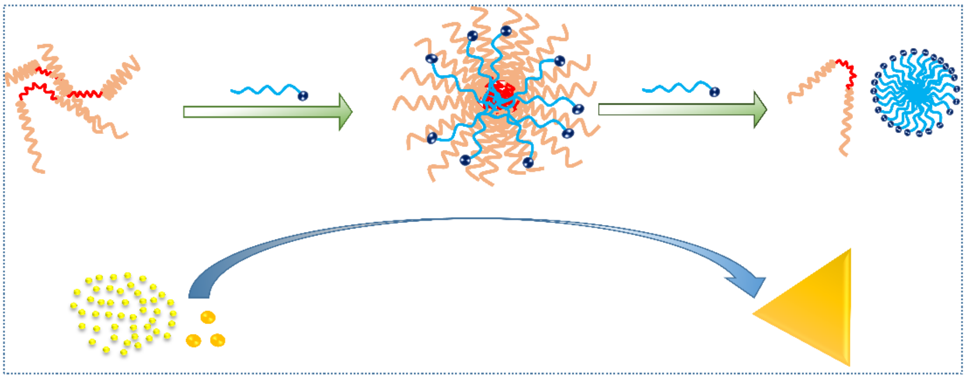

Figure 4.1. Schematic representation of mixed micellar formulation assisted gold nanostructure synthesis.

Chapter 5: Differential Headgroup Charge Induced Differential Interaction Patterns of Zwitterionic and Cationic Surfactants with a Triblock Copolymer Micelle.[39]

In this chapter, we explored the ESPT dynamics of HPTS to investigate the interaction pattern between a triblock copolymer F127 micelle and a zwitterionic sulfobetaine surfactant *N*-dodecyl-*N*, *N*-dimethyl-3-ammoniopropane sulfonate (SB3-12 or SB12) and compared it with that of cationic surfactant DTAB.

Irrespective of charge differences, the two surfactants grossly follow the same pattern, as manifested by the change in the intensity ratio of the protonated and deprotonated emission bands. Interestingly, the ratio attains maximum for a post-micellar (30-35 mM) concentration (~10 times higher than critical micellar concentration or CMC) for SB12, whereas the maximum occurs at a sub-micellar (6-8 mM) concentration (significantly lower than its CMC) for DTAB. Detailed analysis of the time-resolved study reveals that ESPT dynamics is slower in the optimum F127-SB12 assembly than in the case of the cationic surfactant. Thus, although SB12 requires a higher surfactant concentration to acquire the optimum state, it results in a more organized and less hydrated state than the cationic surfactant.

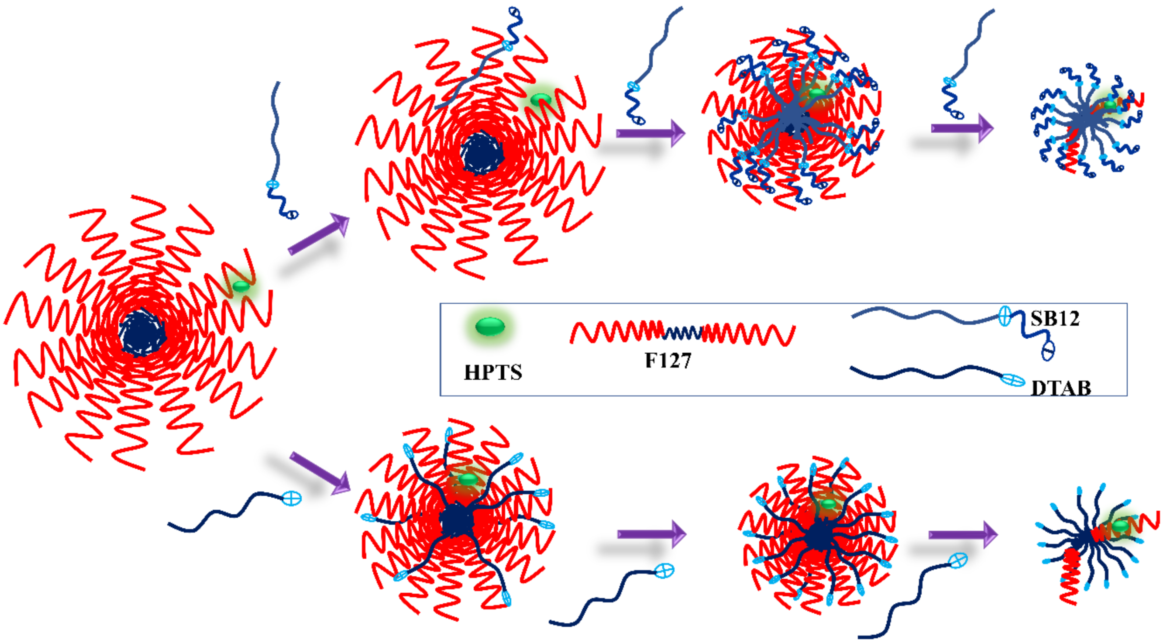

Figure 5.1. Schematic representation of differential interaction pattern of F127 micelle with different surfactants

Chapter 6: Modulation of Excited-State Proton Transfer Dynamics in Pluronic Triblock Copolymer-Zwitterionic Surfactant Mixed-Micellar Interface in the Presence of Salt

In this chapter, we have explored the structural and hydration pattern variation of mixed micelles formed of pluronic triblock copolymer F127 and zwitterionic surfactant SB12 in the absence and presence of salt at various compositions by exploring excited state proton transfer dynamics of molecular probe-cum-photoacid pyranine (HPTS). In the absence of salt, compact assemblies are formed in both the premicellar and post-micellar concentration regimes of F127 with the variation of SB12 but at two different concentrations.

It was determined with the help of the emission intensity ratio (protonated/deprotonated) of steady-state emission spectra of HPTS, steady-state and time-resolved anisotropy decay experiments. Adding salt into the particular most compact mixed assemblies of F127-SB12 medium alters the ESPT dynamics. Mixed micellar interfacial hydration variation and change in structural microheterogeneity are mainly responsible for this dynamical modulation. Time-resolved study and Dynamic Light Scattering study further established the phenomena.

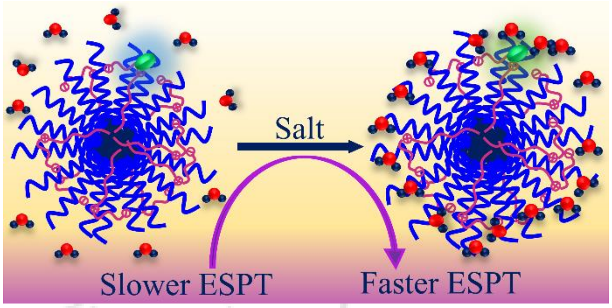

Figure 6.1. The schematic representation of salt-induced hydration enhancement of mixed micellar interface, leading to faster ESPT.

Chapter 7: Exploring Cationic Polyelectrolyte–Micelle Interaction via Excited-State Proton Transfer. Signatures of Probe Transfer.[40]

In this chapter, we investigate the interaction of a cationic polyelectrolyte, poly(diallyl dimethylammonium chloride) (PDADMAC), with micelles of differently charged surfactants (anionic sodium dodecyl sulfate (SDS), cationic dodecyl trimethylammonium bromide (DTAB), and zwitterionic N-dodecyl-N,N-dimethyl-3-ammonio-1-propanesulfonate (SB12), possessing the same alkyl (dodecyl) chain using 8-hydroxypyrene-1,3,6-trisulfonic acid (HPTS) as an ESPT probe.

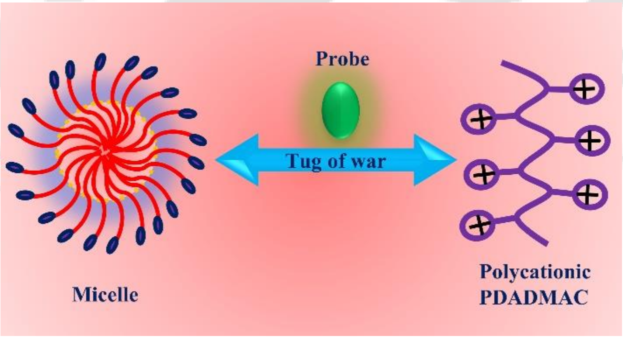

Figure 7.1. Schematic representation of probe transfer between micelle and polyelectrolyte interface.

The fluorescence of HPTS residing initially within the micellar medium modulates differently in the presence of PDADMAC. For the anionic SDS and cationic DTAB micelles, the emission spectrum of HPTS does not alter significantly upon adding

PDADMAC. However, for SB12 micelles, the emission spectrum undergoes a strong modulation upon adding the polyelectrolyte. The TRANES suggests a gradual transfer of the HPTS from the zwitterionic micelle to the PDADMAC assembly in a concentration-dependent manner. At a low concentration of PDADMAC, HPTS mainly resides in the SB12 micelle; at high concentration, it prefers to stay inside the PDADMAC assembly; and in the intermediate region, HPTS distributes over both assemblies. The shuttling of the molecular probe between the micellar assembly and the polycationic molecule resembles a drug sequestration event.

References

1. Weinberg, D. R.; Gagliardi, C. J.; Hull, J. F.; Murphy, C. F.; Kent, C. A.; Westlake, B. C.; Paul, A.; Ess, D. H.; McCafferty, D. G.; Meyer, T. J., Proton-Coupled Electron Transfer. *Chem. Rev* **2012,** *112* (7), 4016-4093.
2. Jacquemin, D.; Zúñiga, J.; Requena, A.; Céron-Carrasco, J. P., Assessing the Importance of Proton Transfer Reactions in DNA. *Acc. Chem. Res.* **2014,** *47* (8), 2467-2474.
3. Zhao, J.; Ji, S.; Chen, Y.; Guo, H.; Yang, P., Excited state intramolecular proton transfer (ESIPT): from principal photophysics to the development of new chromophores and applications in fluorescent molecular probes and luminescent materials. *Phys. Chem. Chem. Phys.* **2012,** *14* (25), 8803-8817.
4. Kwon, J. E.; Park, S. Y., Advanced Organic Optoelectronic Materials: Harnessing Excited-State Intramolecular Proton Transfer (ESIPT) Process. *Adv. Mater.* **2011,** *23* (32), 3615-3642.
5. Amdursky, N., Photoacids as a new fluorescence tool for tracking structural transitions of proteins: following the concentration-induced transition of bovine serum albumin. *Phys. Chem. Chem. Phys.* **2015,** *17* (47), 32023-32032.
6. Cimino, P.; Raucci, U.; Donati, G.; Chiariello, M. G.; Schiazza, M.; Coppola, F.; Rega, N., On the different strength of photoacids. *Theor. Chem. Acc.* **2016,** *135* (5), 117.
7. Pines, E.; Huppert, D., Observation of Geminate Recombination in Excited State Proton Transfer. *J. Chem. Phys.* **1986,** *84* (6), 3576-3577.
8. Agmon, N., Elementary Steps in Excited-State Proton Transfer. *J. Phys. Chem. A* **2005,** *109* (1), 13-35.
9. Bhattacharyya, K., Solvation Dynamics and Proton Transfer in Supramolecular Assemblies. *Acc. Chem. Res.* **2003,** *36* (2), 95-101.
10. Roy, B.; Satpathi, S.; Hazra, P., Topological Influence of the Lyotropic Liquid Crystalline Systems on Excited State Proton Transfer Dynamics. *Langmuir* **2016**.
11. Sahu, K.; Roy, D.; Mondal, S. K.; Karmakar, R.; Bhattacharyya, K., Study of Protein–Surfactant Interaction Using Excited State Proton Transfer. *Chem. Phys. Lett.* **2005,** *404* (4–6), 341-345.
12. Leiderman, P.; Gepshtein, R.; Uritski, A.; Genosar, L.; Huppert, D., Effect of Electrolytes on the Excited-State Proton Transfer and Geminate Recombination. *J. Phys. Chem. A* **2006,** *110* (17), 5573-5584.
13. Amdursky, N.; Lin, Y.; Aho, N.; Groenhof, G., Exploring fast proton transfer events associated with latteral proton diffusion on the surface of membranes. *Proc. Natl. Acad. Sci. U. S. A.* **2019,** *116* (7), 2443-2451.
14. Spry, D. B.; Fayer, M. D., Proton Transfer and Proton Concentrations in Protonated Nafion Fuel Cell Membranes. *J. Phys. Chem. B* **2009,** *113* (30), 10210-10221.
15. Rini, M.; Magnes, B.-Z.; Pines, E.; Nibbering, E. T. J., Real-Time Observation of Bimodal Proton Transfer in Acid-Base Pairs in Water. *Science* **2003,** *301* (5631), 349-352.
16. Genosar, L.; Cohen, B.; Huppert, D., Ultrafast Direct Photoacid−Base Reaction. *J. Phys. Chem. A* **2000,** *104* (29), 6689-6698.
17. Pines, E.; Magnes, B.-Z.; Lang, M. J.; Fleming, G. R., Direct measurement of intrinsic proton transfer rates in diffusion-controlled reactions. *Chem. Phys. Lett.* **1997,** *281* (4), 413-420.
18. Singh, S.; Koley, S.; Mishra, K.; Ghosh, S., An Approach to a Model Free Analysis of Excited-State Proton Transfer Kinetics in a Reverse Micelle. *J. Phys. Chem. C* **2018,** *122* (1), 732-740.
19. Sahu, K.; Nandi, N.; Dolai, S.; Bera, A., A Ratio-Analysis Method for the Dynamics of Excited State Proton Transfer: Pyranine in Water and Micelles. *J. Phys. Chem. B* **2018,** *122* (25), 6610-6615.

20. Politi, M. J.; Chaimovich, H., Water Activity in Reversed Sodium Bis(2-ethylhexyl) Sulfosuccinate Micelles. *J. Phys. Chem.* **1986,** *90* (2), 282-287.

21. Sedgwick, M.; Cole, R. L.; Rithner, C. D.; Crans, D. C.; Levinger, N. E., Correlating Proton Transfer Dynamics To Probe Location in Confined Environments. *J. Am. Chem. Soc* **2012,** *134* (29), 11904-11907.

22. Phukon, A.; Barman, N.; Sahu, K., Wet Interface of Benzylhexadecyldimethylammonium Chloride Reverse Micelle Revealed by Excited State Proton Transfer of a Localized Probe. *Langmuir* **2015,** *31* (46), 12587-12596.

23. Nandi, R.; Yucknovsky, A.; Mazo, M. M.; Amdursky, N., Exploring the inner environment of protein hydrogels with fluorescence spectroscopy towards understanding their drug delivery capabilities. *J. Mater. Chem. B* **2020,** *8* (31), 6964-6974.

24. Ghosh, S.; Dey, S.; Mandal, U.; Adhikari, A.; Mondal, S. K.; Bhattacharyya, K., Ultrafast Proton Transfer of Pyranine in a Supramolecular Assembly: PEO−PPO−PEO Triblock Copolymer and CTAC. *J. Phys. Chem. B* **2007,** *111* (48), 13504-13510.

25. Alexandridis, P.; Holzwarth, J. F.; Hatton, T. A., Micellization of Poly(ethylene oxide)-Poly(propylene oxide)-Poly(ethylene oxide) Triblock Copolymers in Aqueous Solutions: Thermodynamics of Copolymer Association. *Macromolecules* **1994,** *27* (9), 2414-2425.

26. Ghosh, S.; Kuchlyan, J.; Banik, D.; Kundu, N.; Roy, A.; Banerjee, C.; Sarkar, N., Organic Additive, 5-Methylsalicylic Acid Induces Spontaneous Structural Transformation of Aqueous Pluronic Triblock Copolymer Solution: A Spectroscopic Investigation of Interaction of Curcumin with Pluronic Micellar and Vesicular Aggregates. *J. Phys. Chem. B* **2014,** *118* (39), 11437-11448.

27. Rösler, A.; Vandermeulen, G. W. M.; Klok, H.-A., Advanced Drug Delivery Devices via Self-Assembly of Amphiphilic Block Copolymers. *Adv. Drug Deliv. Rev.* **2001,** *53* (1), 95-108.

28. Sanders, S. N.; Gangishetty, M. K.; Sfeir, M. Y.; Congreve, D. N., Photon Upconversion in Aqueous Nanodroplets. *J. Am. Chem. Soc* **2019,** *141* (23), 9180-9184.

29. Liu, J.-Y.; Wang, J.-G.; Li, N.; Zhao, H.; Zhou, H.-J.; Sun, P.-C.; Chen, T.-H., Polyelectrolyte–Surfactant Complex as a Template for the Synthesis of Zeolites with Intracrystalline Mesopores. *Langmuir* **2012,** *28* (23), 8600-8607.

30. Batrakova, E. V.; Kabanov, A. V., Pluronic Block Copolymers: Evolution of Drug Delivery Concept from Inert Nanocarriers to Biological Response Modifiers. *J Control Release* **2008,** *130* (2), 98-106.

31. Mishra, S.; Peddada, L. Y.; Devore, D. I.; Roth, C. M., Poly(alkylene oxide) Copolymers for Nucleic Acid Delivery. *Acc. Chem. Res.* **2012,** *45* (7), 1057-1066.

32. Mora, A. K.; Singh, P. K.; Nath, S., Controlled Sequestration of DNA Intercalated Drug by Polymer–Surfactant Supramolecular Assemblies. *J. Phys. Chem. B* **2016,** *120* (17), 4143-4151.

33. Chai, J.; Buriak, J. M., Using Cylindrical Domains of Block Copolymers To Self-Assemble and Align Metallic Nanowires. *ACS Nano* **2008,** *2* (3), 489-501.

34. Mondal, R.; Ghosh, N.; Mukherjee, S., Enhanced Binding of Phenosafranin to Triblock Copolymer F127 Induced by Sodium Dodecyl Sulfate: A Mixed Micellar System as an Efficient Drug Delivery Vehicle. *J. Phys. Chem. B* **2016,** *120* (11), 2968-2976.

35. Nandi, N.; Sahu, K., Analysis of Excited State Proton Transfer Dynamics of HPTS in Methanol-Water Mixtures from Time-Resolved Area-Normalised Emission Spectrum (TRANES). *J. Photochem. Photobiol. A.* **2019,** *374*, 138-144.

36. Lipari, G.; Szabo, A., Effect of librational motion on fluorescence depolarization and nuclear magnetic resonance relaxation in macromolecules and membranes. *Biophys. J.* **1980,** *30* (3), 489-506.

37. Pal, T.; Sahu, K., Anomalous Variation of Excited-State Proton Transfer Dynamics inside a Triblock Copolymer–Cationic Surfactant Mixed Micelle. *J. Phys. Chem. B* **2019,** *123* (40), 8559-8568.

38. Pal, T.; Sahu, K., Photophysical characterization of a sub-micellar triblock copolymer-cationic surfactant aggregate for nanostructure synthesis. *J. Photochem. Photobiol.* **2021,** *8*, 100066.

39. Pal, T.; Sahu, K., Comparison of interaction patterns of a triblock copolymer micelle with zwitterionic vs. cationic surfactant: An excited-state proton transfer dynamics investigation. *Colloids and Surfaces A: Physicochemical and Engineering Aspects* **2022,** *640*, 128327.

40. Pal, T.; Sahu, K., Exploring cationic polyelectrolyte–micelle interaction via excited-state proton transfer. Signatures of probe transfer. *Phys. Chem. Chem. Phys.* **2023**.

List of Publications

Publications Included in the Thesis

1) **Pal, T**.; Sahu, K., Anomalous Variation of Excited-State Proton Transfer Dynamics inside a Triblock Copolymer–Cationic Surfactant Mixed Micelle. ***J. Phys. Chem. B 2019, 123, 40, 8559-8568.***

2) **Pal, T**.; Sahu, K**;** Photophysical characterization of a sub-micellar triblock copolymer-cationic surfactant aggregate for nanostructure synthesis**. *Journal of Photochemistry and Photobiology 8 (2021) 100066.***

3) **Pal, T**.; Sahu, K**;** Comparison of interaction patterns of a triblock copolymer micelle with zwitterionic vs. cationic surfactant: An excited-state proton transfer dynamics investigation. ***Colloids and Surfaces A: Physicochemical and Engineering Aspects 640 (2022) 128327.***

4) **Pal, T**.; Sahu, K**;** Exploring cationic polyelectrolyte-micelle interaction via excited-state proton transfer. Signatures of probe transfer. ***Phys. Chem. Chem. Phys.***, **2023, 25**, **2963-2977**.

5) **Pal, T**.; Sahu, K**;** Effect of salt on a triblock copolymer-zwitterionic surfactant assembly: Insight from excited-state proton transfer. (**under peer review**)

Publications not included in the thesis

1) Sahu D. K.; **Pal**, **T.;** Sahu, K.; A New Phase Transfer Strategy to Convert Protein-Capped Nanomaterials into Uniform Fluorescent Nanoclusters in Reverse Micellar Phase, ***ChemPhysChem.* 2018,** ***19*, 1.**

Conference Presentations

1. **Poster presentation:** National Workshop on Fluorescence and Raman Spectroscopy, ***FCS 2019***, TIFR Centre for Interdisciplinary Sciences (TCIS) Hyderabad, Hyderabad 2019.

2. **Poster presentation:** International Conference on Emerging Trends in Chemical Sciences, ***ETCS 2020***, Gauhati University, Guwahati 2020.

3. **Poster presentation:** National Workshop on Fluorescence and Raman Spectroscopy, ***FCS 2020*, IIT Bombay.**

4. **Flash talk presentation:** International Conference on Advanced Nanomaterials and Nanotechnology, **ICANN 2021**, IIT Guwahati.

5. **Poster presentation:** National Workshop on Fluorescence and Raman Spectroscopy, **FCS 2021**, IISER Thiruvananthapuram & RGCB.

6. **Poster presentation:** 20th National Conference on Surfactants, Emulsions and Biocolloids, **NATCOSEB-XX-2021**, IIT Guwahati.

7. **Oral presentation:** Research & Industrial Conclave (**RIC)** 2022, IIT Guwahati.

8. **Poster presentation:** 28th CRSI National Symposium in Chemistry, **CRSI NSC 28**, 2022, IIT Guwahati.

9. **Poster presentation:** North East Research Conclave**, NERC, 2022**, IIT Guwahati.

List of Schemes

Chapter 7

List of Tables

Chapter 3

Chapter 4

Chapter 5

Chapter 6

Chapter 7

List of Figures

Chapter 1

Chapter 2

Chapter 3

Chapter 4

Chapter 5

Chapter 6

Chapter 7

protonated/deprotonated band of HPTS in DTAB micellar media with time (b) in the absence (d) in the presence of PDADMAC. The pH of the medium was ~ 5.6.

Figure 7.10. TRANES of HPTS in SDS micelle at different times (a) in the absence (c) in the presence of PDADMAC and the variation of TRANES intensity ratio (b) in the absence (d) in the presence of PDADMAC. The pH of the medium was ~ 5.6.

List of Abbreviations

AOT	Sodium bis(2-ethylhexyl) sulfosuccinate
BSA	Bovine serum albumin
CAC	Critical aggregation concentration
CMC	Critical micellar concentration
CMT	Critical micellar temperature
CTAB	Cetyltrimethylammonium bromide
CTAC	Cetyltrimethylammonium chloride
DLS	Dynamic light scattering
DMSO	Dimethyl sulfoxide
DNA	Deoxyribonucleic acid
DSC	Differential scanning calorimetry
DTAB	Dodecyltrimethylammonium bromide
ESPT	Excited state proton transfer
FETEM	Field emission transmission electron microscope
HSA	Human serum albumin
HPTS	8-hydroxypyrene-1, 3, 6-trisulfonate
ITC	Isothermal titration calorimetry
MPTS	8-methoxypyrene-1,3,6-trisulfonate
NaGDC	Sodium glycodeoxycholate
PDADMAC	Poly(diallyl dimethylammonium chloride)
PEs	Polyelectrolytes
PEO	Polyethylene oxide
PPO	Polypropylene oxide
RMs	Reverse micelles
SB12	3-(dodecyldimethylammonio)-propanesulfonate
SDS	Sodium dodecyl sulfate
TCSPC	Time Correlated Single Photon Counting
TRES	Time Resolved Emission Spectra
TRANES	Time Resolved Area Normalized Emission Spectra
TTAB	Tetradecyltrimethylammonium bromide
WIC	Wobbling in Cone Model

Chapter 1

Introduction

Chapter 1: Introduction

1.1. Self-Assembly of Amphiphilic Molecules

Natural or synthetic amphiphiles are structurally simple molecules with the propensity to form self-assembly in suitable solvent systems. For several years, the self-assembly of amphiphilic molecules (e.g., surfactants, block copolymers or lipids) has become a central topic in colloid and polymer, and material science due to myriad applications in medicinal, food, and cosmetic industry, and controlled synthesis of structured nanomaterials.[1-4] An amphiphilic molecule comprises both hydrophilic and hydrophobic parts. The hydrophobic portion is generally made of a hydrocarbon chain like an n-alkyl group. The hydrophilic part is called the headgroup, and the hydrophobic moiety is called the tail. These hydrophilic polar groups may be ionic or nonionic. The ionic amphiphiles are also of three types: anionic (negatively charged), cationic (positively charged) and zwitterionic (both positive and negative charges present simultaneously). The nonionic amphiphiles are generally polyether molecules with a hydroxyl group at the end (Scheme 1.1). Apart from that, natural steroid amphiphiles and bile salts are also there, which play a crucial role in lipolysis. It contains concave hydrophilic α face consisting of hydroxyl groups and convex hydrophobic β face.[5-6]

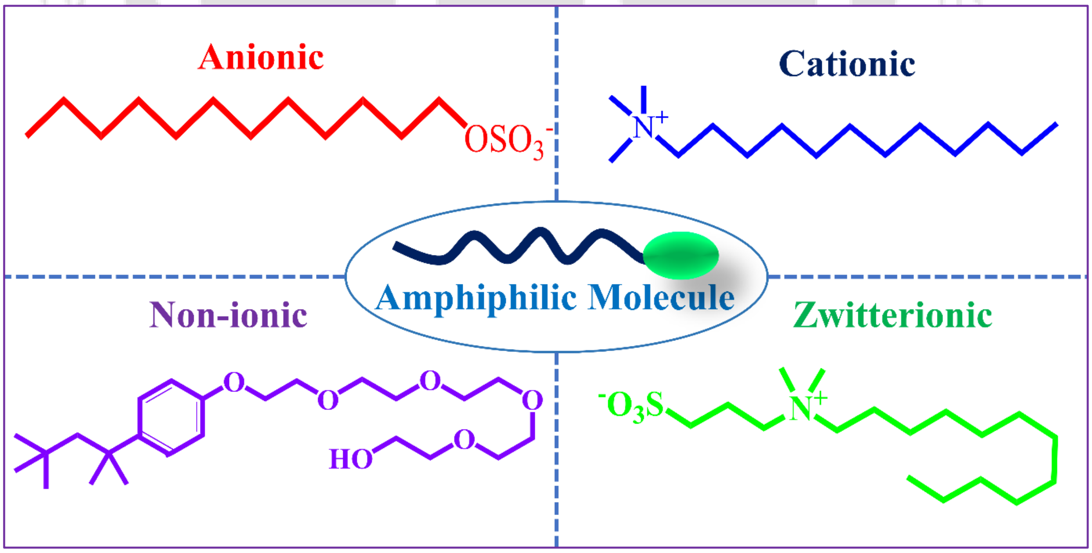

Scheme 1.1. Schematic representation of various amphiphilic surfactant molecules.

Among these amphiphiles, the nonionic and zwitterionic surfactants being less toxic, are getting priorities for their versatile applications in biomedical fields. Both the cationic and anionic charges are in the headgroup of the zwitterionic amphiphiles, separated by a small hydrocarbon tether part, hence acting as almost nonionic and having antifouling properties. The cationic trimethyl ammonium, anionic carboxylate, or sulfonate group may be present in the headgroup. In the sulfobetaine (SB) zwitterionic surfactant, the sulfonate is present along with the cationic trimethyl ammonium moiety; in the case of carbobetaine (CB), carboxylate is present as the anionic moiety along with the cationic part. Due to the differential anionic moieties in the SB and CB, they have distinct hydration, ionic interaction and self-association characteristics.[7] Another nonionic amphiphile that has been getting massive recent attention is the pluronic block copolymer having the polyoxyethylene and polypropylene groups in a block manner. We have discussed pluronic in the next section in detail.

The amphiphilic nature of the molecules drives them to self-aggregations into various structures of various morphologies (spheroid, ellipsoidal prolate, flexible rods or wormlike micelles) in aqueous and nonaqueous solvent systems.[8-9] Amphiphilic molecules in water rearrange themselves such that hydrophilic headgroups remain in solution while the hydrophobic tail avoids direct contact with water. The facial amphiphilicity drives the bile salts to form self-aggregation.[6]

Micelle is the most common type of self-assembly formed during this spontaneous rearrangement of amphiphilic molecules in a polar solvent (e.g., water) above a particular concentration, called the critical micelle concentration (CMC).[10] The micellar structure consists of two parts: an inner hydrophobic core formed of hydrophobic tails shielded from water and another part called the corona, formed of the hydrophilic headgroups. Micellization is generally an entropy-driven process, and the entropic contribution is attributed to the breakage of water's local hydrogen bonding structure.[11-12] The CMC of these amphiphiles depends on both their hydrophobic tail length and the hydrophilic headgroup charge character. Ionic and zwitterionic surfactant amphiphiles with the same alkyl tail length but different headgroup charge properties have different CMC values. Such as, dodecyl trimethylammonium bromide (DTAB) and N-dodecyl-N, N dimethyl-3-ammonio-1-propane sulphonate (SB12) both have the C_{12} alkyl tail length, but the former is cationic, and the latter is zwitterionic, and the CMC values are in the order CMC_{DTAB} (~16 mM) > CMC_{SB12} (~3.5 mM).[13] At the same time, ionic surfactants with the same headgroup charge properties have different CMC values for their alkyl tail lengths. The CMC value varies for cationic surfactant C_nTAB series as $C_{12}TAB>C_{14}TAB>C_{16}TAB$.

1.2. Pluronic Block Copolymer

Nonionic triblock copolymers contain hydrophobic chains of polypropylene oxide (PPO) and hydrophilic chains of polyethylene oxide (PEO). Linear triblock copolymers are also known as a poloxamer or their trade name, Pluronic. Ethylene oxide (EO) and propylene oxide (PO) are arranged in a block manner (A-B-A) in those pluronic block copolymers. Based on the arrangement of the units, they are categorized as pluronic and reverse pluronic. The hydrophilic ethylene oxide (EO) and hydrophobic propylene oxide (PO) moieties are organized as $(EO)_n$-$(PO)_m$-$(EO)_n$, and it is called the pluronic (Scheme 1.2).[14] In the case of reverse pluronic, the arrangement of the EO and PO units are opposite, i.e., the central portion contains the hydrophilic PEO unit. In contrast, the terminal portion is composed of the PPO units, $(PO)_n$-$(EO)_m$-$(PO)_n$. Although both pluronic have opposite structural patterns, they have numerous applications in diverse fields. We are here mainly focused on normal pluronic. Depending on the ratio of EO and PO units along with the room temperature physical form, the naming of pluronic is done (Liquid, Flake or Paste, e.g., L61, F127, P123 etc.). Several pluronic are there; out of these, F127 ($[EO]_{101}$-$[PO]_{56}$-$[EO]_{101}$) is the most sought in various fields because of its non-toxicity, chemical and structural properties.[15-16]

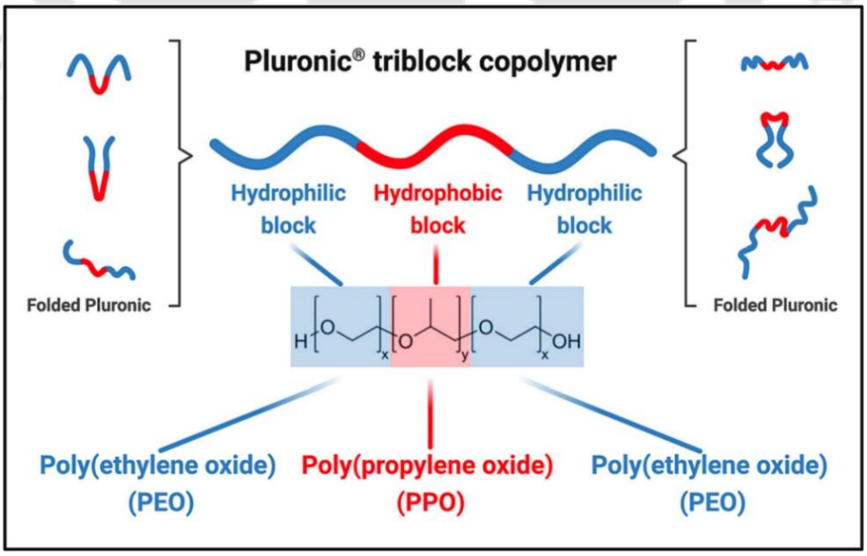

Scheme 1.2. Schematic chemical structure of pluronic triblock copolymer.[17] Reprinted with permission from ref.17. Copyright 2023, Elsevier.

The solubility of Pluronic depends on the composition, i.e., the length of hydrophilic EO block and hydrophobic PO blocks.[18] Temperature plays a crucial role in solubility; at higher temperatures, dehydration occurs from propylene units followed by ethylene oxide units. At a particular temperature (critical micelle temperature or CMT) and concentration (critical micelle concentration or CMC) in aqueous media, it can form micellar self-assembly.[19] The micelle formation is an entropy-driven process. The hydrophobic polypropylene oxide (PPO) blocks form the core part, while the hydrophilic polyethylene oxide (PEO) blocks constitute the corona region. The dimension of the core and corona region can be varied based on the PPO and PEO block lengths. The pluronic copolymers can also form hydrogels at a relatively high concentration than its CMC. Apart from that, another kind of block copolymer, known as tetronic star block copolymer is also capable of gel formation, which have huge applications in medicinal and pharmaceutical industries.[20-21]

The triblock copolymers have many potential applications. The core of the pluronic micelle helps in achieving the upconversion of organic molecules.[22] Pluronic micelles act as potential hydrophobic drug delivery vehicles by encapsulating the drugs in the core part.[23] Binary mixtures of two different pluronic and the drug are often used as drug formulations for cancer treatments. SP1049C is one of such formulations composed of F127 and L61 with the anticancer drug doxorubicin, capable of crossing the blood-brain barrier.[24-26] Apart from the biomedical field, pluronic play a crucial role in nanotechnology, bioprocessing, emulsification, detergents, lubrication, cosmetics etc.[27-31]

1.3. Polyelectrolytes

Polyelectrolytes (PEs) are one kind of polymer having repeating charged units. PEs are often soluble in water. Unlike amphiphilic molecules, PEs are hydrophilic in nature due to their charged interface. Oppositely charged PEs can interact and form insoluble polyelectrolyte complexes (PECs) by liquid-liquid phase separation (LLPS).[32-33] Polyelectrolyte molecules have widespread applications in thin-film coating,[34] biological membrane fabrication,[35] food industry,[36] and wastewater treatment.[37] Polyelectrolytes form mixed aggregate, which functions as nanoconfinement for catalysis,[38] coacervate entities,[39] and biomimicking moieties.[40-43] The interactions are driven by positive entropic enhancements due to the release of counterions and enthalpic components from the electrostatic attractions among opposite charges.[40, 44-45] Small-chain ionic surfactants form mixed aggregates with polyelectrolytes of different charge properties.[46-47] The formation and disassembly of these aggregates are often applied as pattern generation in biomolecular sensing,[34] nanoreactors,[48] and shape-charge controlled anisotropic nanomaterial synthesis.[49-51] The investigation of the polyelectrolyte-micellar systems may provide new insights regarding fundamental principles of coacervation.[52] Often, oppositely charged probe dye molecules can interact with the PEs. The binding of probes with the charged sites of PEs can give insightful information regarding drug/ligand binding properties with polyionic biomolecules; hence it is one kind of biomimicking activity.[53] Also, the highly charged polyionic interface can alter the photoluminescence properties of probe molecules which can be applicable to optoelectronic applications.[54]

1.4. Mixed Micellar Assembly and Applications

Block copolymeric surfactant often forms a mixed micellar aggregate with ionic surfactants. These mixed micelles are more compact and capable of drug delivery, drug sequestration, bile salt sequestration, etc., which is very applicable in the medicinal and pharmaceutical industries. The mix micellization process is also driven by the entropy, i.e., the insertion of hydrophobic tails of ionic amphiphilic surfactant towards the core of pluronic micelle breakdown the trapped water cage, hence increase the entropy of the system. The process is often called synergism/synergistic effect.

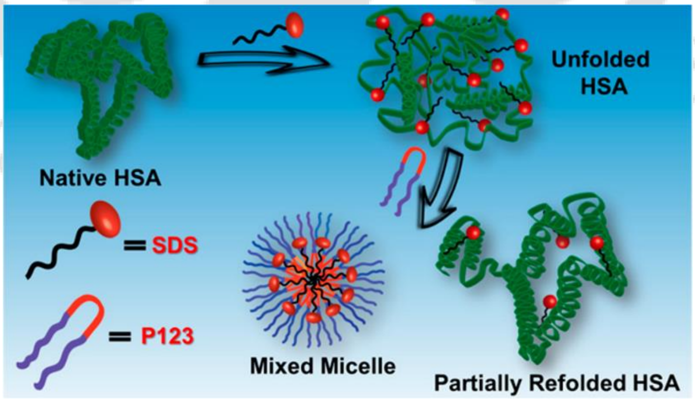

Scheme 1.3. Schematic representation of surfactant assembly induced unfolding and refolding of globular protein HSA.[55] Reprinted with permission from ref.55. Copyright 2018, American Chemical Society.

These block copolymers in the mixed micelle cause drastic sensitization of multidrug-resistant tumors to various anticancer agents,[56] triggers and execute an increased rate of drug delivery across the blood, brain, and intestinal barriers, and augment the transcriptional activation of gene expression.[57-58]

Mukherjee and the group recently investigated a mixed micellar system composed of pluronic block copolymer F127 and anionic SDS surfactant as a drug delivery vehicle with cationic dye phenosafranin as a model drug. They suggested that the interaction of the probe with the F127/SDS mixed micelles is stronger than the interaction with the F127 micelles or SDS micelle alone, resulting in it being the most efficient one, i.e., F127-SDS.[59] Partition coefficient data established that ~58% of PSF becomes entrapped in the F127 micellar matrix. Time-resolved study confirms that the fraction of the probe bound to F127 micelles increases significantly upon adsorption of very low concentrations of SDS below its CMC. ITC experiment confirms that the binding constant of PSF with F127/SDS mixed micelles is higher than that of F127 alone.

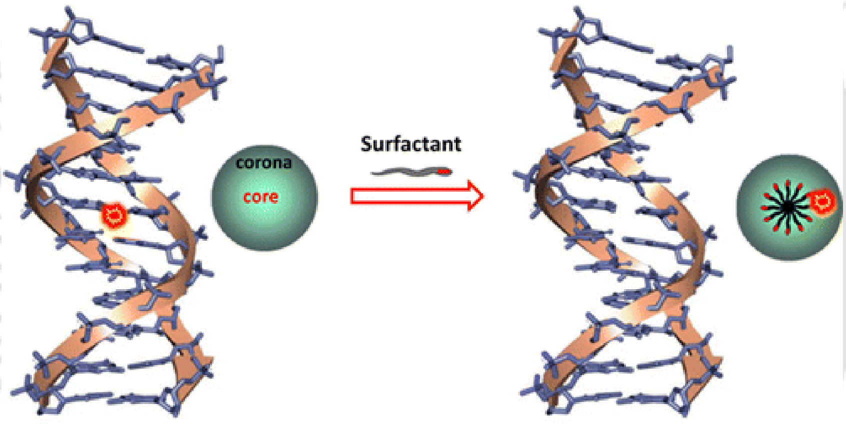

Scheme 1.4. Schematic Representation of the Sequestration of Intercalated EB by Polymer−Surfactant Supramolecular Assemblies.[60] Reprinted with permission from ref.60. Copyright 2016, American Chemical Society.

The propensity of the copolymer to form a mixed aggregate with ionic surfactants has been cleverly exploited in refolding SDS-induced denatured protein. The protein gains back 87% of its folded structure by employing triblock copolymer P123, which forms a mixed micellar aggregate with SDS (Scheme 1.3).[55] In another study, Nath and coworkers have shown that the mixed micellar aggregate of P123 and SDS can sequester a DNA-intercalated drug (Scheme 1.4). The extent of sequestration can be finely tuned by tuning the concentration of the surfactant in the triblock copolymer solution.[60]

Dennis and coworkers have presented that an oil-in-water microemulsion composed of a Pluronic copolymer, sodium salt of fatty acid, and a biocompatible oil (ethyl butyrate) can efficiently extract anesthetic drug bupivacaine from normal saline (0.9% NaCl in water). The extraction efficiency was as high as 90% for the microemulsion composed of F127, sodium caprylate, and ethyl butyrate. The extraction process may be due to the facile adsorption of the drug at the microemulsion droplet interface.[61] Pluronic copolymers can also effectively sequester bile salt by forming mixed aggregate, which can help treat hypercholesterolemia.[62] The Schillén group has explored the interaction pattern of pluronic P123 and bile salt, sodium glycodeoxycholate NaGDC. Based on small angle X-ray scattering (SAXS) and differential scanning calorimetry (DSC) investigations, they concluded that the aggregation pattern depends on the NaGDC/P123 molar ratio.[63]

1.5. How can we probe these assemblies?

Now the question arises of how to probe such micelles or mixed micelle formation. Such systems have been investigated earlier by applying surface tension measurements, viscometry, EPR probes, isothermal titration calorimetry etc.[64-66] Several solvatochromic probes were also applied to check the hydration properties of the assemblies. Following the excitation of a fluorophore, the solvent reorients around the excited-state dipole of the Franck-Condon state, which occurs with a solvent relaxation called solvation dynamics. The solvation dynamics in bulk water and the water near biomolecules, interfacial or restricted environments are different. A Suitable fluorescent probe (provided no excited state reactions like proton transfer) has been incorporated to monitor the solvation dynamics in various systems (micelle, reverse micelle, biomolecular aggregates).[67-68]

A fluorophore exhibiting excited stated proton transfer (ESPT) is also helpful in probing the hydration of these systems. The availability and nature of water molecules (proton acceptor) modulate an ESPT process; hence hydration properties can be ascertained. Since the probe may exhibit two excited state moieties, the ratiometric estimation of the relative emission contribution of the two states provides more clarity to estimating the exact hydration nature. Hence, ESPT can be another appropriate method to gain detailed insight into the hydration pattern variation during synergistic interactions among different surfactant moieties.[69]

1.6. Photoacids

Photoacids are a kind of molecular fluorophores with a massive difference in their pK_a values in the ground and electronically excited states, implying an enormous enhancement of their acidity upon photoexcitation. 8-hydroxypyrene-1,3,6-trisulfonic acid (HPTS or pyranine) is a well-known photoacid with a massive difference in pKa value between the ground (pKa ~7.5) and excited state (pKa*~0.5). Forster pointed out that the Photoacidity of these probes can be thermodynamically explained and proposed the Forster cycle (Scheme 1.5).[70-71] The excited-state pKa value (pKa*) can be obtained from the proton-transfer equilibria of the photoacid for the electronic ground and the excited state, applying the equation (1.1)

$$pKa^* = pKa + \frac{\Delta G_{exci}\,(RO^-) - \Delta G_{exci}\,(ROH)}{RT\ ln(10)} \tag{1.1}$$

Where $\Delta G_{exci}(ROH)$ and $\Delta G_{exci}(RO^-)$ are the excitation Gibbs free energies of the two species protonated ROH and deprotonated RO^-, R is the gas constant, and T is the absolute temperature.

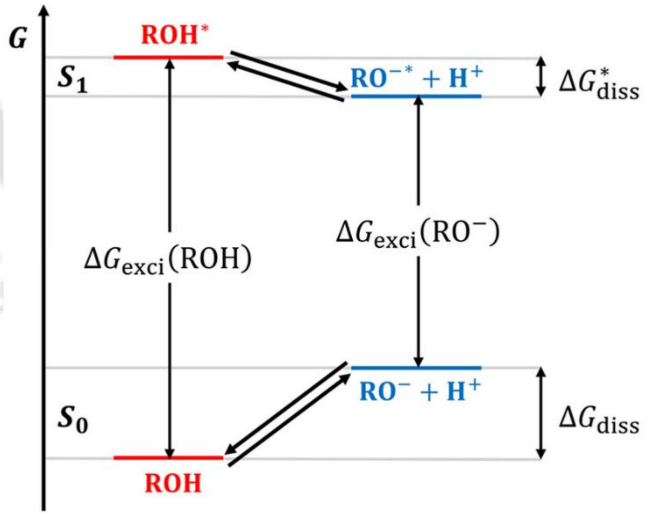

Scheme 1.5. Schematic representation of Forster cycle of a photoacid.[72] Reprinted with permission from ref.72. Copyright 2022, American Chemical Society

1.7. HPTS and Its Utilities

Pyranine (HPTS) is an arylsulfonate photoacid containing hydroxyl group (–OH). It can stay protonated or deprotonated in the ground state or the excited state in the aqueous media, depending on the pH of the medium. The characteristic absorption spectra of HPTS shows an absorbance maximum at 403 nm when the medium pH is below its pKa (~7.5).

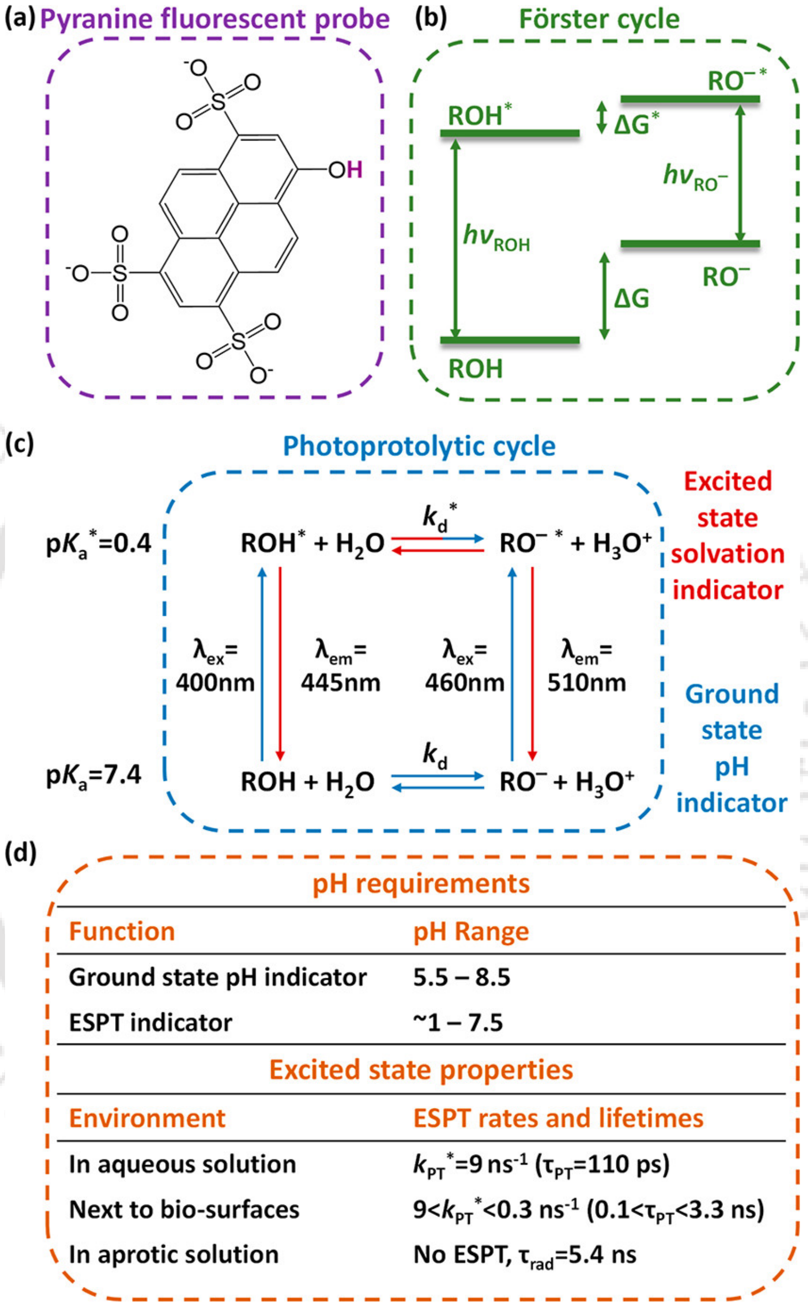

Figure 1.1. (a) Chemical structure (b) Forster cycle (c) photoprotolytic cycle of HPTS and (d) excited state properties.[73] Reprinted from ref.73. Licensed under CC BY.

The deprotonated HPTS has an absorption maximum of ~450 nm. Thus the presence of an absorption band at 450 nm along with 403 nm indicates ground-state proton transfer in the system. The emission spectra of HPTS in aqueous media have a strong peak at 510 nm and a feeble peak at 440 nm, characteristics of the deprotonated and protonated moieties, respectively.

The difference in the Gibbs free energy level in the ground and the excited state of HPTS is responsible for a significant Stokes shift. Due to this large Stokes shift, ΔpKa value is also large ~7 (pKa 7.5, pKa^*~0.5) (Figure 1.1). Based on the ΔpKa value and photoprotolytic cycle, it can be employed as a pH sensor of the surrounding medium. The significant Stokes shift, visible range absorption emission, highly water solubility help the scientific community to apply it as a fluorescent probe for many purposes. The pKa value of HPTS is also close to physiological pH, and it cannot cross the cell membrane, so it can be used for intracellular probing.

The excited state proton transfer of HPTS requires proton acceptor moieties, and water generally plays that role. So, its ESPT directly indicates the medium's hydration nature in the vicinity.

1.8. Excited State Proton Transfer (ESPT) and Associated Kinetic Models

One of the most ubiquitous reactions in many chemical and biological processes is proton transfer. In the last few decades, the proton transfer reactions in the excited state have been extensively investigated experimentally and theoretically and exhibited insightful concepts about acid-base reactions and hydration patterns of microheterogeneous systems. By irradiating short LASER pulses, the proton transfer can be initiated in the protic solvent solutions of photoacid (ROH) probes. The excited-state photoacid instantly releases its proton to nearby protic solvents like water.

Several ESPT kinetic models emerged in the last few decades. The photoacid HPTS often follows the Eigen-Weller scheme (Scheme 1.6) of proton transfer dynamics.[74] According to the scheme, the excited photoacid dissociates to form an intimate ion pair composed of a proton and deprotonated anion at a rate constant k_d. The contact ion pair have two possibilities, to regenerate the photoacid by geminate recombination at a rate constant of k_r or fully dissociate into a proton and deprotonated moiety at a rate constant of k_{diff}. The ESPT may also occur in an irreversible pathway without forming an intimate ion pair (Scheme 1.7). The geminate recombination model was also rigorously explored by N. Agmon and coworkers. They have applied the Debye Smoluchowski model and incorporated a probabilistic approach to explain the proton diffusion process considering the initial protonated species as a reaction sphere; they explained the ESPT mechanism finely.[75-78] A simplified version of it considering system dimensionality as an essential parameter has been introduced recently by Stuchebrukhov et al.[79]

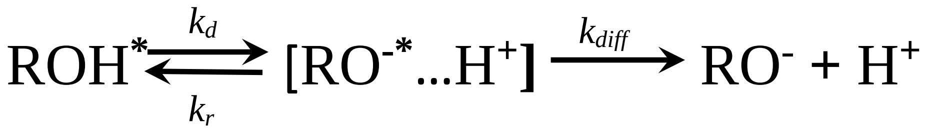

Scheme 1.6. Eigen-Weller scheme of proton transfer dynamics.

Scheme 1.7. Single-step irreversible proton transfer dynamics scheme.

1.9. ESPT of HPTS in several systems

Now, where can we incorporate the probe HPTS to investigate and obtain real-time information regarding the nature of the system? The scientific community has explored the ESPT dynamics starting from simple protic solvent water to binary mixtures of different solvents to extract information like the nature of the proton hopping mechanism and exact dynamical pathway. Apart from that, ESPT studies in confined assemblies like micelle, reverse micelle, vesicle, and cage-like supramolecular systems have been performed earlier to gain insights regarding the interfacial hydration nature along with perturbation arises in ESPT due to confinement. ESPT dynamics in the biomolecular interfaces like membranes, bilayers, protein, polynucleic acid etc., have also been investigated to explore structural evolution or degradation, charge transfer processes along interfaces etc. In the later sections, we will briefly revisit those findings and finally arrive at our objectives for this Thesis.

1.9.1. ESPT of HPTS in water

Water is a suitable receptive solvent and an excellent conductor of protons. It can act as a leveling solvent for many acid-base reactions. A relatively weak photoacid (e.g., pyranine, 2-naphthol) can transfer its proton to water in the 100 ps scale but not to alcohols. Some stronger photoacids can transfer a proton to alcohols and nonaqueous solvents.[80-82] The proton transfer process of photoacid HPTS goes in an adiabatic way leaving an excited anion. The quadruply anionic moieties of deprotonated HPTS may attract the nascent proton. So instead of diffusing away, the newly generated proton may stay in the vicinity of the excited anion (RO^{-*}).

Further, it may generate the initial protonated form of excited HPTS (ROH^{*}) moiety. This phenomenon is called geminate recombination. This recombination is evidenced in neat water in the emission decay of ROH^{*} as a non-exponential long-time tail. So, the recombination process indicates a probability of finding the protonated form of HPTS at a longer time. The bound probability, B(t), i.e., proton and photoacid anion exist as a pair, or bound state follows a $t^{-3/2}$ power law. The diffusion-assisted recombination is explained by the Debye-Smoluchowski equation.[83-86]

The ESPT of HPTS has also been investigated in femtosecond time resolution. The associated time components 0.3 ps, 2.5 ps and 90 ps reveal the solvation dynamics, locally excited charge transfer transition and proton transfer, respectively.[87] Later, the fast components (0.3 ps and 2.5 ps) have been interpreted as the hydrogen bond rearrangements around the probe molecule.[88]

Further, to explain the ESPT of HPTS in bulk water Huppert group has proposed the extended reversible diffusion-influenced two-step model.[89] According to this model, the excited protonated photoacid can generate a contact ion pair in the close attachment of the deprotonated anion and a protonated hydronium ion. The emission properties are the same for both contact ion pairs, $RO^{-} \cdots H_3O^{+}$ and the separated solvated ion, RO^{-}. The proton acceptor water molecule plays a significant role as a bridging component for proton transfer from a donor to an acceptor molecule. Eigen and Zundel have proposed two structural motifs to explain the proton transfer through water. According to Eigen, the proton is associated with a single water molecule, and further, it is solvated by three water molecules resulting $H_3O^{+}(H_2O)_3$, called Eigen cation.[90-91] In contrast, as per Huggins and Zundel, the proton is equally shared by two water molecules, called Zundel cation, i.e. $H_5O_2^{+}$.[92-93] Theoretical and femtosecond spectroscopic experimental studies suggest interconversion (E-Z-E) between these two cations helps to transfer the proton.[94] A recent theoretical study reveals that the proton transfer events from excited HPTS may happen through water wire, a robust hydrogen-bonded water network.[95]

1.9.2. ESPT of HPTS in binary solvent mixtures

Excited state proton transfer is very sensitive to the nature of water molecules and the microenvironment surrounding them. So, it can serve as an indicator of water structure and dynamics. In neat water, the photoacid probe HPTS exhibits proton transfer in the excited state in ~ 100 ps time scale. But in alcohol or organic solvent, the ESPT is hindered. The scientific community is interested in a binary mixture of water and non-protic solvent and whether there will be any ESPT. Recently Awasthi et al. have performed the ESPT dynamics investigation of pyranine in the water-DMSO mixture in various mole fractions.[96] In the presence of DMSO in neat water, the ESPT is hindered, and a particular mole fraction regime (X_{DMSO} = 0.41-0.51) shows maximum suppression to deprotonation. Based on earlier detailed MD simulation reports, steady-state and time-resolved studies, they observed that at that DMSO/water composition, slow solvation dynamics, non-availability of free water molecules (required to solvate the nascent proton) and different dimensionality of proton diffusion compared to neat individual solvents are prominent, contributing to hindered deprotonation dynamics.[96-98]

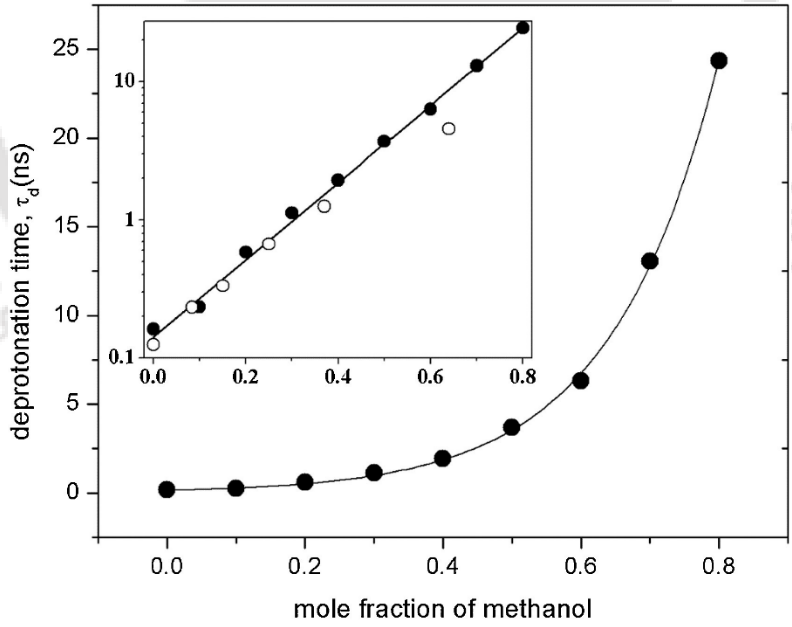

Figure 1.2. Variation of the deprotonation time constant (τ_d) of HPTS in water-methanol mixture with the mole fraction of methanol. Inset shows the same plot in log-linear scales.[99] The data of Agmon et al. has been added (open circle) in the inset for comparison.[100] Reprinted with permission from ref.99. Copyright 2019, Elsevier.

In another study, our group revisited the ESPT dynamics investigation of HPTS in a water-methanol binary mixture.[100] With the increase in methanol mole fraction in neat water, the ESPT becomes suppressed on a significant scale. The detailed time-resolved experiment established an exponential correlation between deprotonation times and mole fraction of methanol in neat water (Figure 1.2). The contributing factor is the higher activation energy with a greater fraction of methanol.[99] Apart from that, disruption of the hydrogen bonding network, decrease in dielectric constant, and slower spectral diffusion also hamper the ESPT dynamics of pyranine in the presence of a non-protic, organic solvent in water.[101-103]

1.9.3. Effect of Ionic Strength on ESPT Dynamics of HPTS

ESPT dynamics is sensitive to the water microstructure surrounding the probe. Now there is a possibility of alteration of rate of ESPT in the presence of additives like salts, electrolytes etc. The scientific community has a long-standing quest to understand how water and ions impact the proton transfer rate and pathway.[104-105] Huppert and teams have explored the modulation of the rate of proton transfer from HPTS to water in the presence of electrolytes (NaCl and $MgCl_2$).[106] According to them, the number of free water molecules close to the probe affects the rate of proton transfer to the water. The presence of salt in the aqueous media reorients the water molecules to the ions by electrostatic or hydrogen bonding interaction. But in a salt-free condition, the probe molecule transfers the proton to a water cluster of more than ten water molecules.[105] Basically, high salt concentration breaks those protons conducting water cluster, which leads to drastic retardation of ESPT rate and increased geminate recombination in the system.[106]

In a seminal work, Bhattacharya and coworkers investigated the effect of salt NaCl on the ESPT rate in water and Niosome.[107] In brief, Niosome is osmotically active, one kind of nonionic surfactant vesicle and structurally similar to liposomes.[108] Along with surfactant, Cholesterol/ polyethylene glycol (PEG) is part of the bilayer structure of the niosome, and it has a water pool at the core.[109] So, it consists of a hydrophobic bilayer part and a hydrophilic water pool.[110] Detail fluorescence correlation spectroscopy and femtosecond upconversion measurement indicate the HPTS molecules are fully encapsulated inside the niosome. Due to confinement, the initial proton transfer (τ_{PT}, 40 ps) in niosome is ~ 8 times slower than that in bulk water (5 ps). Also, the time constants of recombination(τ_{rec}) and dissociation (τ_{diss}) in niosome are ~4 times and ~1.5 times slower, respectively. This is due to the slower solvation, diffusion of RO^-, lower dielectric constant and higher friction inside the niosome than bulk. The ESPT rate is significantly retarded in free water and niosome upon adding NaCl. In the presence of 1 M and 4 M NaCl, τ_{PT} slows down to 80 ps and 225 ps, respectively, in the niosome.[107] The further slowing down of ESPT rate inside the niosome in the presence of NaCl is attributed to the factors like reduction in the number of water molecules required for solvation of proton, deprotonated moieties led to slower diffusion (Scheme 1.8).

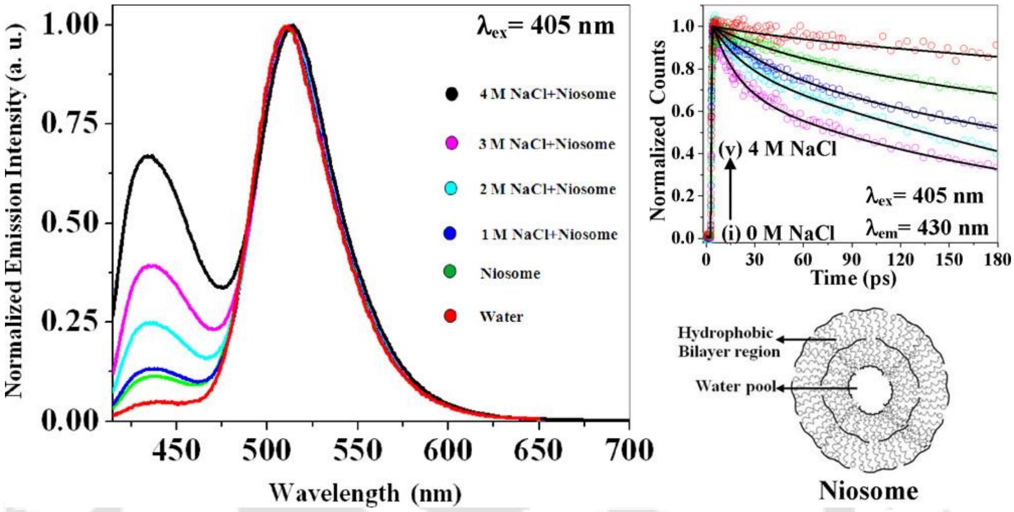

Scheme 1.8. Schematic representation of ESPT rate modulation in niosome and water in the presence of varying NaCl concentrations.[107] Reprinted with permission from ref.107. Copyright 2012, American Chemical Society

The ESPT rate of HPTS also depends on the number of bridged water molecules between the probe and the proton acceptor. In a report, based on femtosecond transient electronic and vibrational spectroscopy, Bakker and team established that the addition of salt does not affect the rate of proton transfer to acetate in case of HPTS are bridged to acetate by more than two water molecules.[111] In other findings, Nibbering and coworkers using mid-IR femtosecond pulses have shown that the ESPT rate is faster between HPTS with a direct hydrogen-bonded acetate ion compared to the case where HPTS and acetate ions are separated by one or more water molecules.[112-113] So the perturbation of the hydrogen bonding network, electrolytic screening, which affects the coulombic attraction between ion pairs and electrostriction caused by the strong electric field of the salt ions markedly alters the ESPT rate of HPTS in various systems.[83, 114-118]

1.9.4. Proton Transfer in the Biomolecular Systems

Proton transfer is one of the fundamental processes of nature. Proton pump activity in proton translocating membrane protein bacteriorhodopsin in halobacteria is associated with proton transfer.[119-120] Translocation of a proton between bulk water and membrane-bound protein interface plays a crucial role in bioenergetics.[121] Well-established examples of long-range proton transfer are vivid in many crucial biological parts like the photosynthetic reaction center [122] transmembrane channel.[123] Biologically vital enzymes like cytochrome c oxidase,[124] carbonic anhydrases,[125-126] alcohol dehydrogenase[127] are also associated with proton transfer while properly functioning in the living body. ATP synthesis proceeds with the help of proton translocation in the inner membrane of mitochondria, chloroplast catalyzed by adenosine triphosphate synthase complex.[128-130] Latteral proton transfer across the biological membrane in the interface of water and phospholipid alters surface potential, which helps the membrane to act in many signal transduction.[131] So Investigation of the proton transfer mechanism using a photoacid probe in a biological interface like in membrane, protein, or vesicles will provide information like local environment, hydration patterns, charge transfer mechanism, structure or folding pattern, bioenergetics and fundamentals of proton or ion gated channels etc.[132]

1.9.4.1. ESPT of HPTS in membranes and bilayers

Researchers have been investigating the membranes, vesicles, and bilayer for the last few decades to track the proton transfer mechanism and the local environmental information like hydration layer properties incorporating several prototropic photoacid probes and various methods.[133-138] Gutman and coworkers have explored the proton diffusion nature in the phospholipid membrane by incorporating the HPTS probe in the hydration layer of the egg phosphatidylcholine membrane. The proton diffusion rate is slower than the bulk medium. The thickness of the hydration layer and the proton diffusion rate is inversely proportional. The slower diffusion is attributed to the inhomogeneity of the aqueous matrix, geometrical restriction, distorted electric field and proton reactivity at the surface.[139] The generated proton from the membrane-trapped HPTS exhibits more significant geminate recombination than bulk.[140] Recently, the scientific community has not been limiting themselves by applying the mere probe molecule but instead incorporating chemically modified tethered probes.[141] Long alkyl chains have been attached to the HPTS probe and tethered to the biological membranes to gain insight regarding proton diffusion from the excited probe on the membrane surface, membrane surface to the bulk or bulk to the surface (Figure 1.3).[142] It has been established that the lipid headgroup strongly influences the fluorescence transient. It has been shown that the nature of phospholipids in the membrane modulates proton diffusion. Protons diffuse latterally mainly in the zwitterionic lipid surface in the membrane, while in negatively charged lipid surface, proton can migrate to bulk and vice versa.

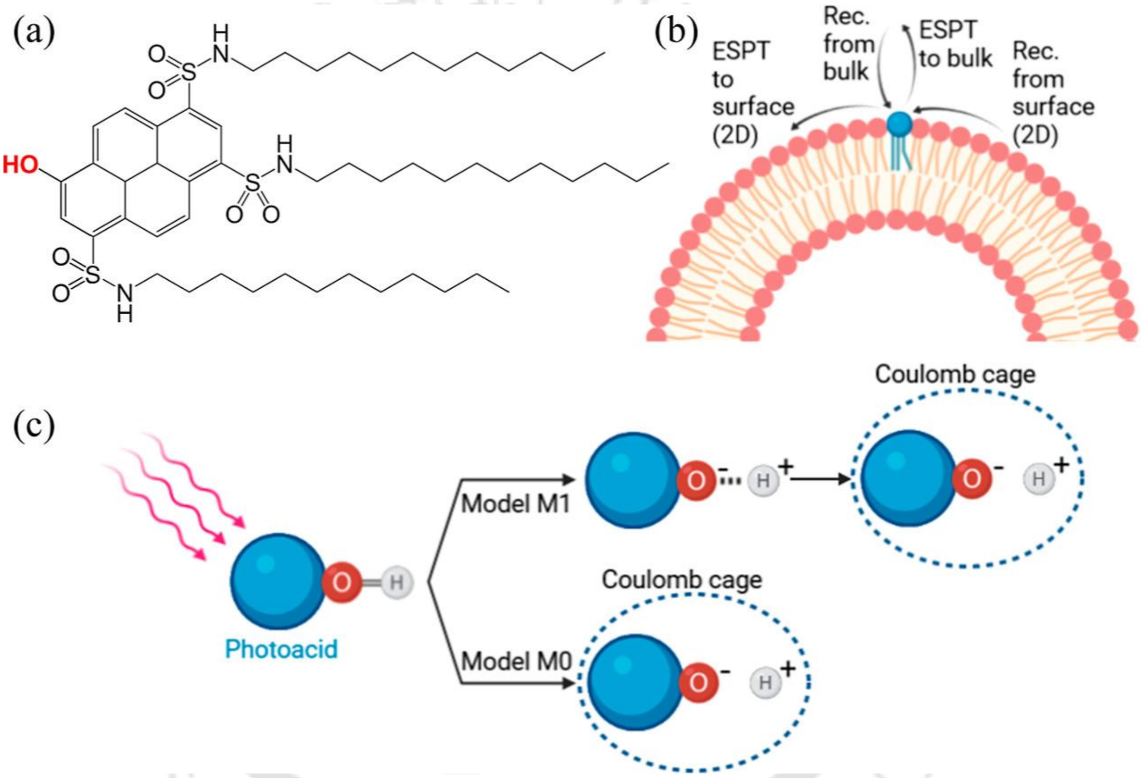

Figure 1.3. (a) Molecular scheme of the C_{12}-HPTS photoacid. The OH-group that gets deprotonated upon photoexcitation is marked in red. (b)The schematic integration of C_{12}-HPTS to the membrane includes the different excited state proton transfer (ESPT) and geminate recombination processes. (c) Schematic of the differences between the two models.[143] Reprinted with permission from ref.143. Copyright 2022, American Chemical Society

In the case of the cationic lipid surface, the proton transfer is relatively slow.[142] They have used the proton dissociation kinetics and geminate recombination model to explain the proton migration in various directions on the membrane surface and generate a new simplified model to explain those findings. They have arbitrarily taken the photoacid probe system's dimension and varied it to fit and explain the slow desorption rate of proton migration in the membrane surface.[143]

1.9.4.2. ESPT of HPTS in protein binding sites

Proton transfer assisted by proteins is an integral part of many biological systems for carrying out different functions.[144-145] Some well-known vital biochemical processes associated with proton transfer are photosynthetic water oxidation, light-activated proton pumping in rhodopsin, and polypeptide cleavage in proteases.[146-148] Proteins spanned across the membrane surface act as proton-specific ion channels. The relay of protons by buried water molecules called "water wires" are mediated by several channels and signaling trans-membrane proteins.[149] Also, the folding and unfolding structural patterns can be assessed by the ESPT of probes.[150] So, investigating excited state proton transfer reactions in protein sites provides valuable information.[151]

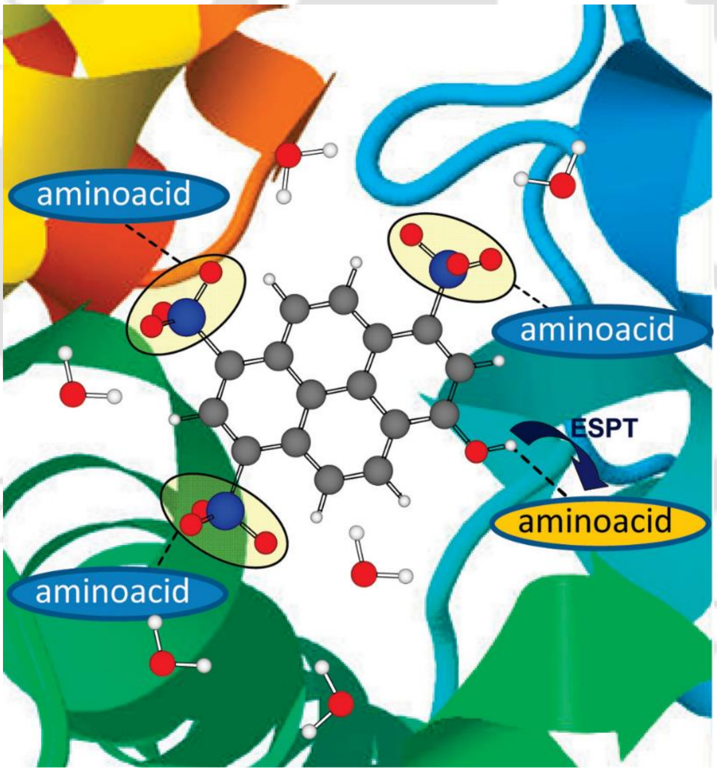

Scheme 1.9. Schematic representation of the location of HPTS in protein binding site showing ESPT.[152] Reprinted with permission from ref.152. Copyright 2011, American Chemical Society

In a report, Cohen et al. have shown the excited state intermolecular proton transfer reaction of 8-hydroxypyrene-1,3,6-trisulfonate (pyranine) with the globular human serum albumin (HSA) protein in the femtosecond to nanosecond time regimes. The proton-transfer reactions in the formed HSA-HPTS complexes proceed from 150 fs to ~1.2 ns in the extended time window. Direct H-bond breaking and making assisted by carboxylate groups of amino acids is evidenced from the ultrafast component in the robust complexes. The slowest time component arises from the biological water's slow dynamics. The caged photoacid gives the conjugated photobase by ESPT in "loose" HSA-HPTS complexes. The observed time components are (3 to 10 picoseconds), and 130 ps and 1.2 ns arise due to the slow dynamics of the water molecules in the vicinity of the probe and protein residue (Scheme 1.9).[152]

Though there are chances of forming robust complexes with definite ratios, the anisotropy data indicate heterogeneity in the system. The probable reason is the differential interaction patterns of the photoacid with the inner or outer parts of the protein residue. They further proposed that the caging of HPTS by the HSA protein alters the electronic redistribution in the formed deprotonated form in a different degree of mixing between the ^1L_a and ^1L_b states.[152]

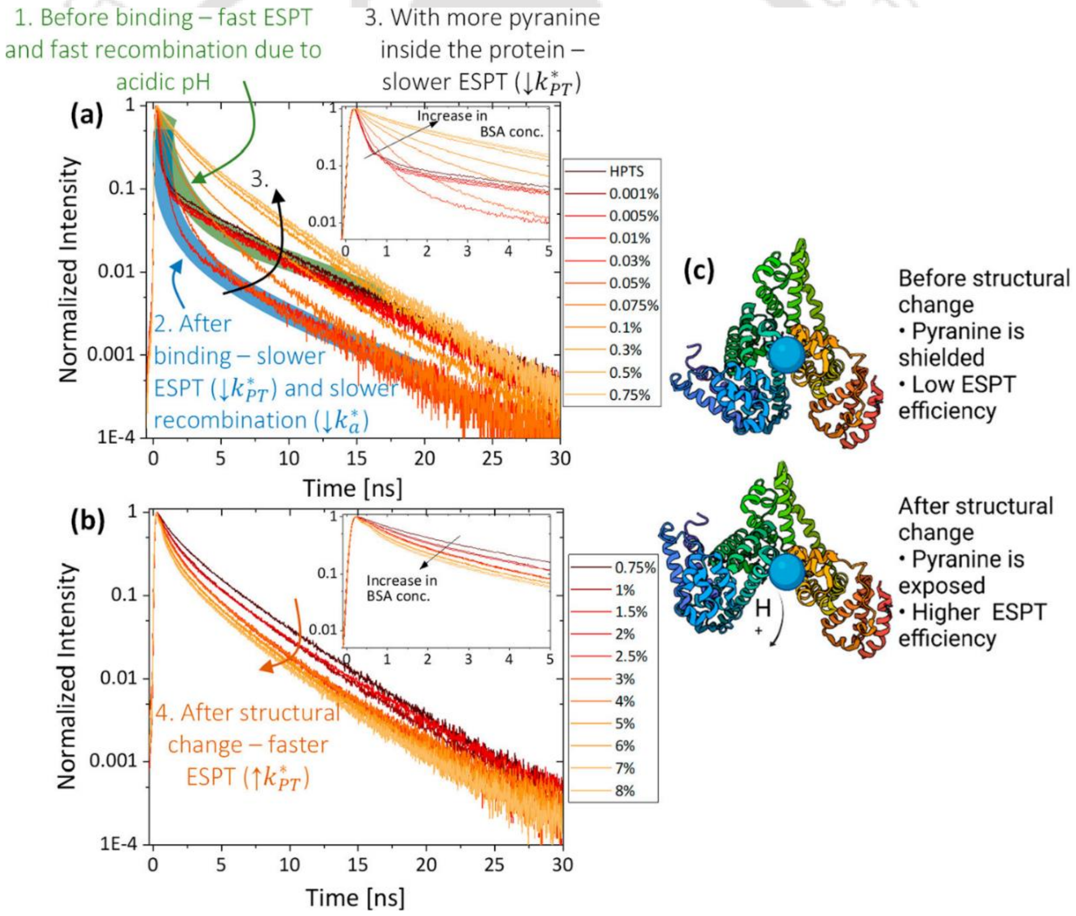

Figure 1.4. Time-resolved emission of pyranine in BSA fractions of (a) ≤ 0.75% and (b) ≥ 0.75%. The insets show magnifications of the first nanoseconds. (c) Schematic of the system.[73] Reprinted from ref.73. Licensed under CC BY.

The photoacid probe pyranine can sense the water accessibility or hydration in the medium. The structural change in a protein may alter the binding site conformation, and accordingly, its accessibility to bulk hydration or confinement may change. So, the probe HPTS can be utilized to probe any structural change in protein binding sites. The probe binding to the protein binding site resulted in poor ESPT efficiency. It indicates that the probe is in a hydrophobic environment surrounded by restricted slower water molecules. In seminal work, Amdursky and their team have explored the ESPT dynamics of HPTS in the binding sites of a globular protein, bovine serum albumin (BSA).[150] At low pH values, the BSA undergoes structural changes as a function of concentration. So, the extent of exposedness of the binding site to the bulk solution will markedly influence the ESPT efficiency of the bound pyranine. As the bound probe gets exposed to bulk, the ESPT rate is enhanced (Figure 1.4). The figure shows the concentration-dependent change in the ROH* transient upon binding to the protein. Which resulted in slower ESPT up to 0.75% of BSA, i.e., the point of the structural change (from $k_{\mathrm{PT}}^* \approx 5\ \mathrm{ns}^{-1}$ before binding to $0.4\ \mathrm{ns}^{-1}$ after binding), after that concentration, the ESPT becomes faster (increasing to $k_{\mathrm{PT}}^* \approx 1\ \mathrm{ns}^{-1}$).[150] The additional proton acceptor, specifically glutamic and aspartic acid residues, may also enhance the ESPT from exposure to bulk hydration in such sites.[153] So, probing concentration-induced structural transition of proteins can also help to explore the amyloidogenesis process.[154]

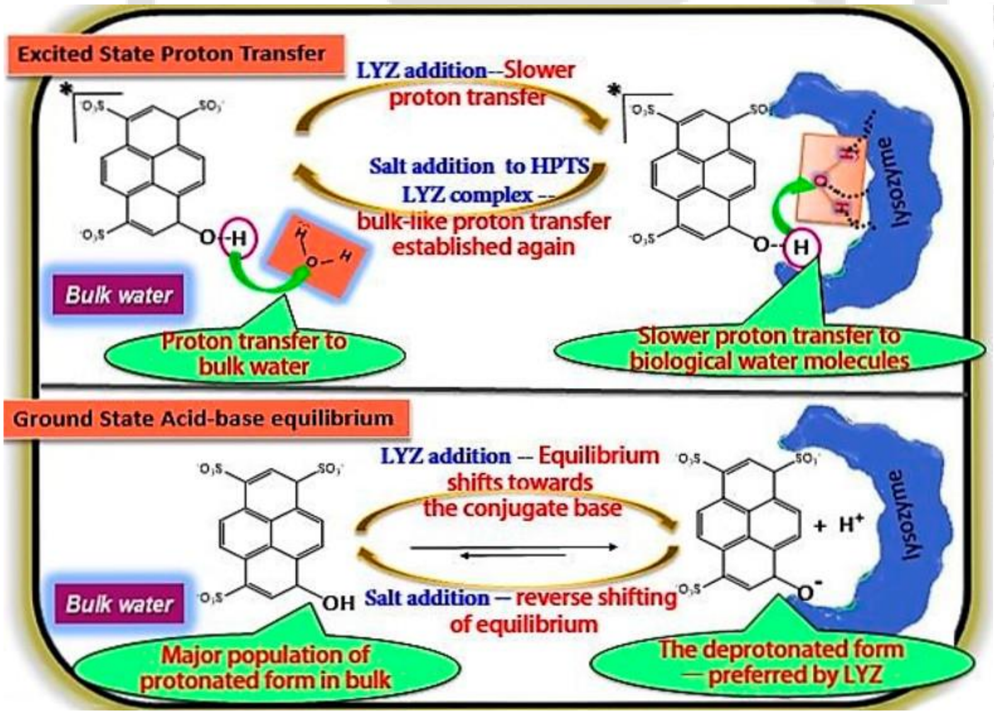

Scheme 1.10. Schematic representation of environment-dependent ESPT process of HPTS in protein Lysozyme.[155] Reprinted with permission from ref.155. Copyright 2016, American Chemical Society

Another study by Halder and coworkers showed that HPTS forms a 1:1 complex with the protein lysozyme in the ground state (binding constant, K_{BH} ~1.4×10^4 M^{-1}). Inside the protein binding site, despite the preference for the deprotonated form of HPTS, the restricted "slow" biological water retards the excited state proton transfer process. But high ionic strength accelerates the ESPT dynamics in lysozyme-bound pyranine by dislodging the fluorophore from the active site of the protein to the bulk again (Scheme 1.10).[155]

So as of now, we have seen due to binding of the probe in the protein binding site retards the ESPT rate due to confinement or slow biological water. In contrast, HPTS exhibits a faster ESPT than bulk in the presence of a therapeutic protein, Protamine. The detailed study shows that the binding sites comprise cationic arginine residues, mainly responsible for ESPT enhancement.[153] So, confinement, as well as the nature of the binding site, will determine the ESPT rate of the probe along with the structural conformation of the protein.

1.9.4.3. ESPT of HPTS in macroscopic biostructures

There are abundant biological macrostructures besides the biological systems like proteins, lipid surfaces or membranes. Several studies have been reported regarding the ESPT dynamics of HPTS on those macromolecular surfaces such as hydrogels, mats, films, fibrils or polysaccharides. The probe pyranine adsorbed to the surface of this bio-structure. So, based on the ESPT nature and proton diffusion on these bio macro surfaces, detailed hydration patterns and structural heterogeneity can be accessed.

The hydrogels are generally prepared from polymer molecules, proteins, fibroins, keratin etc.[156] These hydrogel systems are quite useful for controlled drug release.[157] Physisorption and passive release are the most common drug loading and release procedures. The environment and hydration of gels are quite different than the monomers of it. For instance, the hydrogel can be prepared by thermal induction of BSA above a certain concentration.[158-159] By incorporating the ESPT probe, HPTS, it has been observed that the protein's surface becomes hydrophobic. The significantly slower ESPT rate after gelation (k_{PT}*≈3.5 → 0.9 ns^{-1}) resulted in an insight into the mechanism of gel formation.[158]

Proteins-based materials are good candidates for the formation of proton-conducting materials. The hydrogen bonding network in the abundant water molecules inside the protein structure and the presence of charged amino acids play a vital role in long-range proton conduction in those materials. Proton conductivity across collagen, keratin, and lysozyme layers has been explored.[160-162] Amdursky et al. investigated ESPT and proton diffusion properties in BSA protein mat.[163] These protein mats are composed of electrospun fibrillar BSA, and they absorb large quantities of water. The proton transfer rate and diffusion dimensionality are less on the mat than in bulk. The ESPT rate from HPTS to charged amino acid is faster and independent of hydration. The binding mode of the probe also dictates the ESPT rate. Chemisorption increased ESPT, whereas physisorption to the same protein mat decreased ESPT.[164] ESPT is relatively slower on the surface of another protein-based material, the amyloid fibril, than bulk water. Which indicates the poor accessibility of water on that binding site.[151]

Apart from protein-based proton conducting materials, polysaccharide derivatives have recently been proposed for protonic devices.[165] Polysaccharides, irrespective of linear and branched (cellulose, chitosan, and starch), can be probed using pyranine in the aqueous phase.[166-168] The ESPT of pyranine within polysaccharides is hydration dependent. More hydration will enhance the ESPT rate and vice versa. Exceptions are also there; in the case of chitin (acetylated polysaccharide), the presence of the weakly basic acetyl groups promotes the ESPT rate by serving as proton acceptors even at a very low water content or in the presence of significant amounts of alcohols, methanol and ethanol.[168]

1.9.5. ESPT of HPTS in micelles

In present, tremendous interest has emerged in exploring nanoconfined species.[169-173] These investigations will provide great help in understanding the intimate features of relevant biomimicking interfaces. We can also correlate naturally occurring reactions with the nanoscopic confinement-induced chemical pathways.[174-176] Micelles are one of these organized assemblies. Various experimental and computational studies are being carried out and undergoing to explore the dynamics and thermodynamics of water molecules in micellar confinement.[177-179] Micelles are formed above a critical concentration (critical micellar concentration or CMC) of surfactant or constituent molecules. External factors like temperature and additives can alter CMC value and properties.[180] These micelles can solubilize many potential drugs (poorly soluble in aqueous media) molecules, serve as drug delivery vehicles and can interact with various biological moieties like lipids, bile salts, membranes etc.[181-183] Micelles are generally composed of ionic, nonionic, zwitterionic, polymeric surfactant molecules. The micellar CMC and surface potential of the micelles depend upon the headgroup charge of the surfactant and the chain length.[184]

Excited state proton transfer (ESPT) dynamics of HPTS can give important insights into the nature and dynamics of the water, and the structural pattern of these micellar assemblies.[185-186] The photoacid probe HPTS localizes itself in the interface of the micelle, and its emission property is very sensitive to local hydration inside micelles.[187-189] HPTS has been incorporated to investigate cationic and zwitterionic micelles to explore various properties like the electrostatic nature and ion exchange behavior etc.[190-192] Bhattacharyya and team have shown slower ESPT dynamics of HPTS inside the cationic CTAB micelles.[187]

Our group investigated the compactness and hydration properties of zwitterionic micelles compared with cationic micelles.[193] Both the ESPT and rotational dynamics are slower inside micelles having the same alkyl tail chain length. From detailed steady-state and time-resolved studies, it has been established that in between zwitterionic and cationic surfactant micelle, the latter is densely packed and less hydrated. So, the slower ESPT dynamics may arise due to the strong hydrogen bonding network in the zwitterionic micellar interface, with almost immobile water molecules. The interfacial ESPT dynamics and fluorescence anisotropy decay also counter ion dependent.[193]

1.9.6. ESPT of HPTS in reverse micelle

Reverse micelles (RMs) are aggregated surfactant molecules with an encapsulated water pool at the core within a hydrophobic organic media.[176, 194-195] This assembly offers a simple and easily accessible experimental container for exploring confined aqueous environments. Considerable attention has been raised to studying the structure, interfacial properties, and dynamics of the reverse micelle.[196-198] It has widespread applications as nanoreactors to enhance chemical and enzymatic reactions, for nanoparticle synthesis and also as a model water–membrane interface.[199-205] Surfactants of different ionic properties (e.g., neutral, cationic, anionic, zwitterionic) spontaneously form RMs of different shapes (spherical, ellipsoidal or rod aggregates) in nonaqueous phase with encapsulation of a central water pool or polar solvents.[206] The surfactants are oriented in the reverse micelle so that the ionic headgroup or hydrophilic part stays toward the water pool core, and the hydrophobic tail part stays outside, i.e., directing to the nonpolar solvent.

ESPT dynamic investigation of the dissolved probe in the interior of reverse micelles can provide information regarding the proton transfer, orientational dynamics of the probe, and other properties of water. The nature of the interface, especially the charge specificity, impacts a lot in the ESPT dynamics. Several investigations have been performed applying ultrafast, visible and infrared (IR) spectroscopy and NMR to gain insight into the influence of charged versus nonionic surfactant−water interfaces on the dynamics of dissolved probes and water molecules.

A recent study by Fayer and coworkers have shown that the proton-transfer dynamics of HPTS are quite the opposite in nonionic Igepal RMs compared to that in anionic AOT RMs.[86] In AOT reverse micelle having an anionic interface, the anionic probe stays at the center of the water pool away from the interface; bulk-like ESPT dynamics have been observed (Figure 1.5). In nonionic Igepal RMs, the probe prefers to stay in the interface with two different orientations. One set of HPTS hydroxyl groups stays buried in the RM's organic wall, and the other has the hydroxyl group exposed to the water. Biexponential decay of excited state population, differential deprotonation and recombination times support this phenomenon.[86] Apart from the interface pattern, water nanopool size modulates the ESPT dynamics.[86, 207]

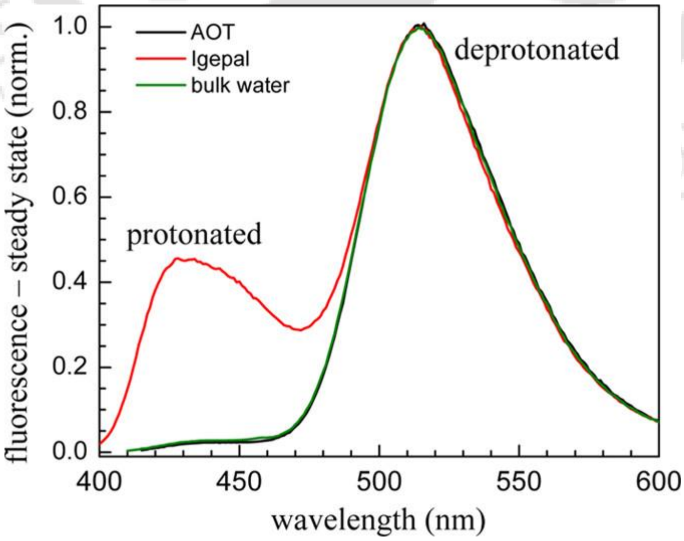

Figure 1.5. Steady-state emission spectra of HPTS in bulk water (green), w_0 = 25 AOT RMs (black), and w_0 = 20 Igepal RMs (red). The AOT and Igepal RMs have the same

size water nanopools, r = 4.2 nm.[86] Reprinted with permission from ref.86. Copyright 2015, American Chemical Society

In another seminal work, Sedgwick et al. compared the ESPT dynamics of HPTS in two different RMs, the cationic CTAB and anionic AOT. Based on ultrafast spectroscopic measurements and 2D NMR studies, they have established that the ESPT dynamics go as usual while staying at the center of the water pool, but in the CTAB RMs, there is no deprotonation occurred.[208] The HPTS stays buried in the cationic interface with the probe hydroxyl group in the hydrophobic regions. So the interfacial environment dampens the deprotonation kinetics and the rotational dynamics (Scheme 1.11).[208-210]

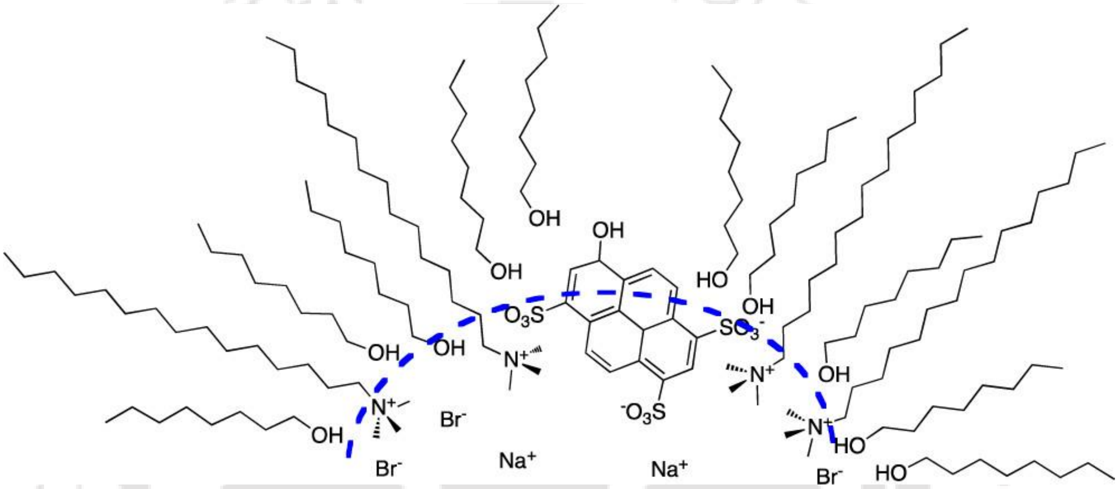

Scheme 1.11. Cartoon suggesting a possible orientation of HPTS embedded in the CTAB/1-octanol RM interface that would lead to the observed time-resolved spectroscopy and NOESY results.[208] Reprinted with permission from ref.208. Copyright 2012, American Chemical Society

Our group also explored the RMs in detail with the help of ESPT dynamics of HPTS and various physicochemical methods. The water nanopool size and interfacial hydration can alter the shape of the reverse micelle from spherical to rod in DDAB/water/cyclohexane composition.[206] The highly immiscible alcohol can be solubilized significantly in the water pool of RMs confinement depending on the core size and water amount. In AOT/water/n-heptane RMs confinement, Phukon et al. established that.[211]

1.9.7. ESPT of HPTS in mixed micelle

Surfactant molecules can form mixed micelles apart from their self-assembly.[212] Many instances are there in the literature that the mixed micellar assembly can have better efficacy compared to its self-assemblies. So, investigating these mixed micelles of different compositions, like short-chain ionic and nonionic surfactants with polymeric surfactants, is essential. Ghosh et al. have done such an investigation on the polymer-surfactant aggregate composed of a pluronic triblock copolymer P123, $(PEO)_{20}$-$(PPO)_{70}$-$(PEO)_{20}$ and a cationic surfactant, cetyltrimethylammonium chloride (CTAC).[213] The polymer interacts with the surfactants above a particular concentration, called the critical aggregation (CAC) constant, which is lower than its CMC.[212, 214] The CAC of CTAC here is ~ 0.25 mM[212] which is relatively lower compared to its CMC of 1.3 mM.[215] Detail steady-state and time-resolved studies indicate that proton transfer in P123-CTAC mixed aggregate is much slower than in their self-assembly or bulk water. The steady-state emission intensity ratio (ROH/RO^-) in P123-CTAC aggregate (2.2) is 2, 12 and 50 times higher than that in CTAC micelle, P123 micelle, and water. ESPT retardation is also reflected in the increase in the rise time of the RO^- emission of HPTS. In P123- CTAC mixed aggregate, RO^- has three rise times: 30, 250, and 2400 ps. These rise times are longer than those in CTAC micelle, P123 micelle, and bulk water. The corresponding rate constants of proton transfer, recombination, and dissociation of the ion pair are also slower. The slower rates manifest the lower polarity and unfavorable geometry in the nanoconfined compact systems. They concluded that the P123-CTAC mixed aggregate has different confinement and microenvironmental properties compared to their self-assembly.[213]

In a study, Mondal et al. have shown a similar mixed micellar assembly composed of Pluronic P123 and room temperature ionic liquid (RTIL) via femtosecond up-conversion investigation of ESPT of HPTS. In RTIL-P123 mixed micelles, slightly faster solvation dynamics have been observed than in P123 micelles.[189] In another seminal work, Halder and team have explored the ESPT dynamics of HPTS in the mixed assembly of pluronic block copolymer F127 micelle, F127 - anionic surfactant SDS mixed assembly and F127-cationic surfactant CTAC mixed assembly.[216] Detail steady-state and time-resolved investigations reveal that two different time constants (160 ps and 1.05 ns) of deprotonation exist for both F127 micelle and F127-SDS mixed micelles. The faster one, 160 ps, arises due to the probe's location in the micellar periphery or the bulk water. However, the probe in the corona region generates the slower 1.05 ns component.

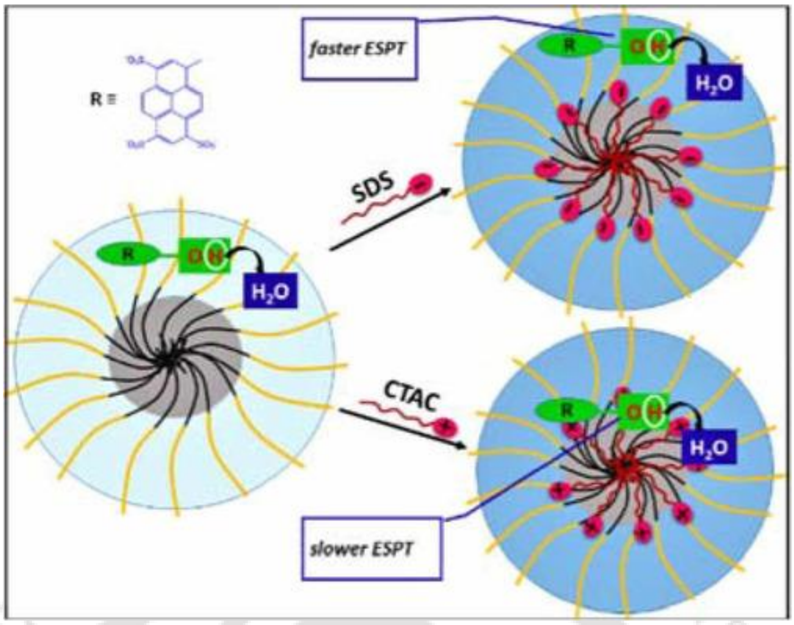

Scheme 1.12. The schematic representation of probe locations and ESPT rate in different micelles.[216] Reprinted with permission from ref.216. Copyright 2018, John Wiley and Sons.

The addition of SDS in F127 micelles enhances water penetration in the corona region and increases the ESPT rate (time constant changes to 140 ps, 640 ps) due to increased hydration. But the ESPT in mixed F127- anionic SDS micelle is opposite to that of mixed F127- cationic CTAC micelle (250 ps, 2.4 ns). The cationic-charged CTAC and probe location near the core (far away from corona hydration) attributed to the slower ESPT in F127-CTAC mixed assembly (Scheme 1.12). So depending on the probe location in the mixed micelles, the headgroup charge property of ionic surfactants and hydration surrounding the probe modulates the ESPT dynamics.[216]

1.10. The objective of the Thesis

ESPT dynamics of HPTS is susceptible to local hydration, and this phenomenon has been utilized to track the reorganization of the mixed micelle at various compositions of copolymer and surfactant molecules. During the formation and further modification of these assemblies, the entrapped HPTS probe exhibited its ESPT properties. We have analyzed it based on the overlap-corrected time-resolved data method and obtained the kinetic parameters. The correlation of the dynamics and mixed micelle formation ascertain us to apply the assembly to various purposes. Differential interaction pattern of surfactant assemblies with polyelectrolytes has also been explored in this Thesis.

Chapter 2

Experimental and Analytical Methods

Chapter 2: Experimental and Analytical Methods

This chapter specifies the details of the instruments used in the thesis works, namely, UV-Vis spectrophotometer, steady-state fluorimeter, time-correlated single photon counting (TCSPC) setup, dynamic light scattering (DLS), isothermal titration calorimetry (ITC), and field-emission transmission electron microscope (FE-TEM). The data analysis methods, models and software are also included. The purity, sources of all the chemicals used and sample preparation procedures are added.

2.1. Steady-state spectroscopic measurements

Absorption spectroscopy is one of the most important spectroscopic techniques. Absorbance is associated with the electronic transition of the molecule upon irradiation of proper wavelength light. It provides crucial information about the transition wavelength and molar extinction coefficient (ε) at that particular wavelength of the molecule under investigation. In our experiment, we used the Perkin Elmer lambda 750 instruments to record the UV-visible spectra of the samples. The instrument consists of deuterium, tungsten and halogen lamps as a light source, double holographic grating monochromators and high sensitivity photomultiplier tube detector (Scheme 2.1)

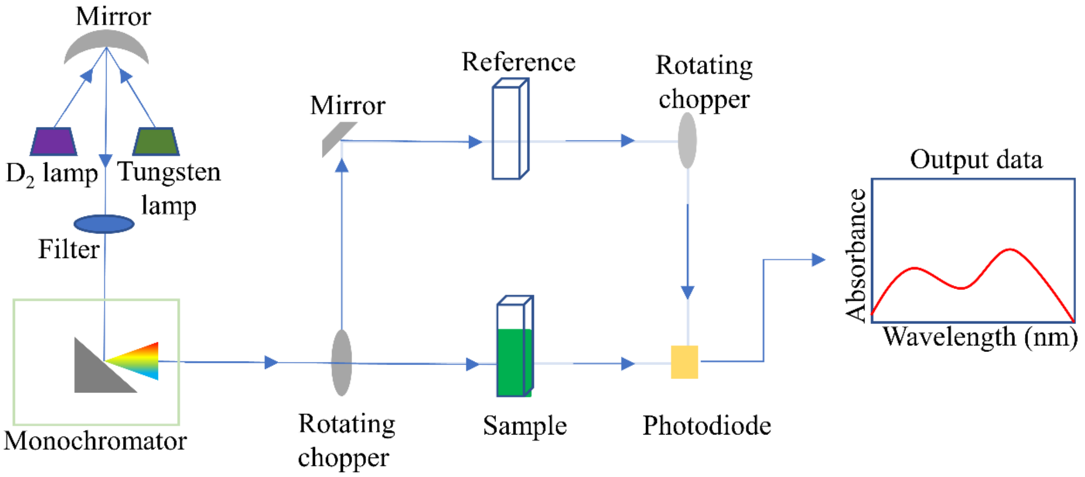

Scheme. 2.1. Schematic representation of UV-Visible spectrophotometer.

Steady-state emission spectra are useful for determining the molecules' nature in the excited state. The samples' emission spectra were recorded on the Jobin Yvon fluoromax4 spectrofluorometer. The instrument is equipped with a xenon arc lamp as the light source. The emitted light from the sample is collected right angle to the incident excitation beam. The detector R928P is used as a photomultiplier tube detector in the device (Scheme 2.2).

The quartz cuvettes of path length 1 cm have been used in all the steady-state absorption and emission.

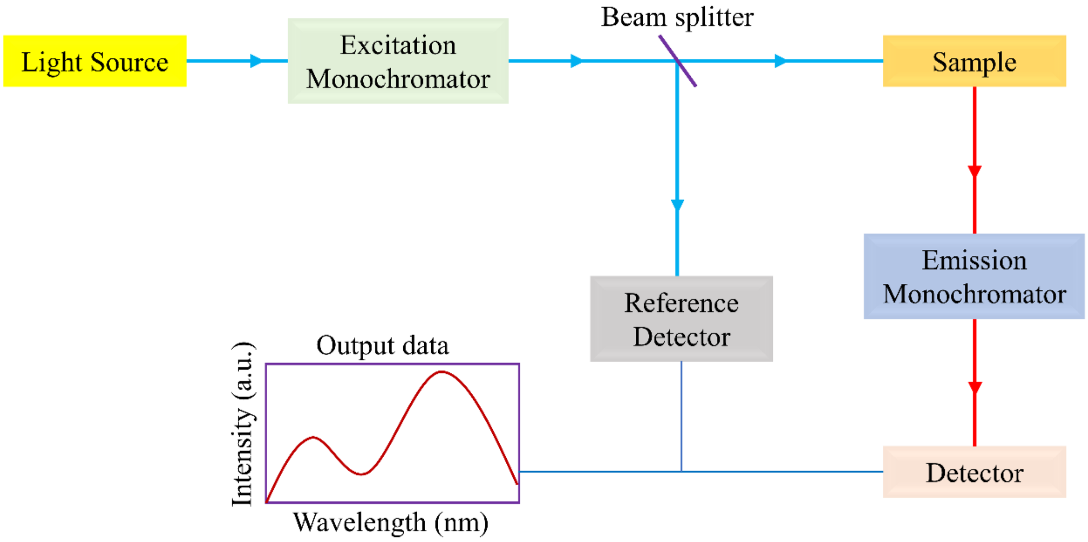

Scheme 2.2. Schematic representation of a spectrofluorometer.

2.2. Time-Correlated Single Photon Counting (TCSPC)

Time-correlated single photon counting (TCSPC) is an advantageous method for measuring emission decay and obtaining the lifetime of fluorescent molecules in the time range of picoseconds to nanoseconds. We have used the TCSPC instrument provided by HORIBA scientific instrument for time resolve emission decay measurements, and the time resolution and measurement time window depend on the light source, assembled electronic components, and sample characteristics.

2.2.1. Principle

TCSPC operates on a unique principle.[217] In the TCSPC instrument, typically, 1% of the photon is detected for 100 excitation pulses. The *y*-axis represents the number of photons detected for the time difference (represents the x-axis) between excitation pulses and observed photons. Currently, all TCSPC measurements are performed in the "reverse mode," i.e., the emission pulse is used to start the time-to-amplitude converter (TAC), and the excitation pulse is used to stop the TAC (Scheme 2.3).[217] A channel detects the pulse from the single detected photon originating from the pulse excitation of the sample. The arrival time of the signal is accurately determined by a CFD (constant fraction discriminator), which sends a signal to a TAC, which generates a voltage ramp that is a voltage that increases linearly with time. The next excitation pulse sends a signal to the electronics to stop this voltage ramp. The TAC now contains a voltage proportional to the time delay (Δt) between the emission and excitation signals. A histogram of detected photons, i.e., the decay, is measured by repeating this process numerous times with a pulsed-light source and analyzed in a multi-channel analyzer (MCA).[217] Finally, the instrument-obtained data is analyzed and fitted with appropriate models and software. The instrument response function (IRF) and full-width half maxima (FWHM) of the IRF for the light source LASER diode 375 nm have been measured using liquid scatter in the cuvette. The IRF of the instrument for the LASER diode 375 nm light source was ~ 90 ps. All intensity decays were measured keeping the emission polarizer at magic angle of 54.7° with respect to vertical excitation polarizer to avoid any rotational contribution to the life time data.

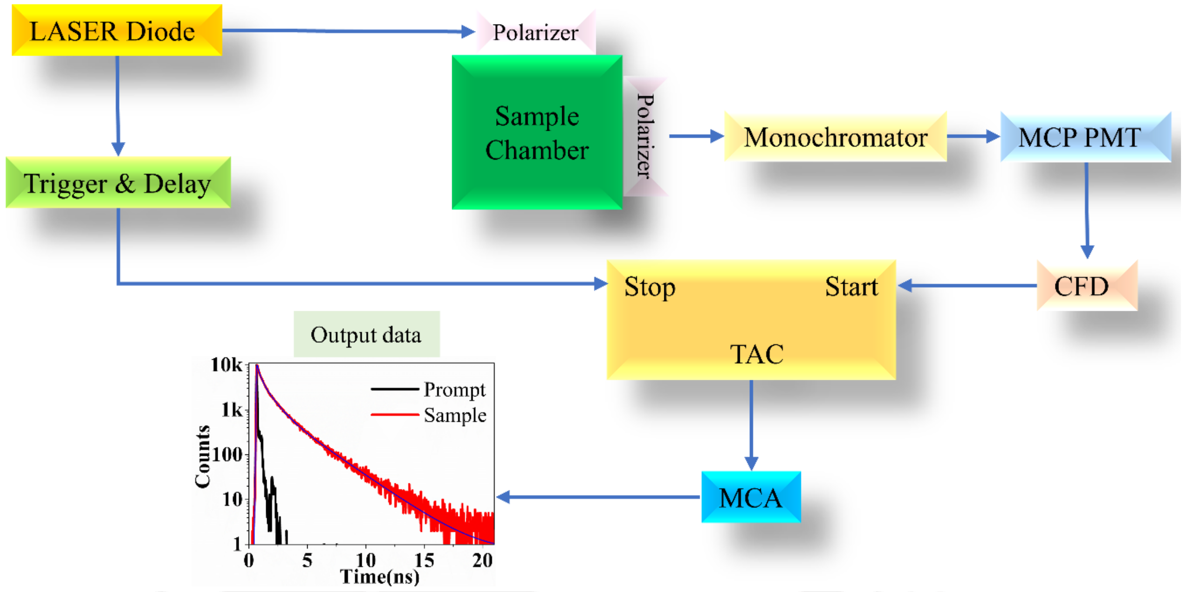

Scheme 2.3. Schematic representation of TCSPC instrument.

2.2.2. Data Analysis

The TCSPC data analysis is not straightforward because the excitation pulse is not a δ function. It has finite width. So, The observed decay is the convoluted form of intensity decay I(t) and instrument response function (IRF), represented as L(t). To analyze the decay, we have to deconvolute the raw data, and the convolution integral is expressed as

$$\mathrm{N}(t) = \int_0^{t'} L(t)I(t'-t)dt \qquad (2.1)$$

Where t represents the variable time delay, the available software (like DAS6, FAST) generally uses the iterative nonlinear least square fitting method. First, an excitation pulse profile is recorded. The deconvolution starts with mixing the excitation pulse and the projected decay to form a new reconvoluted set. This data is compared with experimentally obtained data, and the difference is summed, generating the χ^2 functions for fitting. The χ^2 is expressed as

$$\chi 2 = \sum_{i=1}^{n} \left[\frac{N(t_i) - N_c(t_i)}{\sigma_i}\right]^2 \tag{2.2}$$

Where $N(t_i)$ is the measured data, $N_c(t_i)$ is the calculated decay, N is the total no of data points and σ_i is the standard deviation of the ith data point. The deconvolution proceeds through a series of iterations until an insignificant change in χ^2 occurs between two successive iterations. However, $\chi 2$ is not considered the best choice for a large number of data points; instead, a quantity called reduced χ_R^2 is calculated. It is defined as

$$\chi_R^2 = \frac{\chi^2}{n-p} \tag{2.3}$$

Where n is the number of data points, and p is the number of parameters. The value of χ_R^2 is estimated with different choices of fitting parameters, multiexponential model, i.e.,

$$I(t) = \sum_i a_i \, exp^{-\frac{t}{t_i}} \tag{2.4}$$

The quality of fit is generally assessed by the χ_R^2 value ~1, the plot of the weighted residuals and the autocorrelation function of the residuals.

2.3. Time-Resolved Emission Spectra (TRES) and Time-Resolved Area Normalized Emission Spectra (TRANES) for the Interpretation of ESPT Dynamics

The fluorescence emission decay for protonated and deprotonated species for two particular fixed wavelengths provides only a qualitative idea about the ESPT dynamics. The significant overlaps between the two bands and dynamic Stokes shifts may give an erroneous interpretation. So, to avoid such complications, time-resolved emission spectra have been constructed. Following the methods provided in the literature, we first constructed the time-resolved emission spectra (TRES) and then obtained the time-resolved area-normalized emission spectra (TRANES) following area normalization.[217-221] The fluorescence decays of HPTS were monitored at the wavelengths with an interval of 5-10 nm spanning the entire emission spectrum. The fluorescence decays were fitted by applying the multiexponential model,

$$I(\lambda, t) = \sum_{i=1}^{N} \alpha_i(\lambda) exp[-t/\tau_i(\lambda)] \quad (2.5)$$

TRES was constructed by the procedure provided by Maroncelli and Flemming.[219] For that, we have to compute the normalized intensity decays so that the time-integrated intensity at each wavelength equals the Steady-state intensity at that wavelength. For F (λ) to be the steady-state emission spectrum, we have to calculate a set of H (λ) values using

$$H\ (\lambda) = \frac{F\ (\lambda)}{\int_0^\infty I\ (\lambda,t)dt} \quad (2.6)$$

Which for multiexponential analysis becomes

$$H(\lambda) = \frac{F\ (\lambda)}{\sum_i \alpha_i(\lambda)\tau_i(\lambda)} \quad (2.7)$$

The term H (λ) multiplied by time-integrated intensity equals the Steady-state intensity at that wavelength.

So, to calculate the TRES, the normalized intensity functions are given by

$$I'(\lambda, t) = H(\lambda)I(\lambda, t) = \sum_i \alpha_i{}'(\lambda) exp[-t/\tau_i(\lambda)] \quad (2.8)$$

Where $\alpha'(\lambda) = H(\lambda)\alpha_i(\lambda)$ (2.9)

The values of $I'(\lambda,t)$ give the intensity at any wavelength and at any time, providing the TRES.

The concept of TRANES, provided by the Periasamy group, was also applied here.[220-221] Since the TRANES were constructed by normalizing the area of the TRES, the total population remains constant over time. Thus, visualization of any kinetically coupled species becomes prominent. The TRANES may intersect at a particular wavelength depicting a clear isoemissive point. The isoemissive point in the TRANES helps us ascertain the number of species involved in the excited state dynamics or whether the probe is partitioned in two different locations in the system. Each TRANES can be fitted with a bi-lognormal function to get emission maxima and intensity at maxima (Figure 2.1).

2.3.1. Decomposition of the Emission Spectrum of HPTS into the Protonated and Deprotonated Bands: The steady-state emission spectrum or the time-resolved area normalized emission spectrum (TRANES) of HPTS consists of two bands, protonated and deprotonated.

These emission spectra can be fitted with the following bi-lognormal functions.

$$I(\nu) = I_0^1 \exp\left\{-\ln(2)\left[\frac{\ln\left(1+\frac{2b_1\left(\lambda-\lambda_p^1\right)}{\Delta_1}\right)}{b_1}\right]^2\right\} + I_0^2 \exp\left\{-\ln(2)\left[\frac{\ln\left(1+\frac{2b_2\left(\lambda-\lambda_p^2\right)}{\Delta_2}\right)}{b_2}\right]^2\right\}$$

(2.10)

When both $\frac{2b_1(\lambda-\lambda_p^1)}{\Delta_1} \leq -1$ and $\frac{2b_2(\lambda-\lambda_p^2)}{\Delta_2} \leq -1$

Else, $I(\lambda) = 0$

Here, I_0, λ_p, Δ, b represent the maximum peak intensity, wavelength maximum, asymmetry factor and width parameter of each of the bands. The label (1,2) in the subscript or superscript denotes the protonated and deprotonated bands' parameters, respectively.

The ratio of emission intensities, R, can be calculated as

$$R = \frac{I_0^1}{I_0^2} \qquad (2.11)$$

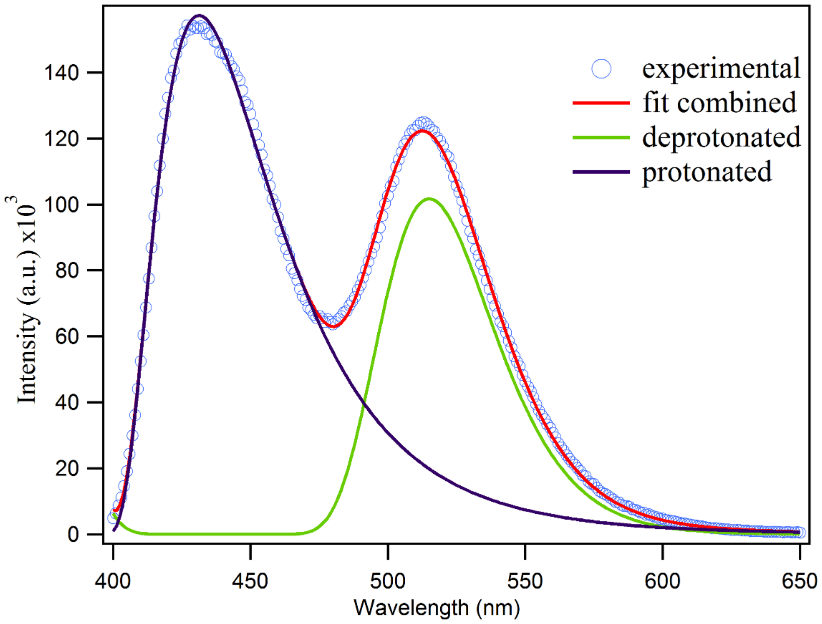

Figure 2.1. An example of splitting the fluorescence emission spectrum of HPTS into the protonated and deprotonated bands.

2.4. Ratiometric Method

Based on the ESPT kinetic schemes (Schemes 1.4 and 1.5), the time dependence of the excited protonated form and the total deprotonated form (including both the contact ion-pair and the dissociated deprotonated species) can be represented as[99]

$$ROH(t) = \frac{\beta_2 - k_d}{\beta_2 - \beta_1} e^{-\beta_1 t} + \frac{k_d - \beta_1}{\beta_2 - \beta_1} e^{-\beta_2 t} \qquad (2.12)$$

$$RO^{-}_{total}(t) = 1 - \frac{\beta_2 - k_d}{\beta_2 - \beta_1} e^{-\beta_1 t} - \frac{k_d - \beta_1}{\beta_2 - \beta_1} e^{-\beta_2 t} \qquad (2.13)$$

Where

$$\beta_{2,1} = \frac{1}{2}\left\{(k_d + k_r + k_{diff}) \pm \sqrt{\left(k_d + k_r + k_{diff}\right)^2 - 4k_d k_{diff}}\right\} \qquad (2.14)$$

Also, $\beta_1 + \beta_2 = k_d + k_r + k_{diff}$ (2.15)

$$\beta_1 \times \beta_2 = k_d \times k_{diff} \qquad (2.16)$$

The time-dependent emission ratio (either of the band area or the peak intensity) can be represented as[99]

$$R(t) = \frac{a_1 e^{-t/\tau_1} + a_2 e^{-t/\tau_2}}{1 - a_1 e^{-t/\tau_1} - a_2 e^{-t/\tau_2}} \qquad (2.17)$$

Where,

$$\beta_1 = \tau_1^{-1} \qquad (2.18)$$

$$\beta_2 = \tau_2^{-1} \qquad (2.19)$$

$$\frac{a_1}{a_2} = \frac{\beta_2 - k_d}{k_d - \beta_1} \qquad (2.20)$$

However, in the case where ESPT is almost irreversible, the ratio may correspond to a more straightforward form,[222]

$$R(t) = \frac{e^{-t/\tau_d}}{1 - e^{-t/\tau_d}} \qquad (2.21)$$

The fitted TRANES intensity ratio provides the time components; further analyzing those, we can calculate the deprotonation, diffusion, and geminate recombination times.

2.5. Time-Resolved Anisotropy Decay

The fluorescence anisotropy decay provides us with the system's local rigidity, viscosity, and rotational correlation time of the probe. In our experiments, we have incorporated MPTS instead of HPTS to avoid a possible error due to the ESPT dynamics on the fluorescence anisotropy (both Steady-state and time-resolved). It shows absorption maxima at 403 nm and emission maxima at 430 nm (Figure 2.2). The advantage of MPTS is that it cannot undergo ESPT.

We recorded the parallel and perpendicular components of the fluorescence anisotropy decay separately by rotating the analyzers at regular intervals to measure the anisotropy decay. Here the sample has been excited from the pulsed LASER diode 375 nm source, and the decay has been recorded at the fixed wavelength at 440 nm for the MPTS probe. Anisotropy is defined as

$$r(t) = \frac{I_{VV}(t) - G I_{VH}(t)}{I_{VV}(t) + 2G I_{VH}(t)} \tag{2.22}$$

The I_{VV} and I_{VH} are the parallel and perpendicular mode intensities with respect to vertically polarized excitation. The G parameter is the correction factor of the detection setup gratings. For our TCSPC setup, the G value was ~ 0.6. further, the anisotropy decay was fitted by applying the biexponential function to obtain the anisotropy decay parameters.

$$r(t) = r_0 \left[\beta \exp\left(-\frac{t}{\tau_s}\right) + (1-\beta) \exp\left(-\frac{t}{\tau_f}\right)\right] \tag{2.23}$$

where τ_f and τ_s are the fast and slow components of the time constants; β is the contribution of the slow component, and r_0 is the initial anisotropy.

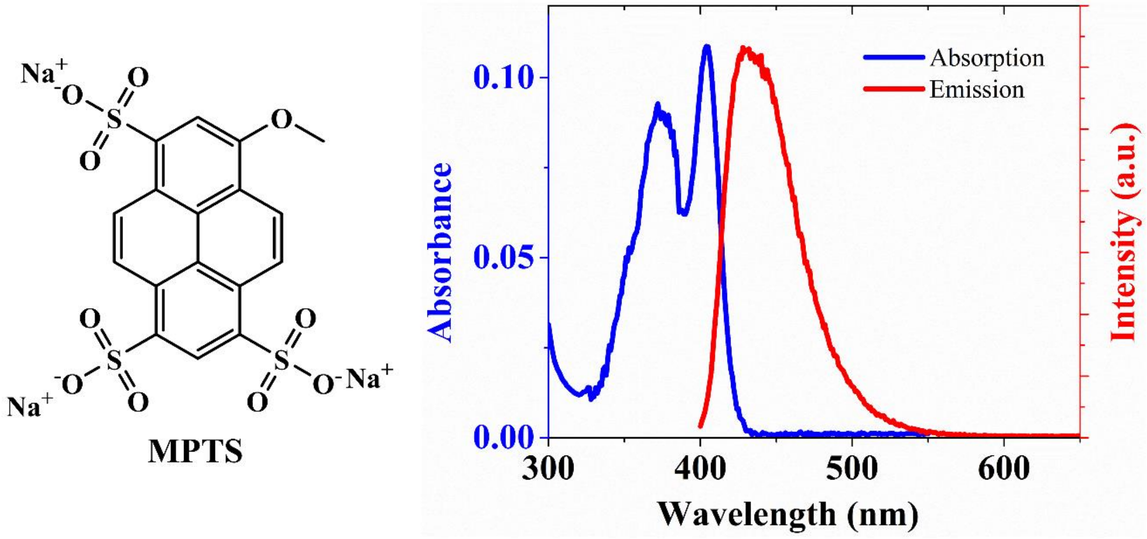

Figure 2.2. Chemical structure and absorption, emission spectra of MPTS in water.

2.5.1. Wobbling in Cone Model (WIC) Analysis of Fluorescence Anisotropy Decay

The bi-exponential behavior of the rotational anisotropy may arise from the "Wobbling-in-cone" motion frequently observed inside micelles or reverse micelle.[223-224] According to the model, the fluorescence anisotropy of a fluorophore may be affected by three independent motions: wobbling of the fluorophore (time constant τ_W), translation diffusion of the fluorophore along the surface of the micelle (time constant τ_D) and the overall rotation of the micelle (time constant τ_M). Since the global motion of the micelle (especially true for large micelles) is much slower than the other two time constants, the contribution of this motion can be ignored. Since the observed anisotropy decay, r(t), may arise from three independent motions, we can write

$$r(t) = r_W(t) r_D(t) r_M(t) \qquad (2.24)$$

According to biexponential data fitting, r(t) can be expressed as

$$r(t) = r_0 \left[\beta \ \exp\left(-\frac{t}{\tau_s}\right) + (1-\beta) \exp\left(-\frac{t}{\tau_f}\right)\right] \qquad (2.25)$$

r(t) may also be represented in terms of order parameter S

$$r(t) = r_0 \left[S^2 + (1 - S^2) \exp\left(-\frac{t}{\tau_W}\right)\right] \exp\left(-t\left(\frac{1}{\tau_D} + \frac{1}{\tau_M}\right)\right) \qquad (2.26)$$

S is related to semicone angle θ as

$$S = \frac{1}{2} \cos\theta (1 + \cos\theta) \qquad (2.27)$$

The time constant (τ_M) of the overall motion of the micelle is given by

$$\tau_M = 4\pi\eta r_h^3 / 3k_B T \qquad (2.28)$$

Where η = viscosity of the solution and r_h is the hydrodynamic radius of the micelle, here, we ignore the τ_M since the overall motion of the micelle is much slower than the other two motions. Comparing equations (2.21) and (2.22), we obtained

$$\beta = S^2 \qquad (2.29)$$

$$\frac{1}{\tau_f} = \frac{1}{\tau_W} + \frac{1}{\tau_D} \qquad (2.30)$$

$$\frac{1}{\tau_S} = \frac{1}{\tau_D} \qquad (2.31)$$

2.6. Dynamic Light Scattering Measurements

The dynamic light scattering method is instrumental in measuring the particle size in the solution phase. We have performed the dynamic light scattering measurement in the Malvern Nano ZS90 instrument to measure micellar and mixed micellar assembly size. The instrument is equipped with He-Ne LASER (= 632.8 nm) as the light source. The scattering was collected at a fixed angle of 90° with respect to the source light direction. Before all experiments, the solutions were filtered with PTFE syringe filters (pore size 0.2 µm). The temperature was fixed at 298K for all experiments.

2.7. Isothermal Titration Calorimetry

Isothermal titration calorimetry (ITC) is an essential procedure for measuring minute heat change due to interaction between molecules like ligand-protein and surfactant-polymers. From ITC, the change in enthalpy (ΔH), entropy (ΔS), Gibb's free energy (ΔG), and binding constant can be obtained. A Nano-ITC instrument (Microcal) was used for isothermal titration calorimetry to determine mixed assembly formation thermodynamic parameters. The temperature was fixed at 298 K during the titration. All the solutions were filtered using PTFE syringe filters of 0.2 µm before titration. Thirty-nine aliquots of solution (1 µl for each injection) were injected from a syringe (rotating 200 rpm), keeping an interval of 120s into the ITC sample chamber. The data were fitted to a curve by a sequential binding model using software provided by Microcal. We also conduct control experiments to eliminate the heat of dilution.

2.8. Field Emission Transmission Electron Microscope (FETEM)

Field-emission transmission electron microscope (FETEM) is one of the best microscopic imaging techniques to measure and characterize particles of nm sizes in the dried condition. The FETEM images were done by JEOL JEM 2100 with an operating voltage of 200 kV. Samples were prepared by drop-casting on a carbon-coated copper grid (300 mesh Cu grid with thick carbon coating) and dried in a desiccator.

2.9. Materials Used

8 hydroxypyrene-1,3,6-trisulfonic acid trisodium salt (HPTS), 8-methoxypyrene-1,3,6 trisulfonate (MPTS), Pluronic triblock copolymer F127, dodecyl trimethylammonium bromide (DTAB, 98%), tetradecyltrimethylammonium bromide (TTAB, 98%), cetyltrimethylammonium bromide (CTAB, 98%), N-dodecyl-N, N dimethyl-3-ammonio-1 propane sulphonate (SB12, 99%), sodium dodecyl sulfate (SDS, 99%),

poly(diallyl dimethylammonium chloride) solution (PDADMAC, 35%, molecular weight~100000), *L*- ascorbic acid, gold (III) chloride hydrate ($HAuCl_4$, xH_2O), silver nitrate ($AgNO_3$,99.99%). sodium chloride (NaCl, ≥ 99%), calcium chloride ($CaCl_2$ ≥ 93%), and aluminum chloride ($AlCl_3$, 99%) were purchased from Sigma Aldrich Chemicals. Sodium borohydride ($NaBH_4$, ≥ 95%) and hydrochloric acid (HCl) were purchased from Merck Chemicals.

All chemicals were used as received without further purification. Ultrapure Milli-Q water (resistivity 18.2 MΩ cm) was used to prepare all solutions.

2.10. Sample Preparation Procedure

All the surfactants and copolymers are fully soluble in water, and a clear homogeneous solution was prepared within the concentration range in our experiments. F127 solutions at different concentrations were prepared by adding the requisite amount of copolymer to water. The surfactants (DTAB, TTAB, CTAB, SB12, SDS, PDADMAC) solutions were also prepared by weighing the exact amount and mixing them with water. The copolymer and surfactant solutions were allowed to equilibrate for ~4 hours to ensure proper dissolution before any measurement.

The concentration of HPTS and MPTS in the solutions was at ~ 4 µM. We selectively chose low dye concentration to avoid partitioning the probe among micelles and bulk solvent.

A 50 mM stock solution of $HAuCl_4$ was prepared and kept at 4 °C temperature for further use. Silver nitrate, ascorbic acid, sodium borohydride, sodium chloride, calcium chloride, and aluminum chloride solutions were prepared by weighing the exact amount to water freshly.

Chapter 3

Anomalous Variation of Excited-State Proton Transfer Dynamics inside a Triblock Copolymer−Cationic Surfactant Mixed Micelle[#]

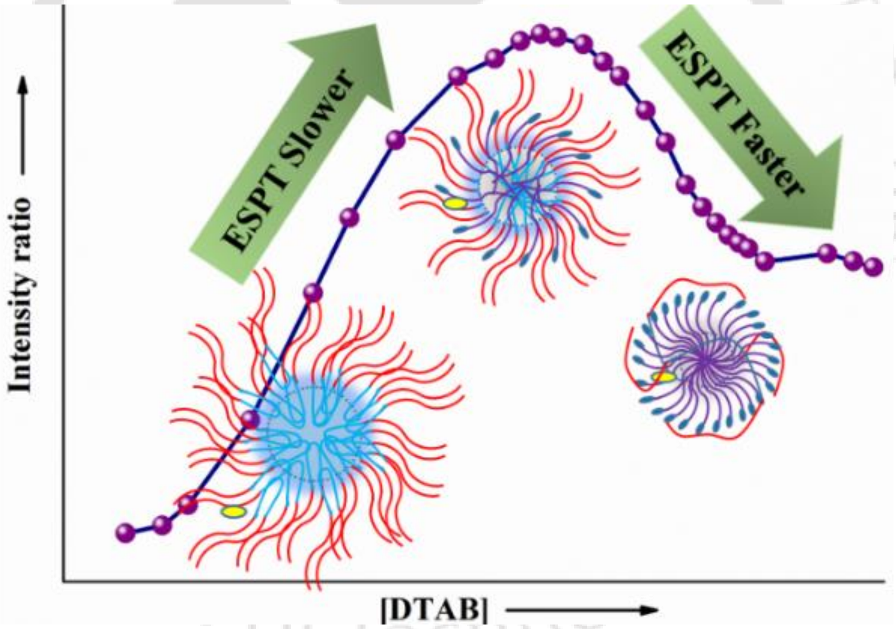

[#] This work has been published in *J. Phys. Chem. B 2019, 123, 40, 8559-8568.*

Chapter 3: Anomalous Variation of Excited-State Proton Transfer Dynamics inside a Triblock Copolymer−Cationic Surfactant Mixed Micelle[69]

3.1. Introduction

Pluronics are often used in combination with conventional ionic surfactants.[225] These mixed surfactant assemblies can be more efficient than the individual copolymer or surfactant micelle. It is crucial to elucidate the molecular models of these mixed assemblies, which may help to improve their chemical applications. Various models have already been proposed based on the scientific insights obtained from various investigations.[15, 226-227] Nevertheless, molecular-level understanding of the organization of surfactants in these mixed assemblies at various compositions remains inadequate.

HPTS has already been employed to investigate Pluronic-surfactant mixed micelles.[213, 216] The location of the photoacid and corresponding ESPT dynamics inside the mixed micelles depend markedly on the nature of the surfactant charge and hydration. It was proposed that the alkyl chains of the surfactants prefer to stay within the hydrophobic PPO core.[228] At the same time, ionic headgroups form a layer of respective charges (positive or negative) at the interface of the core and corona. Thus, the anionic HPTS may be pushed out of the core in the anionic surfactant-Pluronic mixed micelle to a less hindered and more hydrated region conducive to ESPT; for the cationic one, it will be the opposite.

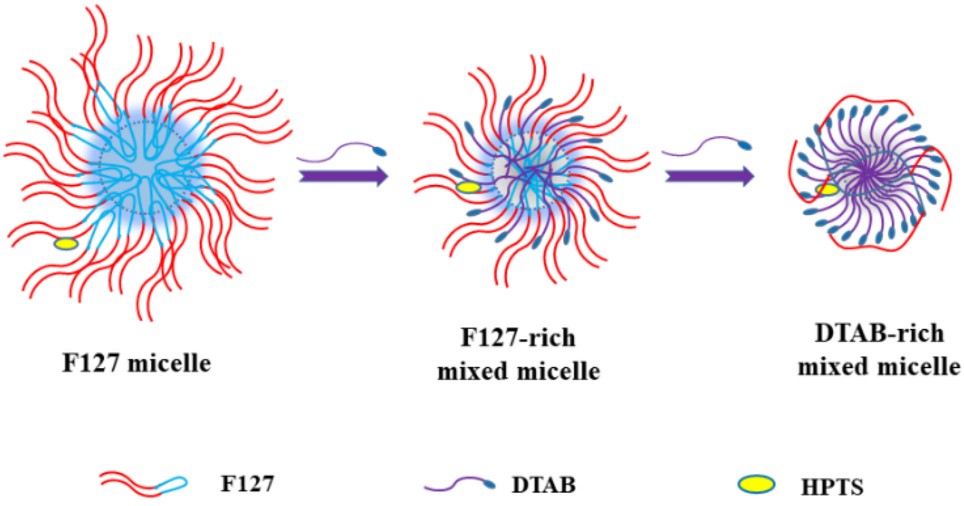

Scheme 3.1. Schematic representation of F127-DTAB aggregation modulated ESPT, a correlation between structure and dynamics.

Migration of polar fluorophore within a mixed Pluronic-ionic surfactant mixed micelle has been reported for other fluorophores as well.[229-230]

Those investigations, although quite informative, have not reported a total composition variation of the Pluronic-surfactant assembly. Moreover, in those studies, ESPT dynamics were extracted directly from single/double wavelength emission transients, which is often complicated by the overlap of the protonated and deprotonated emission bands. So based on ratiometric overlap-corrected time-resolved area-normalized spectra (TRANES)[231-233] method, this chapter presented a more quantitative account of the ESPT dynamics of HPTS inside F127-DTAB mixed micelle over a wide range of DTAB concentrations (Scheme 3.1).

3.2. Results and Discussion

3.2.1. Steady-State Spectroscopy. The absorption spectrum of HPTS remained almost the same in water and inside the F127-DTAB surfactant assembly with the absorption maxima (λ_{max}^{abs}) at 403 nm and 405 nm, respectively. In water, HPTS showed a strong emission band centered at 510 nm, characteristic of the deprotonated form (RO^-), and a feeble emission band at 440 nm representing the protonated form (ROH). The intensity ratio of the bands (ROH/RO^-) was only ~ 0.05. In an aqueous solution of 4.0 mM F127, HPTS exhibited emission bands at the same position, but the ROH/RO^- ratio significantly increased to~ 0.15 (Figure 3.1). The higher ratio indicates that ESPT dynamics was retarded to some extent inside the F127 micelle. Note that the concentration of F127 used here was higher than the CMC (0.56 mM)[234-235] of F127 at 25 °C. Thus, the micellar confinement of F127 has a significant role in slowing down the ESPT dynamics.

However, the addition of DTAB to 4.0 mM F127 solution strongly affects the emission spectrum of HPTS depending on the concentration of DTAB. According to the nature of variation, four different regimes were evident (Figure 3.1 and Figure 3.2). In the low concentration range (0.1-6 mM), the protonated emission band gradually increased with a concomitant decrease of the deprotonated band (Figure 3.1a).

Thus, the emission intensity ratio in this concentration range increased steadily with an increase in the concentration of DTAB (Figure 3.2). However, at an intermediate concentration range (6-16 mM), there was hardly any change in the emission intensity of the two bands (Figure 3.1b), and thus, the ratio almost remained the same (Figure 3.2).

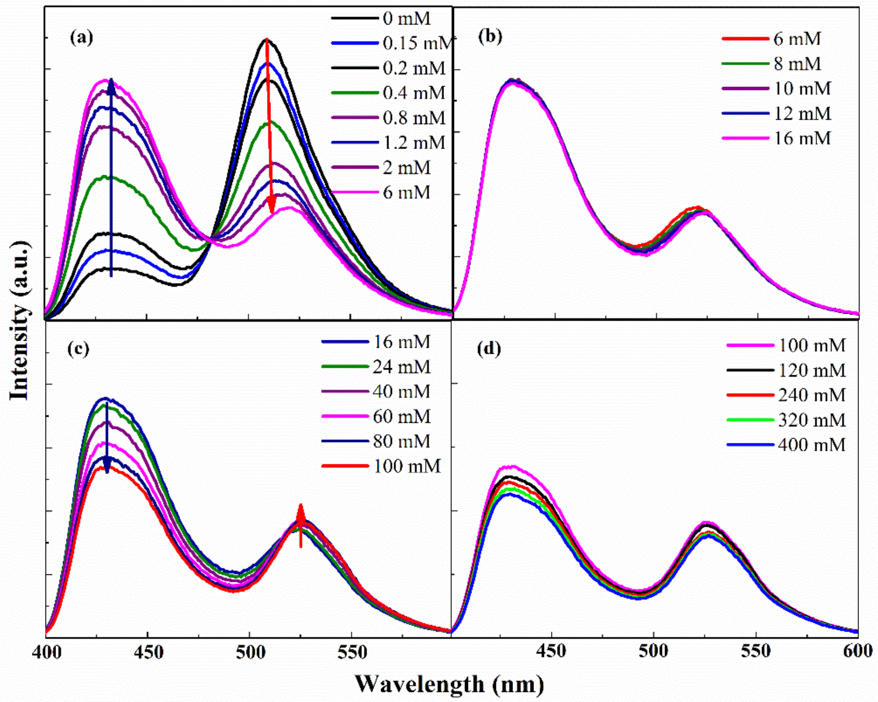

Figure 3.1. Emission spectra of HPTS inside F127-DTAB mixed micelle at various concentrations of DTAB. For convenience, the spectra are grouped into four regions (a) 0-6 mM, (b) 6-16 mM, (c)16-100 mM, and (d)100-400 mM.

Upon further increase of the DTAB concentration (16-100 mM), the emission contribution of the protonated form instead decreased, and that of the deprotonated form increased (Figure 3.1c). Thus, the ratio eventually decreased with increasing DTAB concentration in this range (Figure 3.2). At very high concentrations (100-400 mM), there was hardly any change in the emission spectra (Figure 3.1d) or emission intensity ratio (Figure 3.2).

The most striking observation was that the intensity ratio of the two forms varied unusually with the increase in cationic surfactant concentration in the mixed micelle. Since the emission intensity ratio is linked to ESPT dynamics, it implied that the ESPT dynamics might also be modulated in an unusual way, which will be confirmed through time-resolved measurements.

In an aqueous solution of DTAB (in the absence of F127), the emission intensity of HPTS was severely quenched at a low concentration of DTAB due to HPTS-DTAB complex formation.[236] However, the HPTS-DTAB complex dissolved at higher DTAB concentrations, and HPTS may partition into DTAB micelles. The emission intensity ratio was low in the premicellar region but increased after CMC (16 mM) of DTAB. The protonated and deprotonated bands were almost equally intense in the post-micellar region (Figure 3.2).[236]

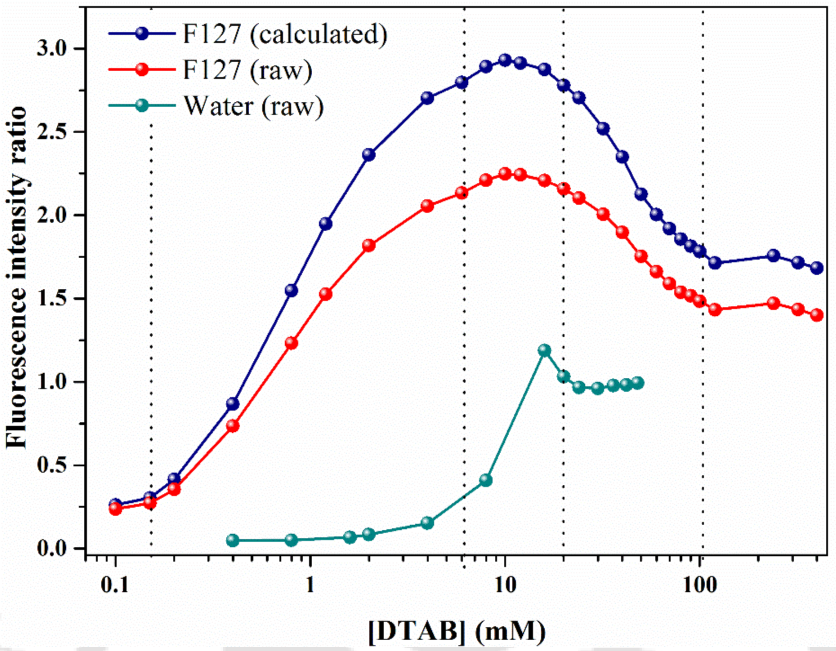

Figure 3.2. Emission intensity ratio (ROH/RO) in the F127-DTAB mixed micelle ([F127] = 4 mM), water at different concentrations of DTAB.

Moreover, there was also a noticeable shift in the emission maxima (λ_{em}^{max}), particularly for the deprotonated band with the DTAB concentration variation. In the low concentration range (0-6 mM), the shift was quite noticeable from 510 nm in pure F127 micelle to 520 nm in the presence of 6 mM DTAB. In the intermediate concentration (6-16 mM), λ_{em}^{max} also underwent shifting but much less steadily from 520 nm at 6 mM DTAB to 525 nm at 16 mM DTAB. After that, the emission maximum showed only a marginal shift with an increase in the DTAB concentration. At very high DTAB concentration (400 mM), λ_{em}^{max} was at 527 nm in the mixed micelle, which matched precisely with λ_{em}^{max} in neat DTAB micelle.[69] The deprotonated emission band often shows a significant red-shift when HPTS resides in a cationic environment, e.g., inside cationic micelles [187, 231] and reverse micelles[206, 237-238]. Although the origin of the red shift is not precisely known, it is probably due to a cation-π interaction between the cationic head group of surfactant and the aromatic ring of HPTS.[238] Thus, the extent of red-shift could be proportional to the positive charge of the microenvironment sensed by HPTS.

3.2.2. Steady-State Anisotropy. We measured the steady-state anisotropy (r_{SS}) of MPTS instead of HPTS to avoid a possible error due to the ESPT dynamics on the fluorescence anisotropy (Chapter 2). Interestingly, we also observed an unusual variation of r_{ss} with the DTAB concentration in the F127-DTAB mixed micelle. r_{ss} increased gradually with an increase in the DTAB concentration at the low concentration range (0-2 mM), remained steady at an intermediate concentration range (2-12 mM), and decreased steadily after that upon further increase of the DTAB concentration (12-100 mM) (Figure 3.3). Thus, the steady-state anisotropy almost followed the same unusual trend as that of the emission intensity ratio of HPTS (Figure 3.2). Note that the emission intensity ratio generally depicts the favorability of the ESPT process. In contrast, steady-state anisotropy indicated the local rigidity or the confinement experienced by the probe. Since both the parameters (intensity ratio and steady-state anisotropy) modulated similarly with the DTAB concentration, we may conclude that the overall arrangement of the mixed micelle and the rigidity vary unusually with the composition of the mixed micelle.

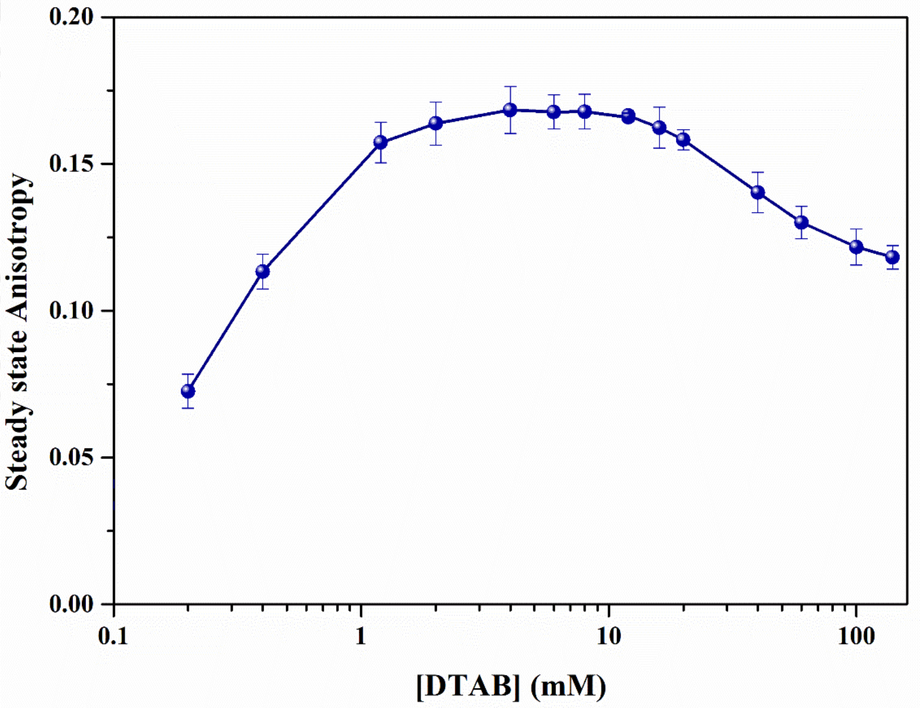

Figure 3.3. Steady-state anisotropy of MPTS inside F127-DTAB mixed micelle at varying DTAB concentration in the F127-DTAB mixed micelle (λ_{em} = 440 nm). The concentration of F127 was 4 mM.

3.2.3. Time-Resolved Fluorescence Anisotropy Decay. Fluorescence anisotropy decay of MPTS exhibits a monoexponential decay with a rotational time of 150 ps in bulk water (Table 3.1). In F127 micelle, the observed rotational relaxation time constants were 220 ps (62%) and 920 ps (38%) with an average time constant ($<\tau_r>$) of 490 ps (Table

3.1). The bi-exponential rotational anisotropy may arise from the "Wobbling-in-Cone" (Chapter 2) motion frequently observed inside micelles or reverse micelle.[223-224] The analyzed parameters are summarized in Table 3.1.

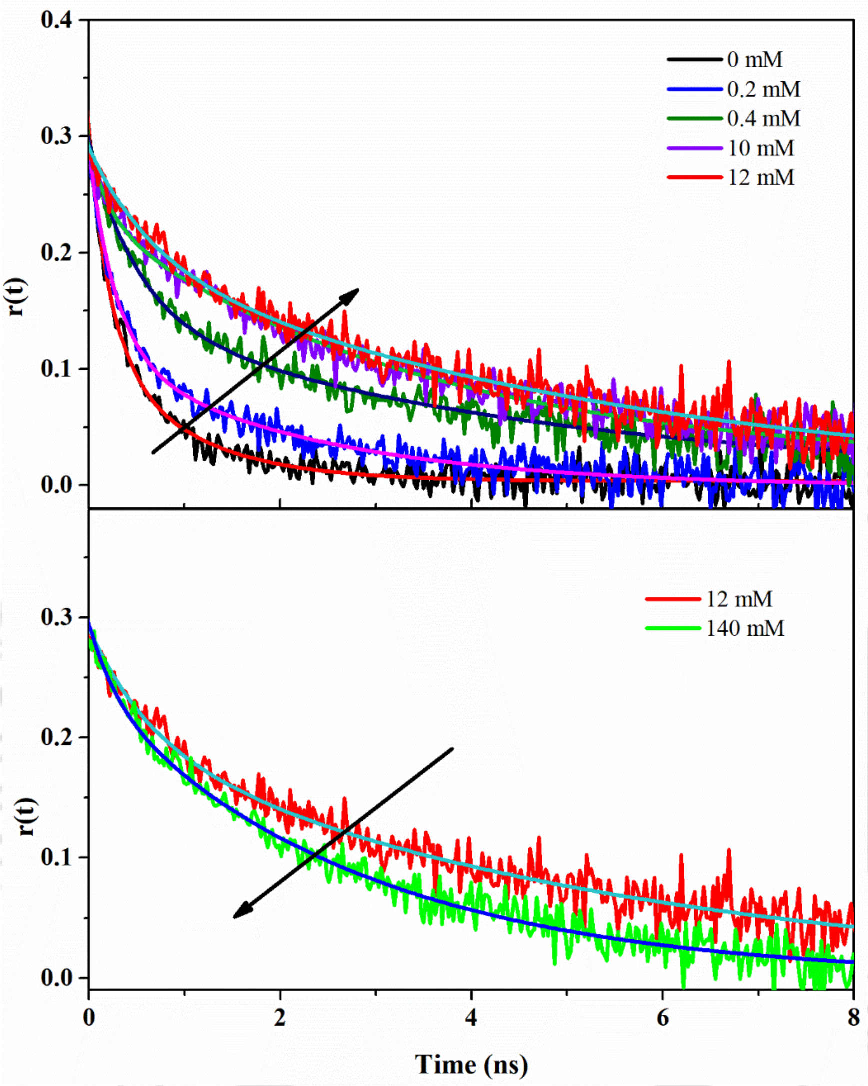

Figure 3.4. Time-resolved fluorescence anisotropy (λ_{em} = 440 nm) of MPTS inside F127-DTAB mixed micelle at different concentrations of DTAB.

Comparing surfactant concentration variation of the r_{ss} at sub-micellar (0.4 mM) vs. post-micellar (4 mM) F127 concentrations is interesting. For the sub-micellar case, the maximum value (0.14) of r_{ss} was much lower, and the peak was relatively sharper compared to the micellar case.[69] Thus, the mixed assemblies may be more labile and more manageable to reorganize by surfactant variation at sub-micellar concentrations than the post-micellar case.[69] At a higher concentration of F127, since the initial micelle was quite large, more surfactant may be needed to induce a structural reorganization in the F127-surfactant assembly.

In the F127-DTAB mixed micellar assembly, the fluorescence anisotropy decay can also be ascribed by a biexponential decay (chapter 2, equation 2.23) at all concentrations of DTAB (Figure 3.4), and the average rotational time varied in a similar anomalous manner with the DTAB concentration, as mentioned earlier, for the emission intensity ratio and steady-state anisotropy (Figure 3.4 and Table 3.1). The $<\tau_r>$ first increased gradually up to 12 mM DTAB and, then decreased with a further increase in the DTAB concentration. A similar anomalous trend was also evident from the variation of other rotational time constants τ_D (= τ_s) and τ_W. All these trends indicated that the rotational motion was gradually retarded up to an intermediate DTAB concentration (12 mM). After that, it became slightly faster with the addition of more DTAB. The semicone angle (θ°) decreased steadily from 44° in the F127 micelle up to 28° inside the mixed micelle containing 12 mM DTAB, manifesting that the probe was in a compact environment, unable to rotate freely. The semicone angle remained almost the same at higher DTAB concentrations. Interestingly, the semicone angle inside the neat DTAB micelle matched that of the mixed micelle at a high DTAB concentration, indicating a similarity in assembly properties.

Table 3.1. Fluorescence anisotropy decay parameters of MPTS in different systems (λ_{ex} = 375, λ_{em} = 440 nm). Error in the data ~ ±3%.

System	r_0	β	τ_f **(ps)**	τ_s **(ps)**	τ_w **(ps)**	$<\tau>^{\S}$ **(ps)**	**θ (deg)**
Water	0.4	-	150	-	-	-	-
4 mM F127	0.34	0.38	220	920	280	490	44
4 mM F127 + 0.2 mM DTAB	0.32	0.37	280	2200	320	990	44
4 mM F127 + 0.4 mM DTAB	0.30	0.52	340	2390	390	1410	36
4 mM F127 + 10 mM DTAB	0.32	0.67	350	4280	400	3000	29
4 mM F127 + 12 mM DTAB	0.31	0.68	460	4500	520	3200	28
4 mM F127 + 20 mM DTAB	0.30	0.72	390	3390	440	2550	26
4 mM F127 + 140 mM DTAB	0.35	0.72	200	2680	220	1990	27
24 mM DTAB	0.37	0.7	260	2300	290	1690	27

§ $<\tau> = \beta \times \tau_s + (1-\beta)\tau_f$

3.2.4. ESPT Dynamics in the F127-DTAB Mixed Micelles. The emission intensity ratio obtained from the TRANES can be fitted nicely with the help of equation (2.17) (Chapter 2) in F127 micelle and the presence of a low concentration of DTAB (≤ 0.5

mM) (Figure 3.5 and Table 3.2). However, in the mixed micelle at a higher concentration of DTAB or in the DTAB micelle alone, equation (2.21) (Chapter 2) was sufficient to describe the ESPT dynamics. Thus, the ESPT scheme may be switching with a change in the microenvironment around HPTS. Inside the F127 micelle and in the presence of low DTAB concentration, the ESPT scheme follows the Eigen-Weller nature (Scheme 1.6, Chapter 1). In contrast, the scheme shows irreversible behavior at higher concentrations of DTAB or inside the DTAB micelle (Scheme 1.7, Chapter 1). Although we reported this simple irreversible ESPT in cationic micelle earlier,[231] it was the first instance where switching between the ESPT mechanisms occurred with the variation of composition in a mixed micelle. We also noted that the deprotonation time varied anomalously with the increased DTAB concentration in the mixed micelle (Table 3.2).

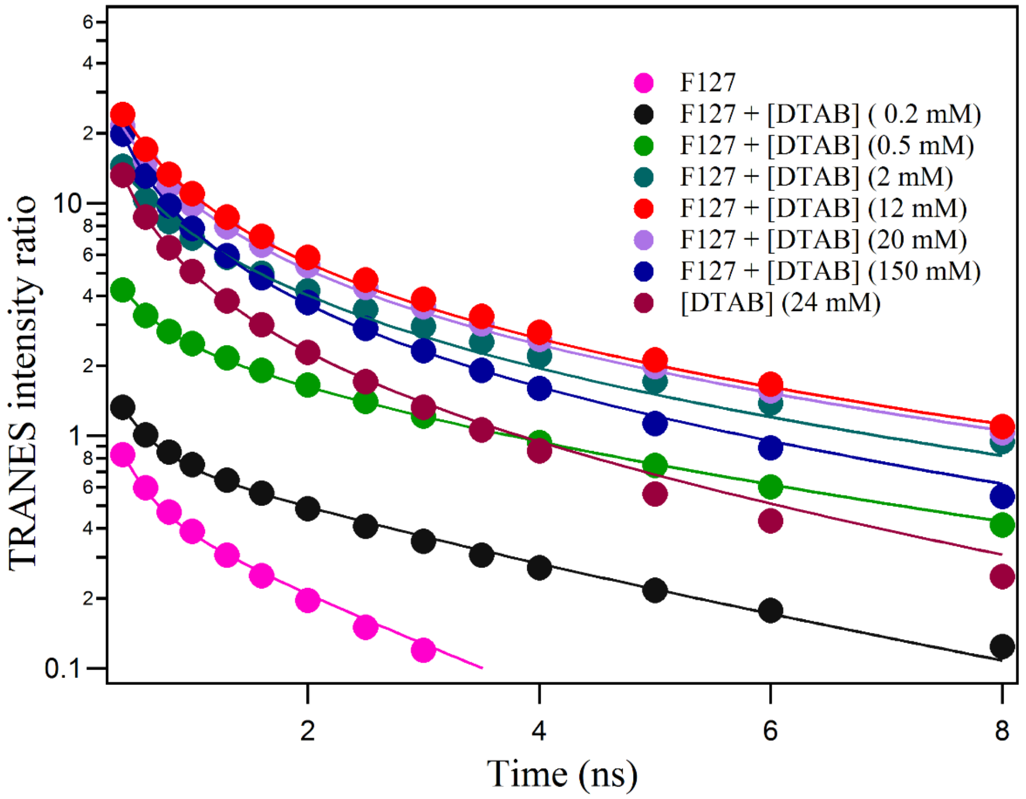

Figure 3.5. TRANES intensity ratio of HPTS inside F127 (4 mM)-DTAB mixed micelle at different DTAB concentrations and inside neat DTAB (24 mM).

The deprotonation time was moderately slower inside the F127 micelle (τ_d = 0.41 ns) compared to that in water (τ_d = 0.15 ns). The moderately favorable ESPT implied a significant hydration level inside the F127 micelle. On the other hand, the emission spectrum of HPTS was strongly modulated inside the DTAB micelle, and the deprotonation time (τ_d = 5.5 ns) was much slower compared to the F127 micelle (τ_d =

0.41 ns). Thus, one might expect that adding DTAB could slow down the ESPT dynamics in the mixed micelle. However, the variation was not gradual but anomalous. The deprotonation time became gradually slower with an increase in the DTAB concentration and reached a maximum of 8-12 mM DTAB. After that, the deprotonation time decreased with increased DTAB concentration. The deprotonation time (τ_d = 12.7 ns) inside the mixed micelle at this optimum concentration was more than two times slower compared to τ_d (5.5 ns) inside the DTAB micelle. The most restricted ESPT dynamics at the intermediate DTAB concentration (8-12 mM) implied that the assembly was least hydrated at this composition. Another notable observation was that the deprotonation time at a very high concentration of DTAB (150 mM) was significantly slower than the deprotonation time in the DTAB micelle (Table 3.2). The rate constants of respective excited state processes are directly correlated to the time constants, i.e., the larger deprotonation time indicates the slower deprotonation kinetics and vice versa. The reason for slower deprotonation kinetics in crowdedness is the non-labile water structure or hydrogen bonding in the respective micellar aggregates.

Table 3.2. Different time constants of ESPT of HPTS inside F127 micelle (4 mM F127), F127-DTAB mixed micelles (4 mM F127 and different concentrations of DTAB) and DTAB micelle (24 mM DTAB). Error in the data ~ ± 3%.

System	**a_1**	**a_2**	**τ_1(ns)**	**τ_2(ns)**	**τ_d(ns)**	**τ_r(ns)**	**τ_{diff}(ns)**
F127 micelle	0.58	0.42	0.26	2.40	0.41	1.51	0.85
F127 + 0.2 mM DTAB	0.46	0.54	0.31	4.90	0.63	2.40	0.70
F127 + 0.5 mM DTAB	0.18	0.82	0.40	8.30	1.83	1.81	0.66
F127 + 2 mM DTAB	1.00	-	10.45	-	10.45	-	-
F127 + 12 mM DTAB	1.00	-	12.70	-	12.70	-	-
F127 + 20 mM DTAB	1.00	-	12.20	-	12.20	-	-
F127 + 150 mM DTAB	1.00	-	8.40	-	8.40	-	-
DTAB micelle	1.00	-	5.50	-	5.50	-	-

3.2.5. Dynamic Light Scattering (DLS). The hydrodynamic diameter of the F127 micelle and the F127-DTAB mixed micelles was measured at different concentrations of

DTAB. In 4.0 mM of F127, a strong peak appeared in the intensity distribution centered at 37 nm, accompanied by a small 4-5 nm peak.[69] The more substantial peak was characteristic of the F127 micelle. As reported earlier, the tiny peak may be due to the monomeric copolymer or small aggregates formed by the association of a few F127 units.[66] The diameter of the mixed micelle decreased with the increase in DTAB concentration, but the variation was biphasic (Figure 3.6). At the low DTAB concentration range, the size of the mixed micelle decreased steeply, but after ~20 mM, the decrease was minimal (Figure 3.6). The low and high-concentration ranges underwent a linear fit with very different slopes (Figure 3.6). Thus, the mixed micelle may exist in two different types at the low and high DTAB contents. The hydrodynamic diameter variation indicated DTAB insertion to the F127 micelle and expulsion of F127 occur in a gradual manner. Although the sizes of the mixed assembly containing very high DTAB and the neat DTAB micelle were almost the same, the hydration levels experienced by HPTS in the two systems were quite different.

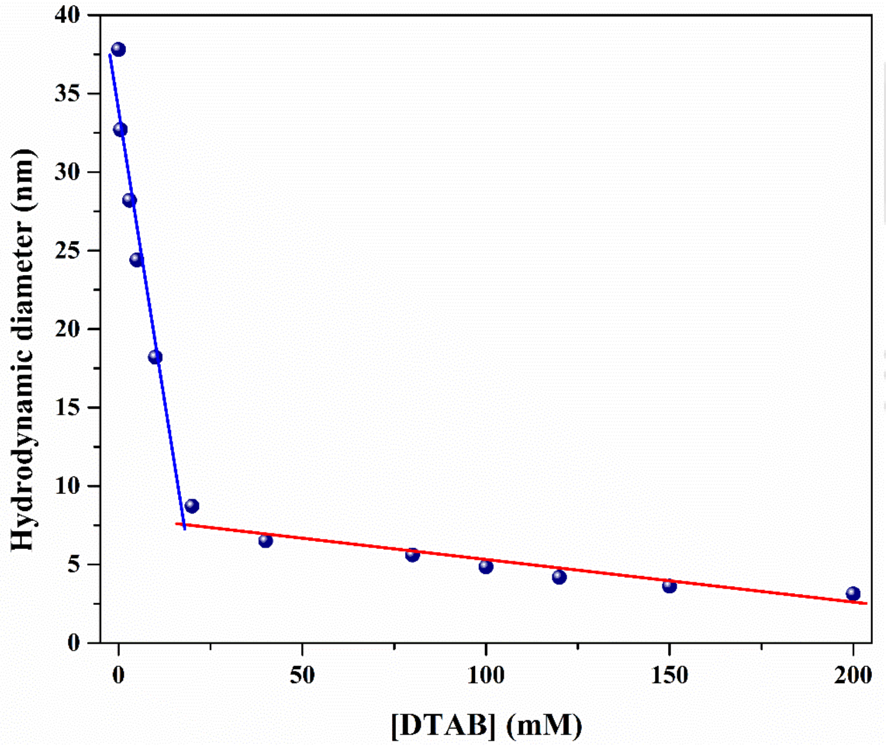

Figure 3.6. Hydrodynamic diameters of the F127-DTAB mixed micelles at different concentrations of DTAB. The blue and red lines represent linear fits at the low and high DTAB concentration regions.

3.2.6. Zeta (ζ) Potential. ζ-potential measurements are often helpful to elucidate the charge state of a supramolecular assembly. The ζ-potential of the F127 micelle was meager (0.01 mV), characteristics of a neutral micelle. The ζ-potential of DTAB micelle was determined to be 57.5±2.5 mV. Adding DTAB surfactant to the F127 micelle led to a gradual increase of the zeta potential, which supported the incorporation of DTAB surfactant into the mixed assembly (Figure 3.7). The ζ-potential varied moderately at low DTAB concentrations but more remarkably in the high-concentration region. Thus, ζ-potential variation also indicated that the nature of the mixed assembly could be distinctly different at low and high DTAB concentrations. Another important observation was that the ζ-potential of the mixed micelle, even at a very high concentration of DTAB, was much lower than that of the DTAB micelle. A similar trend was also reported for the P123-SDS mixed micelle, where the ζ-potential of the mixed assembly (-50 mV) at a high SDS concentration was much lower in magnitude than the SDS micelle (-80 mV) alone.[229] The development of low ζ-potential in the mixed micelle was attributed to negative charges deep inside the mixed assembly (away from the surface).[239] Note that measurement of ζ-potential beyond 100 mM of DTAB was difficult due to oxidation of bromide ion on the electrode creating colored (brownish pink) solution.[240]

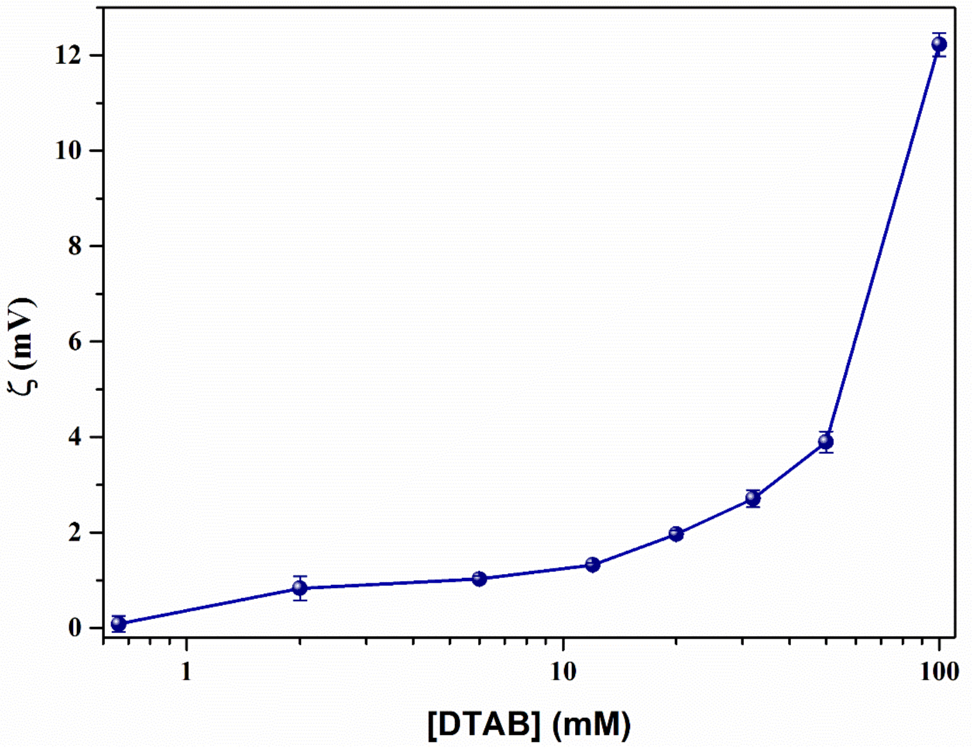

Figure 3.7. Variation of ζ potential with increasing DTAB concentration in F127(4 mM) medium.

3.3. Summary and Conclusions

The chapter 3 revealed that the nature of F127-DTAB mixed micellar assembly was distinctly different at low and high concentrations of DTAB. Both the structural parameters (size and ζ-potential) and dynamical parameters (ESPT of HPTS and rotational dynamics of MPTS) followed unusual trends. We proposed that there could be a drastic change in the organization of the micelle at low and high concentrations. The synergistic retardation of the dynamics at the intermediate concentration (~12 mM) may imply that the mixed micelle at this composition can be a superior surfactant assembly to their respective micelles. The mixed assembly may be helpful in drug delivery and template for nanostructure synthesis.

Chapter 4

Sub-Micellar Triblock Copolymer-Cationic Surfactant Aggregate Assisted Gold Nanostructure Synthesis: A Photophysical Investigation[#]

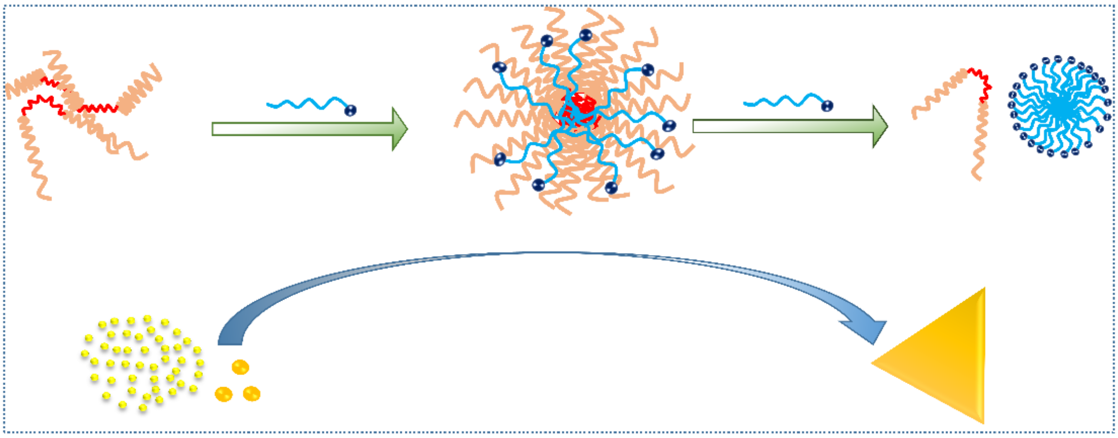

[#] This work has been published in *Journal of Photochemistry and Photobiology 8 (2021) 100066.*

Chapter 4: Sub-Micellar Triblock Copolymer-Cationic Surfactant Aggregate Assisted Gold Nanostructure Synthesis: A Photophysical Investigation[184]

4.1. Introduction

The tunability of surface plasmon resonance (SPR) of anisotropic gold/silver nanomaterials over visible to the near-infrared (NIR) region has triggered many applications, including surface-enhanced Raman scattering (SERS)[241-242], sensing[243], photothermal therapy[244], and drug delivery.[245] The plasmonic properties of these anisotropic nanostructures significantly depend on their shapes, sizes, and morphologies. Various synthesis methods have been prescribed, like biochemical,[246] wet chemical,[247] and photochemical synthesis.[248] In most synthetic procedures, surfactants are often used at significantly high concentrations.[249-250] Surfactant assemblies serve as shape-directing templates, help in dispersing subsequent nanostructures in aqueous media and prevent unwanted aggregation.[251] The size, shape, and charge of the surfactant assemblies are crucial, especially for anisotropic nanostructure synthesis. For example, a high concentration (orders of magnitude higher than the CMC) of the cationic surfactant CTAB is used in gold nanorod synthesis.[252-253] The surfactant assembly may undergo reorganization during the synthesis process and finally breaks down to a bilayer on the surface of a mature nanostructure.[14] However, the use of excessive surfactants in these assemblies is detrimental to biological and medical applications. Herein, we optimized the size and interfacial packing of a sub-micellar aggregate of a triblock copolymer F127, and several cationic alkyl trimethylammonium surfactants at low concentrations and demonstrated the feasibility of the mixed assembly in synthesizing gold nano-triangles.

4.2. Results and Discussion

4.2.1. Steady-State Spectroscopy: As discussed in chapter 3, HPTS emission spectrum has a very weak protonated (ROH) band at ~430 nm and a strong deprotonated band (RO^-) at 510 nm, with the ROH/RO^- band ratio of 0.05. In the presence of a sub-micellar (0.4 mM) concentration of F127 (cmc 0.056 mM), the protonated band emission intensity increased slightly, and ROH/RO^- ratio rose to~ 0.1. However, the protonated band's increment was lesser in the sub-micellar solution than in the post-micellar (4 mM), indicating that the ESPT process may be retarded to some extent in the sub-micellar concentration.

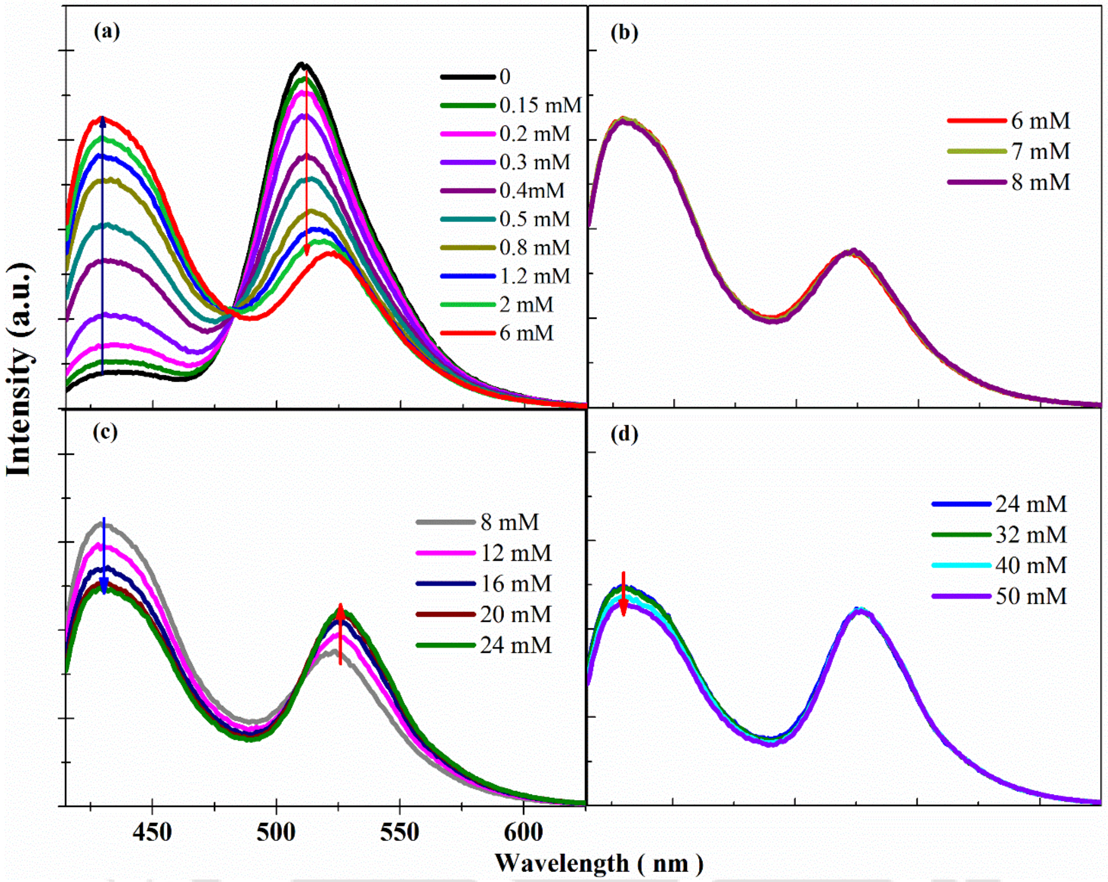

Figure 4.1. Emission spectra of HPTS (λ_{ex} = 375 nm) in F127 (0.4 mM) with gradual increasing of DTAB concentration - (a) 0-6 mM; (b) 6-8 mM;(c) 8-24 mM and (d) 24-50 mM. Fluorescence modulation is quite different at different concentration ranges.

The fluorescence spectrum of HPTS modulated significantly upon the addition of DTAB to the sub-micellar (0.4 mM) F127 solution above a specific concentration (~0.15 mM). The protonated emission intensity increased gradually with a concomitant decrease of the deprotonated emission band up to ~6 mM DTAB (Figure 4.1a). At this concentration, the intensity ratio (ROH/RO$^-$) reached a maximum value of 1.86, 37 times higher than in water. Since the emission intensity ratio manifested the ESPT retardation, we may infer that the ESPT was slowest at this composition. The emission spectrum remained unchanged within a slight DTAB concentration variation (6-8 mM, Figure 4.1b). However, at higher DTAB concentrations (8-20 mM), the protonated band intensity somewhat decreased with a concomitant increase of the deprotonated band, resulting in a lower intensity ratio (Figure 4.1c). At a very high concentration (>20 mM), the emission spectrum almost became invariant to the DTAB concentration (Figure 1d).

We obtained three obvious transition points from the intensity ratio vs. DTAB concentration plot (Figure 4.2a). The first transition point (T_1) at ~0.15 mM DTAB depicted the onset of the mixed assembly formation. The ratio reached a maximum defining the second transition point (T_2) at ~6 mM. Both these transition points were significantly lower than the critical micellar concentration (CMC, 16 mM) of DTAB. The ratio decreased upon further addition of DTAB up to ~20 mM (T_3). The results indicated that DTAB strongly interacts with the sub-micellar copolymer and forms self-assembly, which continually reorganizes depending on the DTAB concentration. The transition points indicating fluorescence modulation depend markedly on the initial concentration of F127 (Figure 4.2b).

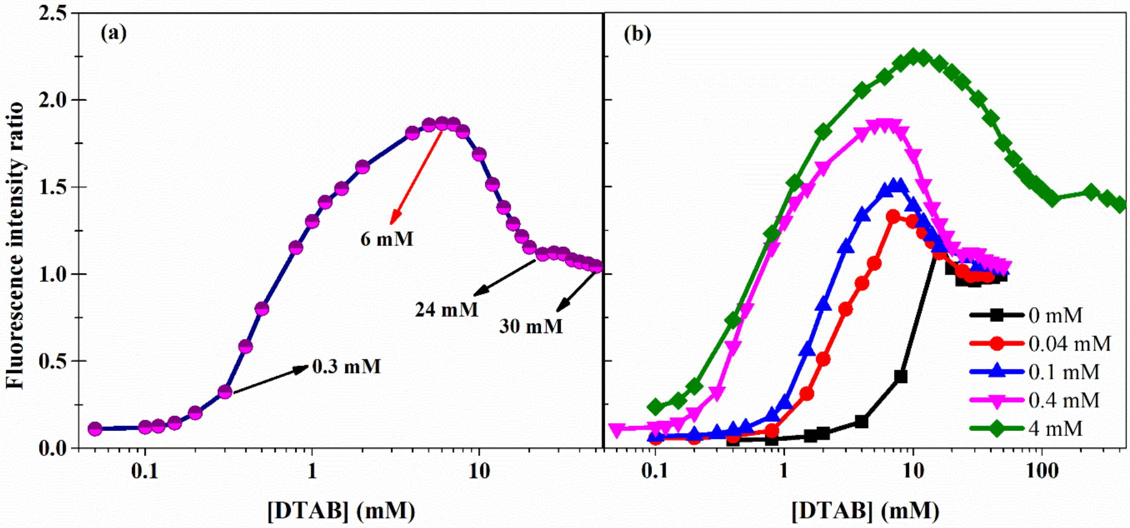

Figure 4.2. The ratio of the protonated and deprotonated emission intensities of HPTS in the presence of (a) a fixed sub-micellar (0.4 mM) concentration of F127 and (b) variable initial concentrations of F127 (0 mM to 4 mM, F127) with increasing DTAB concentration.

The emission maximum of the deprotonated band underwent a gradual red-shift from 512 nm to 527 nm upon the addition of DTAB to an aqueous F127 solution.[184] Since the deprotonated emission band of HPTS often displays a red shift in cationic assemblies (e.g., micelle and reverse micelle), the shift may suggest a gradual increase of cationic environment in the assembly (around the anionic probe HPTS). The total amount of DTAB-induced emission shift was similar at different initial F127 concentrations. However, the increment steepness and the minimum amount of DTAB needed to result in a noticeable shift varied appreciably with the initial F127 concentration. In the case of micellar (4mM) F127, DTAB-rich assembly forms only at high concentrations,[69] but in the case of sub-micellar (0.4 mM) F127, DTAB interacts very strongly to form DTAB-enriched assembly at a much lower concentration, and hence the shift saturates at a much lower concentration in case of premicellar aggregate.[184]

In addition to DTAB (C_{12}), we also used the surfactants TTAB (C_{14}) and CTAB (C_{16}), homologs with higher chain lengths. The fluorescence intensity ratio follows a similar pattern, but the transition points vary from surfactant to surfactant. Longer chain length surfactant shifts the transition points towards a lower concentration, implying a more facile F127-surfactant interaction. The maximum intensity ratio was found at 1.0 mM and 0.5 mM for TTAB and CTAB, respectively. Interestingly, when we normalize the surfactant concentrations with respective CMCs, the intensity ratio plots become almost alike; T_1 is at ~1/10, T_2 is at ~1/3 of the CMC value, and T_3 is close to the CMC.[184]

4.2.2. Steady-State Fluorescence Anisotropy. As in the previous chapter, we used MPTS to measure fluorescence anisotropy. Anisotropy measurement could provide an excellent opportunity to probe the reorganization of the assemblies.

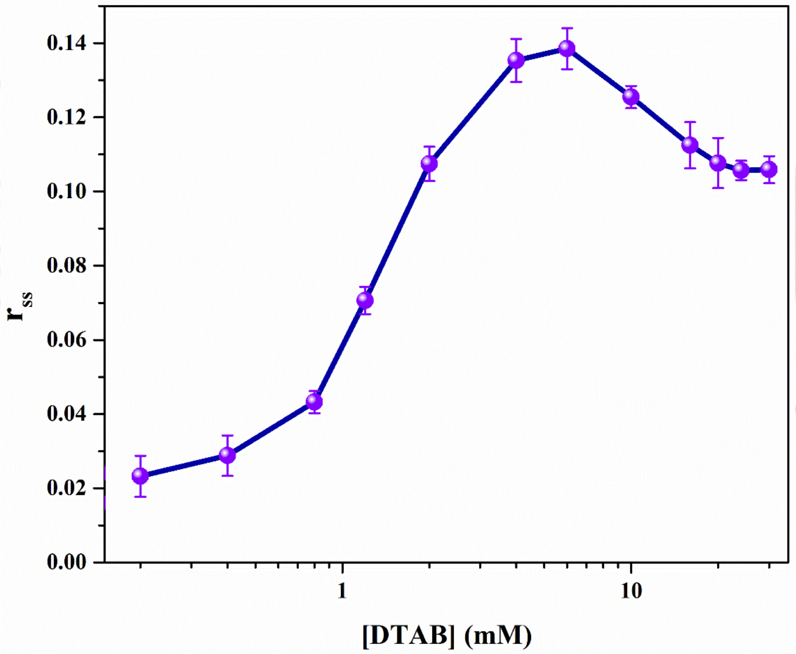

Figure 4.3. Steady-state fluorescence anisotropy of MPTS in the presence of 0.4 mM F127 and varying concentrations of DTAB (λ_{em} = 440 nm and λ_{ex} = 375 nm).

The steady-state anisotropy (r_{ss}) of MPTS was relatively low (0.01) in a sub-micellar F127 (0.4 mM) solution, implying that the rotational restriction of the fluorophore is very less. The r_{ss} increased significantly upon the gradual addition of DTAB and reached a maximum (~0.14) at ~6 mM DTAB (Figure 4.3). Adding more

DTAB somewhat decreased the r_{ss} up to ~20 mM and became almost constant at a relatively high surfactant concentration. Thus, the nature of the r_{ss} variation against DTAB concentration was quite similar to the intensity ratio, implying that the confinement level and hydration level modulated proportionately when the copolymer-surfactant assembly reorganized at different surfactant concentrations.

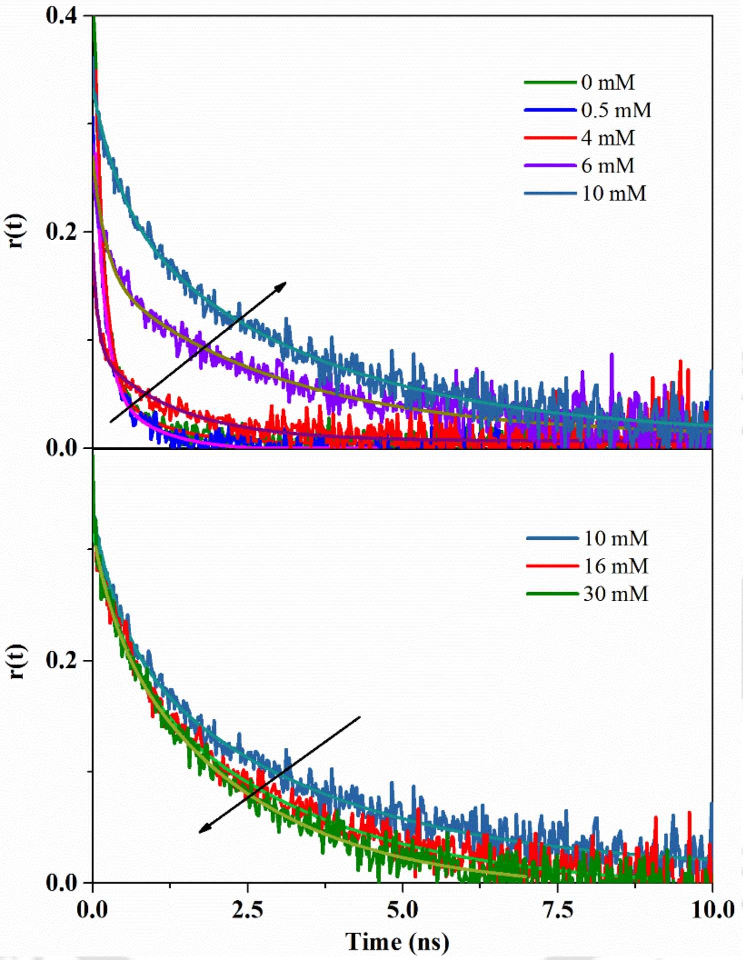

Figure 4.4. Fluorescence anisotropy decays of MPTS in 0.4 mM F127 at different DTAB concentrations at an emission wavelength of 440 nm with an excitation wavelength of 375 nm.

4.2.3. Fluorescence Anisotropy Decay. In sub-micellar (0.4 mM) F127, the fluorescence anisotropy decay became slightly slower than in water (rotational time 150), with an average rotational time of 280 ps (Table 4.1). The average rotational time increased gradually with an increase in the DTAB concentration (Figure 4.4) and became the slowest (2400 ps) at an intermediate (10 mM) DTAB concentration. Note that the DTAB concentration corresponding to the slowest rotational dynamics was slightly higher than the concentration corresponding to the maximum intensity ratio. The anisotropy decay became faster at higher DTAB concentrations in the mixture (Figure 4.4) and became similar to that of the DTAB micelle at a very high surfactant concentration. The slowest anisotropy decay at an intermediate concentration indicated that an optimum amount of DTAB was necessary to get the most compact assembly. The gradually faster anisotropy decay suggested that the mixed assembly may eject out some F127 molecules while incorporating more DTAB molecules. At a very high DTAB concentration, the mixed assembly effectively turned into a pure DTAB-micelle-type assembly. A bi-exponential function (equation 2.23, Chapter 2) adequately fitted the anisotropy decays within the mixed micellar assemblies at all surfactant concentrations.

Table 4.1. Fluorescence anisotropy decay (λ_{em} = 440 nm) parameters of MPTS in different systems in the presence and absence of F127. Error in the data ~ ± 3%.

System	**r_0**	**β**	**τ_f (ps)**	**τ_s (ps)**	**τ_w (ps)**	**<τ> (ps)**	**θ (deg)**
Water	0.40	-	150	-	-	-	-
0.4 mM F127	0.34	0.18	150	870	180	280	57
F127-0.5 mM DTAB	0.28	0.24	160	830	190	320	52
F127-4 mM DTAB	0.32	0.28	100	1300	100	430	49
F127-6 mM DTAB	0.29	0.54	200	2900	230	1700	36
F127-10 mM DTAB	0.32	0.68	470	3280	550	2400	29
F127-16 mM DTAB	0.32	0.69	500	3000	620	2250	28
F127-24 mM DTAB	0.35	0.74	200	2200	210	1700	25
24 mM DTAB	0.32	0.74	500	2500	470	1900	25

We invoked the "Wobbling-in-Cone" model (Chapter 2) to justify the biexponential anisotropy decay[223-224] and summarized the analyzed parameters in Table 4.1. The wobbling time constant also follows the anomalous pattern, fast wobbling at the low and high surfactant contents while slow wobbling at an intermediate concentration. Thus, the assembly exerts the most increased rigidity at an intermediate surfactant concentration. Note, however, that the semicone angle decreases gradually with an increase in the concentration of DTAB. The positive charge level or the cationic surfactant in the assembly may control the semicone angle by which the probe may undergo wobbling motion. Another important observation is that the semicone angle of the F127-DTAB assembly at high DTAB concentration matches precisely with that of the DTAB micelle.[184] Thus, the mixed assembly formed at higher surfactant concentrations may have attained a DTAB-micelle-type structure.

4.2.4. ESPT Dynamics in F127-DTAB Mixed Micelle. We calculated the intensity ratio of protonated and deprotonated bands for TRANES and plotted against the corresponding time (Figure 4.5). The emission intensity ratio obtained from TRANES can be fitted adequately with equation (2.21) (Chapter 2) in the mixed assembly. Thus, the ESPT may follow an irreversible behavior within the F127-DTAB surfactant assembly and inside the DTAB micelle.

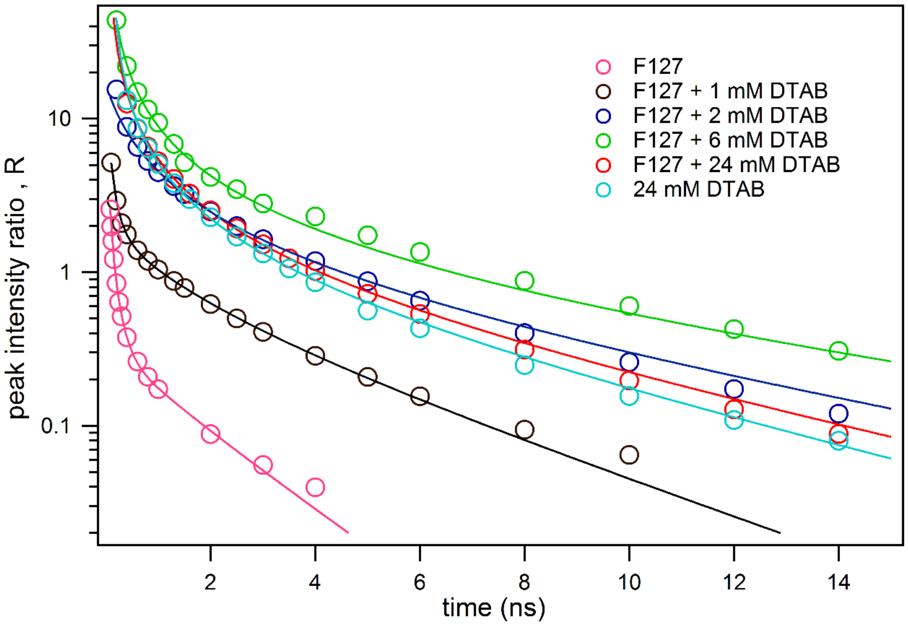

Figure 4.5. TRANES intensity ratio comparison of HPTS in the presence of sub-micellar F127 (0.4 mM), sub-micellar F127 (0.4 mM) with increasing DTAB concentrations (0-24 mM) and in pure DTAB micelle (24 mM).

We have already reported this simple irreversible ESPT in cationic micelle and triblock-surfactant assembly at post-micellar concentrations.[13]

The deprotonation time varies anomalously with an increase in the DTAB concentration in the mixture (Table 4.2). The deprotonation time first increased to 9.56 ns for a specific concentration of DTAB (6 mM) and then decreased with further concentration increments. The deprotonation time at a very high concentration resembles that of the DTAB micelle. However, in that case, the deprotonation time at higher concentrations was much slower than in the DTAB micelle.

Table 4.2. ESPT time-constants of HPTS inside the copolymer-surfactant assemblies at different compositions. The concentration of F127 was 0.4 mM in all the sets.

Systems	**τ_d (ns)**
F127	0.6 ± 0.003
F127 + 1 mM DTAB	1.93 ± 0.09
F127 + 2 mM DTAB	6.81 ± 0.12
F127 + 6 mM DTAB	9.56 ± 0.12
F127 + 24 mM DTAB	6.15 ± 0.03
24 mM DTAB	5.53 ± 0.04

4.2.5. Isothermal Titration Calorimetry. Isothermal titration calorimetry (ITC) was applied to explore further the concentration-dependent interaction between sub-micellar F127 and cationic surfactant (Figure 4.6). Interestingly, the titration curve resembled the intensity ratio; the enthalpy change gradually increased with an increase in the DTAB concentration and reached a maximum at ~6 mM.

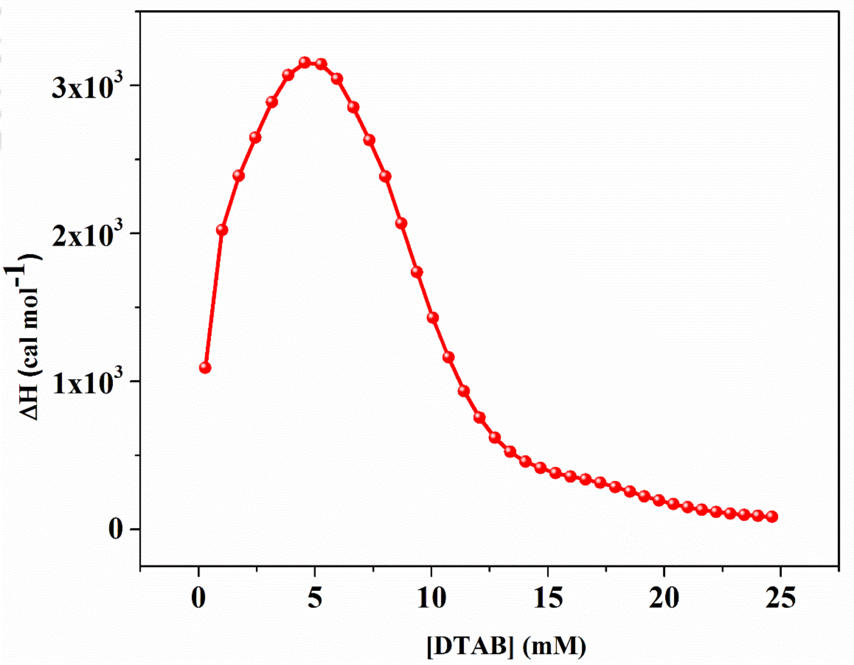

Figure 4.6. Isothermal calorimetric **t**itration curve for adding DTAB to an aqueous 0.4 mM F127 at 25 °C.

The enthalpy change decreased upon further increase of the DTAB concentration. Thus, ITC measurements also revealed a robust interaction between F127 and DTAB when both were in their sub-micellar concentrations.

4.2.6. Dynamic Light Scattering (DLS). DLS can provide valuable insights into the variation of hydrodynamic sizes of the mixed copolymer-surfactant assembly at different DTAB concentrations. Figure 4.7 shows that the distribution of the hydrodynamic diameter of the initial sub-micellar (0.4 mM) F127 solution was quite broad, and the average diameter was ~7 nm. Since the hydrodynamic diameter of F127 micelles is much larger (~35 nm),[69] we may conclude that no micelle is present at this concentration, and only some tiny less-structured sub-micellar aggregates may prevail.

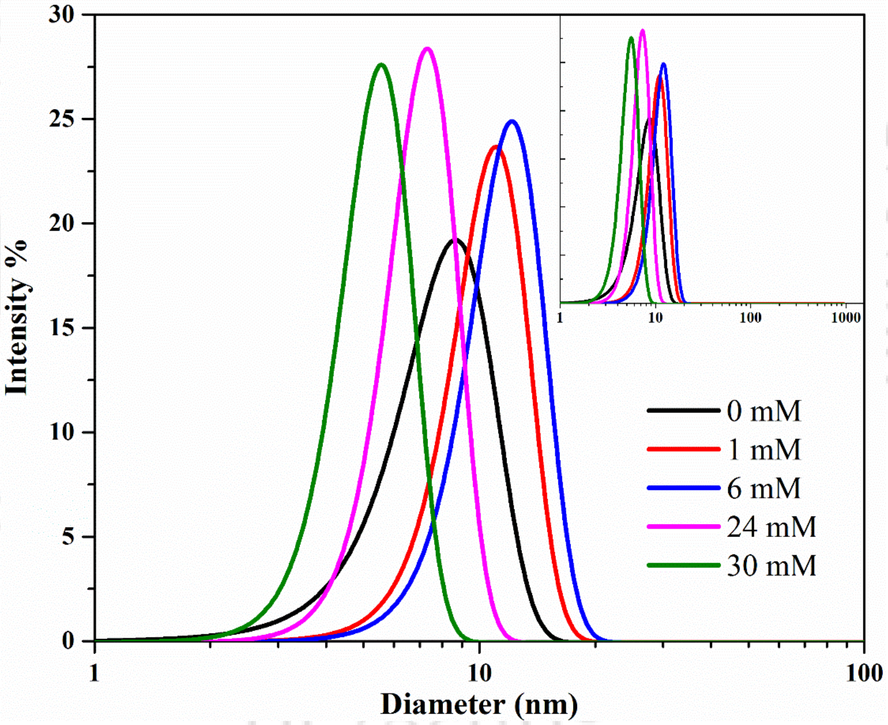

Figure 4.7. Dynamic light scattering intensity distribution of the solution containing 0.4 mM F127 and various DTAB concentrations. (Inset reflects nonexistence of larger aggregates in the extended diameter regions up to 1000 nm).

Upon the addition of DTAB, larger aggregates appeared while the distribution became narrow. The results imply that the sub-micellar aggregates uptake the cationic surfactants forming well-defined aggregates. We detected the most massive aggregates (~12 nm in diameter) at 6 mM DTAB that matched the surfactant concentration corresponding to the maximum intensity ratio or fluorescence intensity. Thus, all the measurements corroborated that the assembly attained the optimized state against DTAB uptake. The assembly became the largest, most compact, and least hydrated at ~ 6mM DTAB. Other cationic surfactants of higher chain lengths (e.g., TTAB, CTAB) showed a similar trend.

4.3. Synthesis of Gold Nanoplates in Mixed Surfactant Assembly

We optimized the sub-micellar aggregate between copolymer F127 and several cationic surfactants (DTAB, TTAB, and CTAB). We further wanted to test the efficiency of such an aggregate as a medium for synthesizing an anisotropic gold nanostructure. For that, we implemented a seed-mediated growth synthesis procedure usually used for nanorod synthesis[254] and used the optimum condition (0.4 mM F127 + 0.5 mM CTAB) as a medium.

From the steady-state spectral study, we showed a prominent similarity in the interaction pattern of all the cationic surfactants with pluronic F127 irrespective of chain length and rigorously studied F127-DTAB assemblies. However, we explicitly applied F127-CTAB mixed assembly for nanomaterial synthesis. The reasons behind selecting CTAB (of optimum concentration of 0.5 mM) over DTAB are (i) a significantly lower amount of CTAB (0.5 mM compared to 6 mM of DTAB) was required; hence less toxicity of the medium (ii) The effects of F127 and CTAB individually on the synthesis of gold nanomaterials and their control on shapes are known.

4.3.1 Gold Seed within F127-CTAB Sub-Micellar Solution. Gold nano-seeds were prepared by rapidly reducing $HAuCl_4$ aqueous solution using $NaBH_4$ in the aqueous medium containing 0.4 mM F127 and 0.5 mM CTAB. We injected 25 µl of 50 mM $HAuCl_4$ into a 10 ml round bottom flask containing 4.7 ml of this stock solution and stirred for 2 minutes at 400 rpm. Then 300 µl of 10 mM $NaBH_4$ solution (freshly prepared ice-cold) was rapidly added into the solution under vigorous stirring (1200 rpm) at room temperature (25^{o}C±1^{o}C). A light brown color solution appeared initially, but it transformed to a brownish-pink within 4-5 minutes. This seed solution was kept at room temperature and used to synthesize anisotropic gold nanostructures.

4.3.2 Growth Solution Containing F127-CTAB Sub-Micellar Aggregate. In another round-bottomed flask, we took 10 ml of the sub-micellar aggregate stock solution along with 190 µl 1M HCl and100 µl of 50 mM $HAuCl_4$ solution. It became a yellowish-colored after gentle shaking and slow stirring at 500 rpm for 5 minutes. We added 120 µl freshly prepared 10 mM $AgNO_3$ solution into this growth solution, followed by 150 µl freshly prepared 100 mM ascorbic acid solution. The immediate reduction of Au(III) ions to Au(I) by ascorbic acid resulted in a colorless solution (Au(I) being a d^{10} metal center, the ligand to metal charge transfer band disappeared). We added 24 µl of the seed solution to this colorless solution under vigorous shaking. Then we left the solution undisturbed for two hours until a bluish-pink-colored solution appeared. We finally purified the resultant solution by centrifugation (8000 rpm) followed by redispersing the precipitate in the optimized sub-micellar aggregate solution (0.4 mM F127 + 0.5 mM CTAB). We performed the whole synthesis at room temperature (25±1 °C).

4.3.3. Characterization. The seed showed an absorption maximum of 534 nm. The characteristics LSPR band of gold nanoparticles occur in the 500 nm-550 nm region. So, the 534 nm absorption maxima indicated the formation of seed gold nanoparticles. On the other hand, the growth solution displays a strong peak at 715 nm. The anisotropic gold structure (nanorods, nanoplates) usually shows absorption maxima from 700 nm to the NIR region. So, in the present scenario, the 715 nm absorption maximum may be due to the anisotropic nanostructures, and the TEM images further corroborated our findings (Figure 4.8a). The FETEM images (Figure 4.8b) confirmed that triangular-shaped gold nanoplates were present with edge lengths of ~300 nm without sharp tips.

4.3.4 Growth Mechanism of Anisotropic Gold Nanoplate. We can propose a mechanism for the sub-micellar aggregate to support the anisotropic growth of the initial spherical AuNP seeds. In this seeded growth method, we have applied ascorbic acid. This weak reducing agent can partially reduce Au(III) to Au(I) but not entirely to Au(0), thus avoiding secondary nucleation. The inserted Au seeds may act as a catalyst to reduce the Au(I) to Au(0) on their surfaces.[254] Two mechanisms for this reduction may be possible. The seeds may produce Au(0) and Au(III) by catalyzing the disproportionation reaction of Au(I) and simultaneous reduction of Au(III) to Au(I) by the remaining reducing agent in the medium.[255-256] Another mechanism may be that the Au(0) surface catalyzes the reduction of Au(I) *in situ* by accepting electrons from the reductant.[257-258] Thus, we can say that the selective adsorption of surfactant assemblies on Au seeds helps the anisotropic growth rather than the solely templating effect of mixed surfactant assembly.[259] The oriented attachment of the sub-micellar aggregate on the seed surface may trigger the anisotropic growth. However, further studies are needed to reveal molecular-level information. There was no lyotropic phase at this significantly lower copolymer concentration to induce structural anisotropy.[260] Following earlier literature reports, we suggested that the surfactant assembly selectively binds to the growing nanostructures' less energetic facets (111 planes), enabling the other facets (110 planes) to grow in a particular shape nanoplates.[261-262]

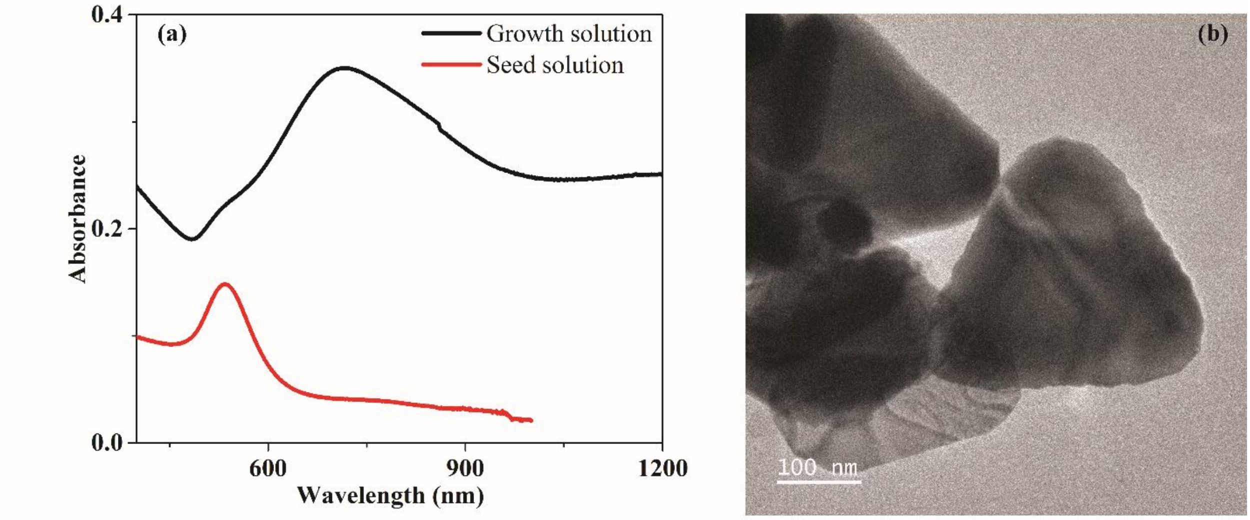

Figure 4. 8. (a) UV-Vis-NIR absorption spectra of seed and growth solution;(b) FETEM image of gold nanoplates.

4.4. Summary and Conclusions

The work demonstrated that even at a sub-micellar concentration, triblock copolymer and cationic surfactant could interact actively to form a compact, organized assembly. The assembly offers much better confinement to the solubilized fluorophore than individual polymeric or surfactant micelles. These sub-micellar assemblies can be an effective medium to produce shape-controlled nanoplates. Such an assembly could be beneficial for shape-controlled nanomaterials synthesis and drug delivery systems with negligible toxicity.

Chapter 5

Differential Headgroup Charge Induced Differential Interaction Patterns of Zwitterionic and Cationic Surfactants with a Triblock Copolymer Micelle[#]

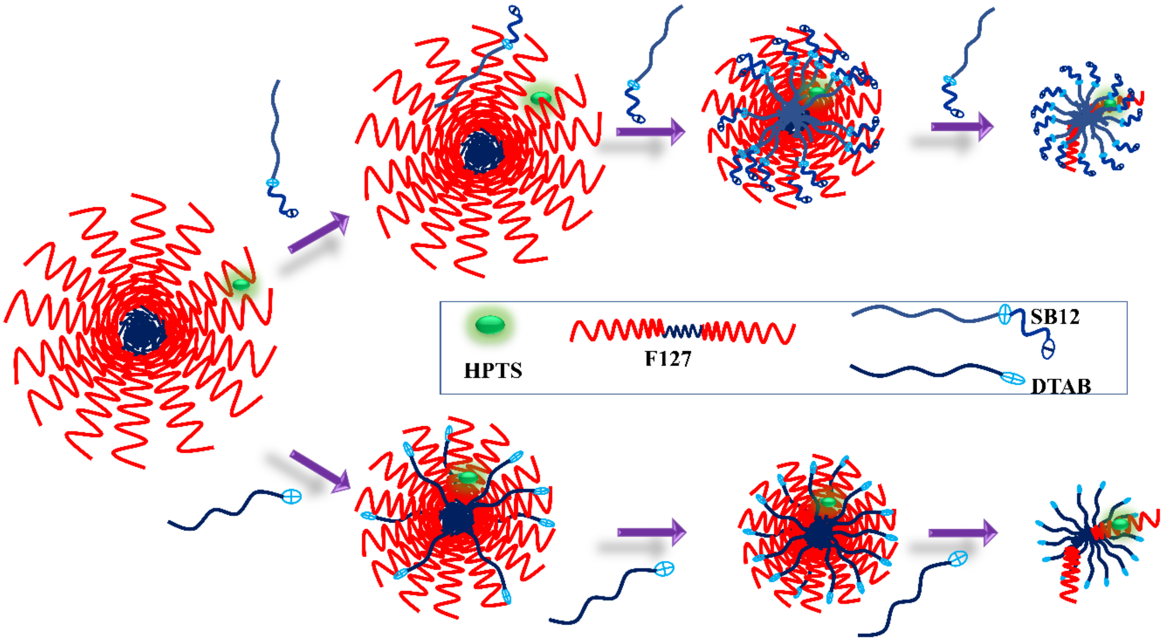

[#]This work has been published in *Colloids and Surfaces A: Physicochemical and Engineering Aspects 640 (2022) 128327*.

Chapter 5: Differential Headgroup Charge Induced Differential Interaction Patterns of Zwitterionic and Cationic Surfactants with a Triblock Copolymer Micelle[263]

5.1. Introduction

How does the headgroup charge affect the self-assembly formation between the triblock copolymers and surfactants? Recently, Vyas et al. used anionic SDS, cationic DTAB, and zwitterionic SB12, all containing the same number of alkyl (C_{12}) chains and three different triblock copolymers (L81, P84, and F88) of varying hydrophobicity.[264] They found that anionic surfactant interacts most strongly, DTAB interacts moderately, and SB12 interacts relatively weakly. A recent study by Nan and co-workers revealed that differential water affinities of the headgroups and counterions of surfactants play a significant role in micellar aggregate formation [265]. The nature and propensity to form the mixed assemblies also depend on both the steric condition and electrostatic behavior of the respective headgroups and the length and nature of the hydrophobic tail.[266] A bulky headgroup creates more shielding to the core of the mixed micellar assembly leading to more hydrophobicity.[267] This investigation explored the interaction between a triblock copolymer F127 micelle and a zwitterionic sulfobetaine surfactant SB12, primarily utilizing ESPT dynamics of HPTS. We compared the obtained interaction pattern to that of the cationic surfactant DTAB or C_{12}TAB, with the same alkyl chains. SB12 requires a higher surfactant concentration to acquire the optimum state; it results in a more organized and less hydrated state than the cationic surfactant.

5.2. Results

5.2.1. Steady-state Emission Spectra. HPTS shows two characteristic emission bands for the protonated (at 440 nm) and deprotonated (at 510 nm) forms. The relative intensity of the two bands (protonated/deprotonated) is a convenient indicator of the feasibility of ESPT. A low ratio indicates a facile ESPT, while a high ratio designates a retarded ESPT.

Adding SB12 surfactants to the micellar F127 solution induces distinct changes in the emission bands depending on the concentration. The change is minimal at low concentrations (<3 mM), but as the surfactant concentration increases, the protonated emission intensity increases with a concomitant decrease in the deprotonated emission intensity (Figure 5.1a). The corresponding intensity ratio increases dramatically at a moderate SB12 concentration range up to a critical concentration (35 mM) (Figure 5.2).

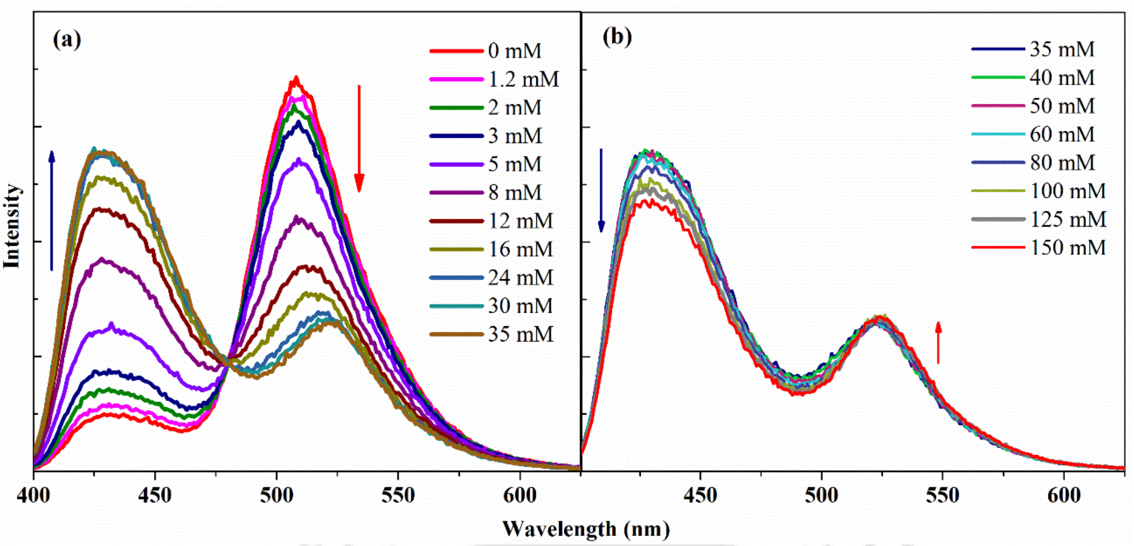

Figure 5.1. Emission spectra of HPTS inside the F127-SB12 mixed assemblies with increasing SB12 concentrations. The spectra are grouped into two regions (a) 0-35 mM, (b) 35-150 mM. The concentration of F127 was fixed at 4 mM.

However, the trend reverses at a higher SB12 concentration; the intensity of the protonated emission band decreases while the deprotonated emission intensity increases (Figure 5.1b). Consequently, the emission intensity ratio decreases at a higher concentration (35-125 mM) and becomes steady at a very high (>125 mM) SB12 concentration (Figure 5.2).

From Figure 5.2, it is apparent that the variation of emission intensity ratio with SB12 concentration is quite distinct in water and F127 micellar medium. In water, the ratio follows a clear trend; it sharply increases at ~3 mM, indicating the formation of the micelle, and becomes steady at higher concentrations implying the formation of more micelles without further structural reorganization.[231] However, for the micellar F127 case, the ratio depicts three transitions (T_{1-3}) points depending on the concentrations, suggesting that the mixed assembly undergoes a continuous rearrangement depending on the concentration of the surfactant.

The interaction of SB12 surfactant with F127 micelle starts at a ~ 3mM (T_1) surfactant concentration close to its CMC. There is almost no change in the emission ratio in the premicellar SB12 concentration. Although the change in the intensity ratio starts at the same concentration in both the presence and absence of F127 micelle, their slopes afterward are very different. Thus, we may conclude that the F127 micelles prevent self-aggregation of SB12 surfactants into neat micelle, instead uptake small clusters of SB12 surfactants to form a mixed micelle. However, the interaction starts well below the CMC for the DTAB case, implying that the F127 micelle has more propensity to uptake DTAB monomers than SB12 monomers (Figure 5.2).

The intensity ratio rises to a maximum value of ~3.3 at ~35 mM SB12 (T_2), which is ~10 times higher than its CMC. Note that the maximum intensity ratio is much higher than the (~1.1) ratio in the neat SB12 micelle. Thus, the ESPT dynamics become severely retarded inside the mixed assembly at this composition. For the DTAB case, the maximum intensity ratio was observed at a much lower (~10 mM) concentration, less than the CMC (16 mM) of DTAB. However, the maximum value of the ratio (2.9) in the DTAB case is less than the maximum ratio (3.3) in the case of SB12 surfactant. Thus, although SB12 requires a higher concentration than DTAB to achieve the most retarded state, the level of retardation is more in SB12 than in DTAB.

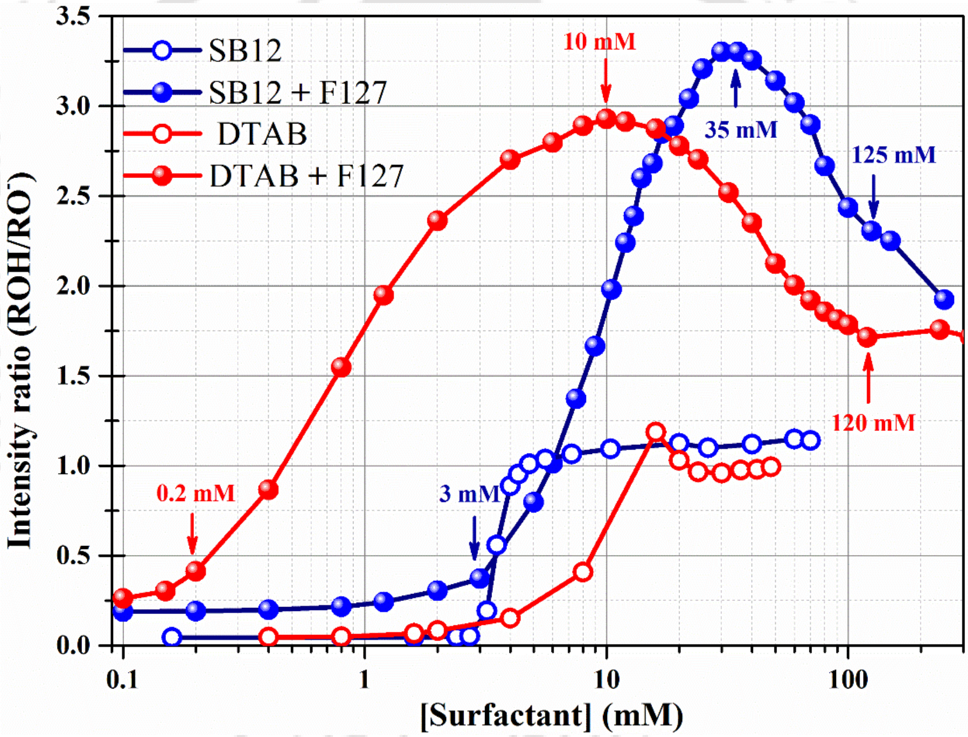

Figure 5.2. Variation of the emission intensity ratio (ROH/RO) against SB12 surfactant concentration in 4 mM F127 and water, respectively.

The peak position of the emission bands, especially the deprotonated emission maximum, underwent a remarkable redshift from 510 nm to 527 nm upon the addition of SB12 surfactant. A similar shift of emission band was also observed for the uptake of DTAB by F127 micelle[268] and other cationic interfaces.[206, 237] The redshift of the emission maximum indicates the extent of the cationic environment surrounding HPTS and may originate from cation-π interaction. While comparing this emission peak shift for these two surfactants, DTAB and SB12 looked notably different (Figure 5.3). The main difference was in the onset point and the initial slope. In DTAB, the emission maximum started to shift at a low concentration (~0.2 mM) and shifted gradually up to 527 nm at ~20 mM DTAB, which depicts constant insertion and reorganization of DTAB surfactant chains into the F127 micelle. Whereas for SB12, the scenario was quite different; the change in slope, in the beginning, was negligible up to 3 mM, and after that, a drastic change occurred in slope (from 510 nm to 525 nm) up to 35 mM (Figure 5.3). Thus, we may conclude that surfactant monomer insertion was unfavorable for SB12 at a low concentration below its CMC (3.4 mM at 25 °C).[269] So, the cationic environment induces a redshift of the deprotonated band in both cases but to a different extent, indicating that the orientation of the surfactant in F127 or the fluorophore location is quite different.

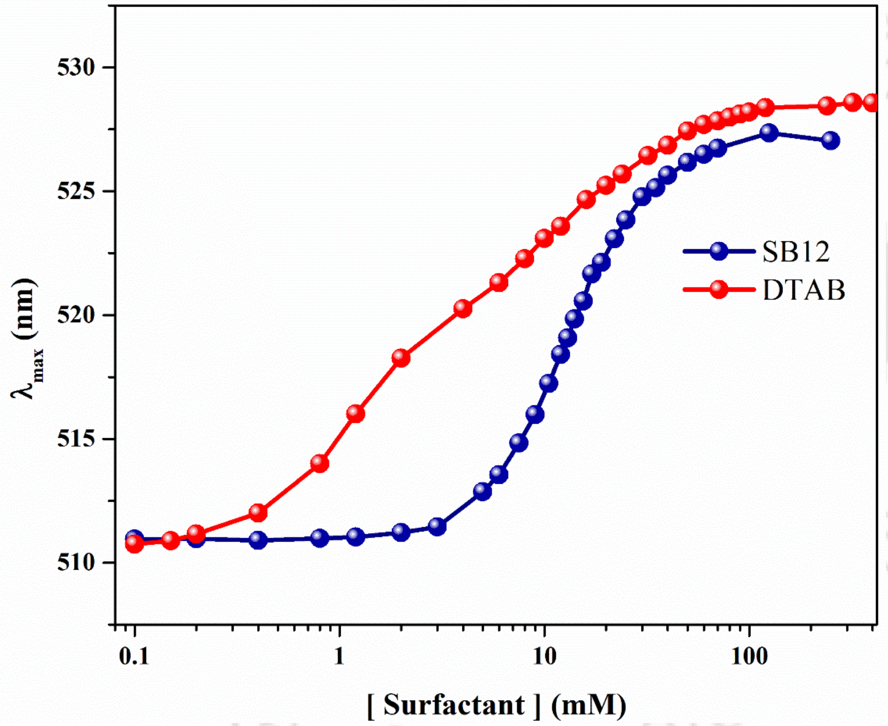

Figure 5.3. Variation of the emission maximum of the deprotonated form in the F127-SB12 assembly at different surfactant concentrations.

5.2.2. Steady-State Anisotropy. The steady-state anisotropy also follows the same trend against the SB12 concentration as the emission intensity ratio (Figure 5.4). The fluorescence anisotropy increased after adding a particular SB12 concentration (~2 mM), reaching the maximum value at ~20–30 mM. The fluorescence anisotropy decreases at higher concentrations. The uptake of SB12 surfactant results in a denser packing up to a specific concentration, but local rigidity somewhat reduces after that. Thus, the nature of the reorganization of the mixed micellar interface may be biphasic.

There was a striking similarity between the steady-state anisotropy (r_{ss}) variation between the cationic and zwitterionic surfactants. However, the concentration corresponding to the maximum anisotropy was much higher for the SB12 than the DTAB surfactant. The maximum anisotropy value was slightly higher for the SB12 surfactant than the DTAB case, implying that SB12 confers better confinement to the entrapped fluorophore.

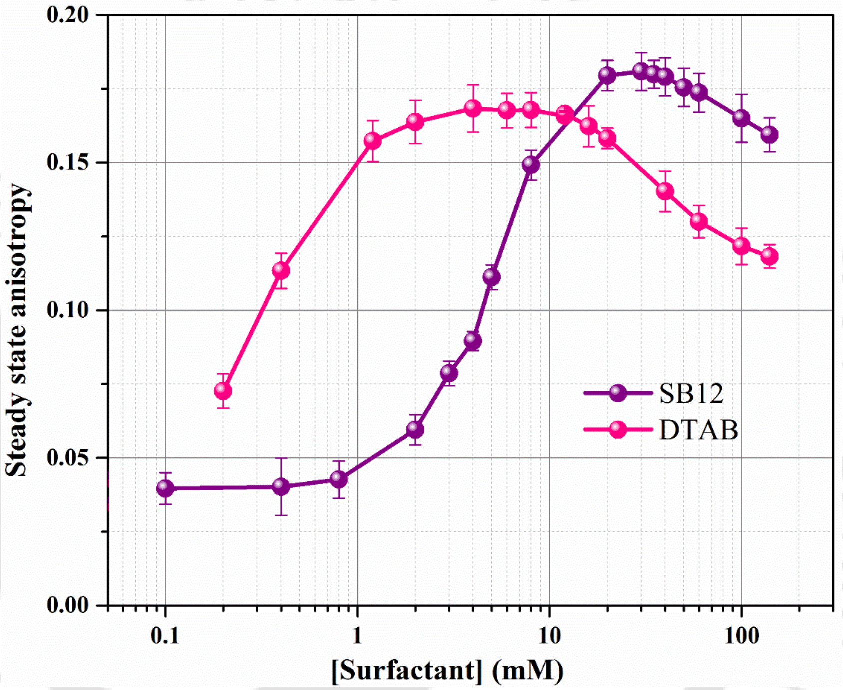

Figure 5.4. Variation of steady-state anisotropy of MPTS in F127-surfactant assembly with increasing concentration of concerned surfactants (SB12 or DTAB).

5.2.3. Fluorescence Anisotropy Decays. MPTS displays a monoexponential anisotropy decay in water with a time constant of 150 ps. However, the anisotropy decays for the F127-SB12 systems can be fitted best to a bi-exponential function. The semicone angle (obtained from wobbling in cone model analysis, Chapter 2) gradually reduces with the surfactant concentration, indicating that the space available for the rotation becomes restricted (Table 5.1). The wobbling time constant (τ_W) also exhibits the same tendency, i.e., it increases up to 35 mM SB12 concentration and decreases after that. Thus, the maximum compactness and confinement occur at 30-35 mM of SB12 in the mixed assembly. Up to this particular concentration (35 mM), the mixed assembly renders maximum hindrance to the rotation of the probe. After that, some reorganization around the probe, relocation of the probe, or breakdown of assemblies may occur, which eases the rotation restriction at higher concentrations (Figure 5.5).

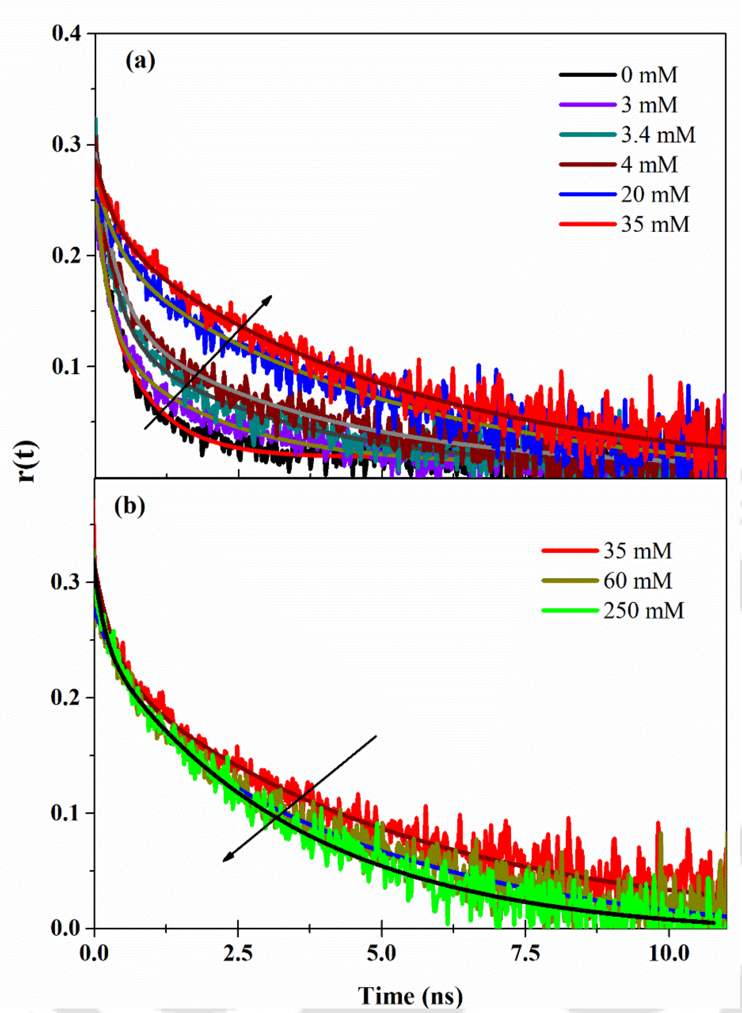

Figure 5.5. Fluorescence anisotropy decay of MPTS (λ_{em} = 440 nm) in the F127-SB12 assembly at varying SB12 concentrations: (a) 0- 35 mM (b) 35 – 250 mM.

The same tendency was also observed in the DTAB-F127 system, but the optimum DTAB concentration of 8-10 mM was below its CMC of 16 mM.[268] The average rotational time (<τ>) in the F127-DTAB assembly was slightly faster than the F127-SB12 assembly, which is probably due to more compactness in the latter case.

Table 5.1. Time-resolved anisotropy decay parameters of MPTS in 4 mM F127 with increasing concentrations of SB12. Error in the data ~ ± 3%.

System	**[SB12] (mM)**	r_0	a_s	τ_f **(ps)**	τ_s **(ps)**	τ_w**(ps)**	**<τ> (ps)**	**θ (deg)**
4 mM F127	0	0.34	0.38	220 ± 10	920 ± 68	280	490	44
	0.8	0.40	0.39	205 ± 10	1020 ± 65	260	520	43
	3.4	0.31	0.41	315 ± 15	3190 ± 290	350	1490	42
	4	0.31	0.45	385 ± 35	3620 ± 240	430	1840	40
	7.5	0.32	0.55	315 ± 30	3860 ± 170	340	2260	35
	20	0.30	0.67	410 ± 60	5120 ± 250	450	3570	29
	30	0.32	0.68	520 ± 40	5490 ± 400	570	3900	28
	60	0.30	0.74	715 ± 50	4990 ± 225	830	3880	25
	250	0.35	0.74	308 ± 40	4300 ± 100	330	3260	25

5.2.4. ESPT Dynamics.

The intensity ratio best fits equation. 2.17 (Chapter 2) for HPTS in F127 micelle and at low SB12 concentration (up to 7.5 mM), but at higher concentration and neat SB12 micelle, the dynamics follow equation. 2.21 (Chapter 2) (scheme 5.6). Similar swapping of the ESPT schemes was also observed for the F127-DTAB case where the ESPT scheme follows Eigen-Weller nature at low DTAB concentration but shows an irreversible behavior at higher DTAB concentration.[268] The probable reason for the kinetic scheme switching may be sudden microenvironmental change arising from the accumulation of positive charge and dehydration of the corona region, destabilizing the geminate ion pair.

The deprotonation dynamics reflect the nature and availability of water near HPTS. In bulk water, deprotonation occurs with a time constant of ~0.10 ns. The deprotonation time slows down to 0.41 ns in the F127 and as slow as 15 ns in SB12 (35 mM) micelle (Table 5.2). Thus, the HPTS residing on the corona of the F127 micelle experiences significant hydration reflecting the hydrophilicity of the region. On the contrary, the hydration level is much lower in the interfacial region of the zwitterionic SB12 micelle.

The deprotonation dynamics of HPTS in F127 micelle become gradually slower with the addition of SB12 up to 35 mM (Table 5.2).

Table 5.2. ESPT time constants of HPTS obtained from TRANES intensity ratio. Error in the data ~ ± 3%.

System	**[SB12] (mM)**	**a_1**	**a_2**	**τ_1 (ns)**	**τ_2 (ns)**	**τ_d (ns)**	**τ_r (ns)**	**τ_{diff} (ns)**
4 mM F127	0	0.58	0.42	0.26	2.4	0.41	1.51	0.85
	3	0.47	0.53	0.27	4.98	0.54	2.47	0.60
	7.5	0.26	0.74	0.35	9.94	1.24	2.80	0.56
	14	1.0		8.31		8.31		
	35	1.0		15.09		15.09		
	60	1.0		13.93		13.93		
	125	1.0		10.61		10.61		
	SB12 Micelle	1.0		6.61		6.61		

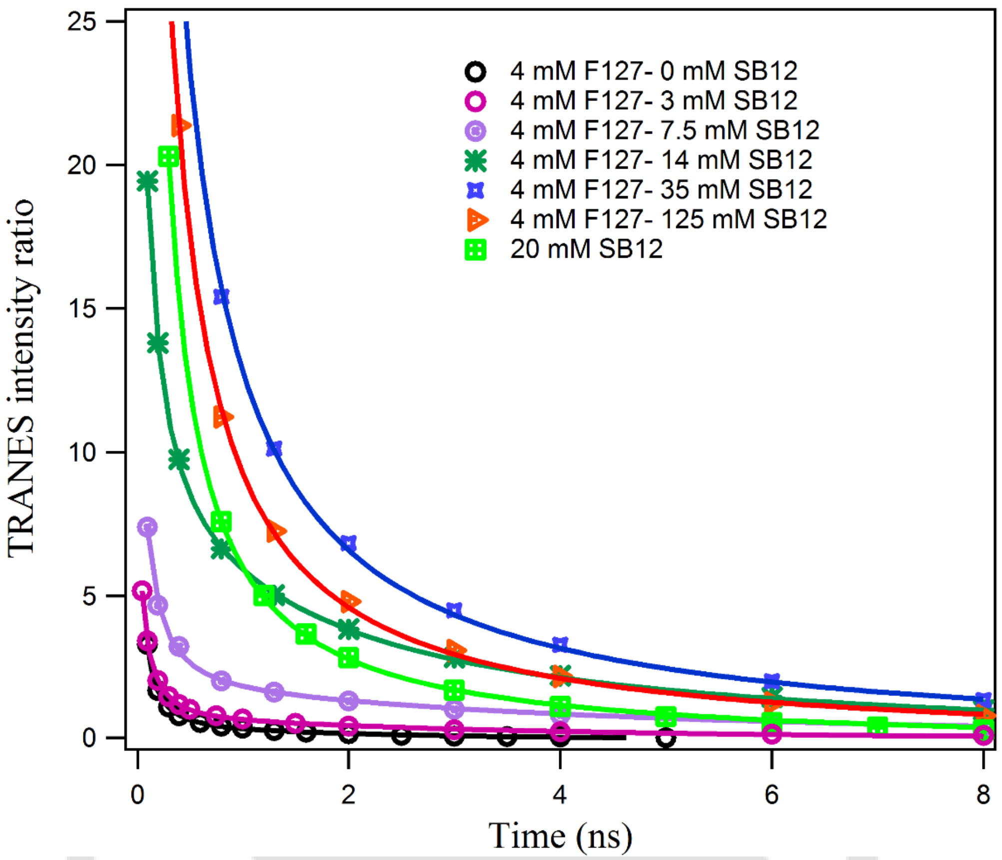

Figure 5.6. Decay of the TRANES intensity ratio of HPTS in different assemblies.

The dynamics become relatively faster with a further increase in the surfactant concentration. Thus, the deprotonation times also follow a similar unusual trend as that of the steady-state emission intensity ratio implying that the intensity ratio is a good indicator of the retardation of ESPT dynamics.

5.2.5. Dynamic Light Scattering (DLS). DLS was employed to get insight into the assembly size at different stages. Initially, the size of the F127 micelle is quite large, with a hydrodynamic diameter of ~38 nm. The assembly size decreases biphasically with the increase in the SB12 concentration. The assembly shrinks more steeply up to 30 - 35 mM of SB12, producing assemblies with a diameter of 10-11 nm, and then decreases less steeply at higher surfactant concentrations. Note that up to 3 mM concentration, the assembly size does not change much, supporting that SB12 surfactant monomer insertion to F127 is negligible.

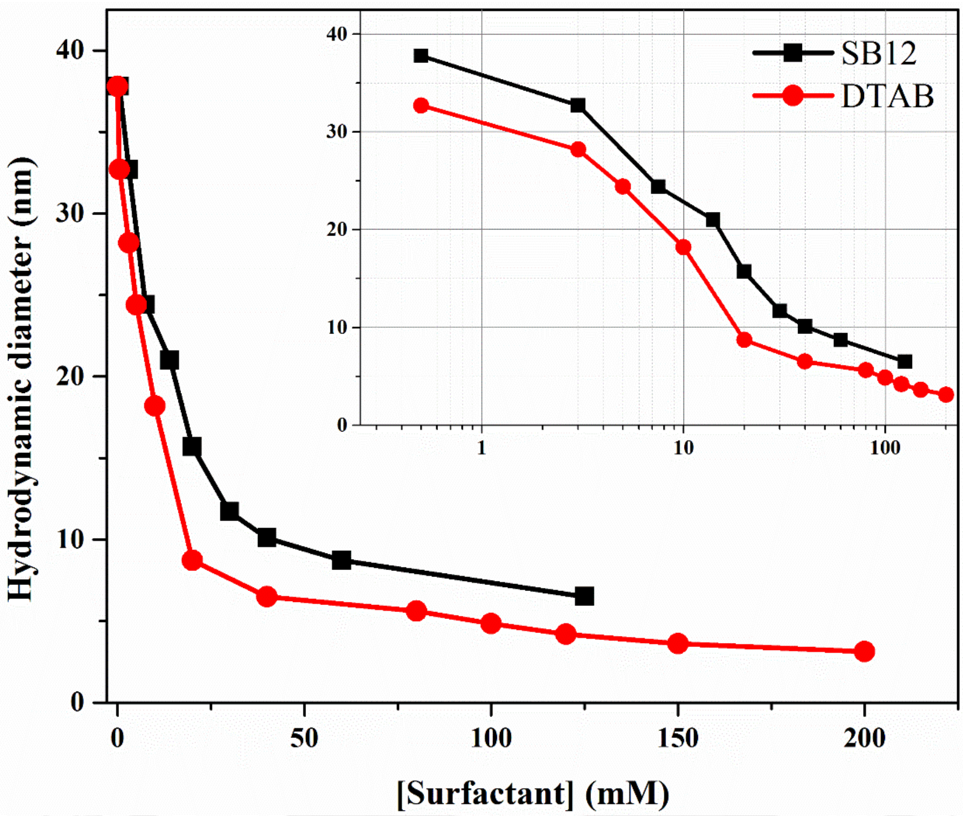

Figure 5.7. Variation of the hydrodynamic diameters of the F127-SB12 (black square) and F127-DTAB (red circle) assemblies with increasing concentration of the corresponding surfactants in the F127 micelle. Inset shows the same plot in the log scale.

This shrinkage of the assembly after CMC signifies the incorporation of SB12 surfactant clusters into the F127 micelle and the formation of mixed aggregate. The insertion of SB12 into the pluronic F127 micelle leads to dehydration of the initially hydrated swollen assembly resulting in shrinkage into smaller hydrodynamic sizes. The higher concentration regime forms such assembly where SB12 contributes more than F127. Note that the size of the neat SB12 micelle was found to be 5 nm. The gradual shift of the autocorrelation function to the lower delay time scale also supports our finding of a concomitant decreasing trend of the mixed assembly size to a smaller hydrodynamic diameter.[263]

There was a striking similarity between the hydrodynamic diameter pattern variation of the F127 micelle upon interaction with DTAB vs. SB12 surfactants. Both showed two regimes with different slopes at lower and higher concentration regions. Note that the change in size was more pronounced for DTAB than for SB12 surfactant (Figure 5.7). For DTAB, the slope was steeper than SB12. The reason may be that DTAB surfactant monomers incorporated themselves into the F127 micelle at the initial stage. However, SB12 may only incorporate itself into the F127 micelle as clusters after reaching a concentration close to its CMC. For both cases, it is evident that two different kinds of assemblies are forming at the two extremes of the concentration variation from hydrated to the less hydrated assembly through a more compact, less hydrated mixed assembly at the transition point.

5.3. Discussion

Although the alkyl tail of the surfactant mainly drives the interaction, the nature of the headgroup, like charges, steric properties, and water affinities, also decide the fate of the mixed-assembly for a particular composition.[265, 267, 270] Surfactants with a tiny headgroup, irrespective of charges can insert into the core of the copolymer micelle. In contrast, the surfactant with a bulky headgroup may have a lesser tendency to go deep and stay in the corona. The main difference in the observed ESPT dynamics or the fluorescence anisotropy for the two surfactants, DTAB and SB12, may be attributed to this cause, especially at low concentrations. The SB12, having a comparatively larger headgroup, may not allow the alkyl tail insertion into the F127 micellar core due to steric hindrance.

Our results showed that the uptake of surfactant (DTAB or SB12) induced remarkable dehydration and compactness of the corona region. At the optimum organization, dehydration was most severe for SB12 due to the bulky headgroup's better shielding of the micellar interface, which justifies the slowest deprotonation time (15 ns) in the F127-SB12 assembly compared to the DTAB-F127 assembly (12 ns). Since the dramatic retardation of the ESPT dynamics and the fluorescence anisotropy decays continue up to ~35 mM of SB12 concentration, we may conclude that surfactant insertion continues up to this concentration. The reorganization of the mixed assembly was also evident from the shift of the emission maximum of the deprotonated emission band, resulting from positive charge density around the photoacid. Since further addition of SB12 surfactant did not change the deprotonated band position, we assumed that the assembly was already saturated by the surfactant, hence no change in the positive charge density around the probe.

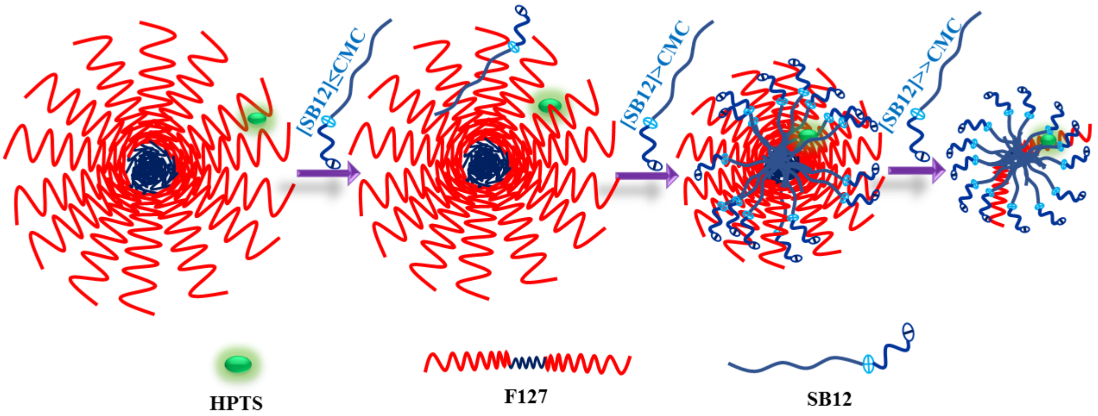

Scheme 5.1. Schematic representation of surfactant reorganization leading to mixed assembly formations.

It was essential to ascertain the characteristic differences in the interaction pattern of the SB12 surfactant from the cationic surfactant DTAB containing the same number of alkyl tails. We found the same type of variations of the emission intensity ratio, deprotonation time, and rotational relaxation times with the surfactant concentration; however, for the SB12 system, the most retardation of ESPT occurred at a post micellar concentration of the surfactant. In comparison, for the cationic surfactant DTAB, we obtained the slowest ESPT at a pre-micellar concentration (6 mM) below the CMC (CMC 15-16 mM).[271] Thus, DTAB preferred to form a mixed aggregate with F127 micelle at low concentration instead of self-aggregate, which was precisely the opposite for the SB12 surfactant in the F127 micellar medium. At very low SB12 concentration (below CMC), the intensity ratio or the fluorescence anisotropy of HPTS did not change much from that of the F127 micelle (Scheme 5.1). This implied that SB12 surfactant monomers have less tendency to interact with the F127 micelle. Interestingly, the interaction of SB12 with F127 micelle became significant only after CMC. Thus, we may assume that SB12 surfactant forms small clusters or micelles and then interacts with F127.

5.4. Summary and Conclusions

In summary, we followed different stages of the copolymer-zwitterionic surfactant assembly resulting from the uptake of SB12 surfactants by F127 micelle and compared them to that of the cationic DTAB surfactant through the investigation of excited-state proton transfer dynamics modulation of photoacid probe HPTS. Despite different headgroup charges, both surfactants displayed some common characteristics and distinct differences. Both showed the same irregular pattern; the confinement and dehydration levels increased to a specific surfactant concentration and decreased at higher concentrations. The SB12 surfactant required a much higher surfactant than its CMC to attain a compact assembly with F127, whereas DTAB surfactants needed much less (less than its CMC) to result in the most compact state. We may conclude that the cationic surfactant has much more propensity to form a mixed aggregate with F127 micelle than the zwitterionic surfactant possessing the same alkyl tail due to differences in steric and charge properties. However, despite the weaker interaction, SB12 surfactant creates the most compact assembly with F127 micelle than DTAB. Thus, a milder surfactant may lead to a hybrid formulation, which may not be achieved by a surfactant interacting even strongly.

Chapter 6

Modulation of Excited-State Proton Transfer Dynamics in Pluronic Triblock Copolymer-Zwitterionic Surfactant Mixed-Micellar Interface in the Presence of Salt[#]

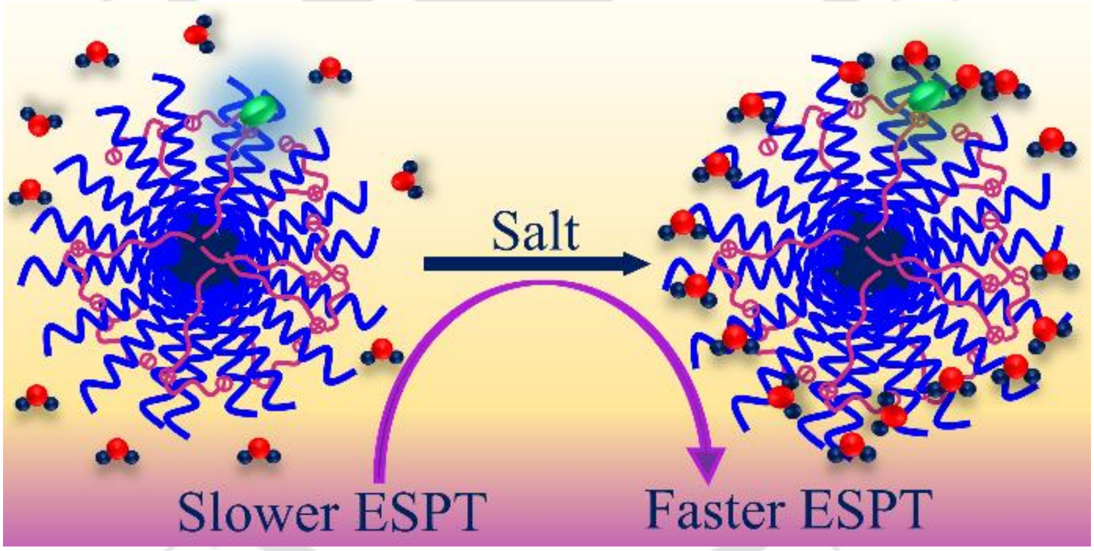

[#]This work has been communicated, 2023

Chapter 6: Modulation of Excited-State Proton Transfer Dynamics in Pluronic Triblock Copolymer-Zwitterionic Surfactant Mixed-Micellar Interface in the Presence of Salt

6.1. Introduction

Whether and how salt affects the ESPT process in aqueous and confined media remains a longstanding question. Ions preferentially interact with ionic surfactants by localizing themselves within the interface due to favorable surface potential, which may change micellar properties.[272-273] However, it is often believed that the effect of salt is nominal on nonionic surfactants due to the absence of net charge on the surfactant headgroup or lack of surface potential.[274] In a recent work, Shahidzadeh and coworkers reported a drastic reduction of critical micellar concentration (CMC) of the cationic surfactant CTAB at high salt (NaCl, 5.5 M) but no change for the nonionic surfactant Tween 80.[275] Although the effect of salt on ionic, polyelectrolyte micelles has been studied in details,[273, 276-277] however, its effect on zwitterionic micelle or mixed Pluronic-zwitterionic micelle had not been explored much.

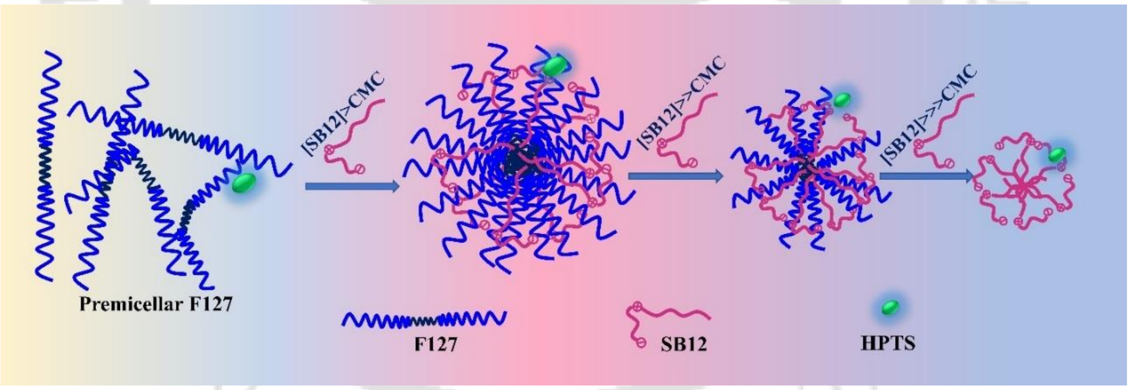

Scheme 6.1. Schematic representation of mixed micelle formation of premicellar F127 and SB12.

Alteration of hydration level and the solvation dynamics in the palisade layer of the micelle may occur due to salts.[278-279] Common salts (e.g., NaCl) that exert a salting out effect can change the solubility of the blocks of the copolymer, especially dehydration of the propylene oxide or ethylene oxide (EO).[280-282] The presence of salts in the micellar medium affects the CMC, CMT and alters shape transformations in many cases.[19, 283-285] There is a possibility of change in headgroup orientations in the micellar assemblies and membrane in the presence of ions.[286] It may also impact the interfacial property and biological or physiological properties of membranes.[287-288]

The interaction between the ions and the interface of micellar assemblies and membranes is crucial as it plays a vital role in signal transduction in neuronal synapses and membrane fusions.[289] In case the non-toxic mixed micelles are incorporated for biomedical purposes, the micelle has to encounter various salts or ionic substances. Then, will the micelle cope with this salt concentration, whether it disintegrates or becomes more compact? To gain insight into this, we first investigated the interaction pattern of pluronic F127 copolymer with zwitterionic surfactant SB12 in the absence of salt (Scheme 6.1). Then we employed various salts (from monovalent to trivalent - NaCl, $CaCl_2$ and $AlCl_3$) to vary the ionic strengths in these assemblies. The impact of the salt was monitored by modulation of ESPT dynamics to elucidate the micellar interfacial hydration patterns.

6.2. Results

6.2.1 Steady-state Spectra: We varied the SB12 concentration to a solution containing a fixed F127 concentration without salt and followed the absorption and emission spectra of HPTS. Two representative F127 concentrations (0.4 mM and 4.0 mM) were explicitly chosen below and above the CMC (0.56 mM at 25°C)[14, 235]. The absorption spectrum shows a distinct maximum at 403-405 nm, which does not alter significantly with SB12 concentration.

The intensity ratios of protonated to deprotonated (ROH/RO^-) emission bands were 0.10 and 0.15 in the premicellar and post-micellar F127, respectively, marginally higher than the ratio obtained in the water (0.05). The gradual addition of SB12 to the F127 solution alters the intensity of the respective emission bands and the corresponding emission intensity ratio for both premicellar and post-micellar cases (Figure 6.1). However, the intensity ratio varies anomalously with the SB12 concentration. For the pre-micellar F127, the intensity ratio initially increases to a maximum at 6.4 mM SB12, but after that, the ratio decreases for up to 70 mM SB12 and finally remains unchanged at higher concentrations (Figure 6.1). The trend is similar to that observed for the post-micellar case, but the maximum ratio (3.3) was much higher than the pre-micellar case (2.6), and the maximum ratio appeared at a much higher SB12 concentration (35 mM) than in the premicellar case (6.4 mM).[263] Note that such a maximum was absent for SB12 addition in water; the ratio attains a steady value above CMC, suggesting micelle formation.

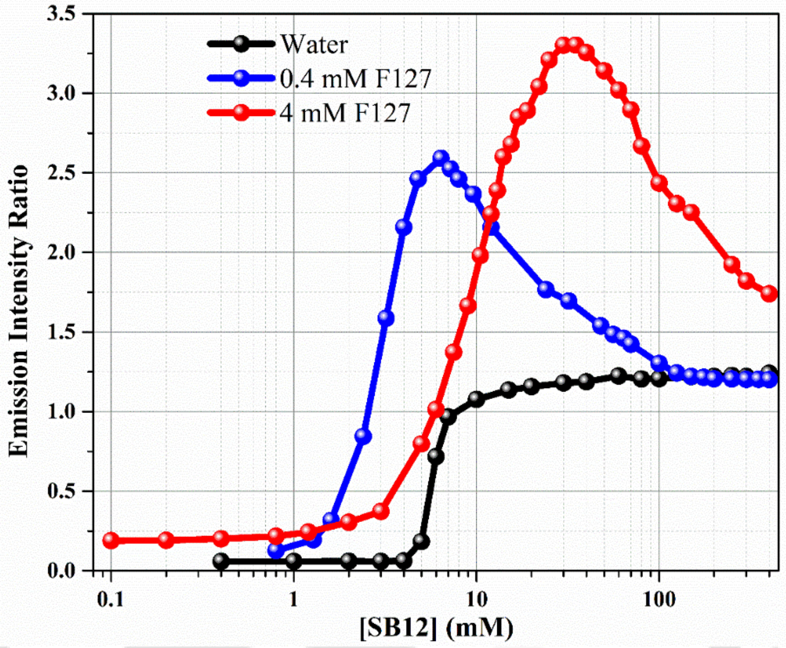

Figure 6.1. Variation of the emission intensity ratio (protonated/deprotonated) of HPTS against SB12 concentrations in water and premicellar (0.4 mM) and post-micellar (4.0 mM) F127.

The intensity ratio determines the extent of retardation of ESPT, which is linked to the local hydration and microenvironment of the photoacid. Thus, the highest intensity ratios observed at the maxima for the premicellar pluronic-zwitterionic complex (prePZC, 0.4 mM F127- 6.4 mM SB12) and post-micellar pluronic-zwitterionic complex (postPZC, 4.0 mM F127 - 35 mM SB12) denote the most hindrance to the ESPT process and may suggest most compact and least hydrated assemblies for the given F127 concentration.

In this work, our primary focus is to explore the effect of salt on the mixed assembly. We first check the effect of NaCl on individual premicellar and micellar assemblies of F127 and SB12. Interestingly, the salt has no significant effect on the emission properties of HPTS within the SB12 micelle or inside the premicellar and micellar F127 systems. The reason may be due to the neutral interface of SB12 micelle, unassembled premicellar F127, and quite diffused hydrated corona segment of F127 micelle. However, NaCl remarkably affected the emission spectrum when added to the prePZC or postPZC mixed assemblies. For both these assemblies, the emission intensity of the protonated band decreases, and that of the deprotonated band increases gradually upon adding NaCl solution (Figures 6.2a and 6.2b). The corresponding intensity ratio decreases for both systems but more drastically for the prePZC assembly than the postPZC assembly (Figure 6.2c). The lowering of the intensity ratio emphasizes more favorable ESPT in the systems in the presence of salt.

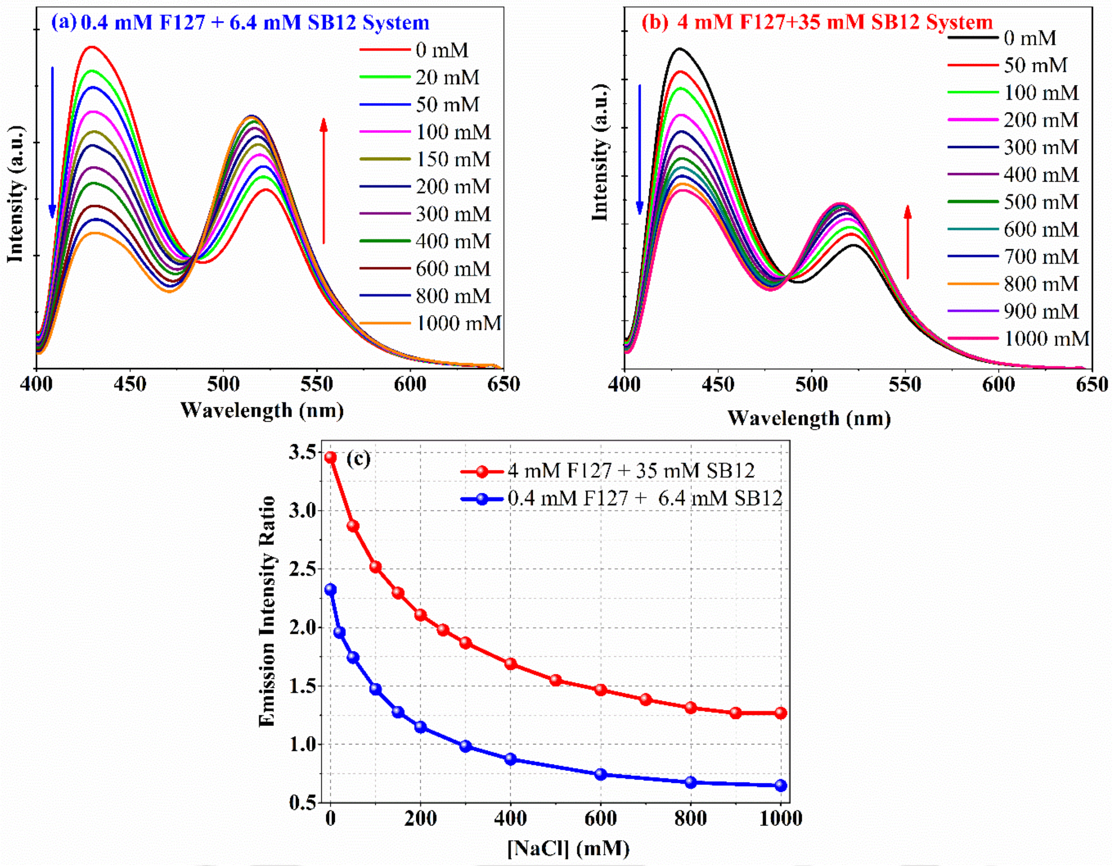

Figure 6.2. Modulation of the emission spectra of HPTS in the mixed assembly of (a) premicellar 0.4 mM F127- 6.4 mM SB12 and (b) post-micellar 4.0 mM F127- 35 mM SB12 with increasing NaCl concentration. (c) The emission intensity ratio of HPTS in the mixed assembly with increasing NaCl concentration.

The deprotonated emission band undergoes a remarkable blue shift with the increase in NaCl concentration for both cases. For prePZC, the emission maximum shifts from 523 nm to 515 nm, while in the case of postPZC, the maximum emission shifts from 523 nm to 516 nm (Figure 6.3b) at 1M NaCl. The emission maximum of the deprotonated band was initially at ~510 nm in the F127 assembly. However, the addition of SB12 triggers a remarkable redshift of the emission band up to 523 nm. Thus, the effect of NaCl is opposite to that of SB12 surfactant in terms of shifting the emission band position. The SB12-induced redshift (from 510 nm to 523 nm) of the deprotonated band maximum was probably due to the π-cationic interaction between HPTS and the surfactant headgroup inside the assembly (Figure 6.3a).[187] Thus, the blue shift suggests lesser interaction of the aromatic ring with the cationic headgroup of the SB12 surfactant, indicating significant rearrangement of the headgroups. The charge screening between the probe and surfactant headgroup at high ionic strength may be responsible for a lesser π-cationic interaction.

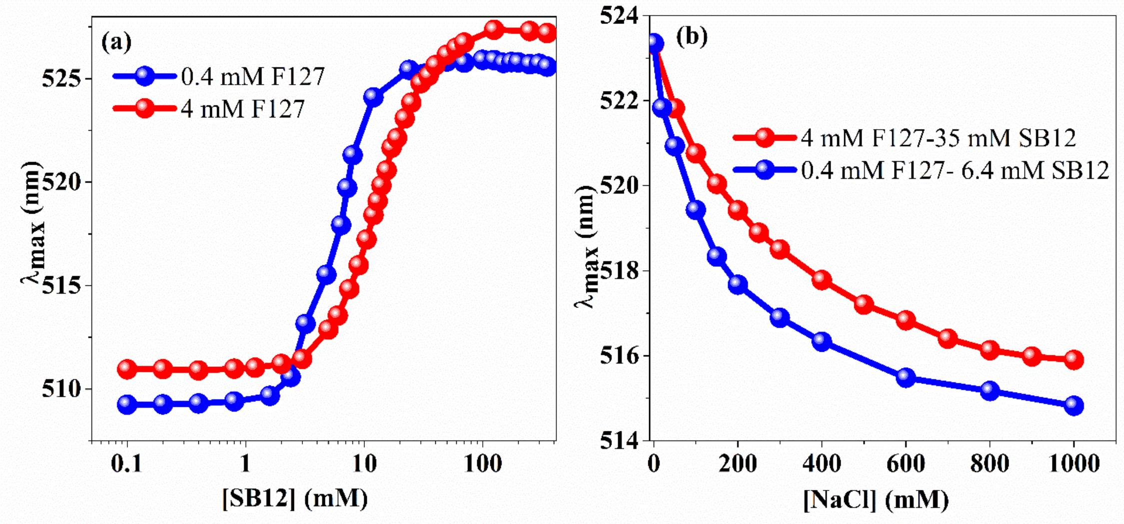

Figure 6.3. Variation of deprotonated emission band maxima of HPTS with (a) SB12 concentration in premicellar 0.4 mM and post micellar 4.0 mM F127 and (b) NaCl concentration in the respective compact assemblies prePZC (0.4 mM F127 - 6.4 mM SB12) and postPZC (4.0 mM F127 - 35 mM SB12).

Apart from NaCl (monovalent salt), we also applied other salts, calcium chloride (divalent salt) and aluminum chloride (trivalent salt), on these two compact assemblies and followed the emission spectra and intensity ratio (Figure 6.4). The intensity ratio follows the same trend when plotted against ionic strength. The intensity ratio decreases with increasing ionic strength, and after a particular ionic strength (~1 M), there is not much change in the ratio for the salts, irrespective of their valency (Figure 6.4).

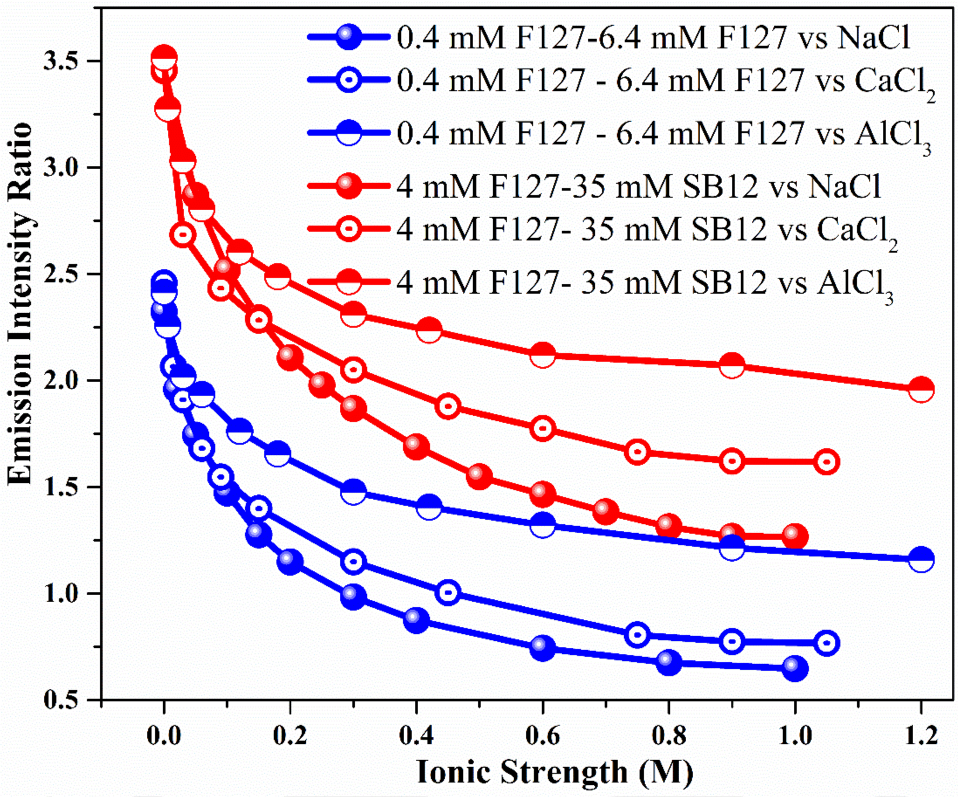

Figure 6.4. Variation of emission intensity ratio (protonated/deprotonated) of HPTS in premicellar 0.4 mM F127-6.4 mM SB12 and micellar 4.0 mM F127-35 mM SB12 with ionic strength for different salts (NaCl, $CaCl_2$ and $AlCl_3$).

Further, we also varied SB12 concentration at a fixed NaCl concentration to check whether the saline environment may alter mixed micelle formation and if there is any change to the anomalous variation of the intensity ratio. The maximum intensity ratio decreases in the NaCl medium, and the maximum appears at a relatively higher SB12 concentration than in the absence of salt for both the premicellar and post-micellar F127 cases. In the premicellar F127 case, in the presence of initially added 10 mM and 100 mM of NaCl, the maximum intensity ratio position shifted to the SB12 concentration values of 12 mM and 15 mM, and the ratio value decreased to 2.2 and 1.38, respectively. For 1000 mM NaCl concentration, we did not get any distinct maximum for the intensity ratio. In all the above cases at higher SB12 concentrations (<100 mM), the intensity ratio merges to ~ 1.2, which is closer to the intensity ratio obtained in the SB12 micelle of the value ~1.

In the case of post micellar F127, the maximum peak intensity ratio position shifted to 70 mM, 80 mM, and 125 mM of SB12, and the intensity ratio became 2.73, 2.2, and 2.08 for the NaCl concentrations of 10 mM, 100 mM, and 1000 mM, respectively.

6.2.2. Steady-State Anisotropy: The steady-state anisotropy of MPTS follows the same trend as the emission intensity ratio of HPTS in those assemblies depicting maximum rotational hindrance at a concentration range of 6 mM to 8 mM of SB12 in the premicellar F127 which indicates the formation of compact mixed micellar assembly at this particular concentration zone. While comparing the value of r_{ss} between post and premicellar concentrations of F127, it has been observed that for the post micellar case, the r_{ss} is higher due to its more compact nature.

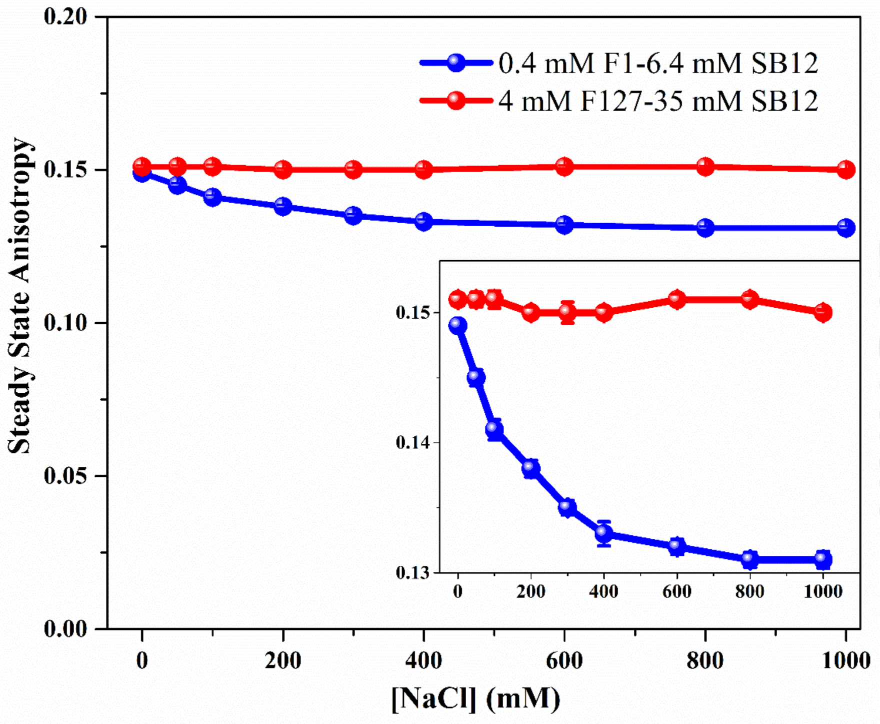

Figure 6.5. Variation of Steady-state anisotropy of MPTS with increasing NaCl concentration in 0.4 mM F127- 6.4 mM SB12 (prePZC) and 4 mM F127- 35 mM SB12 (postPZC), respectively. Inset represents an enlarged view of anisotropy change.

There is not much change in Steady-state anisotropy value inside the compact assembly of prePZC and postPZC due to NaCl variation, which contrasts with the observed intensity ratio change in the same systems. For the prePZC case, there is a slight decrease in steady-state anisotropy value compared to the postPZC, which is almost unchanged throughout the NaCl concentration variation (Figure 6.5). The rigidity near the probe may not alter much due to the presence of salt, but the proton transfer rate enhances.

Apart from SB12 variation in the F127 solution, we added NaCl of different concentrations (0 mM, 10 mM, 100 mM and 1000 mM) and then varied SB12 to check the r_{ss} values. For the premicellar and post micellar F127, the Steady-state anisotropy value varied in the same trend as the emission intensity ratio change.

6.2.3. Dynamic Light Scattering (DLS)

The hydrodynamic diameter gradually varies with the addition of SB12 to premicellar F127; the assembly size initially increases to 11.7 nm, and after that, the size decreases and finally attains a size (6 nm) similar to the SB12 micelle. Thus, the premicellar F127 first formed a compact mixed micelle, and after that, some F127 molecules may leave the assembly resulting in size reduction at a higher concentration of SB12. SB12 addition to micellar F127 leads to a gradual decrease in the size of the assembly, which finally attains a size similar to neat SB12 micelle at a high concentration.

We checked the impact of NaCl on the size of individual SB12 micelle, premicellar, and micellar F127 assemblies. The diameter of the SB12 micelle does not change by the variation of NaCl concentration. However, the diameter of the premicellar F127 assembly increases from ~7 nm (in the absence of NaCl) to 26 nm at 1 M NaCl, possibly due to the monomer to micelle transformation. In the case of micellar F127, the increase in NaCl concentration causes a shrinking of the micelle size from 38 nm to 25 nm; the reason might be the salting out.[290] Interestingly, the hydrodynamic diameter of both the premicellar and post-micellar F127 ultimately reached a typical assembly size of ~26 nm at a high NaCl concentration.

Our primary interest is to find the effect of the salt concentration on the most compact assembly of premicellar F127-SB12 (prePZC) and post micellar F127- SB12 (postPZC). In the compact assemblies of premicellar and post micellar F127 with SB12, the variation of NaCl does not affect the hydrodynamic diameter too much, a little increase from its initial value. Other divalent $CaCl_2$ and trivalent $AlCl_3$ also have no significant effect on the hydrodynamic diameter of those compact assemblies (Figure 6.6).

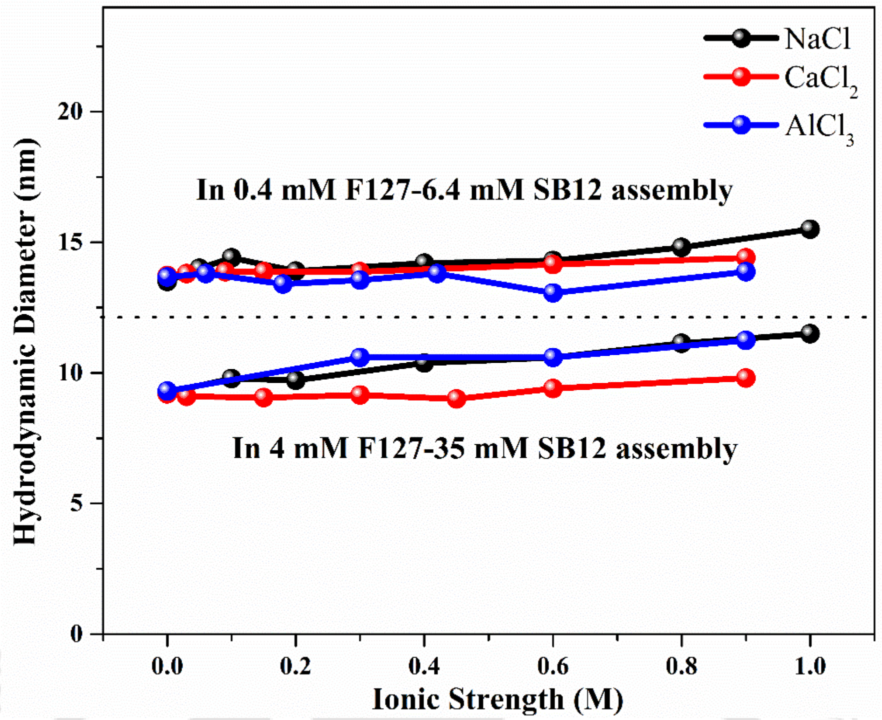

Figure 6.6. Hydrodynamic diameter variation of premicellar F127- 6.4 mM SB12 and post micellar F127- 35 mM SB12 assemblies with ionic strength variation.

Another important observation is that there is no effect of ionic strengths of salts (NaCl, $CaCl_2$, and $AlCl_3$) on SB12 micellar media; its size remains almost the same. Also, the emission intensity ratio of HPTS remains unaffected during the ionic strength variation. So, it indicates that the external salt ionic strength does not alter the zwitterionic micellar structure or hydration.

We also want to know how the F127-SB12 mixed micelle grows at different SB12 concentrations in a fixed NaCl solution. The change in size due to the SB12 concentration variation on the premicellar F127 in the presence of a lower concentration of NaCl (10 mM, 100 mM) follows the same trend as in the absence of NaCl, i.e., the diameter first increases, then it gradually decreases and attains the diameter of SB12 micelle. However, at high NaCl concentrations (1000 mM), the diameter regularly decreases with the addition of SB12 and attains the value of SB12 micelle at high concentrations. Note that at high NaCl concentrations, the premicellar assembly undergoes micellization even before adding any SB12 surfactant. For micellar F127, the presence of NaCl follows the same trend as in the absence of NaCl; the size decreases gradually and tends to attain the diameter of SB12. Thus, the hydrodynamic diameter variations in the presence of initially added NaCl indicates that there is not much difference compared to that in the absence of salt except for a higher concentration of NaCl (~1M).

6.2.4. Fluorescence Anisotropy Decay. Fluorescence anisotropy shows a biexponential decay pattern with two rotational correlation times in the F127 micelle and F127-SB12 assembly. The anisotropy decays exhibit an anomalous trend with SB12 concentration variation in premicellar F127; the decay becomes remarkably slower up to 6.4 mM, but above this concentration, the decay becomes faster (Figure 6.7). The decay parameters revealed that the slow rotational component becomes gradually even slower up to 6.4 mM SB12 but becomes faster after that, depicting the variation of compactness and rigidness of the assemblies throughout the concentration of SB12 variation (Table 6.1).

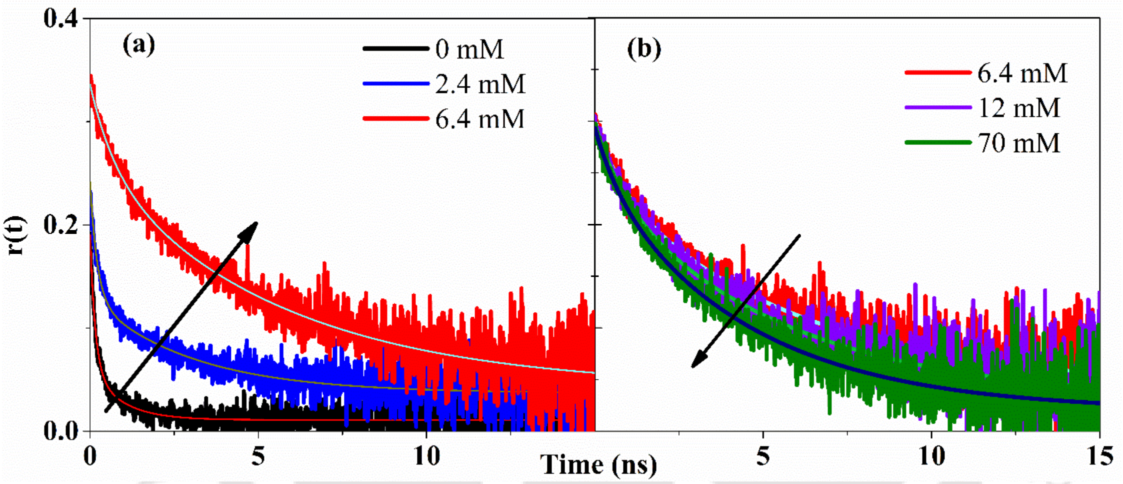

Figure 6.7. Fluorescence anisotropy decay of MPTS (λ_{ex} 375 nm, λ_{em} 440 nm) of MPTS in premicellar 0.4 mM F127 with increasing SB12 concentration (a) 0 mM to 6.4 mM; (b) 6.4 mM to 70 mM.

The slowest wobbling time (690 ps) was obtained for the particular composition, prePZC (premicellar 0.4 mM F127-6.4 mM SB12). The average rotational correlation time for MPTS in prePZC is 5.1 ns which is faster compared to that of the postPZC (5.5 ns).[263] The concentration of NaCl was varied on the most compact mixed micellar assemblies of 0.4 mM F127-6.4 mM SB12 (prePZC) and 4 mM F127- 35 mM SB12 (postPZC) systems.

Table 6.1. Time-resolved anisotropy decay parameters of MPTS (λ_{ex} 375 nm, λ_{em} 440 nm) in different F127-SB12 compositions. Error in the data ~ ± 3%.

System	**[SB12] (mM)**	**r_0**	**α_s**	**τ_f (ps)**	**τ_s (ps)**	**τ_w (ps)**	**<τ> (ps)**	**θ (deg)**
0.4 mM F127	0	0.37	0.17	150	870	180	270	58
	1.6	0.37	0.18	170	1380	190	360	57
	2.4	0.32	0.30	210	3020	230	1050	48
	4.8	0.33	0.69	340	4350	370	3110	28
	6.4	0.32	0.70	690	5190	690	3800	28
	8	0.32	0.72	530	5030	640	3760	26
	24	0.33	0.72	780	4770	600	3560	26
	70	0.34	0.75	690	4020	540	3200	24

However, there was no change in anisotropy decay with the increase in salt concentration in the postPZC system. In contrast, the anisotropy decay becomes slightly faster upon adding NaCl in the prePZC (Figure 6.8). The slightly faster anisotropy decay pattern for the prePZC might be due to comparatively less compactness.

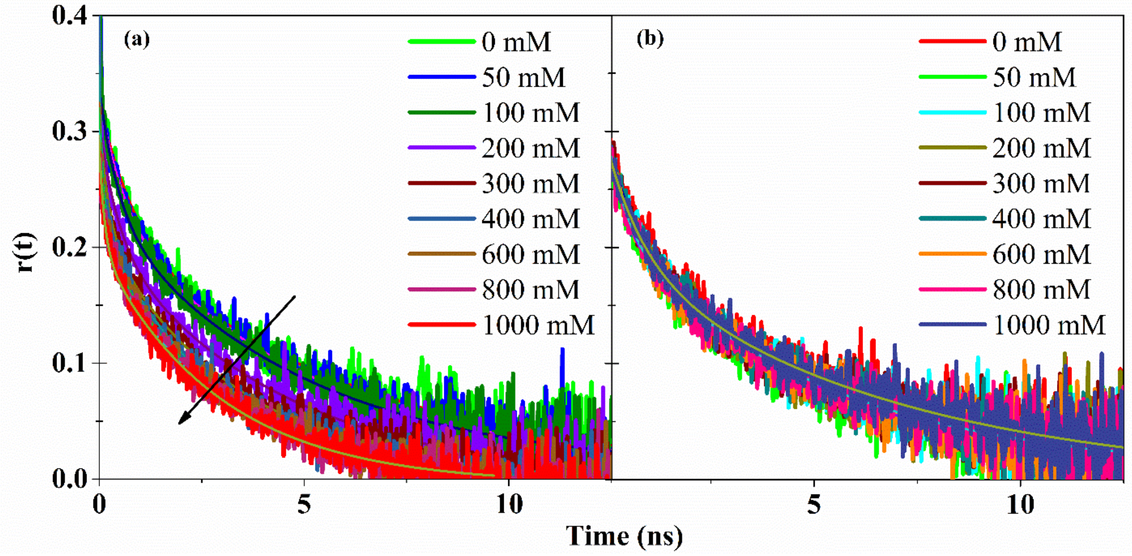

Figure 6.8. Fluorescence anisotropy decays of MPTS (λ_{ex} 375 nm, λ_{em} 440 nm) with increasing NaCl concentration in (a) premicellar 0.4 mM F127-6.4 mM SB12, (b) post micellar 4.0 mM F127-35 mM SB12.

6.2.5. ESPT Dynamics.

The TRANES intensity ratio and the deprotonation time vary with the concentration of SB12. First, it increases up to 6.4 mM concentration of SB12 and then decreases (Figure 6.9 and Table 6.2). The deprotonation time of HPTS for premicellar F127- 6.4 mM SB12 is 12.6 ns. In comparison, in micellar F127 – 35 mM SB12 assembly, it is 15 ns. The reason might be the different hydration levels near the probe. In both prePZC and postPZC, the deprotonation time decreases with an increase in NaCl concentration (Table 6.3). The deprotonation time decreases comparatively faster for the prePZC system with the variation of NaCl.

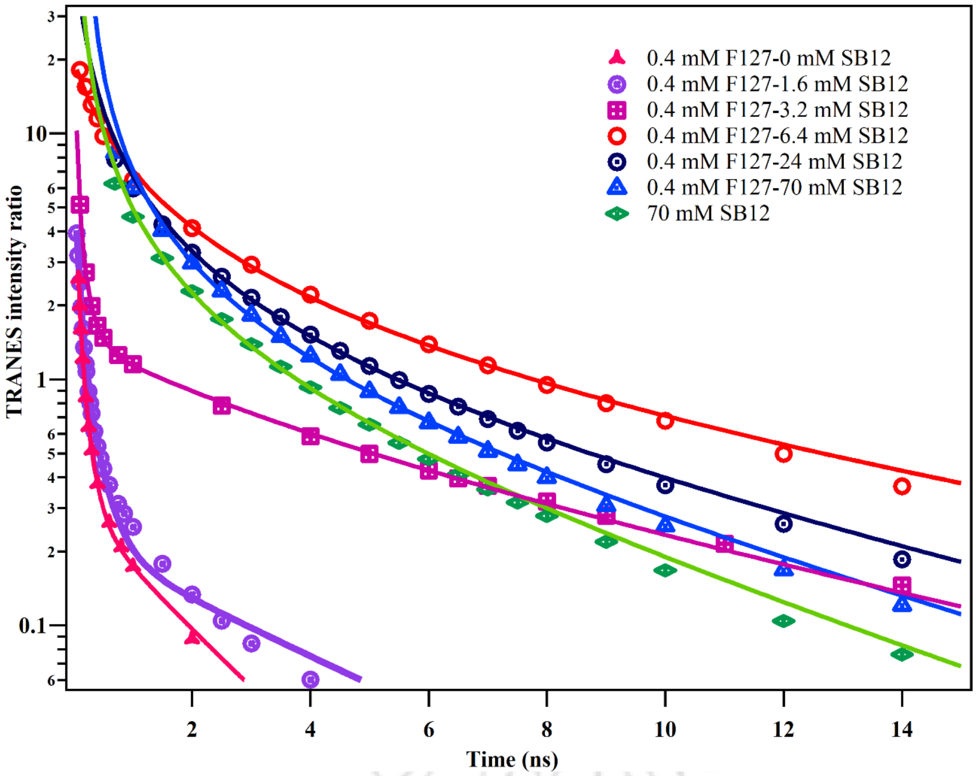

Figure 6.9. Variation of the TRANES intensity ratio (protonated/deprotonated) of HPTS in premicellar aggregates of F127 with varying SB12 concentration and in pure SB12 micelle.

The TRANES isoemissive point indicates whether there are two kinetically coupled moieties or more than two. It also indicates location changes of these kinetically coupled moieties due to composition changes.[220-221, 291] In the absence and presence of 1 M NaCl, the respective TRANES of HPTS for the two systems, prePZC and postPZC, have been constructed to identify the isoemissive point.

Table 6.2: ESPT time constants of HPTS obtained from TRANES intensity ratio in premicellar 0.4 mM F127- SB12 mixed assemblies and SB12 micelle. Error in the data ~ ± 3%.

System	SB12 (mM)	a_1	a_2	τ_1 (ns)	τ_2 (ns)	τ_d (ns)	τ_r (ns)	τ_{diff} (ns)
0.4 mM F127	0	0.76	0.24	0.16	1.85	0.21	1.44	0.82
	1.6	0.8	0.2	0.29	4.11	0.36	3.35	1.73
	3.2	0.41	0.59	0.198	8.72	0.47	3.69	0.36
	6.4	1		12.64		12.64		
	24	1		7.9		7.9		
	70	1		6.45		6.45		
Water	70	1		6		6		

Table 6.3: ESPT time constants of HPTS obtained from TRANES intensity ratio in F127-SB12 mixed assemblies with the variation of NaCl concentration.

System	NaCl (mM)	τ_d (ns)
0.4 mM F127- 6.4 mM SB12	0	12.64
	200	8.66
	400	7.62
	600	7.51
	1000	7.01
4.0 mM F127- 35 mM SB12	0	15.09
	200	11.62
	400	10.70
	600	10.25
	1000	9.22

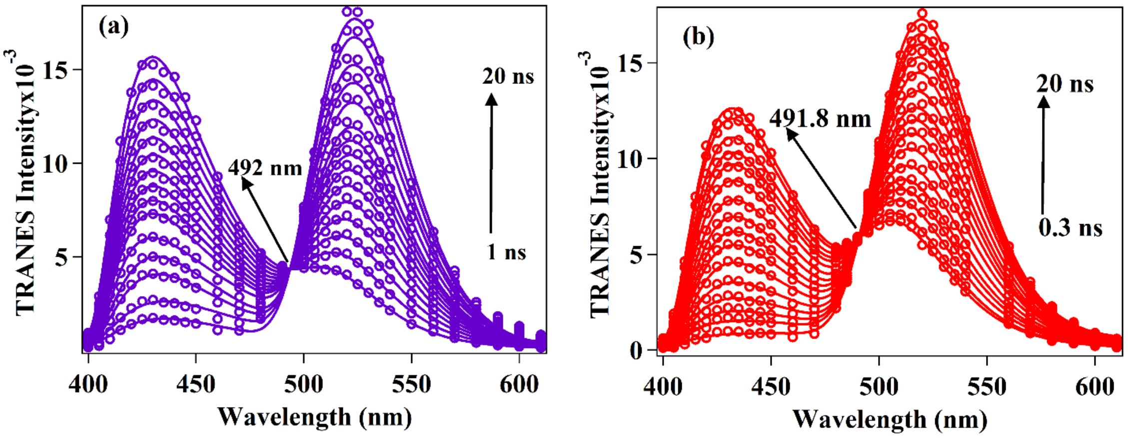

Figure 6.10. TRANES of HPTS in 0.4 mM F127 – 6.4 mM SB12 (a) in the absence of NaCl, (b) in the presence of 1000 mM NaCl.

In the premicellar F127- 6.4 mM SB12 assembly case, there is almost no change in isoemissive point location (~ 492 nm) in the TRANES in the absence and presence of 1 M NaCl (Figure 6.10).

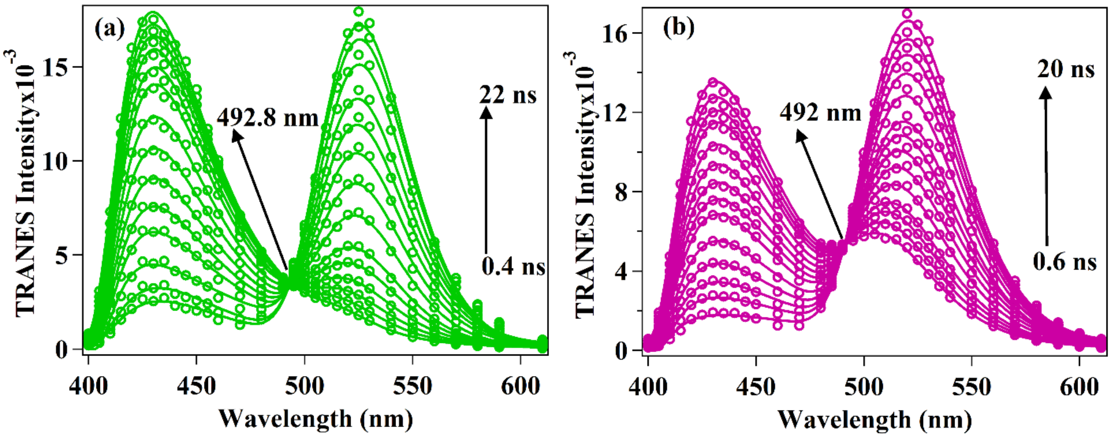

Figure 6.11. TRANES of HPTS in 4.0 mM F127 – 35 mM SB12 (a) in the absence of NaCl, (b) in the presence of 1000 mM NaCl.

Similarly, in the case of micellar F127- 35 mM SB12, irrespective of the presence or absence of NaCl, the isoemissive point (~ 492 nm) in the TRANES remains unaltered (Figure 6.11). So, in both cases, the unchanged location of the isoemissive points indicates that the kinetically coupled two moieties of HPTS (protonated and deprotonated) do not migrate or change location due to the presence of NaCl.

6.3. Discussion

The ESPT enhancement in the presence of higher salt concentrations indicates many possibilities (i) the micellar disintegration or reduced compactness of the assemblies which may expose the probe to the bulk media, (ii) water penetration may occur towards the core from the palisade layer of the interface and the micellar structure may swell, (iii) the migration of the probe may occur to the more hydrated regions of the assembly or (iv) reorientation or interfacial reorganization of surfactant headgroups, water molecules, changes in hydrogen bonding patterns due to the presence of salt.

In Steady-state anisotropy measurement, we have not observed much change in the r_{ss} value, a slight decrease for the prePZC system, and remains almost unchanged for postPZC. So, the steady-state anisotropy does not support the phenomena of mixed micellar disintegration, which would cause a drastic change in the r_{ss} value. Further, we have not observed any considerable changes in the hydrodynamic diameter in the DLS experiments due to variation of salts in these two particular mixed assemblies, which supports that the presence of salts does not disintegrate or break the compactness of the mixed assemblies (Figure 6.6).

Another option is that probe HPTS may migrate to the more hydrated region. Since there is no shift of isoemissive points in TRANES due to the addition of NaCl into the system (Figures 6.10 and 6.11), the probe location or distribution is not changing here.

Thus, although the ESPT dynamics become faster with the increase in NaCl concentrations, the micellar disintegration or size change does not occur. It becomes a little intriguing or contradictory compared to earlier reports to explain our data directly. Instead, a change in the interfacial hydration pattern and surfactant headgroup orientation or charge screening among the headgroups due to salt ions in the medium may be responsible for these observed changes.

Hence considering the drastic decrease in deprotonation times with increasing NaCl concentration in those compact assemblies but almost consistent steady-state and time-resolved anisotropy data, and assembly sizes, we can say that change in local interfacial hydration may lead to specific enhancement of ESPT dynamics (Scheme 6.2).

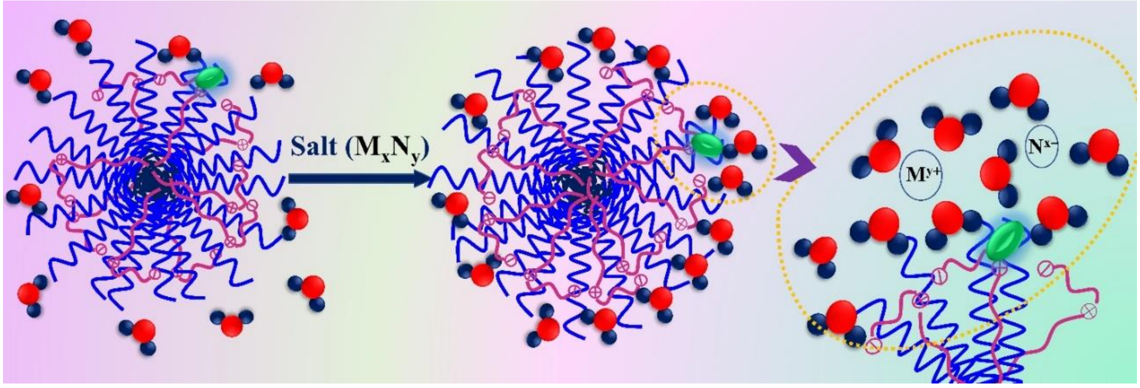

Scheme 6.2. Schematic representation of salt ionic strength induced hydration at the mixed micellar interface leading to ESPT rate enhancement.

No ESPT rate enhancement in the case of SB12 micellar assembly in the presence of salt may contradict our proposal. However, HPTS may experience a different location in the mixed micelle and SB12 micelle. The probe may stay in a zwitterionic or nonionic environment in the SB12 micellar interface. Thus, salt does not accumulate or perturb the hydration pattern due to this neutral surface potential. However, in the case of a mixed micellar interface, the two adjacent SB12 headgroups in the palisade layer of the mixed micelle are separated by the PEO chain end of the F127. So, in this case, the local surface potential may not be the same as the SB12 micelle interface, which triggers the salt to alter the local hydration patterns in the interface of the mixed micelle palisade layer, which may cause ESPT rate enhancement.

For other salts $CaCl_2$ and $AlCl_3$, the emission spectra also vary in the same way as in the case of NaCl, and the intensity ratio decreases even more strongly at a lower concentration zone than in the case of NaCl. In DLS, we also find no size change in that concentration regime (Figure 6.6). Regarding ionic strength, we get the same signature of ESPT modulation in the mixed assembly for all the salts NaCl, $CaCl_2$, and $AlCl_3$. However, the ratio value is somewhat different for each salt, which indicates that the hydration effect differs slightly (Figure 6.4).

The probable reason is that the pre-added salt in the F127 systems drains the thermodynamically trapped water molecules from the corona regions.[290] So, when we add the SB12 into it, there might be a lack of the positive entropic effect found in the absence of salt in the system. Hence, the interaction started at a higher concentration of SB12 than in salt-less conditions, or the interaction was not more favorable than earlier.

6.4. Summary and Conclusions

In summary, zwitterionic SB12 surfactant can form a compact mixed assembly with the triblock copolymer F127 at both premicellar and post-micellar concentrations. However, the SB12 concentration required for mixed micelle formation was lower in the case of premicellar F127, showing synergistic interaction. The situation differs for the post-micellar concentration of F127, where the most compact assembly requires much more SB12. Salting out can alter or transform the premicellar or micellar nonionic F127 structure. That is why initially added salt in the F127 assembly alters the interaction pattern of SB12. However, salt has no effect on zwitterionic SB12 micelle or the ESPT rate of HPTS in it.

Interestingly the presence of salt modulates the ESPT dynamics in the F127-SB12 mixed micellar interface by perturbing the hydration pattern in the palisade layer without altering its structural integrity. From the position of the fixed TRANES isoemissive point, both in the presence and absence of salt established that no probe migration occurs in the presence of salt in those mixed micelles. Again, the ionic strength of salts matters most compared to their nature of valency (NaCl, $CaCl_2$, or $AlCl_3$). Hence local hydration in the mixed micellar interface is responsible for the dynamical enhancement of ESPT. In summary, salt cannot change the overall size or compactness of the nonionic-zwitterionic surfactant mixed assembly instead disrupts the water network in the interfacial part of the system. So, we can say that this salt concentration regime can modulate an excited state reaction inside a mixed micellar entrapment without altering or hampering the probe location and host structure.

Chapter 7

Exploring Cationic Polyelectrolyte–Micelle Interaction via Excited-State Proton Transfer. Signatures of Probe Transfer.#

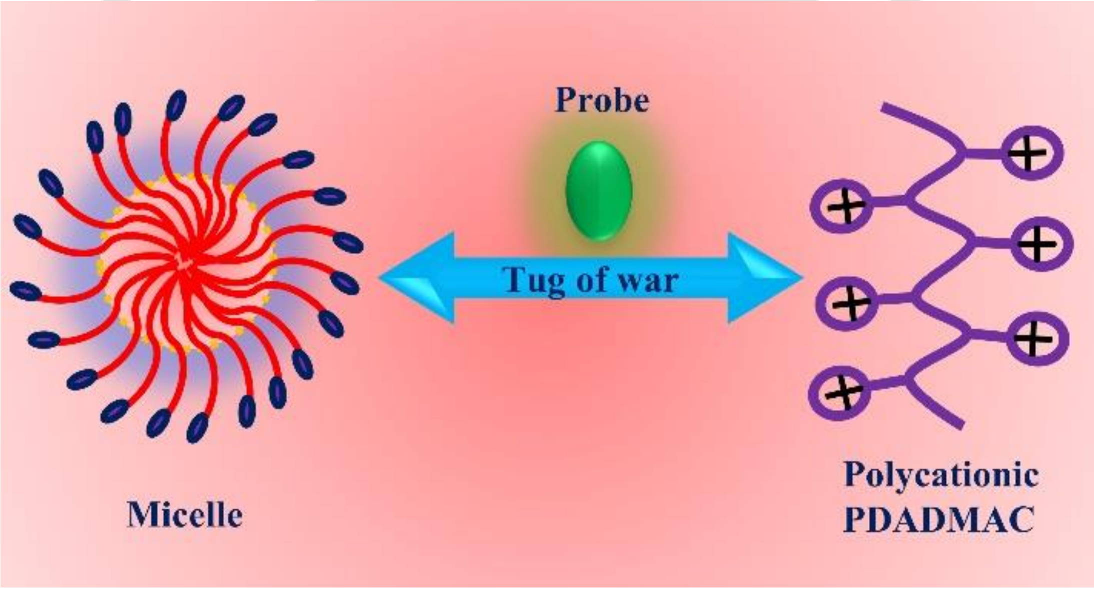

#This work has been published in ***Phys. Chem. Chem. Phys.*****,** 2023**, 25,** 2963-2977

Chapter 7: Exploring Cationic Polyelectrolyte–Micelle Interaction via Excited-State Proton Transfer. Signatures of Probe Transfer

7.1. Introduction

The investigation of the polyelectrolyte-micellar systems may provide new insights into the interaction among polyionic biomolecules and molecular drug delivery vehicles.[292] Small chain ionic surfactants form mixed aggregates with polyelectrolytes of different charge properties.[46-47] Positive entropic enhancements due to the release of counterions or enthalpy components due to the electrostatic attractions among opposite charges may drive the interactions.[293-295] The formation and disassembly of these aggregates are often applied as pattern generation in biomolecular sensing,[296] nanoreactors,[297] and shape-charge controlled anisotropic nanomaterial synthesis nanoconfinement for catalysis,[298] coacervate entities,[299] and biomimicking moieties.[32, 41, 49, 51, 184, 295, 300] Polyelectrolyte-micelle interactions have been investigated extensively based on thermodynamics,[301] tensiometry,[302] conductivity,[33] zeta potential,[303] small-angle x-ray scattering (SAXS),[304] and neutron-reflectometry.[305]

In this investigation, we exploit the ESPT process of HPTS to investigate the interaction of a cationic polyelectrolyte, poly(diallyl dimethylammonium chloride) (PDADMAC), with micelles of differently charged surfactants. We have selected three surfactants: anionic SDS, cationic DTAB, and zwitterionic SB12, all owning the same alkyl (dodecyl) chain but differential headgroup charges. HPTS was incorporated into micellar assemblies, and emission modulation was followed upon adding the polycationic PDADMAC.

7.2. Results

7.2.1. Steady-State Spectra: The absorption spectrum of HPTS displays a maximum at 403 nm, characteristics of the protonated form in slightly acidic water (pH ~6). However, a gradual increase in PDADMAC concentration develops a prominent absorption band at ~455 nm, corresponding to the deprotonated form in water and SB12 micellar media. Interestingly, we found that the pH of the medium becomes more acidic in the presence of PDADMAC. The pH of the medium was adjusted to 2.5 by adding HCl to suppress the ground-state proton transfer completely. However, at low PDADMAC concentrations (0.056 µM and 0.084 µM), a low but sustained absorbance was noticed in the region 440 nm to 500 nm. A probable reason for this may be the formation of large aggregates between the anionic HPTS and the cationic PDADMAC due to electrostatic attraction.[53-54, 306-307] Similar observations were also reported for the interaction between anionic HPTS and cationic surfactant CTAB at sub-micellar concentrations. In cationic DTAB micelles, the absorption spectra remain unaltered in the presence of PDADMAC. However, turbidity arises with the addition of PDADMAC into anionic SDS micelles.[54] Note that pH lowering was unnecessary for this micellar medium, indicating that PDADMAC addition does not significantly perturb protonation equilibrium in these micelles.

As discussed in chapter 3, HPTS shows a faint emission band at 440 nm and a prominent emission band at 510 nm in water, representing the protonated and deprotonated species. However, in cationic DTAB and zwitterionic SB12 micelles, HPTS manifests severe suppression of the ESPT process.[13] The protonated emission band is comparable to the deprotonated emission band in these micelles. In contrast, the emission spectrum in anionic SDS micelles is very similar to water, signifying an insignificant effect of micelle on the ESPT.

In the present investigation, we studied the spectral modulation of HPTS in water, zwitterionic micelle SB12, cationic micelle DTAB, and anionic micelle SDS at different concentrations of PDADMAC. Variation of PDADMAC concentrations in water leads to an anomalous modulation of the emission spectrum; the emission intensity first quenches up to 0.084 µM. After that, emission recovery occurs gradually and almost regains its initial spectral intensity at high PDADMAC concentration (Figure 7.1a and 7.1b). The addition of PDADMAC to the SB12 micelle initially leads to the quenching of both the emission bands up to an intermediate concentration, and further addition of PDADMAC recovers the emission intensities of the two bands but not in an identical fashion; the deprotonated band recovers its intensity much more effectively than the protonated one (Figures 7.1c,7.1d and 7.2a).

The overall integrated intensity decreases gradually up to 0.084 µM, and after that, increases up to 2.1 µM. The modulation of integrated intensity against PDADMAC concentration was very similar in water and SB12 micelle, suggesting that the photoacid may migrate from the SB12 micelle to the PDADMAC interface, experiencing an identical environment.

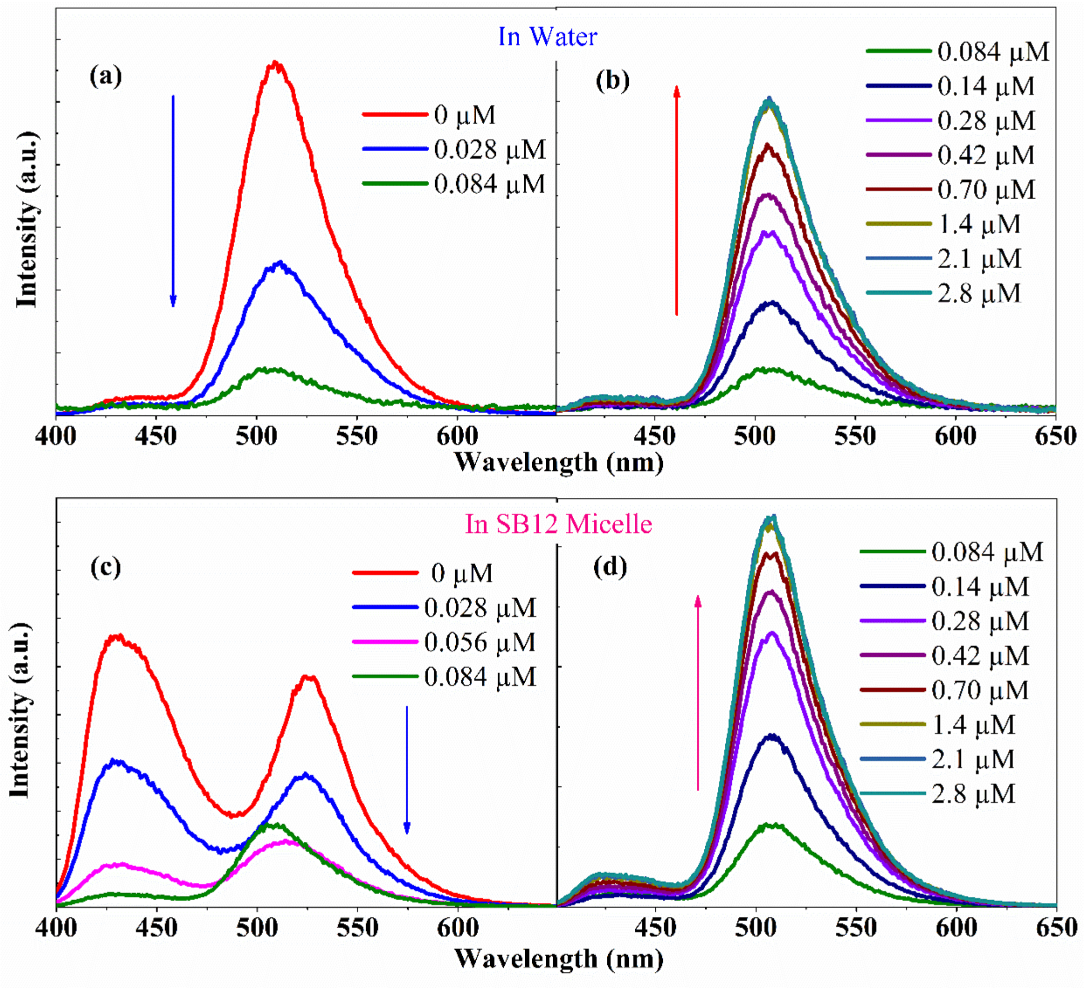

Figure 7.1. Emission spectra of HPTS in water (a and b) and PDADMAC solution-SB12 micellar interface (c and d) with increasing concentration of PDADMAC at 25^{0}±1 C. pH of the medium is 2.5.

In the case of the DTAB micellar solution, the emission spectrum hardly changes the intensities or intensity ratio. Thus, HPTS might stay confined in the micellar interface at all PDADMAC concentrations. In the SDS micellar medium, the emission band of HPTS remains very similar to the emission spectrum in water, indicating that HPTS remains in water at all PDADMAC concentrations.

The emission intensity ratio of the protonated to deprotonated band indicates the feasibility of ESPT; a low ratio suggests a fast or favorable ESPT, while a higher value designates a slow or unfavorable ESPT (Chapter 1). The emission spectrum of HPTS displays an emission intensity ratio of 1.18 in the SB12 (10 mM) micellar medium. The addition of PDADMAC significantly affects the intensity ratio, decreasing it to ~ 0.07, indicating that ESPT becomes highly favorable at high concentrations (Figure 7.2a). Although the emission intensity ratio is very different in water and SB12 micelles without

PDADMAC, the intensity ratio follows very similar values after adding the polyelectrolyte (Figure 7.2a), reaffirming that HPTS may be sequestered from the micelle by the polyelectrolyte. The intensity ratio remains at a high (1.08) value in the DTAB micelle, even in the presence of PDADMAC. Also, there is no change in the emission intensity ratio for SDS micellar case (Figure 7.2a).

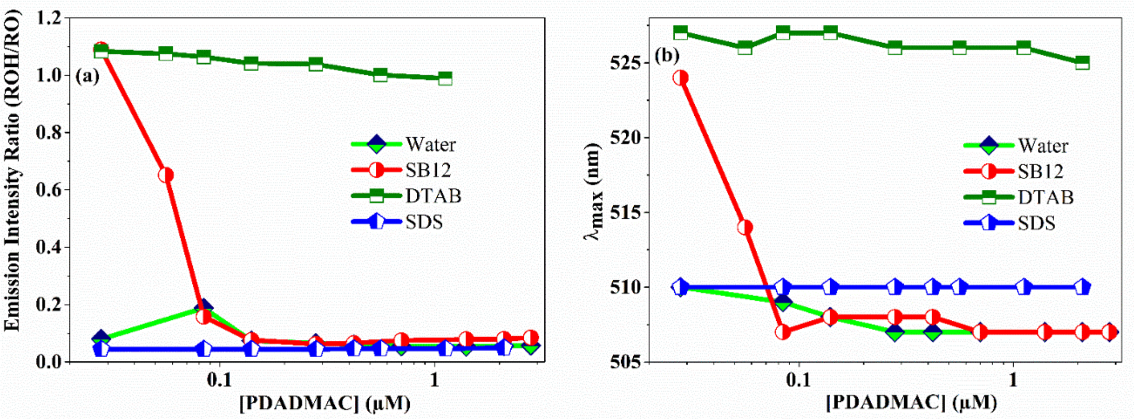

Figure 7.2. Variation of (a) intensity ratio (protonated/deprotonated) and (b) deprotonated band wavelength maxima of HPTS in water, SB12, DTAB, and SDS micellar media, respectively, at different PDADMAC concentrations.

The deprotonated emission maximum (λ_{max}) of HPTS is very sensitive to the microenvironment. For example, λ_{max} in water is at 511 nm, while it shifts remarkably to 526 nm in the SB12 micelle, consistent with earlier observation.[263] However, after adding PDADMAC to SB12 micelles, the deprotonated band undergoes a remarkable blue shift to 508 nm, similar to λ_{max} in the aqueous PDADMAC solution (Figure 7.2b). The observation supports our initial interpretation that the probe migrates to a different microenvironment.

Additionally, the deprotonated emission maximum in DTAB and SDS micellar environments remain at 526 nm and 510 nm, respectively, at all PDADMAC concentrations, indicating that the probe does not migrate from its initial location (Figure 7.2b).

Thus it is evident from the above analysis that there is no specific effect of PDADMAC on the emission properties of HPTS inside the DTAB and SDS micellar media, but in the SB12 micellar case, the probe migrates from micelle to PDADMAC. Thus, we have extended time-resolved studies rigorously for the SB12 micellar case only.

7.2.2. Fluorescence Anisotropy Decay. The anisotropy decay is biexponential in nature in PDADMAC medium (Figure 7.3c and Table 7.1). Note that low initial anisotropy (r_0) and somewhat irregular variation of the rotational time components at low PDADMAC concentrations (≤ 0.084 µM) in water may arise from the homo-FRET or energy hopping occurring within several closely-spaced MPTS molecules bound to cationic PDADMAC molecules consistent with the fluorescence quenching observed at low concentrations (Table 7.1).[308]

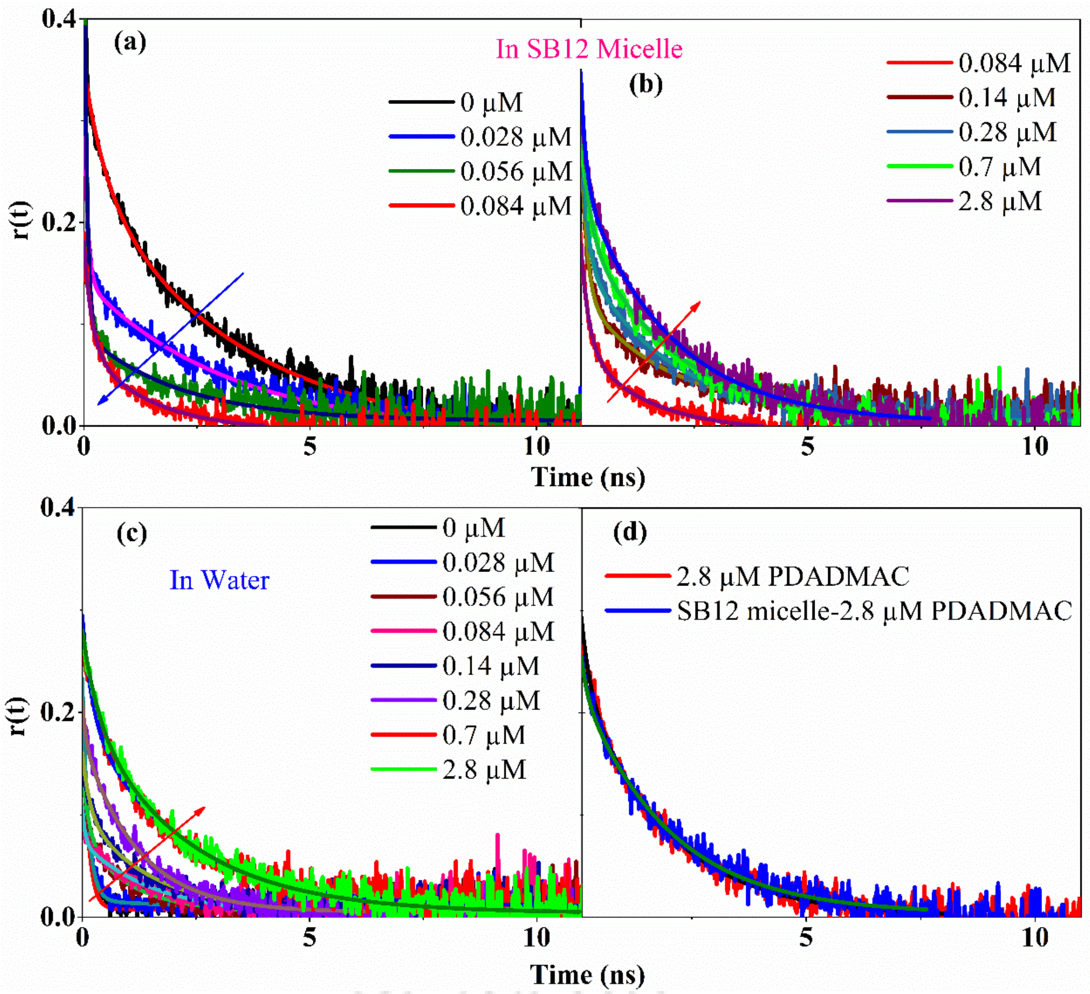

Figure 7.3. Fluorescence anisotropy decays of MPTS in (a and b) SB12 micelle (c) water with increasing PDADMAC concentrations. (d) similar anisotropy decays of MPTS in water and SB12 micelle in the presence of 2.8 µM PDADMAC. Excitation and emission wavelengths are at 375 nm and 440 nm, respectively. The pH of the medium is 2.5.

The fast component may arise from the free probe in water or from the wobbling motion of the probe in the PDADMAC assembly. However, the slow motion may arise exclusively from the HPTS bound to the PDADMAC assembly. The variation of the magnitude or contributions of the components was not very regular up to 0.084 µM

PDADMAC due to the drastic reduction of MPTS lifetime at low concentrations. Above this concentration, the contribution of the slow component increases gradually, indicating more probe sequestration by the polyelectrolyte assemblies (Figure 7.3c and Table 7.1).

The fluorescence anisotropy decay is biexponential in SB12 micelle with rotational components of 475 ps (28%) and 3300 ps (72%), possibly due to the "Wobbling-in-Cone" motion (chapter 2). The anisotropy decay becomes faster at low PDADMAC concentrations but slower at high concentrations of PDADMAC (Figures 7.3a and 7.3b). The contribution of the fast component (α_f) first increases and then decreases, while a reversed trend was observed for the slow component. The anomalous trend emphasizes that the probe transfers to polyelectrolyte assembly from micellar confinement (Table 7.1).

Table 7.1. Fluorescence anisotropy decay parameters of MPTS in water and SB12 micelle in the presence of different PDADMAC concentrations. Error in the data ~ ± 3%.

System	[PDADMAC] (μM)	**r_0**	**α_f**	**τ_f (ps)**	**α_s**	**τ_s (ps)**
Water	0	0.40		150		
	0.028	0.24	0.96	150	0.04	2520
	0.056	0.14	0.42	130	0.58	1050
	0.084	0.38	0.69	80	0.31	1230
	0.14	0.33	0.60	100	0.40	1260
	0.28	0.37	0.48	100	0.52	1410
	0.70	0.37	0.42	160	0.58	1800
	2.80	0.35	0.30	200	0.70	1860
SB12 micelle	0	0.35	0.28	475	0.72	3300
	0.028	0.29	0.49	90	0.51	3170
	0.056	0.39	0.78	80	0.22	2110
	0.084	0.24	0.68	170	0.32	1450
	0.14	0.37	0.64	120	0.36	1830
	0.28	0.36	0.65	115	0.35	1930
	0.70	0.33	0.40	170	0.60	2040
	2.80	0.37	0.35	140	0.65	2045

It is also interesting to note that at high PDADMAC concentrations (2.8 µM), the anisotropy decays are precisely the same in water and SB12 micellar systems (Figure 7.3d), indicating that the probe resides in the same environment. Thus, PDADMAC assembly at high concentrations can completely sequester the HPTS from water and SB12 micelle.

7.2.3. Dynamic Light Scattering (DLS). The hydrodynamic size of the assemblies at various PDADMAC concentrations was measured to determine the effect of the cationic polyelectrolyte on different micelles. The diameter does not change much at various PDADMAC concentrations in SB12 micelles (Figure 7.4), implying that the cationic polymer may not perturb the micelle significantly. Also, for the cationic DTAB micelle, the initial hydrodynamic size remains unchanged with the addition of PDADMAC.

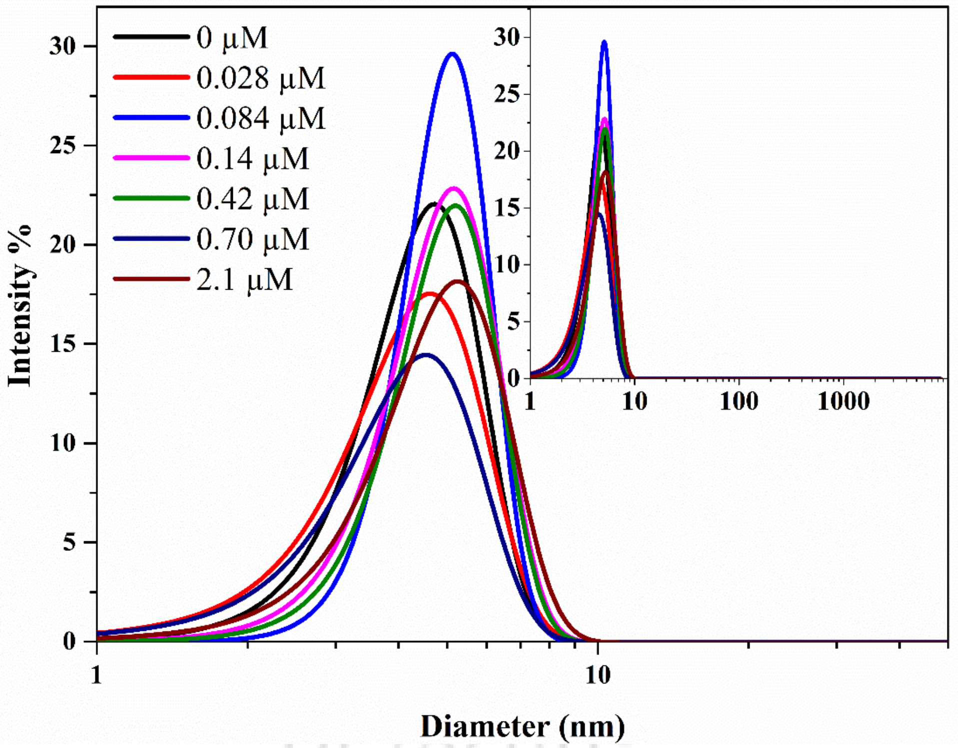

Figure 7.4. The hydrodynamic diameter of SB12 micelle in the presence of increasing PDADMAC concentration in the dynamic light scattering. The pH of the medium is 2.5 (Inset: Semilogarithmic plot of the DLS with full scale).

However, the result was very different in the anionic SDS micelle. The typical micellar diameter was ~ 5 nm, but it increased to 250-300 nm with the addition of PDADMAC. The giant assembly substantiates that the anionic SDS micelle strongly interacts with polycationic PDADMAC.

7.2.4. TRANES Analysis and ESPT Dynamics: The steady-state emission and anisotropy decay indicate probe migration from SB12 micelle to polycationic PDADMAC interface. Further evaluation of the ESPT dynamics can reinforce the probe transfer phenomena. TRANES is an effective tool to confirm the distribution of the fluorophore and ESPT dynamics. The occurrence of isoemissive points can provide insight into the probe location,[221, 309] while analyzing the intensity ratio of the protonated to deprotonated bands in TRANES can provide accurate ESPT dynamics.[69, 220-222]

The TRANES of HPTS in water shows a distinct isoemissive point at 485 nm. The TRANES displays usual deprotonation kinetics, with the protonated band decreasing and the deprotonated band increasing with time. The TRANES intensity ratio of the protonated to deprotonated band follows equation (2.17) (Chapter 2). ESPT kinetic parameters of HPTS in water obtained from the fittings of the protonated to the deprotonated band of TRANES intensities have the characteristics deprotonation time (τ_d), recombination time (τ_r) and diffusion time (τ_{diff}) of 180 ps, 1470 ps, and 2390 ps, respectively (Table 7.2). The individual intensities of the protonated and deprotonated forms in the TRANES band follow single exponential behavior consistent with earlier reports.

The TRANES displays a distinct isoemissive point at 498 nm in SB12 micellar medium. The ESPT dynamics is very slow (~6 ns) as extracted from the TRANES ratio or individual protonated and deprotonated TRANES intensities.

In an aqueous medium with a lower PDADMAC concentration regime, the isoemissive point appears at the same wavelength (485 nm) as in water. The ESPT dynamics is also very similar to water, but at higher concentrations, the isoemissive point shifts to a lower wavelength (480 nm).

A distinct isoemissive point suggests that a probe may exist in two emissive forms in the excited state or distribute in two different regions.[220-221] Since the ESPT probe exists in two forms (protonated and deprotonated) in the excited state, a single isoemissive point implies that the probe must present in a uniform environment.

The knowledge of the TRANES pattern, the position of the isoemissive point, and the ESPT dynamics of HPTS in water, in an aqueous PDADMAC solution, and inside the SB12 micellar medium helps us to understand the complex TRANES pattern and dynamics of HPTS in SB12 micelles at different PDADMAC concentrations.

Three distinct PDADMAC concentrations were chosen to construct the TRANES; these are at the point where quenching started (0.056 µM), at the point where quenching is highest (0.084 µM), and at a high concentration (2.1 µM) where intensity recovers fully.

(i) Low PDADMAC Concentration (0.056 µM): For 0.056 µM PDADMAC in the micellar SB12, the TRANES show an interesting pattern; the isoemissive point shifts with time. For clarity, the TRANES was grouped into three-time regimes (0.01 - 0.15 ns, 0.20 – 1.0 ns, and 2 - 16 ns). In the initial time regime (0.01 to 0.15 ns), TRANES shows an isoemissive point at 480 nm and while the long-time regime TRANES shows an isoemissive point at 500 nm (Figure 7.5 and Table 7.2). In the intermediate times (0.20 ns to 1 ns), the TRANES do not show any particular isoemissive point.

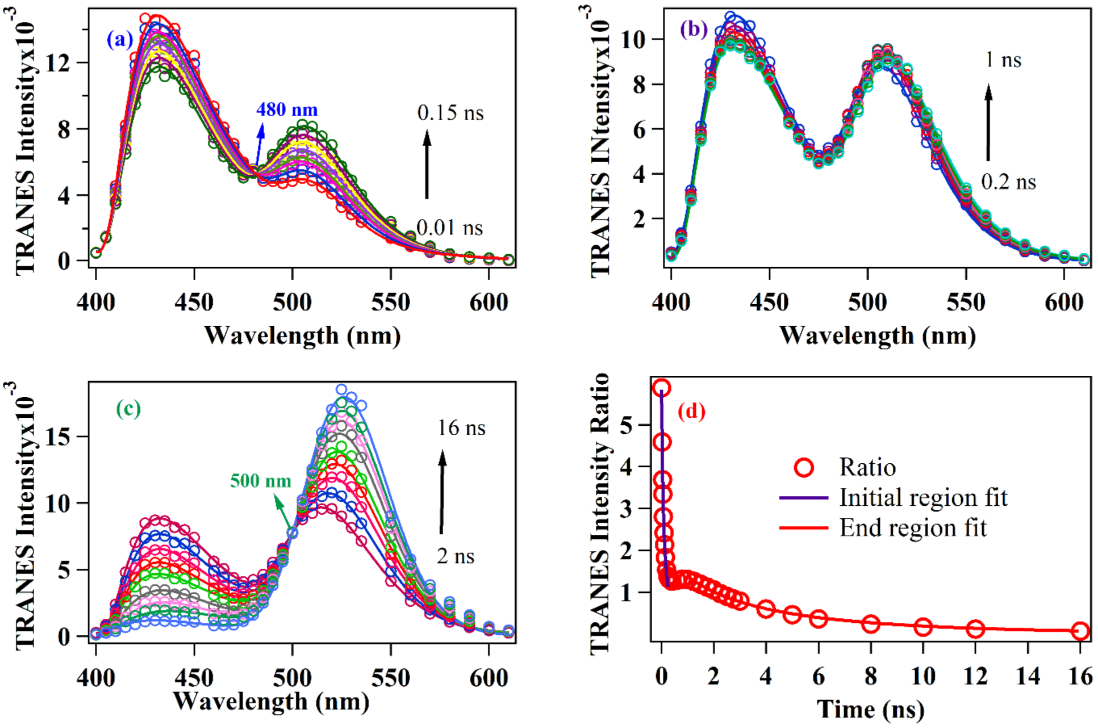

Figure 7.5. TRANES profile of HPTS in micellar SB12- 0.056 µM PDADMAC with different time zone (a) 0.01 ns to 0.15 ns (b) 0.2 ns 1 ns (c) 2 ns to 16 ns with two isoemissive points and (d) TRANES intensity ratio. The pH of the medium is 2.5.

The isoemissive point at 480 nm observed in the early time window differs from the isoemissive point in neat SB12 micelle or bulk water but is similar to the isoemissive point observed for the aqueous PDADMAC solution. The other isoemissive point at 500 nm observed in the late time regime (2-16 ns) resembles the neat SB12 micelle case. The intermediate time zone of 0.20 ns to 1 ns signifies that the probes may be distributed over various regions.

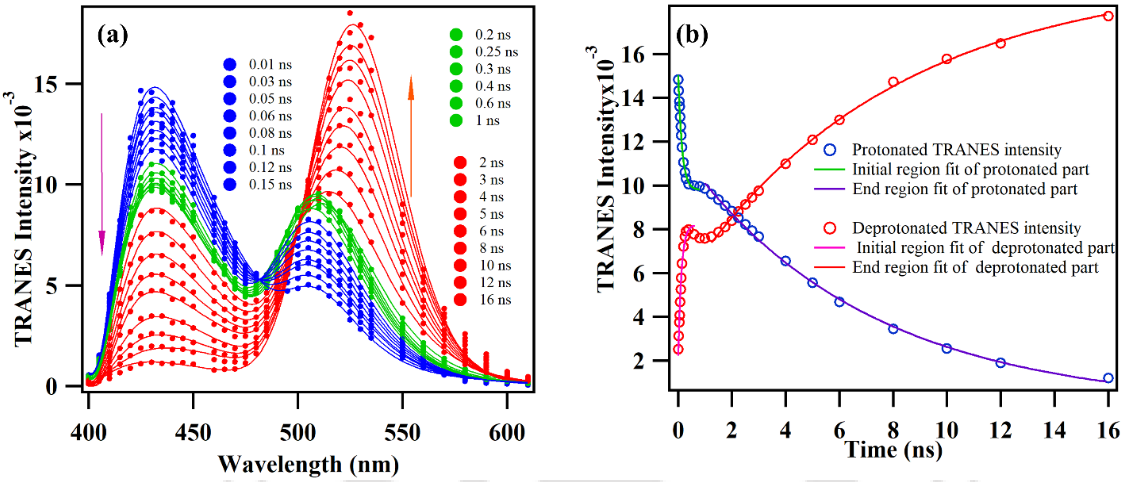

Figure 7.6. (a) The complete TRANES and (b) fitted time evolution of protonated and deprotonated moieties obtained from TRANES of HPTS in micellar SB12-0.056 µM PDADMAC media.

We also find two contrasting dynamics in the time evolution of the protonated and deprotonated intensities of TRANES. The early time region (<1 ns) follows faster dynamics for both the protonated and deprotonated species. In comparison, the time evolution becomes slower in the longer time part (1 ns to 16 ns) (Figure 7.6). Thus, we fit the TRANES intensity ratio separately in two different segments, the early and late parts (Figure 7.5d). The deprotonation time constants are 500 ps and 6970 ps for the respective segments, out of which the 6970 ps is similar to the deprotonation time in SB12 micelle, and the 500 ps component might arise from the partially bound probe in the PDADMAC interface (Table 7.2). Figure 7.6 displays the complete TRANES and the time evolution of protonated and deprotonated moieties with segmental fittings. Hence, based on this evidence, we can say that photoacid is partitioned between two distinct locations in our system.

(ii) Intermediate PDADMAC Concentration (0.084 µM). At the intermediate concentration (0.084 µM) of PDADMAC, where quenching was maximum in SB12 micelle, the TRANES may be grouped into three different time regimes (0.10 – 0.18 ns, 0.20 – 2 ns, and 3 – 10 ns), each showing a distinct isoemissive point at 478 nm, 482 nm, and 488 nm, respectively (Figure 7.7 and Table 7.2).

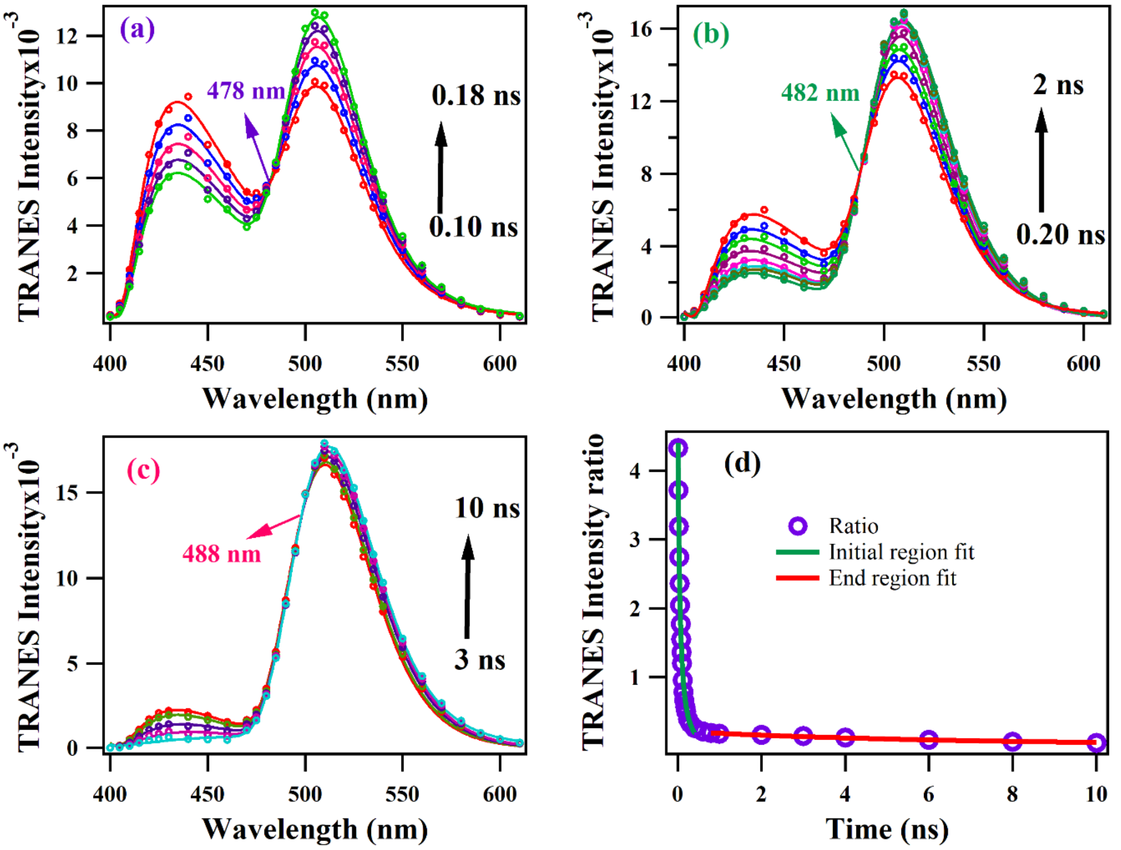

Figure 7.7. TRANES profile of HPTS in micellar SB12- 0.084 µM PDADMAC with different time zone (a) 0.10 ns 0.18 ns (b) 0.2 ns to 2 ns (c) 3 ns to 10 ns with three isoemissive points and (d) variation of TRANES emission intensity ratio of protonated/deprotonated (ROH/RO) forms with time. The pH of the medium is 2.5.

The isoemissive points at 478 nm and 482 nm are different from the isoemissive point characteristics of SB12 micelle and are similar to that in the aqueous PDADMAC medium. However, the 488 nm isoemissive point indicates that a fraction number of probes remains in the micelle.

The TRANES intensity ratio cannot be fitted fully with conventional models; instead, the segmental fitting was performed for the initial and the end portions (Figure 7.7d). The latter part of the TRANES ratio decay displays an SB12 micellar-like slow deprotonation time component of 7500 ps. The initial part reveals a fast component of 240 ps (Table 7.2), possibly due to the ESPT within the PDADMAC assembly. The probe is mainly exposed to the PDADMAC assembly at this concentration, whereas some may still be in the SB12 micelle. So, the three isoemissive points at 478 nm, 482 nm, and 488 nm indicate that HPTS molecules are distributed over a vast region among the SB12 micelle and PDADMAC interface.

(iii) High PDADMAC Concentration (2.1 µM): TRANES shows an isoemissive point at 480 nm at high PDADMAC concentration in SB12 micellar medium (Figure 7.8a), which is precisely the isoemissive point at the same wavelength in the absence of SB12 micelle. The TRANES intensity ratios are similar to the aqueous PDADMAC medium (Figure 7.8b). Table 7.2 supplies the fit parameters of the TRANES ratio decay. The results show that HPTS experiences a similar environment at high PDADMAC concentration in the absence and presence of SB12 micelle. Thus, HPTS may be sequestered completely at high concentrations by the PDADMAC assembly.

We can fit the TRANES intensity ratio for this particular case with a reversible two-step ESPT kinetic model (Scheme 1.6 in chapter 1, equation 2.17 in Chapter 2) and obtain similar time components for deprotonation, recombination, and diffusion for both the absence and presence of the SB12 micellar system (Table 7.2). Thus, no perturbation to the ESPT kinetics was observed from the SB12 micelle.

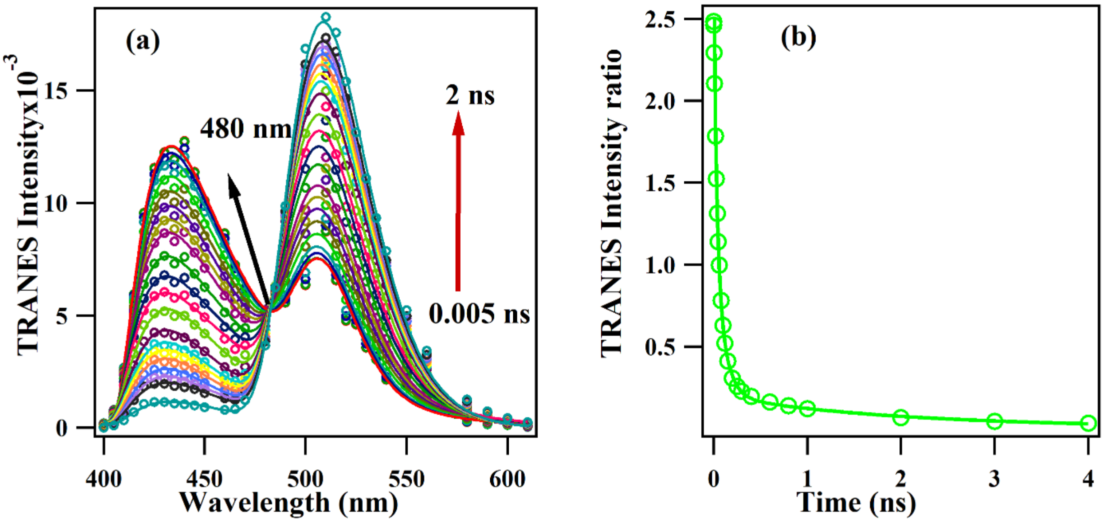

Figure 7.8. TRANES profile of HPTS in micellar SB12- 2.1 µM PDADMAC at different times with a single isoemissive point at 480 nm and (b) The decay of TRANES emission intensity ratio, protonated/deprotonated (ROH/RO) with time. The pH of the medium was 2.5.

We have also constructed the TRANES for DTAB micelle in the absence and presence of 1.4 µM PDADMAC. For both cases, we obtained the same isoemissive point at 495 nm, with deprotonation time in the range of 5500 – 5600 ps (Figure 7.9, Table 7.2), which substantiates that there is no effect of PDADMAC on the micelle entrapped photoacid.

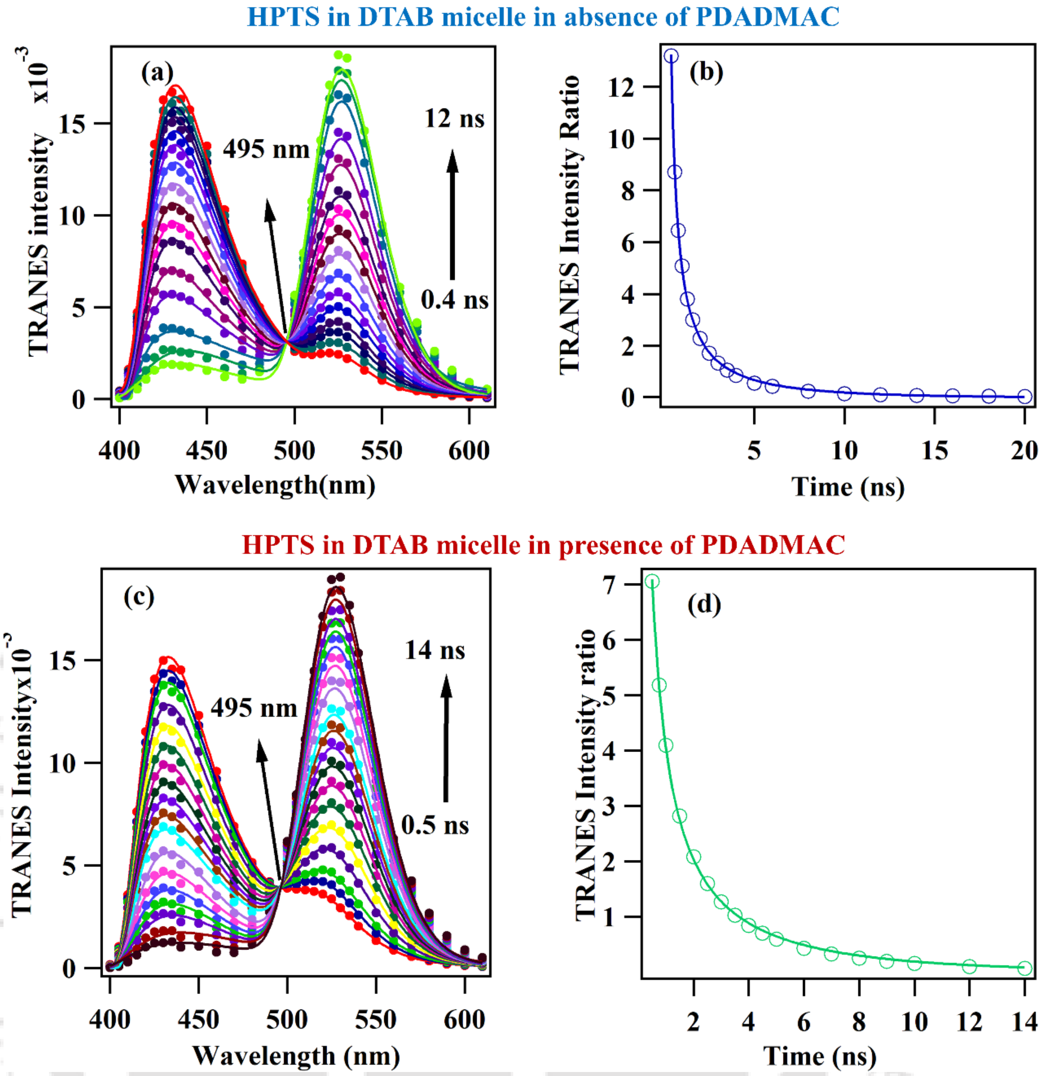

Figure 7.9. TRANES of HPTS in DTAB micelle at different times (a) in the absence (c) in the presence of PDADMAC and the variation of TRANES intensity ratio of protonated/deprotonated band of HPTS in DTAB micellar media with time (b) in the absence (d) in the presence of PDADMAC. The pH of the medium was ~ 5.6.

Similarly, we also constructed TRANES in anionic SDS micelle in both the absence and presence of PDADMAC. For both cases, the isoemissive point (485 nm) and deprotonation time (200 ps) were alike (Figure 7.10 and Table 7.2), which supports that the probe stays in bulk only rather than in the SDS micelle or the PDADMAC interface.

HPTS in SDS micelle in absence of PDADMAC

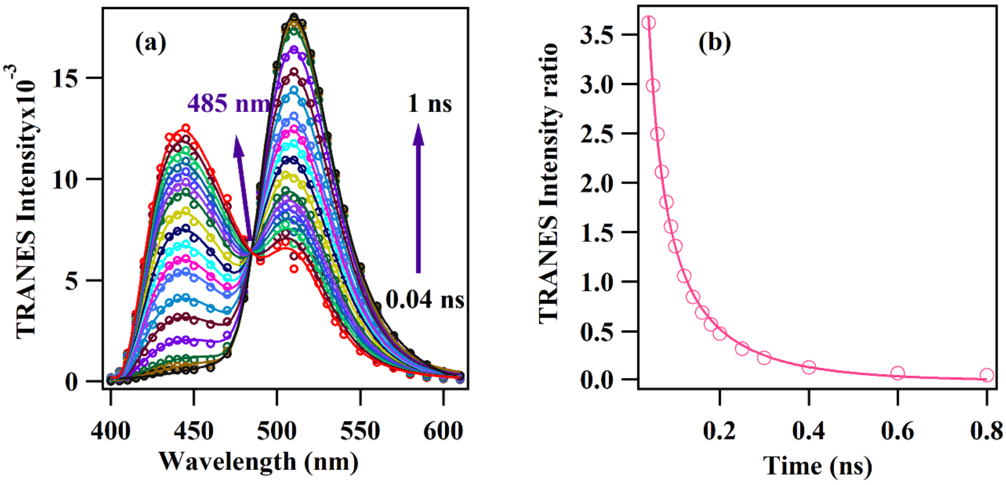

HPTS in SDS micelle in presence of PDADMAC

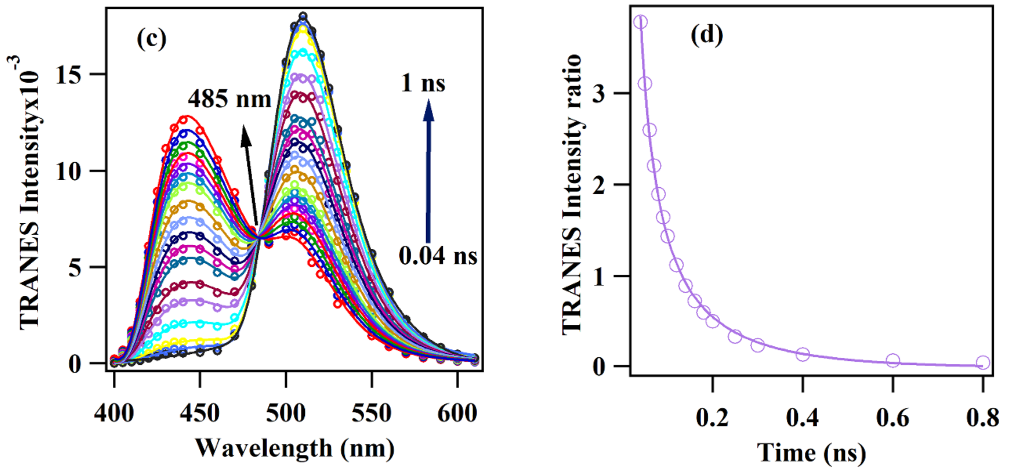

Figure 7.10. TRANES of HPTS in SDS micelle at different times (a) in the absence (c) in the presence of PDADMAC and the variation of TRANES intensity ratio of protonated/deprotonated band of HPTS in SDS micellar media with time (b) in the absence (d) in the presence of PDADMAC. The pH of the medium was ~ 5.6.

Table 7.2. Characteristics of TRANES and ESPT kinetic parameters (isoemissive points, time window of isoemissive point, time components, deprotonation times, recombination times, and diffusion times) in different systems. Error in the data ~ ± 3%.

System	**[PDADMAC] (μM)**	**Isoemissive Point (nm)**	**Time window (ns)**	**τ_1 (ps)**	**τ_2 (ps)**	**τ_d (ps)**	**τ_r (ps)**	**τ_{diff} (ps)**
Water	0	485	Full	170	1600	180	1470	2390
	0.028	485	Full	180		180	-	-
	2.1	480	full	100	2130	100	1760	520
SB12 Micelle	0	498	full	6600		6600	-	-
	0.056	480 500	0.01-0.15 2-16	500 6970		500 6970	- -	- -
	0.084	478 482 488	0.10-0.18 0.20-2 3-10	240 - 7500		240 - 7500	- -	- -
	2.1	480	full	100	2200	100	1760	430
DTAB Micelle	0	495	full	5540		5540	-	-
	1.4	495	full	5600		5600	-	-
SDS Micelle	0	485	full	190		190	-	-
	0.14	485	full	200		200	-	-

7.3. Discussion

In this investigation, we observed the quenching of HPTS emission in the presence of PDADMAC in water and various micelles. We have also shown earlier that HPTS emission in water undergoes very strong quenching upon adding DTAB or CTAB surfactants at a concentration well below the critical micellar concentration (CMC).[307] The quenching was attributed to the close association of several HPTS molecules within the premicellar aggregate resulting in homo-FRET.[307] Such fluorescence modulation was also observed for the interaction of pyrenetetrasulfonate with cationic polyelectrolytes poly(allylamine hydrochloride) (PAH) and PDADMAC.[53] The electrostatically favorable interaction between the oppositely charged groups of the anionic fluorophore and the cationic polyelectrolytes assists proximity of the pyrene aromatic rings resulting in π-stacking interaction.[53] The intramolecular stacking interaction was further supported by the formation of excimer fluorescence and strong quenching of monomeric fluorescence.[53] Although no excimer fluorescence was observed in our cases, the fluorescence quenching may be mediated by π-stacking interaction considering the similarity between the fluorophores HPTS and pyrene tetrasulfonate.

The strong quenching at low concentrations of PDADMAC can be explained by the sequestration of HPTS by the polyelectrolyte, increasing the local concentration of the probe molecules along the polymer chain. Also, physical crosslinking of the negatively charged probe and polycationic PDADMAC might happen, leading to the proximity of the probes in the polymeric thread. Whenever we excite the system at this particular composition, radiative energy transfers from protonated form to the instantaneously formed deprotonated moieties, as those are nearby. The process occurs in an energy-hopping fashion. Due to this energy hopping, self-quenching might happen, which results in a decrease in emission intensity.[53, 308] As the polyelectrolyte concentration further increases, the probe molecules can redistribute along the polymer chain due to the adequate number of binding sites available in the polyelectrolyte (Scheme 7.1).[53]

.

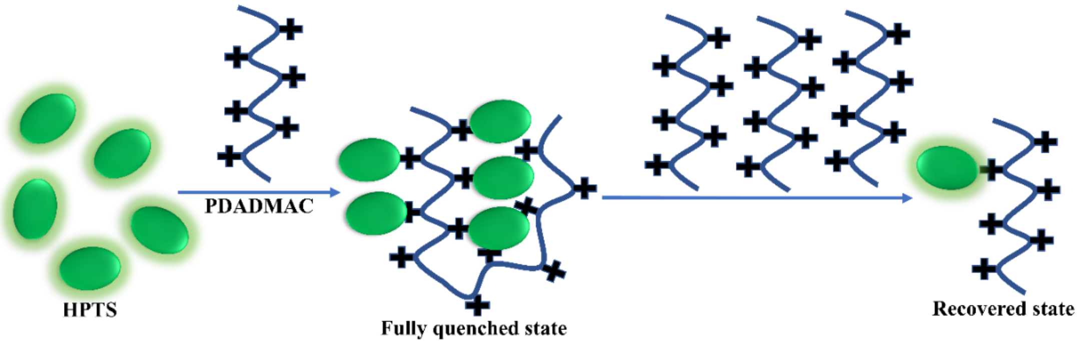

Scheme 7.1. Schematic representation of quenching and emission recovery of probe HPTS with increasing PDADMAC concentration in water.

The HPTS concentration was very low (4 μM) to avoid the inner filter effect, and no micelle contains more than one probe molecule to avoid ambiguous kinetics from location heterogeneity. As each polyelectrolyte contains many cationic sites for probe binding, we definitely have to take polyelectrolyte concentration much lower than the probe. Otherwise, we will not visualize the probe transfer process effectively.

The similarity in the emission intensity ratio of protonated/deprotonated bands of HPTS in the presence and absence of SB12 micellar media with increasing PDADMAC concentration depicts the migration and redistribution of HPTS from SB12 micelle or aqueous media to PDADMAC polycationic thread interface. Moreover, the deprotonated emission maximum of HPTS also shows a blue shift from 526 nm to 508 nm with increasing PDADMAC concentration (Figure 7.2b). Both these observations denote the movement of the probe from the SB12 micelle to the PDADMAC interface. For the DTAB and SDS cases, the absence of any deprotonated emission maxima shift indicates no such migration. The DLS measurement helps to ascertain the hydrodynamic diameters of the micelles or any new assemblies formed after the addition of PDADMAC. There is no change in the diameter of the SB12 micelle in the presence of PDADMAC, so the micelle remains intact throughout the model drug-like probe HPTS sequestration process. Thus, the model drug delivers successfully to the target bio-mimic polycationic PDADMAC.

The TRANES observations of the isoemissive points, their shifts in different time zones, and the similarity in deprotonation times in the respective systems further cemented our proposed probe migration phenomena. The unique property of TRANES is that the position of isoemissive points determines the probe location in a particular system, and the TRANES intensity ratio provides the excited state dynamical nature in terms of the rate constants or deprotonation times. So, correlating all these, we can locate the probe and analyze its excited state dynamics finely.

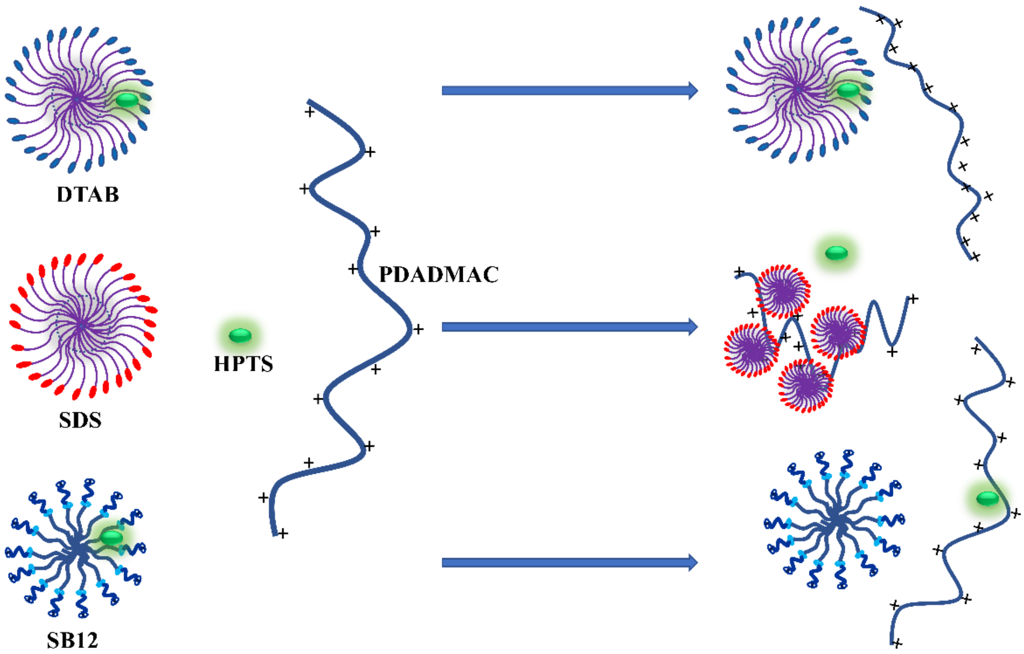

Scheme 7.2. Schematic presenting the location of HPTS after adding the polycationic PDADMAC to various micelles.

This investigation shows that the electrostatic interaction becomes vital in the presence of a cationic polyelectrolyte. The cationic micelle provides better protection to the anionic probe and repels the cationic polyelectrolyte, which prevents the exchange of the photoacid from the cationic micelle to the polyelectrolyte interface. However, the zwitterionic micelle cannot compete with the cationic polyelectrolyte to keep HPTS inside.

So far in the investigation, PDADMAC was applied to HPTS entrapped in micelles. Now we check the reverse addition, that is, the addition of the surfactants to PDADMAC in the presence of HPTS. In the case of SB12, there is no effect on the emission spectrum of HPTS; it remained attached to PDADMAC. However, in the case of DTAB addition to PDADMAC containing bound HPTS, the spectrum regained the emission characteristic the same as in DTAB encapsulation, which reveals the migration of the probe to the DTAB micelle. In the case of SDS, the quenching disappears upon adding surfactants to the PDADMAC, which substantiates the preferential interaction of SDS with PDADMAC. The probe is removed from the polyelectrolyte; hence becomes free into the solution. So, the reverse addition procedure of PDADMAC and surfactants also established our proposal of probe migration from the PDADMAC interface to the DTAB micelle and probe expulsion from the PDADMAC interface to bulk due to SDS-PDADMAC interaction. Interestingly, there is no effect of SB12 micelle on the probe already bound to the PDADMAC interface, revealing that SB12 micelles cannot compete with PDADMAC assembly in terms of electrostatic interaction.

The micellar formulation often mimics many biological systems, and the polyelectrolyte molecules resemble biomacromolecules like protein, DNA, and RNA. So, an ionic probe that selectively migrates to its preferable location can be used as a model drug in micellar, polycationic interfaces. In the present study, we intend to elucidate that the probe in these systems is compelled to shuttle between the two assemblies depending on the electrostatic force it experiences. Depending on the molecular environment, it can be modeled as the drug being delivered or sequestered.

7.4. Summary and Conclusions

In summary, the polycationic molecule PDADMAC can sequester a model drug-cum-fluorophore HPTS without hampering the structure of the host zwitterionic micelle. The sequestration process was evident from the shift of the isoemissive point in TRANES. On the contrary, cationic DTAB micelles do not interact with PDADMAC or allow the PDADMAC to sequester the probe entrapped inside the micellar environment. Instead, DTAB can sequester the fluorophore from the PDADMAC interface. The anionic SDS micelles interact with PDADMAC leaving the fluorophore in bulk hence no modulation of the ESPT dynamics. This study gives insight into the location-dependent dynamics of ESPT and the migration of the probe, which is vivid from TRANES isoemissive points and intensity ratio. It also opens a new challenge to elucidate the detailed dynamics when multiple partitioning is possible. Thus, it gives an approach for applying micellar systems as drug delivery/drug sequestration vehicles for biomimicking polyionic molecules. Also, the polyelectrolyte molecules can act as an environmentally hazardous dye removal agent for treating wastewater

References

1. Molla, M. R.; Ghosh, S., Aqueous self-assembly of chromophore-conjugated amphiphiles. *Phys. Chem. Chem. Phys.* **2014,** *16* (48), 26672-26683.
2. Zhu, J.-H.; Yu, C.; Chen, Y.; Shin, J.; Cao, Q.-Y.; Kim, J. S., A self-assembled amphiphilic imidazolium-based ATP probe. *Chem. commun.* **2017,** *53* (31), 4342-4345.
3. Ariga, K.; Hill, J. P.; Ji, Q., Biomaterials and Biofunctionality in Layered Macromolecular Assemblies. *Macromol. Biosci.* **2008,** *8* (11), 981-990.
4. Ariga, K.; McShane, M.; Lvov, Y. M.; Ji, Q.; Hill, J. P., Layer-by-layer assembly for drug delivery and related applications. *Expert Opin Drug Deliv* **2011,** *8* (5), 633-644.
5. Monte, M. J.; Marin, J. J.; Antelo, A.; Vazquez-Tato, J., Bile acids: chemistry, physiology, and pathophysiology. *World J. Gastroenterol.* **2009,** *15* (7), 804-16.
6. Mukhopadhyay, S.; Maitra, U., Chemistry and biology of bile acids. *Curr. Sci.* **2004,** *87*, 1666-1683.
7. Shao, Q.; Jiang, S., Molecular Understanding and Design of Zwitterionic Materials. *Adv. Mater.* **2015,** *27* (1), 15-26.
8. Raghavan, S. R.; Kaler, E. W., Highly Viscoelastic Wormlike Micellar Solutions Formed by Cationic Surfactants with Long Unsaturated Tails. *Langmuir* **2001,** *17* (2), 300-306.
9. Danino, D.; Talmon, Y.; Levy, H.; Beinert, G.; Zana, R., Branched Threadlike Micelles in an Aqueous Solution of a Trimeric Surfactant. *Science* **1995,** *269* (5229), 1420-1421.
10. Shrestha, R. G.; Shrestha, L. K.; Aramaki, K., Formation of wormlike micelle in a mixed amino-acid based anionic surfactant and cationic surfactant systems. *J. Colloid Interface Sci.* **2007,** *311* (1), 276-284.
11. Nagarajan, R.; Ruckenstein, E., Theory of surfactant self-assembly: a predictive molecular thermodynamic approach. *Langmuir* **1991,** *7* (12), 2934-2969.
12. Chen, L.-J.; Lin, S.-Y.; Huang, C.-C., Effect of Hydrophobic Chain Length of Surfactants on Enthalpy−Entropy Compensation of Micellization. *J. Phys. Chem. B* **1998,** *102* (22), 4350-4356.
13. Phukon, A.; Sahu, K., How Do the Interfacial Properties of Zwitterionic Sulfobetaine Micelles Differ from those of Cationic Alkyl Quaternary Ammonium Micelles? An Excited State Proton Transfer Study. *Phys. Chem. Chem. Phys.* **2017,** *19*, 31461-31468.
14. Ghosh, S.; Kuchlyan, J.; Banik, D.; Kundu, N.; Roy, A.; Banerjee, C.; Sarkar, N., Organic Additive, 5-Methylsalicylic Acid Induces Spontaneous Structural Transformation of Aqueous Pluronic Triblock Copolymer Solution: A Spectroscopic Investigation of Interaction of Curcumin with Pluronic Micellar and Vesicular Aggregates. *J. Phys. Chem. B* **2014,** *118* (39), 11437-11448.
15. Mishra, J.; Swain, J.; Mishra, A. K., Molecular Level Understanding of Sodium Dodecyl Sulfate (SDS) Induced Sol–Gel Transition of Pluronic F127 Using Fisetin as a Fluorescent Molecular Probe. *J. Phys. Chem. B* **2018,** *122* (1), 181-193.
16. Basak, R.; Bandyopadhyay, R., Encapsulation of Hydrophobic Drugs in Pluronic F127 Micelles: Effects of Drug Hydrophobicity, Solution Temperature, and pH. *Langmuir* **2013,** *29* (13), 4350-4356.
17. de Castro, K. C.; Coco, J. C.; dos Santos, É. M.; Ataide, J. A.; Martinez, R. M.; do Nascimento, M. H. M.; Prata, J.; da Fonte, P. R. M. L.; Severino, P.; Mazzola, P. G.; Baby, A. R.; Souto, E. B.; de Araujo, D. R.; Lopes, A. M., Pluronic® triblock copolymer-based nanoformulations for cancer therapy: A 10-year overview. *J Control Release* **2023,** *353*, 802-822.
18. Patel, D.; Bhojani, A. K.; Ray, D.; Singh, D. K.; Bhattacharjee, S.; Seth, D.; Aswal, V. K.; Kuperkar, K.; Bahadur, P., Glucose-induced self-assembly and phase separation in hydrophilic triblock copolymers and the governing mechanism. *Phys. Chem. Chem. Phys.* **2022,** *24* (35), 21141-21156.
19. Sahu, S.; Karan, P.; Mishra, A. K., Nature of Saccharide-Induced F127 Micellar Dehydration: An Insight with FDAPT (2-Formyl-5-(4′-N,N-dimethylaminophenyl)thiophene), a Multiparametric Fluorescent Probe. *Langmuir* **2021,** *37* (10), 3067-3074.

20. Gonzalez-Lopez, J.; Alvarez-Lorenzo, C.; Taboada, P.; Sosnik, A.; Sandez-Macho, I.; Concheiro, A., Self-Associative Behavior and Drug-Solubilizing Ability of Poloxamine (Tetronic) Block Copolymers. *Langmuir* **2008,** *24* (19), 10688-10697.

21. Alvarez-Lorenzo, C.; Gonzalez-Lopez, J.; Fernandez-Tarrio, M.; Sandez-Macho, I.; Concheiro, A., Tetronic micellization, gelation and drug solubilization: Influence of pH and ionic strength. *Eur J Pharm Biopharm* **2007,** *66* (2), 244-252.

22. Sanders, S. N.; Gangishetty, M. K.; Sfeir, M. Y.; Congreve, D. N., Photon Upconversion in Aqueous Nanodroplets. *J. Am. Chem. Soc* **2019,** *141* (23), 9180-9184.

23. Zhang, Y.; Song, W.; Geng, J.; Chitgupi, U.; Unsal, H.; Federizon, J.; Rzayev, J.; Sukumaran, D. K.; Alexandridis, P.; Lovell, J. F., Therapeutic surfactant-stripped frozen micelles. *Nature Commun.* **2016,** *7* (1), 11649.

24. Kabanov, A. V.; Batrakova, E. V.; Alakhov, V. Y., Pluronic® block copolymers as novel polymer therapeutics for drug and gene delivery. *J Control Release* **2002,** *82* (2), 189-212.

25. Kabanov, A. V.; Batrakova, E. V.; Miller, D. W., Pluronic® block copolymers as modulators of drug efflux transporter activity in the blood–brain barrier. *Adv. Drug Deliv. Rev.* **2003,** *55* (1), 151-164.

26. Danson, S.; Ferry, D.; Alakhov, V.; Margison, J.; Kerr, D.; Jowle, D.; Brampton, M.; Halbert, G.; Ranson, M., Phase I dose escalation and pharmacokinetic study of pluronic polymer-bound doxorubicin (SP1049C) in patients with advanced cancer. *Br. J. Cancer* **2004,** *90* (11), 2085-2091.

27. Alexandridis, P.; Holzwarth, J. F.; Hatton, T. A., Micellization of Poly(ethylene oxide)-Poly(propylene oxide)-Poly(ethylene oxide) Triblock Copolymers in Aqueous Solutions: Thermodynamics of Copolymer Association. *Macromolecules* **1994,** *27* (9), 2414-2425.

28. Drozdov, A. D.; deClaville Christiansen, J., The effect of saccharides on equilibrium swelling of thermo-responsive gels. *RSC Adv.* **2020,** *10* (51), 30723-30733.

29. Singla, P.; Singh, O.; Sharma, S.; Betlem, K.; Aswal, V. K.; Peeters, M.; Mahajan, R. K., Temperature-Dependent Solubilization of the Hydrophobic Antiepileptic Drug Lamotrigine in Different Pluronic Micelles—A Spectroscopic, Heat Transfer Method, Small-Angle Neutron Scattering, Dynamic Light Scattering, and in Vitro Release Study. *ACS Omega* **2019,** *4* (6), 11251-11262.

30. Pitto-Barry, A.; Barry, N. P. E., Pluronic® block-copolymers in medicine: from chemical and biological versatility to rationalisation and clinical advances. *Polym. Chem.* **2014,** *5* (10), 3291-3297.

31. Tiwari, S.; Kansara, V.; Bahadur, P., Targeting anticancer drugs with pluronic aggregates: Recent updates. *Int. J. Pharm.* **2020,** *586*, 119544.

32. Hyman, A. A.; Weber, C. A.; Jülicher, F., Liquid-Liquid Phase Separation in Biology. *Annu. Rev. Cell Dev. Biol.* **2014,** *30* (1), 39-58.

33. Ostendorf, A.; Schönhoff, M.; Cramer, C., Ionic conductivity of solid polyelectrolyte complexes with varying water content: application of the dynamic structure model. *Phys. Chem. Chem. Phys.* **2019,** *21* (14), 7321-7329.

34. Savariar, E. N.; Ghosh, S.; González, D. C.; Thayumanavan, S., Disassembly of Noncovalent Amphiphilic Polymers with Proteins and Utility in Pattern Sensing. *Journal of the American Chemical Society* **2008,** *130* (16), 5416-5417.

35. Lapitsky, Y.; Zahir, T.; Shoichet, M. S., Modular Biodegradable Biomaterials from Surfactant and Polyelectrolyte Mixtures. *Biomacromolecules* **2008,** *9* (1), 166-174.

36. Turgeon, S. L.; Schmitt, C.; Sanchez, C., Protein–polysaccharide complexes and coacervates. *Curr. Opin. Colloid Interface Sci.* **2007,** *12* (4), 166-178.

37. Zhao, W.; Fan, Y.; Wang, H.; Wang, Y., Coacervate of Polyacrylamide and Cationic Gemini Surfactant for the Extraction of Methyl Orange from Aqueous Solution. *Langmuir* **2017,** *33* (27), 6846-6856.

38. Saini, B.; Singh, S.; Mukherjee, T. K., Nanocatalysis under Nanoconfinement: A Metal-Free Hybrid Coacervate Nanodroplet as a Catalytic Nanoreactor for Efficient Redox and Photocatalytic Reactions. *ACS Applied Materials & Interfaces* **2021,** *13* (43), 51117-51131.

39. Kizilay, E.; Maccarrone, S.; Foun, E.; Dinsmore, A. D.; Dubin, P. L., Cluster Formation in Polyelectrolyte−Micelle Complex Coacervation. *The Journal of Physical Chemistry B* **2011,** *115* (22), 7256-7263.

40. Pergushov, D. V.; Müller, A. H. E.; Schacher, F. H., Micellar interpolyelectrolyte complexes. *Chemical Society Reviews* **2012,** *41* (21), 6888-6901.

41. Li, X.; Liu, C.; Van der Bruggen, B., Polyelectrolytes self-assembly: versatile membrane fabrication strategy. *J. Mater. Chem. A* **2020,** *8* (40), 20870-20896.

42. Hyman, A. A.; Weber, C. A.; Jülicher, F., Liquid-Liquid Phase Separation in Biology. *Annual Review of Cell and Developmental Biology* **2014,** *30* (1), 39-58.

43. Sakuta, H.; Fujimoto, T.; Yamana, Y.; Hoda, Y.; Tsumoto, K.; Yoshikawa, K., Aqueous/Aqueous Micro Phase Separation: Construction of an Artificial Model of Cellular Assembly. *Frontiers in Chemistry* **2019,** *7*.

44. Chang, L.-W.; Lytle, T. K.; Radhakrishna, M.; Madinya, J. J.; Vélez, J.; Sing, C. E.; Perry, S. L., Sequence and entropy-based control of complex coacervates. *Nature Communications* **2017,** *8* (1), 1273.

45. Fu, J.; Schlenoff, J. B., Driving Forces for Oppositely Charged Polyion Association in Aqueous Solutions: Enthalpic, Entropic, but Not Electrostatic. *Journal of the American Chemical Society* **2016,** *138* (3), 980-990.

46. Mukherjee, S.; Dan, A.; Bhattacharya, S. C.; Panda, A. K.; Moulik, S. P., Physicochemistry of Interaction between the Cationic Polymer Poly(diallyldimethylammonium chloride) and the Anionic Surfactants Sodium Dodecyl Sulfate, Sodium Dodecylbenzenesulfonate, and Sodium N-Dodecanoylsarcosinate in Water and Isopropyl Alcohol−Water Media. *Langmuir* **2011,** *27* (9), 5222-5233.

47. Patel, L.; Mansour, O.; Bryant, H.; Abdullahi, W.; Dalgliesh, R. M.; Griffiths, P. C., Interaction of Low Molecular Weight Poly(diallyldimethylammonium chloride) and Sodium Dodecyl Sulfate in Low Surfactant–Polyelectrolyte Ratio, Salt-Free Solutions. *Langmuir* **2020,** *36* (30), 8815-8825.

48. Palivan, C. G.; Fischer-Onaca, O.; Delcea, M.; Itel, F.; Meier, W., Protein–polymer nanoreactors for medical applications. *Chemical Society Reviews* **2012,** *41* (7), 2800-2823.

49. Azman, N. A.; Bekale, L.; Nguyen, T. X.; Kah, J. C. Y., Polyelectrolyte stiffness on gold nanorods mediates cell membrane damage. *Nanoscale* **2020,** *12* (26), 14021-14036.

50. Pal, T.; Sahu, K., Photophysical characterization of a sub-micellar triblock copolymer-cationic surfactant aggregate for nanostructure synthesis. *Journal of Photochemistry and Photobiology* **2021,** *8*, 100066.

51. Sahu, D. K.; Pal, T.; Sahu, K., A New Phase Transfer Strategy to Convert Protein-Capped Nanomaterials into Uniform Fluorescent Nanoclusters in Reverse Micellar Phase. *ChemPhysChem* **2018,** *19* (17), 2153-2158.

52. Kizilay, E.; Dinsmore, A. D.; Hoagland, D. A.; Sun, L.; Dubin, P. L., Evolution of hierarchical structures in polyelectrolyte–micelle coacervates. *Soft Matter* **2013,** *9* (30), 7320-7332.

53. Caruso, F.; Donath, E.; Möhwald, H.; Georgieva, R., Fluorescence Studies of the Binding of Anionic Derivatives of Pyrene and Fluorescein to Cationic Polyelectrolytes in Aqueous Solution. *Macromolecules* **1998,** *31* (21), 7365-7377.

54. Pal, T.; Sahu, K., Exploring cationic polyelectrolyte–micelle interaction via excited-state proton transfer. Signatures of probe transfer. *Phys. Chem. Chem. Phys.* **2023,** *25* (4), 2963-2977.

55. Mondal, R.; Ghosh, N.; Paul, B. K.; Mukherjee, S., Triblock-Copolymer-Assisted Mixed-Micelle Formation Results in the Refolding of Unfolded Protein. *Langmuir* **2018,** *34* (3), 896-903.

56. Zhang, W.; Shi, Y. A.; Chen, Y. Z.; Ye, J. A.; Sha, X. Y.; Fang, X. L., Multifunctional Pluronic P123/F127 mixed polymeric micelles loaded with paclitaxel for the treatment of multidrug resistant tumors. *Biomaterials* **2011,** *32* (11), 2894-2906.

57. Batrakova, E. V.; Kabanov, A. V., Pluronic Block Copolymers: Evolution of Drug Delivery Concept from Inert Nanocarriers to Biological Response Modifiers. *J Control Release* **2008,** *130* (2), 98-106.

58. Sezgin, Z.; Yuksel, N.; Baykara, T., Preparation and characterization of polymeric micelles for solubilization of poorly soluble anticancer drugs. *Eur J Pharm Biopharm* **2006,** *64* (3), 261-268.

59. Mondal, R.; Ghosh, N.; Mukherjee, S., Enhanced Binding of Phenosafranin to Triblock Copolymer F127 Induced by Sodium Dodecyl Sulfate: A Mixed Micellar System as an Efficient Drug Delivery Vehicle. *J Phys Chem B* **2016,** *120* (11), 2968-2976.

60. Mora, A. K.; Singh, P. K.; Nath, S., Controlled Sequestration of DNA Intercalated Drug by Polymer-Surfactant Supramolecular Assemblies. *J Phys Chem B* **2016,** *120* (17), 4143-4151.

61. Varshney, M.; Morey, T. E.; Shah, D. O.; Flint, J. A.; Moudgil, B. M.; Seubert, C. N.; Dennis, D. M., Pluronic microemulsions as nanoreservoirs for extraction of bupivacaine from normal saline. *Journal of the American Chemical Society* **2004,** *126* (16), 5108-5112.

62. Bayati, S.; Galantini, L.; Knudsen, K. D.; Schillen, K., Effects of Bile Salt Sodium Glycodeoxycholate on the Self-Assembly of PEO-PPO-PEO Triblock Copolymer P123 in Aqueous Solution. *Langmuir* **2015,** *31* (50), 13519-13527.

63. Bayati, S.; Galantini, L.; Knudsen, K. D.; Schillén, K., Effects of Bile Salt Sodium Glycodeoxycholate on the Self-Assembly of PEO–PPO–PEO Triblock Copolymer P123 in Aqueous Solution. *Langmuir* **2015,** *31* (50), 13519-13527.

64. Neacsu, M. V.; Matei, I.; Micutz, M.; Staicu, T.; Precupas, A.; Popa, V. T.; Salifoglou, A.; Ionita, G., Interaction between Albumin and Pluronic F127 Block Copolymer Revealed by Global and Local Physicochemical Profiling. *J. Phys. Chem. B* **2016,** *120* (18), 4258-4267.

65. Brinatti, C.; Mello, L. B.; Loh, W., Thermodynamic Study of the Micellization of Zwitterionic Surfactants and Their Interaction with Polymers in Water by Isothermal Titration Calorimetry. *Langmuir* **2014,** *30* (21), 6002-6010.

66. Desai, P. R.; Jain, N. J.; Sharma, R. K.; Bahadur, P., Effect of Additives on the Micellization of PEO/PPO/PEO Block Copolymer F127 in Aqueous Solution. *Colloids Surf. A* **2001,** *178* (1), 57-69.

67. Halder, A.; Sen, P.; Burman, A. D.; Bhattacharyya, K., Solvation Dynamics of DCM in a Polypeptide−Surfactant Aggregate: Gelatin−Sodium Dodecyl Sulfate. *Langmuir* **2004,** *20* (3), 653-657.

68. Chakrabarty, D.; Hazra, P.; Chakraborty, A.; Sarkar, N., Solvation Dynamics of Coumarin 480 in Bile Salt−Cetyltrimethylammonium Bromide (CTAB) and Bile Salt−Tween 80 Mixed Micelles. *J. Phys. Chem. B* **2003,** *107* (49), 13643-13648.

69. Pal, T.; Sahu, K., Anomalous Variation of Excited-State Proton Transfer Dynamics inside a Triblock Copolymer–Cationic Surfactant Mixed Micelle. *J. Phys. Chem. B* **2019,** *123* (40), 8559-8568.

70. Förster, T., Fluoreszenzspektrum und Wasserstoffionen-konzentration. *Naturwissenschaften* **1949,** *36* (6), 186-187.

71. Förster, T., Elektrolytische Dissoziation angeregter Moleküle. *Zeitschrift für Elektrochemie und angewandte physikalische Chemie* **1950,** *54* (1), 42-46.

72. Sülzner, N.; Hättig, C., Theoretical Study on the Photoacidity of Hydroxypyrene Derivatives in DMSO Using ADC(2) and CC2. *J. Phys. Chem. A* **2022,** *126* (35), 5911-5923.

73. Nandi, R.; Amdursky, N., The Dual Use of the Pyranine (HPTS) Fluorescent Probe: A Ground-State pH Indicator and an Excited-State Proton Transfer Probe. *Acc. Chem. Res.* **2022,** *55* (18), 2728-2739.

74. Eigen, M., Proton Transfer, Acid-Base Catalysis, and Enzymatic Hydrolysis. Part I: ELEMENTARY PROCESSES. *Angew. Chem. Int. Ed.* **1964,** *3* (1), 1-19.
75. Pines, E.; Huppert, D.; Agmon, N., Geminate recombination in excited-state proton-transfer reactions: Numerical solution of the Debye–Smoluchowski equation with backreaction and comparison with experimental results. *J. Chem. Phys.* **1988,** *88* (9), 5620-5630.
76. Agmon, N., Geminate recombination in proton-transfer reactions. III. Kinetics and equilibrium inside a finite sphere. *J. Chem. Phys.* **1988,** *88* (9), 5639-5642.
77. Agmon, N., Excited State Proton Transfer Reactions. In *Theoretical and Computational Models for Organic Chemistry*, Formosinho, S. J.; Csizmadia, I. G.; Arnaut, L. G., Eds. Springer Netherlands: Dordrecht, 1991; pp 315-334.
78. Simkovitch, R.; Pines, D.; Agmon, N.; Pines, E.; Huppert, D., Reversible Excited-State Proton Geminate Recombination: Revisited. *J. Phys. Chem. B* **2016,** *120* (49), 12615-12632.
79. Stuchebrukhov, A. A.; Variyam, A. R.; Amdursky, N., Using Proton Geminate Recombination as a Probe of Proton Migration on Biological Membranes. *J. Phys. Chem. B* **2022,** *126* (32), 6026-6038.
80. Tolbert, L. M.; Solntsev, K. M., Excited-State Proton Transfer: From Constrained Systems to “Super” Photoacids to Superfast Proton Transfer. *Acc. Chem. Res.* **2002,** *35* (1), 19-27.
81. Szczepanik, B., Protolytic dissociation of cyano derivatives of naphthol, biphenyl and phenol in the excited state: A review. *J. Mol. Struct.* **2015,** *1099*, 209-214.
82. Simkovitch, R.; Shomer, S.; Gepshtein, R.; Huppert, D., How Fast Can a Proton-Transfer Reaction Be beyond the Solvent-Control Limit? *J. Phys. Chem. B* **2015,** *119* (6), 2253-2262.
83. Agmon, N., Elementary Steps in Excited-State Proton Transfer. *J. Phys. Chem. A* **2005,** *109* (1), 13-35.
84. Agmon, N.; Szabo, A., Theory of reversible diffusion-influenced reactions. *J. Chem. Phys.* **1990,** *92* (9), 5270-5284.
85. Goun, A.; Glusac, K.; Fayer, M. D., Photoinduced electron transfer and geminate recombination in liquids on short time scales: Experiments and theory. *J. Chem. Phys.* **2006,** *124* (8), 084504.
86. Lawler, C.; Fayer, M. D., Proton Transfer in Ionic and Neutral Reverse Micelles. *J. Phys. Chem. B* **2015,** *119* (19), 6024-6034.
87. Tran-Thi, T. H.; Gustavsson, T.; Prayer, C.; Pommeret, S.; Hynes, J. T., Primary ultrafast events preceding the photoinduced proton transfer from pyranine to water. *Chem. Phys. Lett.* **2000,** *329* (5), 421-430.
88. Mohammed, O. F.; Dreyer, J.; Magnes, B.-Z.; Pines, E.; Nibbering, E. T. J., Solvent-Dependent Photoacidity State of Pyranine Monitored by Transient Mid-Infrared Spectroscopy. *ChemPhysChem* **2005,** *6* (4), 625-636.
89. Leiderman, P.; Genosar, L.; Huppert, D., Excited-State Proton Transfer: Indication of Three Steps in the Dissociation and Recombination Process. *J. Phys. Chem. A* **2005,** *109* (27), 5965-5977.
90. Eigen, M.; De Maeyer, L.; Bernal, J. D., Self-dissociation and protonic charge transport in water and. *Proc. Math. Phys. Eng. Sci.* **1997,** *247* (1251), 505-533.
91. Eigen, M., Proton Transfer, Acid-Base Catalysis, and Enzymatic Hydrolysis. Part I: ELEMENTARY PROCESSES. *Angew. Chem. Int. Ed.* **1964,** *3* (1), 1-19.
92. Zundel, G., Hydration Structure and Intermolecular Interaction in Polyelectrolytes. *Angew. Chem. Int. Ed.* **1969,** *8* (7), 499-509.
93. Huggins, M. L., Hydrogen Bridges in Ice and Liquid Water. *J. Phys. Chem.* **1936,** *40* (6), 723-731.
94. Markovitch, O.; Chen, H.; Izvekov, S.; Paesani, F.; Voth, G. A.; Agmon, N., Special Pair Dance and Partner Selection: Elementary Steps in Proton Transport in Liquid Water. *J. Phys. Chem. B* **2008,** *112* (31), 9456-9466.

95. Walker, A. R.; Wu, B.; Meisner, J.; Fayer, M. D.; Martínez, T. J., Proton Transfer from a Photoacid to a Water Wire: First Principles Simulations and Fast Fluorescence Spectroscopy. *J. Phys. Chem. B* **2021,** *125* (45), 12539-12551.

96. Awasthi, A. A.; Singh, P. K., Proton Transfer Reaction Dynamics of Pyranine in DMSO/Water Mixtures. *ChemPhysChem* **2018,** *19* (2), 198-207.

97. Banik, D.; Kundu, N.; Kuchlyan, J.; Roy, A.; Banerjee, C.; Ghosh, S.; Sarkar, N., Picosecond solvation dynamics—A potential viewer of DMSO—Water binary mixtures. *J. Chem. Phys.* **2015,** *142* (5), 054505.

98. Oh, K.-I.; Rajesh, K.; Stanton, J. F.; Baiz, C. R., Quantifying Hydrogen-Bond Populations in Dimethyl Sulfoxide/Water Mixtures. *Angew. Chem. Int. Ed.* **2017,** *56* (38), 11375-11379.

99. Nandi, N.; Sahu, K., Analysis of Excited State Proton Transfer Dynamics of HPTS in Methanol-Water Mixtures from Time-Resolved Area-Normalised Emission Spectrum (TRANES). *J. Photochem. Photobiol. A.* **2019,** *374*, 138-144.

100. Agmon, N.; Huppert, D.; Masad, A.; Pines, E., Excited-state proton transfer to methanol-water mixtures. *J. Phys. Chem.* **1991,** *95* (25), 10407-10413.

101. Suwaiyan, A.; Al-Adel, F.; Hamdan, A.; Klein, U. K. A., Dynamics of proton transfer from photon-initiated acids in alcohol/water mixtures. *J. Phys. Chem.* **1990,** *94* (19), 7423-7429.

102. Wong, D. B.; Sokolowsky, K. P.; El-Barghouthi, M. I.; Fenn, E. E.; Giammanco, C. H.; Sturlaugson, A. L.; Fayer, M. D., Water Dynamics in Water/DMSO Binary Mixtures. *J. Phys. Chem. B* **2012,** *116* (18), 5479-5490.

103. Dutt, G. B.; Doraiswamy, S., Picosecond reorientational dynamics of polar dye probes in binary aqueous mixtures. *J. Chem. Phys.* **1992,** *96* (4), 2475-2491.

104. Agmon, N.; Goldberg, S. Y.; Huppert, D., Salt effect on transient proton transfer to solvent and microscopic proton mobility. *J. Mol. Liq.* **1995,** *64* (1), 161-195.

105. Huppert, D.; Kolodney, E.; Gutman, M.; Nachliel, E., Effect of water activity on the rate of proton dissociation. *J. Am. Chem. Soc* **1982,** *104* (25), 6949-6953.

106. Leiderman, P.; Gepshtein, R.; Uritski, A.; Genosar, L.; Huppert, D., Effect of Electrolytes on the Excited-State Proton Transfer and Geminate Recombination. *J. Phys. Chem. A* **2006,** *110* (17), 5573-5584.

107. Mondal, T.; Ghosh, S.; Das, A. K.; Mandal, A. K.; Bhattacharyya, K., Salt Effect on the Ultrafast Proton Transfer in Niosome. *J. Phys. Chem. B* **2012,** *116* (28), 8105-8112.

108. Kato, K.; Walde, P.; Koine, N.; Ichikawa, S.; Ishikawa, T.; Nagahama, R.; Ishihara, T.; Tsujii, T.; Shudou, M.; Omokawa, Y.; Kuroiwa, T., Temperature-Sensitive Nonionic Vesicles Prepared from Span 80 (Sorbitan Monooleate). *Langmuir* **2008,** *24* (19), 10762-10770.

109. Pozzi, D.; Caminiti, R.; Marianecci, C.; Carafa, M.; Santucci, E.; De Sanctis, S. C.; Caracciolo, G., Effect of Cholesterol on the Formation and Hydration Behavior of Solid-Supported Niosomal Membranes. *Langmuir* **2010,** *26* (4), 2268-2273.

110. Lo, C. T.; Jahn, A.; Locascio, L. E.; Vreeland, W. N., Controlled Self-Assembly of Monodisperse Niosomes by Microfluidic Hydrodynamic Focusing. *Langmuir* **2010,** *26* (11), 8559-8566.

111. Cox, M. J.; Siwick, B. J.; Bakker, H. J., Influence of Ions on Aqueous Acid–Base Reactions. *ChemPhysChem* **2009,** *10* (1), 236-244.

112. Rini, M.; Magnes, B.-Z.; Pines, E.; Nibbering, E. T. J., Real-Time Observation of Bimodal Proton Transfer in Acid-Base Pairs in Water. *Science* **2003,** *301* (5631), 349.

113. Mohammed, O. F.; Pines, D.; Dreyer, J.; Pines, E.; Nibbering, E. T. J., Sequential Proton Transfer Through Water Bridges in Acid-Base Reactions. *Science* **2005,** *310* (5745), 83-86.

114. Mancinelli, R.; Botti, A.; Bruni, F.; Ricci, M. A.; Soper, A. K., Hydration of Sodium, Potassium, and Chloride Ions in Solution and the Concept of Structure Maker/Breaker. *J. Phys. Chem. B* **2007,** *111* (48), 13570-13577.

115. Mancinelli, R.; Botti, A.; Bruni, F.; Ricci, M. A.; Soper, A. K., Perturbation of water structure due to monovalent ions in solution. *Phys. Chem. Chem. Phys.* **2007,** *9* (23), 2959-2967.

116. Chandra, A., Effects of Ion Atmosphere on Hydrogen-Bond Dynamics in Aqueous Electrolyte Solutions. *Phys. Rev. Lett.* **2000,** *85* (4), 768-771.
117. Uritski, A.; Leiderman, P.; Huppert, D., Electrolyte Screening Effect on the Photoprotolytic Cycle of Excited Photoacid in Ice. *J. Phys. Chem. A* **2006,** *110* (51), 13686-13695.
118. Maurer, P.; Thomas, V.; Rivard, U.; Iftimie, R., A computational study of ultrafast acid dissociation and acid-base neutralization reactions. I. The model. *J. Chem. Phys.* **2010,** *133* (4), 044108.
119. Heberle, J., Proton transfer reactions across bacteriorhodopsin and along the membrane. *Biochim Biophys Acta Bioenerg* **2000,** *1458* (1), 135-147.
120. Luecke, H.; Richter, H.-T.; Lanyi, J. K., Proton Transfer Pathways in Bacteriorhodopsin at 2.3 Angstrom Resolution. *Science* **1998,** *280* (5371), 1934-1937.
121. Mulkidjanian, A. Y.; Cherepanov, D. A.; Heberle, J.; Junge, W., Proton transfer dynamics at membrane/water interface and mechanism of biological energy conversion. *Biochemistry (Moscow)* **2005,** *70* (2), 251-256.
122. Stowell, M. H. B.; McPhillips, T. M.; Rees, D. C.; Soltis, S. M.; Abresch, E.; Feher, G., Light-Induced Structural Changes in Photosynthetic Reaction Center: Implications for Mechanism of Electron-Proton Transfer. *Science* **1997,** *276* (5313), 812-816.
123. Akeson, M.; Deamer, D. W., Proton conductance by the gramicidin water wire. Model for proton conductance in the F1F0 ATPases? *Biophys. J.* **1991,** *60* (1), 101-109.
124. Olkhova, E.; Hutter, M. C.; Lill, M. A.; Helms, V.; Michel, H., Dynamic Water Networks in Cytochrome c Oxidase from Paracoccus denitrificans Investigated by Molecular Dynamics Simulations. *Biophys. J.* **2004,** *86* (4), 1873-1889.
125. Cui, Q.; Karplus, M., Is a "Proton Wire" Concerted or Stepwise? A Model Study of Proton Transfer in Carbonic Anhydrase. *J. Phys. Chem. B* **2003,** *107* (4), 1071-1078.
126. Zanetti-Polzi, L.; Aschi, M.; Daidone, I., Cooperative protein–solvent tuning of proton transfer energetics: carbonic anhydrase as a case study. *Phys. Chem. Chem. Phys.* **2020,** *22* (35), 19975-19981.
127. Shearer, G. L.; Kim, K.; Lee, K. M.; Wang, C. K.; Plapp, B. V., Alternative pathways and reactions of benzyl alcohol and benzaldehyde with horse liver alcohol dehydrogenase. *Biochemistry* **1993,** *32* (41), 11186-11194.
128. Weber, J.; Senior, A. E., ATP synthesis driven by proton transport in F1F0-ATP synthase. *FEBS Letters* **2003,** *545* (1), 61-70.
129. Boyer, P. D., THE ATP SYNTHASE—A SPLENDID MOLECULAR MACHINE. *Annu. Rev. Biochem.* **1997,** *66* (1), 717-749.
130. Williams, R. J. P., Proton Circuits in Biological Energy Interconversions. *Annu. Rev. Biophys.* **1988,** *17* (1), 71-97.
131. Prats, M.; Teissié, J.; Tocanne, J.-F., Latteral proton conduction at lipid–water interfaces and its implications for the chemiosmotic-coupling hypothesis. *Nature* **1986,** *322* (6081), 756-758.
132. Mondal, S.; Agam, Y.; Nandi, R.; Amdursky, N., Exploring long-range proton conduction, the conduction mechanism and inner hydration state of protein biopolymers. *Chem. Sci.* **2020,** *11* (13), 3547-3556.
133. Gutman, M.; Nachliel, E.; Moshiach, S., Dynamics of proton diffusion within the hydration layer of phospholipid membrane. *Biochemistry* **1989,** *28* (7), 2936-2940.
134. Shyamala, T.; Mishra, A. K., Ground- and Excited-state Proton Transfer Reaction of 3-Hydroxyflavone in Dimyristoylphosphatidylcholine Liposome Membrane¶. *Photochem. Photobiol.* **2004,** *80* (2), 309-315.
135. Kotlyar, A. B.; Borovok, N.; Kiryati, S.; Nachliel, E.; Gutman, M., The dynamics of proton transfer at the C side of the mitochondrial membrane: Picosecond and microsecond measurements. *Biochemistry* **1994,** *33* (4), 873-879.

136. Fernandez, C.; Politi, M. J., Effects of probe-amphiphile interaction on pyranine proton transfer reactions in lecithin vesicles. *J. Photochem. Photobiol. A* **1997,** *104* (1), 165-172.

137. Antonenko, Y. N.; Pohl, P., Microinjection in combination with microfluorimetry to study proton diffusion along phospholipid membranes. *Eur. Biophys. J.* **2008,** *37* (6), 865-870.

138. Voicescu, M., On the role of pH and temperature on ground – and excited – state proton transfer of hydroxyflavones in lipidic bilayers of lecithin. *J. Mol. Liq.* **2022,** *352*, 118696.

139. Rochel, S.; Nachliel, E.; Huppert, D.; Gutman, M., Proton dissociation dynamics in the aqueous layer of multilamellar phospholipid vesicles. *J. Membr. Biol.* **1990,** *118* (3), 225-232.

140. Agmon, N.; Pines, E.; Huppert, D., Geminate recombination in proton-transfer reactions. II. Comparison of diffusional and kinetic schemes. *J. Chem. Phys.* **1988,** *88* (9), 5631-5638.

141. Amdursky, N.; Lin, Y., Tracking Subtle Membrane Disruptions with a Tethered Photoacid. *ChemPhotoChem* **2020,** *4* (8), 592-600.

142. Amdursky, N.; Lin, Y.; Aho, N.; Groenhof, G., Exploring fast proton transfer events associated with latteral proton diffusion on the surface of membranes. *Proc. Natl. Acad. Sci. U. S. A.* **2019,** *116* (7), 2443-2451.

143. Stuchebrukhov, A. A.; Variyam, A. R.; Amdursky, N., Using Proton Geminate Recombination as a Probe of Proton Migration on Biological Membranes. *J. Phys. Chem. B* **2022,** *126* (32), 6026-6038.

144. Roy, A.; Taraphder, S., Identification of Proton-Transfer Pathways in Human Carbonic Anhydrase II. *J. Phys. Chem. B* **2007,** *111* (35), 10563-10576.

145. Wikström, M., Proton translocation by bacteriorhodopsin and heme-copper oxidases. *Curr. Opin. Struct. Biol.* **1998,** *8* (4), 480-488.

146. Feldbauer, K.; Zimmermann, D.; Pintschovius, V.; Spitz, J.; Bamann, C.; Bamberg, E., Channelrhodopsin-2 is a leaky proton pump. *Proc. Natl. Acad. Sci. U. S. A.* **2009,** *106* (30), 12317-12322.

147. Klauss, A.; Haumann, M.; Dau, H., Alternating electron and proton transfer steps in photosynthetic water oxidation. *Proc. Natl. Acad. Sci. U. S. A.* **2012,** *109* (40), 16035-16040.

148. Gerlits, O.; Wymore, T.; Das, A.; Shen, C.-H.; Parks, J. M.; Smith, J. C.; Weiss, K. L.; Keen, D. A.; Blakeley, M. P.; Louis, J. M.; Langan, P.; Weber, I. T.; Kovalevsky, A., Long-Range Electrostatics-Induced Two-Proton Transfer Captured by Neutron Crystallography in an Enzyme Catalytic Site. *Angew. Chem. Int. Ed.* **2016,** *55* (16), 4924-4927.

149. Dencher, N. A., Bacteriorhodopsin: A Spectroscopic Intermediate with Two Conformations and Three Relay Events Is Voltage Sensitive. *Biophys. J.* **1998,** *74* (1), 1-2.

150. Amdursky, N., Photoacids as a new fluorescence tool for tracking structural transitions of proteins: following the concentration-induced transition of bovine serum albumin. *Phys. Chem. Chem. Phys.* **2015,** *17* (47), 32023-32032.

151. Amdursky, N.; Rashid, M. H.; Stevens, M. M.; Yarovsky, I., Exploring the binding sites and proton diffusion on insulin amyloid fibril surfaces by naphthol-based photoacid fluorescence and molecular simulations. *Sci. Rep.* **2017,** *7* (1), 6245.

152. Cohen, B.; Martin Álvarez, C.; Alarcos Carmona, N.; Organero, J. A.; Douhal, A., Proton-Transfer Reaction Dynamics within the Human Serum Albumin Protein. *J. Phys. Chem. B* **2011,** *115* (23), 7637-7647.

153. Awasthi, A. A.; Singh, P. K., Excited-State Proton Transfer on the Surface of a Therapeutic Protein, Protamine. *J. Phys. Chem. B* **2017,** *121* (45), 10306-10317.

154. Selkoe, D. J., Folding proteins in fatal ways. *Nature* **2003,** *426* (6968), 900-904.

155. Das, I.; Panja, S.; Halder, M., Modulation and Salt-Induced Reverse Modulation of the Excited-State Proton-Transfer Process of Lysozymized Pyranine: The Contrasting Scenario of the Ground-State Acid–Base Equilibrium of the Photoacid. *J. Phys. Chem. B* **2016,** *120* (29), 7076-7087.

156. Jao, D.; Xue, Y.; Medina, J.; Hu, X. Protein-Based Drug-Delivery Materials *Materials* [Online], 2017.

157. Fan, C.; Shi, J.; Zhuang, Y.; Zhang, L.; Huang, L.; Yang, W.; Chen, B.; Chen, Y.; Xiao, Z.; Shen, H.; Zhao, Y.; Dai, J., Myocardial-Infarction-Responsive Smart Hydrogels Targeting Matrix Metalloproteinase for On-Demand Growth Factor Delivery. *Adv. Mater.* **2019,** *31* (40), 1902900.
158. Nandi, R.; Yucknovsky, A.; Mazo, M. M.; Amdursky, N., Exploring the inner environment of protein hydrogels with fluorescence spectroscopy towards understanding their drug delivery capabilities. *J. Mater. Chem. B* **2020,** *8* (31), 6964-6974.
159. Amdursky, N.; Mazo, M. M.; Thomas, M. R.; Humphrey, E. J.; Puetzer, J. L.; St-Pierre, J.-P.; Skaalure, S. C.; Richardson, R. M.; Terracciano, C. M.; Stevens, M. M., Elastic serum-albumin based hydrogels: mechanism of formation and application in cardiac tissue engineering. *J. Mater. Chem. B* **2018,** *6* (35), 5604-5612.
160. Bardelmeyer, G. H., Electrical conduction in hydrated collagen. I. Conductivity mechanisms. *Biopolymers* **1973,** *12* (10), 2289-2302.
161. Murphy, E. J., Ionic conduction in keratin (wool). *J. Colloid Interface Sci.* **1976,** *54* (3), 400-408.
162. Tredgold, R. H.; Sproule, R. C.; McCanny, J., Proton conduction in protein films. *J. Chem. Soc., Faraday trans.* **1976,** *72* (0), 509-512.
163. Amdursky, N.; Wang, X.; Meredith, P.; Bradley, D. D. C.; Stevens, M. M., Long-Range Proton Conduction across Free-Standing Serum Albumin Mats. *Adv. Mater.* **2016,** *28* (14), 2692-2698.
164. Burnstine-Townley, A.; Mondal, S.; Agam, Y.; Nandi, R.; Amdursky, N., Light-Modulated Cationic and Anionic Transport across Protein Biopolymers**. *Angew. Chem. Int. Ed.* **2021,** *60* (46), 24676-24685.
165. Zhong, C.; Deng, Y.; Roudsari, A. F.; Kapetanovic, A.; Anantram, M. P.; Rolandi, M., A polysaccharide bioprotonic field-effect transistor. *Nature Commun.* **2011,** *2* (1), 476.
166. Amdursky, N.; Simkovitch, R.; Huppert, D., Excited-State Proton Transfer of Photoacids Adsorbed on Biomaterials. *J. Phys. Chem. B* **2014,** *118* (48), 13859-13869.
167. Simkovitch, R.; Huppert, D., Excited-State Proton Transfer of Weak Photoacids Adsorbed on Biomaterials: Proton Transfer on Starch. *J. Phys. Chem. B* **2015,** *119* (30), 9795-9804.
168. Simkovitch, R.; Huppert, D., Excited-State Proton Transfer of Weak Photoacids Adsorbed on Biomaterials: 8-Hydroxy-1,3,6-pyrenetrisulfonate on Chitin and Cellulose. *J. Phys. Chem. A* **2015,** *119* (10), 1973-1982.
169. Park, S.; Moilanen, D. E.; Fayer, M. D., Water DynamicsThe Effects of Ions and Nanoconfinement. *J. Phys. Chem. B* **2008,** *112* (17), 5279-5290.
170. Farrer, R. A.; Fourkas, J. T., Orientational Dynamics of Liquids Confined in Nanoporous Sol–Gel Glasses Studied by Optical Kerr Effect Spectroscopy. *Acc. Chem. Res.* **2003,** *36* (8), 605-612.
171. Bhattacharyya, K.; Bagchi, B., Slow Dynamics of Constrained Water in Complex Geometries. *J. Phys. Chem. A* **2000,** *104* (46), 10603-10613.
172. Faeder, J.; Ladanyi, B. M., Solvation Dynamics in Aqueous Reverse Micelles: A Computer Simulation Study. *J. Phys. Chem. B* **2001,** *105* (45), 11148-11158.
173. Senapati, S.; Berkowitz, M. L., Computer Simulation Studies of Water States in Perfluoro Polyether Reverse Micelles: Effects of Changing the Counterion. *J. Phys. Chem. A* **2004,** *108* (45), 9768-9776.
174. Angulo, G.; Organero, J. A.; Carranza, M. A.; Douhal, A., Probing the Behavior of Confined Water by Proton-Transfer Reactions. *J. Phys. Chem. B* **2006,** *110* (47), 24231-24237.
175. Mancini, G.; Schiavo, C.; Cerichelli, G., Trapping of Counterions and Water on the Surface of Cationic Micelles. *Langmuir* **1996,** *12* (15), 3567-3573.
176. Tielrooij, K. J.; Cox, M. J.; Bakker, H. J., Effect of Confinement on Proton-Transfer Reactions in Water Nanopools. *ChemPhysChem* **2009,** *10* (1), 245-251.

177. Rodrigues, R.; Vautier-Giongo, C.; Silva, P. F.; Fernandes, A. C.; Cruz, R.; Maçanita, A. L.; Quina, F. H., Geminate Proton Recombination at the Surface of SDS and CTAC Micelles Probed with a Micelle-Anchored Anthocyanin. *Langmuir* **2006,** *22* (3), 933-940.
178. Banerjee, C.; Ghatak, C.; Mandal, S.; Ghosh, S.; Kuchlyan, J.; Sarkar, N., Curcumin in Reverse Micelle: An Example to Control Excited-State Intramolecular Proton Transfer (ESIPT) in Confined Media. *J. Phys. Chem. B* **2013,** *117* (23), 6906-6916.
179. Rai, R.; Pandey, S., Evidence of Water-in-Ionic Liquid Microemulsion Formation by Nonionic Surfactant Brij-35. *Langmuir* **2014,** *30* (34), 10156-10160.
180. Sharma, V. K.; Srinivasan, H.; Mitra, S.; Garcia-Sakai, V.; Mukhopadhyay, R., Effects of Hydrotropic Salt on the Nanoscopic Dynamics of DTAB Micelles. *J Phys Chem B* **2017,** *121* (22), 5562-5572.
181. Karsa, D. R.; Stephenson, R. A., *Chemical aspects of drug delivery systems*. Royal Society of Chemistry: 1996; Vol. 178.
182. Lee, E. S.; Na, K.; Bae, Y. H., Super pH-Sensitive Multifunctional Polymeric Micelle. *Nano Lett.* **2005,** *5* (2), 325-329.
183. Gavvala, K.; Koninti, R. K.; Sengupta, A.; Hazra, P., Excited state proton transfer dynamics of an eminent anticancer drug, ellipticine, in octyl glucoside micelle. *Phys. Chem. Chem. Phys.* **2014,** *16* (28), 14953-14960.
184. Pal, T.; Sahu, K., Photophysical characterization of a sub-micellar triblock copolymer-cationic surfactant aggregate for nanostructure synthesis. *J. Photochem. Photobiol.* **2021,** *8*, 100066.
185. Mortara, L.; Lima, F. D.; Cuccovia, I. M.; Nazet, A.; Horinek, D.; Buchner, R.; Chaimovich, H., Specific Ion Effects on Zwitterionic Micelles Are Independent of Interfacial Hydration Changes. *Langmuir* **2018,** *34* (37), 11049-11057.
186. Sahu, K.; Roy, D.; Mondal, S. K.; Karmakar, R.; Bhattacharyya, K., Study of protein–surfactant interaction using excited state proton transfer. *Chem. Phys. Lett.* **2005,** *404* (4), 341-345.
187. Roy, D.; Karmakar, R.; Mondal, S. K.; Sahu, K.; Bhattacharyya, K., Excited State Proton Transfer from Pyranine to Acetate in a CTAB Picelle. *Chem. Phys. Lett.* **2004,** *399* (1–3), 147-151.
188. Mandal, A. K.; Ghosh, S.; Das, A. K.; Mondal, T.; Bhattacharyya, K., Effect of NaCl on ESPT-Mediated FRET in a CTAC Micelle: A Femtosecond and FCS Study. *ChemPhysChem* **2013,** *14* (4), 788-796.
189. Mondal, T.; Das, A. K.; Sasmal, D. K.; Bhattacharyya, K., Excited State Proton Transfer in Ionic Liquid Mixed Micelles. *J. Phys. Chem. B* **2010,** *114* (41), 13136-13142.
190. Baptista, M. S.; Politi, M. J., Dipole oriented anion binding and exchange in zwitterionic micelles. *J. Phys. Chem.* **1991,** *95* (15), 5936-5942.
191. Baptista, M. d. S.; Cuccovia, I.; Chaimovich, H.; Politi, M. J.; Reed, W. F., Electrostatic properties of zwitterionic micelles. *J. Phys. Chem.* **1992,** *96* (15), 6442-6449.
192. Barnadas-Rodríguez, R.; Cladera, J., Steroidal Surfactants: Detection of Premicellar Aggregation, Secondary Aggregation Changes in Micelles, and Hosting of a Highly Charged Negative Substance. *Langmuir* **2015,** *31* (33), 8980-8988.
193. Phukon, A.; Sahu, K., How do the interfacial properties of zwitterionic sulfobetaine micelles differ from those of cationic alkyl quaternary ammonium micelles? An excited state proton transfer study. *Phys. Chem. Chem. Phys.* **2017,** *19* (46), 31461-31468.
194. Nandi, N.; Bhattacharyya, K.; Bagchi, B., Dielectric Relaxation and Solvation Dynamics of Water in Complex Chemical and Biological Systems. *Chem. Rev* **2000,** *100* (6), 2013-2046.
195. Levinger, N. E., Water in Confinement. *Science* **2002,** *298* (5599), 1722-1723.
196. Halliday, N. A.; Peet, A. C.; Britton, M. M., Detection of pH in Microemulsions, without a Probe Molecule, Using Magnetic Resonance. *J. Phys. Chem. B* **2010,** *114* (43), 13745-13751.

197. Wittouck, N.; Negri, R. M.; Ameloot, M.; De Schryver, F. C., AOT Reversed Micelles Investigated by Fluorescence Anisotropy of Cresyl Violet. *J. Am. Chem. Soc* **1994,** *116* (23), 10601-10611.

198. Fenn, E. E.; Wong, D. B.; Fayer, M. D., Water dynamics at neutral and ionic interfaces. *Proc. Natl. Acad. Sci. U. S. A.* **2009,** *106* (36), 15243-15248.

199. Eastoe, J.; Hollamby, M. J.; Hudson, L., Recent advances in nanoparticle synthesis with reversed micelles. *Adv. Colloid Interface Sci.* **2006,** *128-130*, 5-15.

200. Singha, D.; Barman, N.; Sahu, K., A facile synthesis of high optical quality silver nanoparticles by ascorbic acid reduction in reverse micelles at room temperature. *J. Colloid Interface Sci.* **2014,** *413*, 37-42.

201. Singha, D.; Barman, N.; Phukon, A.; Sahu, K., Selective Probing of Reverse Micelle Interfacial Layer upon Silver Nanoparticle Formation using Dynamic Stokes Shift Measurements. *J. Phys. Chem. C* **2014,** *118* (19), 10366-10374.

202. Moyano, F.; Setien, E.; Silber, J. J.; Correa, N. M., Enzymatic Hydrolysis of N-Benzoyl-l-Tyrosine p-Nitroanilide by α-Chymotrypsin in DMSO-Water/AOT/n-Heptane Reverse Micelles. A Unique Interfacial Effect on the Enzymatic Activity. *Langmuir* **2013,** *29* (26), 8245-8254.

203. Shome, A.; Roy, S.; Das, P. K., Nonionic Surfactants: A Key to Enhance the Enzyme Activity at Cationic Reverse Micellar Interface. *Langmuir* **2007,** *23* (8), 4130-4136.

204. Correa, N. M.; Zorzan, D. H.; D'Anteo, L.; Lasta, E.; Chiarini, M.; Cerichelli, G., Reverse Micellar Aggregates: Effect on Ketone Reduction. 2. Surfactant Role. *J. Org. Chem.* **2004,** *69* (24), 8231-8238.

205. Mukherjee, S.; Chowdhury, P.; DeGrado, W. F.; Gai, F., Site-Specific Hydration Status of an Amphipathic Peptide in AOT Reverse Micelles. *Langmuir* **2007,** *23* (22), 11174-11179.

206. Phukon, A.; Ray, S.; Sahu, K., How Does Interfacial Hydration Alter during Rod to Sphere Transition in DDAB/Water/Cyclohexane Reverse Micelles? Insights from Excited State Proton Transfer and Fluorescence Anisotropy. *Langmuir* **2016,** *32* (26), 6656-6665.

207. Spry, D. B.; Goun, A.; Glusac, K.; Moilanen, D. E.; Fayer, M. D., Proton Transport and the Water Environment in Nafion Fuel Cell Membranes and AOT Reverse Micelles. *J. Am. Chem. Soc* **2007,** *129* (26), 8122-8130.

208. Sedgwick, M.; Cole, R. L.; Rithner, C. D.; Crans, D. C.; Levinger, N. E., Correlating Proton Transfer Dynamics To Probe Location in Confined Environments. *J. Am. Chem. Soc.* **2012,** *134* (29), 11904-11907.

209. Baruah, B.; Roden, J. M.; Sedgwick, M.; Correa, N. M.; Crans, D. C.; Levinger, N. E., When Is Water Not Water? Exploring Water Confined in Large Reverse Micelles Using a Highly Charged Inorganic Molecular Probe. *J. Am. Chem. Soc* **2006,** *128* (39), 12758-12765.

210. Sedgwick, M. A.; Crans, D. C.; Levinger, N. E., What Is Inside a Nonionic Reverse Micelle? Probing the Interior of Igepal Reverse Micelles Using Decavanadate. *Langmuir* **2009,** *25* (10), 5496-5503.

211. Phukon, A.; Sahu, K., The strikingly different miscibility of n-octanol in highly-confined and quasi-confined water. *Chem. commun.* **2015,** *51* (74), 14103-14106.

212. Jansson, J.; Schillén, K.; Nilsson, M.; Söderman, O.; Fritz, G.; Bergmann, A.; Glatter, O., Small-Angle X-ray Scattering, Light Scattering, and NMR Study of PEO−PPO−PEO Triblock Copolymer/Cationic Surfactant Complexes in Aqueous Solution. *J. Phys. Chem. B* **2005,** *109* (15), 7073-7083.

213. Ghosh, S.; Dey, S.; Mandal, U.; Adhikari, A.; Mondal, S. K.; Bhattacharyya, K., Ultrafast Proton Transfer of Pyranine in a Supramolecular Assembly: PEO−PPO−PEO Triblock Copolymer and CTAC. *J. Phys. Chem. B* **2007,** *111* (48), 13504-13510.

214. Almgren, M.; Van Stam, J.; Lindblad, C.; Li, P.; Stilbs, P.; Bahadur, P., Aggregation of poly(ethylene oxide)-poly(propylene oxide)-poly(ethylene oxide) triblock copolymers in the presence of sodium dodecyl sulfate in aqueous solution. *J. Phys. Chem.* **1991,** *95* (14), 5677-5684.

215. Kaneta, T.; Tanaka, S.; Taga, M.; Yoshida, H., Migration behavior of inorganic anions in micellar electrokinetic capillary chromatography using cationic surfactant. *Anal. Chem.* **1992,** *64* (7), 798-801.
216. Das, I.; Halder, M., A Global Scenario on the Dynamics of Excited State Proton Transfer of Pyranine in the Mixed Micellar Assemblies: Role of Water Accessibility in the Probe Location+. *ChemistrySelect* **2018,** *3* (16), 4527-4535.
217. Lakowicz, J. R., *Principles of fluorescence spectroscopy*. Springer: 2006.
218. Horng, M. L.; Gardecki, J. A.; Papazyan, A.; Maroncelli, M., Subpicosecond Measurements of Polar Solvation Dynamics: Coumarin 153 Revisited. *J. Phys. Chem.* **1995,** *99* (48), 17311-17337.
219. Maroncelli, M.; Fleming, G. R., Picosecond solvation dynamics of coumarin 153: The importance of molecular aspects of solvation. *J. Chem. Phys.* **1987,** *86* (11), 6221-6239.
220. Koti, A. S. R.; Periasamy, N., Time Resolved Area Normalized Emission Spectroscopy (TRANES) of DMABN Confirms Emission from Two States. *Res. Chem. Intermed.* **2002,** *28* (7), 831-836.
221. Koti, A. S. R.; Krishna, M. M. G.; Periasamy, N., Time-Resolved Area-Normalized Emission Spectroscopy (TRANES): A Novel Method for Confirming Emission from Two Excited States. *J. Phys. Chem. A* **2001,** *105* (10), 1767-1771.
222. Sahu, K.; Nandi, N.; Dolai, S.; Bera, A., A Ratio-Analysis Method for the Dynamics of Excited State Proton Transfer: Pyranine in Water and Micelles. *J. Phys. Chem. B* **2018,** *122* (25), 6610-6615.
223. Lipari, G.; Szabo, A., Effect of Librational Motion on Fluorescence Depolarization and Nuclear Magnetic Resonance Relaxation in Macromolecules and Membranes. *Biophys. J.* **1980,** *30* (3), 489-506.
224. Sahu, K.; Mondal, S. K.; Ghosh, S.; Roy, D.; Bhattacharyya, K., Temperature Dependence of Solvation Dynamics and Anisotropy Decay in a Protein: ANS in Bovine Serum Albumin. *J. Chem. Phys.* **2006,** *124* (12), 124909-7.
225. Song, H.-M.; Zink, J. I., Hard Pd Nanorods in the Soft Surfactant Mixture of CTAB and Pluronics: Seedless Synthesis and Their Self-Assembly. *Langmuir* **2018,** *34* (14), 4271-4281.
226. Nambam, J. S.; Philip, J., Effects of Interaction of Ionic and Nonionic Surfactants on Self-Assembly of PEO–PPO–PEO Triblock Copolymer in Aqueous Solution. *J. Phys. Chem. B* **2012,** *116* (5), 1499-1507.
227. Dai, S.; Tam, K. C.; Li, L., Isothermal Titration Calorimetric Studies on Interactions of Ionic Surfactant and Poly(oxypropylene)−Poly(oxyethylene)− Poly(oxypropylene) Triblock Copolymers in Aqueous Solutions. *Macromolecules* **2001,** *34* (20), 7049-7055.
228. James-Smith, M. A.; Shekhawat, D.; Cheung, S.; Moudgil, B. M.; Shah, D. O., Effect of chain length on binding of fatty acids to Pluronics in microemulsions. *Colloids and Surfaces B: Biointerfaces* **2008,** *62* (1), 5-10.
229. Singh, P. K.; Kumbhakar, M.; Ganguly, R.; Aswal, V. K.; Pal, H.; Nath, S., Time-Resolved Fluorescence and Small Angle Neutron Scattering Study in Pluronics−Surfactant Supramolecular Assemblies. *J. Phys. Chem. B* **2010,** *114* (11), 3818-3826.
230. Mondal, R.; Ghosh, N.; Mukherjee, S., Enhanced Binding of Phenosafranin to Triblock Copolymer F127 Induced by Sodium Dodecyl Sulfate: A Mixed Micellar System as an Efficient Drug Delivery Vehicle. *J. Phys. Chem. B* **2016,** *120* (11), 2968-2976.
231. Phukon, A.; Sahu, K., How Do the Interfacial Properties of Zwitterionic Sulfobetaine Micelles Differ from those of Cationic Alkyl Quaternary Ammonium Micelles? An Excited State Proton Transfer Study. *Phys. Chem. Chem. Phys.* **2017,** *19*, 31461-31468.
232. Sahu, K.; Nandi, N.; Dolai, S.; Bera, A., A Ratio-Analysis Method for the Dynamics of Excited State Proton Transfer: Pyranine in Water and Micelles. *J. Phys. Chem. B* **2018,** *122* (25), 6610-6615.

233. Nandi, N.; Sahu, K., Analysis of Excited State Proton Transfer Dynamics of HPTS in Methanol-Water Mixtures from Time-Resolved Area-Normalised Emission Spectrum (TRANES). *J. Photochem. Photobiol. A* **2019,** *374*, 138-144.

234. Ghosh, S.; Kuchlyan, J.; Banik, D.; Kundu, N.; Roy, A.; Banerjee, C.; Sarkar, N., Organic Additive, 5-Methylsalicylic Acid Induces Spontaneous Structural Transformation of Aqueous Pluronic Triblock Copolymer Solution: A Spectroscopic Investigation of Interaction of Curcumin with Pluronic Micellar and Vesicular Aggregates. *J Phys Chem B* **2014,** *118* (39), 11437-11448.

235. Anand, U.; Mukherjee, S., Microheterogeneity and Microviscosity of F127 Micelle: The Counter Effects of Urea and Temperature. *Langmuir* **2014,** *30* (4), 1012-1021.

236. Phukon, A.; Nandi, N.; Sahu, K., Pre-Micellar Interaction or Direct Monomer to Micelle Transition for Zwitterionic Sulfobetaine Surfactant in Water? A Comparative Fluorescence Study with Cationic Surfactant. *J. Photochem. Photobiol. A* **2018,** *357*, 140-148.

237. Phukon, A.; Barman, N.; Sahu, K., Wet Interface of Benzylhexadecyldimethylammonium Chloride Reverse Micelle Revealed by Excited State Proton Transfer of a Localized Probe. *Langmuir* **2015,** *31* (46), 12587-12596.

238. Phukon, A.; Ray, S.; Sahu, K., Effect of Cosurfactants on the Interfacial Hydration of CTAB Quaternary Reverse Micelle Probed Using Excited State Proton Transfer. *Langmuir* **2016,** *32* (41), 10659-10667.

239. Mora, A. K.; Singh, P. K.; Nath, S., Controlled Sequestration of DNA Intercalated Drug by Polymer–Surfactant Supramolecular Assemblies. *J. Phys. Chem. B* **2016,** *120* (17), 4143-4151.

240. Naskar, B.; Dey, A.; Moulik, S. P., Counter-ion Effect on Micellization of Ionic Surfactants: A Comprehensive Understanding with Two Representatives, Sodium Dodecyl Sulfate (SDS) and Dodecyltrimethylammonium Bromide (DTAB). *J Surfactants Deterg* **2013,** *16* (5), 785-794.

241. Lin, W.-H.; Lu, Y.-H.; Hsu, Y.-J., Au Nanoplates as Robust, Recyclable SERS Substrates for Ultrasensitive Chemical Sensing. *J. Colloid Interface Sci.* **2014,** *418*, 87-94.

242. Scarabelli, L.; Coronado-Puchau, M.; Giner-Casares, J. J.; Langer, J.; Liz-Marzán, L. M., Monodisperse Gold Nanotriangles: Size Control, Large-Scale Self-Assembly, and Performance in Surface-Enhanced Raman Scattering. *ACS Nano* **2014,** *8* (6), 5833-5842.

243. Chang, C.-C.; Wang, G.; Takarada, T.; Maeda, M., Iodine-Mediated Etching of Triangular Gold Nanoplates for Colorimetric Sensing of Copper Ion and Aptasensing of Chloramphenicol. *ACS Appl. Mater. Interfaces* **2017,** *9* (39), 34518-34525.

244. Wu, G.; Mikhailovsky, A.; Khant, H. A.; Fu, C.; Chiu, W.; Zasadzinski, J. A., Remotely Triggered Liposome Release by Near-Infrared Light Absorption via Hollow Gold Nanoshells. *J. Am. Chem. Soc* **2008,** *130* (26), 8175-8177.

245. Singh, A. V.; Batuwangala, M.; Mundra, R.; Mehta, K.; Patke, S.; Falletta, E.; Patil, R.; Gade, W. N., Biomineralized Anisotropic Gold Microplate–Macrophage Interactions Reveal Frustrated Phagocytosis-like Phenomenon: A Novel Paclitaxel Drug Delivery Vehicle. *ACS Appl. Mater. Interfaces* **2014,** *6* (16), 14679-14689.

246. Shankar, S. S.; Rai, A.; Ankamwar, B.; Singh, A.; Ahmad, A.; Sastry, M., Biological Synthesis of Triangular Gold Nanoprisms. *Nat. Mater* **2004,** *3* (7), 482-488.

247. Palui, G.; Ray, S.; Banerjee, A., Synthesis of Multiple Shaped Gold Nanoparticles Using Wet Chemical Method by Different Dendritic Peptides at Room Temperature. *J. Mat. Chem.* **2009,** *19* (21), 3457-3468.

248. Osonga, F. J.; Kariuki, V. M.; Wambua, V. M.; Kalra, S.; Nweke, B.; Miller, R. M.; Çeşme, M.; Sadik, O. A., Photochemical Synthesis and Catalytic Applications of Gold Nanoplates Fabricated Using Quercetin Diphosphate Macromolecules. *ACS Omega* **2019,** *4* (4), 6511-6520.

249. Vigderman, L.; Manna, P.; Zubarev, E. R., Quantitative Replacement of Cetyl Trimethylammonium Bromide by Cationic Thiol Ligands on the Surface of Gold Nanorods and Their Extremely Large Uptake by Cancer Cells. *Angew. Chem. Int. Ed.* **2012,** *51* (3), 636-641.

250. Sardar, R.; Park, J.-W.; Shumaker-Parry, J. S., Polymer-Induced Synthesis of Stable Gold and Silver Nanoparticles and Subsequent Ligand Exchange in Water. *Langmuir* **2007,** *23* (23), 11883-11889.

251. Burda, C.; Chen, X.; Narayanan, R.; El-Sayed, M. A., Chemistry and Properties of Nanocrystals of Different Shapes. *Chem. Rev* **2005,** *105* (4), 1025-1102.

252. Jana, N. R.; Gearheart, L.; Murphy, C. J., Seed-Mediated Growth Approach for Shape-Controlled Synthesis of Spheroidal and Rod-like Gold Nanoparticles Using a Surfactant Template. *Adv. Mater.* **2001,** *13* (18), 1389-1393.

253. Lohse, S. E.; Murphy, C. J., The Quest for Shape Control: A History of Gold Nanorod Synthesis. *Chem. Mater.* **2013,** *25* (8), 1250-1261.

254. Scarabelli, L.; Sánchez-Iglesias, A.; Pérez-Juste, J.; Liz-Marzán, L. M., A “Tips and Tricks” Practical Guide to the Synthesis of Gold Nanorods. *J. Phys. Chem. Lett.* **2015,** *6* (21), 4270-4279.

255. Kumar, S.; Gandhi, K. S.; Kumar, R., Modeling of Formation of Gold Nanoparticles by Citrate Method. *J Ind Eng Chem* **2007,** *46* (10), 3128-3136.

256. Ojea-Jiménez, I.; Romero, F. M.; Bastús, N. G.; Puntes, V., Small Gold Nanoparticles Synthesized with Sodium Citrate and Heavy Water: Insights into the Reaction Mechanism. *J. Phys. Chem. C* **2010,** *114* (4), 1800-1804.

257. Rodríguez-Fernández, J.; Pérez-Juste, J.; García de Abajo, F. J.; Liz-Marzán, L. M., Seeded Growth of Submicron Au Colloids with Quadrupole Plasmon Resonance Modes. *Langmuir* **2006,** *22* (16), 7007-7010.

258. Pérez-Juste, J.; Liz-Marzán, L. M.; Carnie, S.; Chan, D. Y. C.; Mulvaney, P., Electric-Field-Directed Growth of Gold Nanorods in Aqueous Surfactant Solutions. *Adv. Funct. Mater.* **2004,** *14* (6), 571-579.

259. Pileni, M.-P., The role of soft colloidal templates in controlling the size and shape of inorganic nanocrystals. *Nat. Mater.* **2003,** *2* (3), 145-150.

260. Wang, L.; Chen, X.; Zhan, J.; Chai, Y.; Yang, C.; Xu, L.; Zhuang, W.; Jing, B., Synthesis of Gold Nano- and Microplates in Hexagonal Liquid Crystals. *J. Phys. Chem. B* **2005,** *109* (8), 3189-3194.

261. Xia, J.; Dong, Z.; Cai, Y.; Guan, G.; Zhang, S.; Kovács, A.; Boothroyd, C.; Phang, I. Y.; Liu, S.; Wu, M.; Zhang, Y. W.; Hu, X.; Han, M.-Y., Morphological Growth and Theoretical Understanding of Gold and Other Noble Metal Nanoplates. *Chem. Eur. J.* **2018,** *24* (58), 15589-15595.

262. Chen, L.; Ji, F.; Xu, Y.; He, L.; Mi, Y.; Bao, F.; Sun, B.; Zhang, X.; Zhang, Q., High-Yield Seedless Synthesis of Triangular Gold Nanoplates through Oxidative Etching. *Nano Lett.* **2014,** *14* (12), 7201-7206.

263. Pal, T.; Sahu, K., Comparison of interaction patterns of a triblock copolymer micelle with zwitterionic vs. cationic surfactant: An excited-state proton transfer dynamics investigation. *Colloids Surf. A Physicochem. Eng. Asp.* **2022,** *640*, 128327.

264. Vyas, B.; Pillai, S. A.; Bahadur, P., Influence of surfactant's polar head group charge on the self-assembly of three PEO–PPO–PEO triblock copolymers of widely varying hydrophobicity. *J. Mol. Liq.* **2020,** *316*, 113858.

265. Hao, L.-S.; Xiao, K.; Hu, Y.; Zhang, S.-S.; Liu, J.-X.; Wei, Y.-Y.; Chen, Y.; Nan, Y.-Q., Mixed Micellization of Cationic/Anionic Surfactants: Role of Matching Water Affinities between Oppositely Charged Headgroups and That between Oppositely Charged Constituent Counterions. *J. Phys. Chem. B* **2019,** *123* (38), 8140-8153.

266. Penfold, J.; Tucker, I.; Thomas, R. K.; Staples, E.; Schuermann, R., Structure of Mixed Anionic/Nonionic Surfactant Micelles: Experimental Observations Relating to the Role of Headgroup Electrostatic and Steric Effects and the Effects of Added Electrolyte. *J. Phys. Chem. B* **2005,** *109* (21), 10760-10770.

267. Kaur, R.; Kumar, S.; Aswal, V. K.; Mahajan, R. K., Influence of Headgroup on the Aggregation and Interactional Behavior of Twin-Tailed Cationic Surfactants with Pluronics. *Langmuir* **2013,** *29* (38), 11821-11833.

268. Pal, T.; Sahu, K., Anomalous Variation of Excited-State Proton Transfer Dynamics inside a Triblock Copolymer–Cationic Surfactant Mixed Micelle. *J. Phys. Chem. B* **2019,** *123* (40), 8559-8568.

269. MacNeil, J. A.; Ray, G. B.; Leaist, D. G., Activity Coefficients and Free Energies of Nonionic Mixed Surfactant Solutions from Vapor-Pressure and Freezing-Point Osmometry. *J. Phys. Chem. B* **2011,** *115* (19), 5947-5957.

270. Penfold, J.; Tucker, I.; Thomas, R. K.; Taylor, D. J. F.; Zhang, X. L.; Bell, C.; Breward, C.; Howell, P., The Interaction between Sodium Alkyl Sulfate Surfactants and the Oppositely Charged Polyelectrolyte, polyDMDAAC, at the Air−Water Interface: The Role of Alkyl Chain Length and Electrolyte and Comparison with Theoretical Predictions. *Langmuir* **2007,** *23* (6), 3128-3136.

271. Dan, A.; Ghosh, S.; Moulik, S. P., Physicochemistry of the Interaction between Inulin and Alkyltrimethylammonium Bromides in Aqueous Medium and the Formed Coacervates. *J. Phys. Chem. B* **2009,** *113* (25), 8505-8513.

272. Park, B. J.; Pantina, J. P.; Furst, E. M.; Oettel, M.; Reynaert, S.; Vermant, J., Direct Measurements of the Effects of Salt and Surfactant on Interaction Forces between Colloidal Particles at Water−Oil Interfaces. *Langmuir* **2008,** *24* (5), 1686-1694.

273. Sharma, V. K.; Srinivasan, H.; Mitra, S.; Garcia-Sakai, V.; Mukhopadhyay, R., Effects of Hydrotropic Salt on the Nanoscopic Dynamics of DTAB Micelles. *The Journal of Physical Chemistry B* **2017,** *121* (22), 5562-5572.

274. Hou, B.; Jia, R.; Fu, M.; Wang, Y.; Bai, Y.; Huang, Y., Wettability Alteration of an Oil-Wet Sandstone Surface by Synergistic Adsorption/Desorption of Cationic/Nonionic Surfactant Mixtures. *Energy Fuels* **2018,** *32* (12), 12462-12468.

275. Qazi, M. J.; Schlegel, S. J.; Backus, E. H. G.; Bonn, M.; Bonn, D.; Shahidzadeh, N., Dynamic Surface Tension of Surfactants in the Presence of High Salt Concentrations. *Langmuir* **2020,** *36* (27), 7956-7964.

276. Rafique, A. S.; Khodaparast, S.; Poulos, A. S.; Sharratt, W. N.; Robles, E. S. J.; Cabral, J. T., Micellar structure and transformations in sodium alkylbenzenesulfonate (NaLAS) aqueous solutions: effects of concentration, temperature, and salt. *Soft Matter* **2020,** *16* (33), 7835-7844.

277. Fehér, B.; Zhu, K.; Nyström, B.; Varga, I.; Pedersen, J. S., Effect of Temperature and Ionic Strength on Micellar Aggregates of Oppositely Charged Thermoresponsive Block Copolymer Polyelectrolytes. *Langmuir* **2019,** *35* (42), 13614-13623.

278. Kumbhakar, M.; Goel, T.; Mukherjee, T.; Pal, H., Nature of the Water Molecules in the Palisade Layer of a Triton X-100 Micelle in the Presence of Added Salts: A Solvation Dynamics Study. *J. Phys. Chem. B* **2005,** *109* (29), 14168-14174.

279. Charlton, I. D.; Doherty, A. P., Electrolyte-Induced Structural Evolution of Triton X-100 Micelles. *J. Phys. Chem. B* **2000,** *104* (34), 8327-8332.

280. Hyde, A. M.; Zultanski, S. L.; Waldman, J. H.; Zhong, Y.-L.; Shevlin, M.; Peng, F., General Principles and Strategies for Salting-Out Informed by the Hofmeister Series. *Org. Process Res. Dev.* **2017,** *21* (9), 1355-1370.

281. Patidar, P.; Bahadur, A., Modulating effect of different biomolecules and other additives on cloud point and aggregation of amphiphilic linear and starblock copolymer. *J. Mol. Liq.* **2018,** *249*, 219-226.

282. Patel, D.; Rathod, S.; Tiwari, S.; Ray, D.; Kuperkar, K.; Aswal, V. K.; Bahadur, P., Self-Association in EO–BO–EO Triblock Copolymers as a Nanocarrier Template for Sustainable Release of Anticancer Drugs. *The Journal of Physical Chemistry B* **2020,** *124* (51), 11750-11761.

283. Bhattacharjee, S.; Pandit, S.; Seth, D., How Kosmotropic and Chaotropic Osmolytes Perturb the Properties of an Aqueous Solution of a Pluronic Block Copolymer? *Langmuir* **2022,** *38* (30), 9347-9362.

284. Isabettini, S.; Böni, L. J.; Baumgartner, M.; Saito, K.; Kuster, S.; Fischer, P.; Lutz-Bueno, V., Higher Salt Hydrophobicity Lengthens Ionic Wormlike Micelles and Stabilizes Them upon Heating. *Langmuir* **2021,** *37* (1), 132-138.

285. Jensen, G. V.; Lund, R.; Narayanan, T.; Pedersen, J. S., Transformation from Globular to Cylindrical Mixed Micelles through Molecular Exchange that Induces Micelle Fusion. *J. Phys. Chem. Lett.* **2016,** *7* (11), 2039-2043.

286. Burnstine-Townley, A.; Mondal, S.; Agam, Y.; Nandi, R.; Amdursky, N., Light-Modulated Cationic and Anionic Transport across Protein Biopolymers**. *Angew. Chem. Int. Ed.* **2021,** *60* (46), 24676-24685.

287. Akutsu, H.; Seelig, J., Interaction of metal ions with phosphatidylcholine bilayer membranes. *Biochemistry* **1981,** *20* (26), 7366-7373.

288. Seelig, J.; MacDonald, P. M.; Scherer, P. G., Phospholipid head groups as sensors of electric charge in membranes. *Biochemistry* **1987,** *26* (24), 7535-7541.

289. Szule, J. A.; Jarvis, S. E.; Hibbert, J. E.; Spafford, J. D.; Braun, J. E. A.; Zamponi, G. W.; Wessel, G. M.; Coorssen, J. R., Calcium-triggered Membrane Fusion Proceeds Independently of Specific Presynaptic Proteins*. *Journal of Biological Chemistry* **2003,** *278* (27), 24251-24254.

290. Ma, J.-h.; Guo, C.; Tang, Y.-l.; Wang, J.; Zheng, L.; Liang, X.-f.; Chen, S.; Liu, H.-z., Salt-Induced Micellization of a Triblock Copolymer in Aqueous Solution: A 1H Nuclear Magnetic Resonance Spectroscopy Study. *Langmuir* **2007,** *23* (6), 3075-3083.

291. Singh, S.; Koley, S.; Mishra, K.; Ghosh, S., An Approach to a Model Free Analysis of Excited-State Proton Transfer Kinetics in a Reverse Micelle. *J. Phys. Chem. C* **2018,** *122* (1), 732-740.

292. Kalel, R.; Mora, A. K.; Patro, B. S.; Palit, D. K.; Nath, S., Synergistic Enhancement in the Drug Sequestration Power and Reduction in the Cytotoxicity of Surfactants. *Phys. Chem. Chem. Phys.* **2017,** *19* (37), 25446-25455.

293. Chang, L.-W.; Lytle, T. K.; Radhakrishna, M.; Madinya, J. J.; Vélez, J.; Sing, C. E.; Perry, S. L., Sequence and entropy-based control of complex coacervates. *Nature Commun.* **2017,** *8* (1), 1273.

294. Fu, J.; Schlenoff, J. B., Driving Forces for Oppositely Charged Polyion Association in Aqueous Solutions: Enthalpic, Entropic, but Not Electrostatic. *J. Am. Chem. Soc.* **2016,** *138* (3), 980-990.

295. Pergushov, D. V.; Müller, A. H. E.; Schacher, F. H., Micellar interpolyelectrolyte complexes. *Chem. Soc. Rev.* **2012,** *41* (21), 6888-6901.

296. Savariar, E. N.; Ghosh, S.; González, D. C.; Thayumanavan, S., Disassembly of Noncovalent Amphiphilic Polymers with Proteins and Utility in Pattern Sensing. *J. Am. Chem. Soc.* **2008,** *130* (16), 5416-5417.

297. Palivan, C. G.; Fischer-Onaca, O.; Delcea, M.; Itel, F.; Meier, W., Protein–polymer nanoreactors for medical applications. *Chem. Soc. Rev.* **2012,** *41* (7), 2800-2823.

298. Saini, B.; Singh, S.; Mukherjee, T. K., Nanocatalysis under Nanoconfinement: A Metal-Free Hybrid Coacervate Nanodroplet as a Catalytic Nanoreactor for Efficient Redox and Photocatalytic Reactions. *ACS Appl. Mater. Interfaces* **2021,** *13* (43), 51117-51131.

299. Kizilay, E.; Maccarrone, S.; Foun, E.; Dinsmore, A. D.; Dubin, P. L., Cluster Formation in Polyelectrolyte−Micelle Complex Coacervation. *J. Phys. Chem. B* **2011,** *115* (22), 7256-7263.

300. Sakuta, H.; Fujimoto, T.; Yamana, Y.; Hoda, Y.; Tsumoto, K.; Yoshikawa, K., Aqueous/Aqueous Micro Phase Separation: Construction of an Artificial Model of Cellular Assembly. *Front Chem* **2019,** *7, 44*.

301. Niskanen, J.; Peltekoff, A. J.; Bullet, J.-R.; Lessard, B. H.; Winnik, F. M., Enthalpy of the Complexation in Electrolyte Solutions of Polycations and Polyzwitterions of Different Structures and Topologies. *Macromolecules* **2021,** *54* (14), 6678-6690.
302. Piculell, L., Understanding and Exploiting the Phase Behavior of Mixtures of Oppositely Charged Polymers and Surfactants in Water. *Langmuir* **2013,** *29* (33), 10313-10329.
303. Fan, Y.; Kellermeier, M.; Xu, A. Y.; Boyko, V.; Mirtschin, S.; Dubin, P. L., Modulation of Polyelectrolyte–Micelle Interactions via Zeta Potentials. *Macromolecules* **2017,** *50* (14), 5518-5526.
304. Plazzotta, B.; Fegyver, E.; Mészáros, R.; Pedersen, J. S., Anisometric Polyelectrolyte/Mixed Surfactant Nanoassemblies Formed by the Association of Poly(diallyldimethylammonium chloride) with Sodium Dodecyl Sulfate and Dodecyl Maltoside. *Langmuir* **2015,** *31* (26), 7242-7250.
305. Dodoo, S.; Steitz, R.; Laschewsky, A.; von Klitzing, R., Effect of ionic strength and type of ions on the structure of water swollen polyelectrolyte multilayers. *Phys. Chem. Chem. Phys.* **2011,** *13* (21), 10318-10325.
306. Politi, M. J.; Fendler, J. H., Laser pH-jump initiated proton transfer on charged micellar surfaces. *J. Am. Chem. Soc.* **1984,** *106* (2), 265-273.
307. Phukon, A.; Nandi, N.; Sahu, K., Pre-Micellar Interaction or Direct Monomer to Micelle Transition for Zwitterionic Sulfobetaine Surfactant in Water? A Comparative Fluorescence Study with Cationic Surfactant. *J. Photochem. Photobiol. A.* **2018,** *357*, 140-148.
308. Müller, J. G.; Atas, E.; Tan, C.; Schanze, K. S.; Kleiman, V. D., The Role of Exciton Hopping and Direct Energy Transfer in the Efficient Quenching of Conjugated Polyelectrolytes. *J. Am. Chem. Soc.* **2006,** *128* (12), 4007-4016.
309. Koti, A. S. R.; Periasamy, N., Application of Time Resolved Area Normalized Emission Spectroscopy to Multicomponent Systems. *J. Chem. Phys.* **2001,** *115* (15), 7094-7099.